Title

Synoptic and local influences on boundary layer processes, with an application to California wind power

Permalink

Author

Mansbach, David K.

Publication Date

2010

UNIVERSITY OF CALIFORNIA, SAN DIEGO

Synoptic and local influences on boundary layer processes, with an application to California wind power

A dissertation submitted in partial satisfaction of the
requirements for the degree
Doctor of Philosophy

in

Oceanography

by

David K. Mansbach

Committee in charge:

Joel R. Norris, Chair
Daniel Cayan, Co-Chair
Masao Kanamitsu
Dimitris Politis
V. Ramanathan
Lynne Talley

2010

The dissertation of David K. Mansbach is approved, and it is acceptable in quality and form for publication on microfilm and electronically:

Co-Chair

Chair

University of California, San Diego

2010

DEDICATION

To Lane, Jú, and the jaña.

TABLE OF CONTENTS

LIST OF FIGURES

LIST OF TABLES

ACKNOWLEDGEMENTS

This work would not have been possible without the support, patience, and guidance of several exceptional individuals. Dan Cayan provided invaluable scientific steering, perspective on research strategy, and the common sense needed to get things back on track after setbacks, and these will always serve as a guide on any project I undertake. Joel Norris shared with me a copious amount of scientific expertise regarding everything from cloud microphysics to global climate dynamics, which still forms the core of my knowledge of climate science research. Moreover, he did this while generously treating me, from day one, with all the respect he would afford to an accomplished scientific peer, and supported me and showed confidence in my abilities long after I had lost it.

Kanamitsu provided frequent support about any topic I brought to him, as well as the frequent pleasant sound of laughter in an otherwise silent hallway. The other members of my committee, Dimitris Politis, V. Ramanathan, and Lynne Talley, each lent their own mixture of perspective and helpful questioning to guide my investigations and my overall progress.

Beyond these core contributors to my research, I am indebted to the diverse group of professors at Scripps who provided me with a thorough and powerful scientific background through coursework.

Additionally, I would like to thank Art Miller, who has always been generous with his scientific expertise and practical knowledge. Sasha Gershunov likewise has been edifying scientifically and has lent great perspective to matters less related to research. Martin Olivera provided me with the best systems support I will ever see. Glenn Ierley, Sam Iacobellis, Dawn Huffman, Mary Tyree, Jennifer Johns, and many others have also markedly improved my time here.

I was fortunate to carry out my coursework and research with minimal worries about funding — a privilege that many graduate students and scientists deserve but do not enjoy. I owe this happy fact to the qualifications and grantwriting prowess of my advisors, in addition to the funding sources themselves: the National Science Foundation, the Department of Energy, NASA (including the extensive support of an Earth System Science Fellowship), the Scripps Graduate Fellowship, a California Space Institute/Space Grant fellowship, the NOAA RISA program through the California Applications Program, and the California Energy Commission through the California Climate Change

Center.

All the resources and scientific guidance in the world would have been insufficient for me to carry out this work if not for the love and support of my wife, Lane. My parents, Nancy and Charlie, were also instrumental in our lives throughout this period, and I have also relied on my brother, Adam, and cousins, Ben and Matt.

While at Scripps I have been lucky to enjoy great friendships and support from my classmates. Jamie Holte, Marissa Yates, and Aurelien Ponte were peers and companions from coursework through to defending, and will always remain great friends. Kaustubha Raghukumar, Guillaume Mauger, Steve Taylor, Ashley Medin, Neil Gordon, Theresa Carpenter and too many others to name have all given me the gift of their friendship.

To all, thank you.

Chapter 2 in its entirety is a reprint with no modifications to content of the article "Low-Level Cloud Variability over the Equatorial Cold Tongue in Observations and Models" that appeared in *Journal of Climate*, 2007, **20**, 1555-1570 (Copyright of the American Meteorological Society 2007). The dissertation author was the first author and primary researcher with guidance and contributions from the second author, J.R. Norris.

Chapter 3, in full, is a reprint with minor modifications of the article "Climatology and meteorological influences on California's wind energy resource. Part 1: General characteristics and seasonal cycle," to be submitted for publication. The author of the dissertation is the first author and primary researcher, and contributions were also made by the scond author, D. Cayan.

Chapter 4, in part, is a reprint with minor modifications of the article "Climatology and meteorological influences on California's wind energy resource. Part 2: Synoptic and diurnal characteristics," to be submitted for publication. The author of the dissertation is the first author and primary researcher, and contributions were also made by the scond author, D. Cayan.

Chapter 5, in full, is a reprint with minor modifications of the article "Formulation of a statistical downscaling model for California site winds, with an application to 21$^{\text{st}}$ century climate scenarios," to be submitted for publication. The author of the dissertation is the sole author.

VITA

2002	A.B. with dual concentration in Math-Physics and International Relations, Brown University
2010	Ph.D. in Oceanography, Scripps Institution of Oceanography, University of California, San Diego

ABSTRACT OF THE DISSERTATION

Synoptic and local influences on boundary layer processes, with an application to California wind power

by

David K. Mansbach

Doctor of Philosophy in Oceanography

University of California, San Diego, 2010

Joel R. Norris, Chair
Daniel Cayan, Co-Chair

This dissertation examines atmospheric boundary-layer processes.

The equatorial Pacific cold tongue region is examined, with observations showing that monthly anomalies in low-level cloud amount and near-surface atmospheric temperature advection are negatively correlated. In warm advection, soundings show the surface layer is stably stratified, inhibiting the upward mixing of moisture, while cold advection favors a more convective atmospheric boundary layer and greater cloud amount. Two global coupled climate models fail to simulate this, suggesting specific areas for possible improvement.

Climatology and low-level wind variability near three California wind farms are then explored: San Gorgonio Pass and Tehachapi Pass in Southern California, and Solano

County further north. Each site has a pronounced annual cycle with highest wind speeds in the warm months. While winter winds depend more on SLP, summertime winds are stronger, more diurnally dependent, and show more topographic influence on direction, though SLP variability is lesser.

Self-organizing maps reveal that oceanic high SLP and continental low SLP synoptic patterns lead to higher wind speeds. SLP gradients at 100km separation are strongly correlated to cotemporaneous site wind speeds. Dynamically downscaled reanalysis data at 10km resolution reveals that a thermally driven flow at the northern site commences at the coast and propagates inland in a distinct packet. The 10km model does not resolve the Gorgonio Pass flow, but another model at 2.5km validates well and shows that the observed winds depend on interactions between solar and lateral boundary forcing.

A statistical downscaling scheme is developed for relating GCM output to site winds. The multilinear regression model integrates weather type information and observational findings to reproduce wind speeds, showing skill for both monthly and daily data. Monthly mean wind speed changes over the 21st century are implied of up to 0.6 m/s in the summertime in three downscaled coupled climate models under greenhouse forcing. However, the discrepancies between models prevent consensus. Analysis of the discrepancies reveal that in one model the western North American surface heating coincides with a decrease in SLP, while others show increased continental SLP. The coupled models' representations of these regional patterns are discussed.

Chapter 1

Introduction

The atmospheric boundary layer serves a key role in many processes on Earth. In marine environments, the boundary layer regulates air-sea exchanges of many things: gases, horizontal momentum, sensible heat, moisture, and aerosol particles. The presence and characteristics of boundary-layer clouds can also strongly affect radiative transfer and column-integrated energy balance. Atmospheric boundary layers over land also regulate sensible and latent heat, gases, and particulate matter, and can be a major sink of horizontal momentum, especially in the presence of topography or significant vegetation. The atmospheric boundary layer is naturally the site where the human, animal, and ecosystem impacts of most weather and climate phenomena are realized, and also holds great importance for trace gas and contaminant fate determination. This dissertation contains studies of both marine and terrestrial atmospheric boundary layers, looking at processes on a variety of spatial and temporal scales with three main goals: to better understand the boundary layer marine clouds that are crucial to Earth's energy balance, to elucidate the details of low-level circulations that drive wind farms, and to consider the effects of anthropogenic climate change in these winds.

Although exact definitions vary with setting, atmospheric boundary layers tend to develop wherever deep convection is not present (Stull, 1988). A qualitative explanation for such a layer's existence is intuitive for the case of a cool sea surface temperature (SST) area under an atmospheric subsidence regime. In such a setting the relatively warmer descending air will naturally settle above the cold area influenced by the ocean surface, leading to a sharp inversion that caps the boundary layer (Lilly, 1968). For land areas — our focus being California — the contrast is less dramatic, as subsidence often overlies air influenced by daytime surface heating, and a boundary layer with more pronounced diurnal variations can develop, as seen in vertical profiles of temperature and momentum (ie Warner, 2004; Iacobellis et al., 2009). Although the principal elements of marine boundary layers are present also in continental settings, the more efficient solar heating of land than water and the presence of vegetation and topography means that, in practice, the focus is quite different in the two cases. Both marine and continental boundary layers reflect forcing on many scales. Larger-scale forcing mechanisms include subsidence related to deep tropical convection, large-scale ocean gyres that dictate SST, or synoptic-scale dynamics such as effects of horizontal momentum excited by free-tropospheric pressure gradients and frontal passage, while local vertical boundary forcing mechanisms include patchy oceanic upwelling, surface fluxes into the atmosphere, and surface drag.

The importance of marine boundary layers, however, is by no means limited to local scales. Marine stratocumulus clouds reflect far more incoming radiation back to space than they trap in outgoing longwave radiation emitted from the surface, and contribute greatly to the global negative radiative forcing role of clouds in the current climate (Ramanathan et al., 1989). The stability or change in this condition in response to forcing on different scales under global climate change, however, is unknown, and motivates the first study in this dissertation (Bony and Dufresne, 2005; Stephens, 2005).

Chapter 2 focuses on marine boundary layer clouds near the low SST region of the eastern equatorial Pacific cold tongue. The area, which has mainly stratocumulus clouds as well as some shallow cumulus clouds (Norris, 1998a), provides a sort of natural laboratory because it holds similar SST ranges and lower-troposoheric conditions as the eastern subtropical ocean areas where stratocumulus clouds predominate (Klein and Hartmann, 1993), but the spatial distribution of the SSTs in relationship to the characteristic low-level wind streamlines is markedly different. Rather than a typical condition of winds blowing from cool to warm areas, the cold tongue region has a notable area of low-level advection from warm to cool SST areas just south of the equator. Chapter 2 shows how satellite-observed monthly mean cloudiness is related to variations in “SST advection” by wind, implying that some of the stratocumulus variability explored in past studies (ie, Klein and Hartmann, 1993; Albrecht et al., 1995, 1988) may not have explored the full importance of SST advection because it is consistently negative in these regions. It further demonstrates that several major GCMs fail to capture observed SST advection-cloud covariability around the cold tongue region, and suggests that improving performance in this area could lead to a better representation of low-level clouds and their variability.

Chapters 3-5 represent a change in focus toward the terrestrial atmospheric boundary layer and the detailed meteorology and climatology forcing the wind at three major California wind farms. This is clearly a much more applied topic than Chapter 2, and overall the studies attempt to walk a careful path between general meteorology and overspecialization. In particular, although California overall has had large-scale wind farms for decades, the peer-reviewed literature does not comprehensively diagnose the interactions between synoptic, topographic, and local forcings that drive the winds at these sites (Gipe, 1995). Our focus on the most important, previously overlooked aspects of wind power meteorology, for instance, leads to a focus on variability at the annual, synoptic, and diurnal time scales, as clearly suggested by spectral analysis for every data set examined. This focus leans toward the basic meteorological aspect of the problems as objectively defined by periodograms, while a more applied approach than ours would give more attention to hourly and seasonal time scales. The reason such a highly applied study would do so is that the former are of great importance to short-term electricity markets (McSharry et al., 2005), while the latter are often critical to determining the level of fuel risk that might harm a wind farm developer's ability to repay financial obligations. Although these are mentioned in our study, they are not emphasized as much as the objectively determined scales of variability.

The California wind farm studies in chapters 3-5 touch on annual cycles of regional meteorological conditions, synoptic weather pattern analysis and classification, and local circulations in areas of complex orography and vegetation patterns. While much of the work relies on and refers to previous, more general theoretical and observational studies, the work in the dissertation has relevance to future meteorological studies beyond the application to wind power. In particular, the analysis of southern California winds can further inform future work on coastal winds and upwelling (such as previously examined in Dorman and Winant, 1995; Taylor et al., 2008), southern California climate, precipitation, and fire risk (Conil and Hall, 2006; Westerling et al., 2004; Hughes and Hall, 2009), and air pollution meteorology (Zhong et al., 2004; Bao et al., 2008), just as it draws on these topics in the first place.

The final component of the dissertation, in chapter 5, reconnects with the issue of global climate change by examining its possible effects on wind power in California. Since chapters 3-4 are inspired and based around the complex terrain and presence of local circulations in California, direct analysis of low-level winds from GCMs is inaccurate and some form of downscaling is necessary. The chapter serves the twin purposes of showing a method to relate thorough observational analysis to a statistical downscaling model and using this model to bracket potential changes in wind speed at the sites of interest under a certain greenhouse gas emissions storyline. The methodology described could easily be adapted to different sites or different forcing data sets, and to other fields besides wind speed. The results of applying the models to forced GCMs, in addition to their relevance to wind generation and long-term public utility planning, also highlight the strengths and limitations of using the current crop of forced GCM climate scenarios to inform questions of regional climate change. Our intention is to show what the downscaling model implies for wind energy at the same time that we illustrate larger issues and uncertainties regarding 21st century regional climate change.

For all of the research undertaken, analysis of observations is the principal tool used to understand the atmospheric boundary layer processes. This is not to belittle the value of analytic or numerically modeled research; past studies in energy balance models, dynamics and thermodynamics of boundary layers, and models from regional scale down through mesoscale to large eddy simulations are constantly referred to in this dissertation. The chosen approach is simply recognition of the fact that boundary layers fundamentally contain high Reynolds number flow and turbulent fluxes that cannot be explicitly resolved, and furthermore that uncertainties regarding physical and microphysical fluxes and processes are important questions the science has not yet fully captured in theory and models. The overall aim of this dissertation, then, is to use targeted observational analysis to understand boundary layer processes that are not fully described by current theory and numerical modeling work.

Chapter 2

Low-level cloud variability over the equatorial cold tongue in observations and models

2.1 Abstract

Examination of cloud and meteorological observations from satellite, surface, and reanalysis datasets indicates that monthly anomalies in low-level cloud amount and near-surface temperature advection are strongly negatively correlated on the southern side of the equatorial Pacific cold tongue. This inverse correlation occurs independently of relationships between cloud amount and sea surface temperature (SST) or lower tropospheric static stability (LTS) and the combination of advection plus SST or LTS explains significantly more interannual cloud variability in a multilinear regression than does SST or LTS alone. Warm anomalous advection occurs when the equatorial cold tongue is well defined and the southeastern Pacific trade winds bring relatively warm air over colder water. Ship meteorological reports and soundings show that the atmospheric surface layer becomes stratified under these conditions, thus inhibiting the upward mixing of moisture needed to sustain cloudiness against subsidence and entrainment drying. Cold anomalous advection primarily occurs when the equatorial cold tongue is weak or absent and the air-sea temperature difference is substantially negative. These conditions favor a more convective atmospheric boundary layer, greater cloud amount, and less frequent occurrence of clear sky.

Examination of output from global climate models developed by the Geophysical

Fluid Dynamics Laboratory (GFDL) and the National Center for Atmospheric Research (NCAR) indicates that both models generally fail to simulate the cloud-advection relationships observed on the northern and southern sides of the equatorial cold tongue. Although the GFDL atmosphere model does reproduce the expected signs of cloud-advection correlations when forced with prescribed historical SST variations, it does not consistently do so when coupled to an ocean model. The NCAR model has difficulty reproducing the observed correlations in both atmosphere-only and coupled versions. This suggests that boundary layer cloud parameterizations could be improved through better representation of the effects of advection over varying SST.

2.2 Introduction

Low-level clouds combine a small greenhouse effect with a generally high albedo and thus contribute significantly to the overall net cooling role of clouds in Earth's climate (Ramanathan et al., 1989). Currently, lack of both resolution and appropriate physical parameterizations prohibit reliable large-scale numerical prediction of cloud-climate feedbacks (e.g. Stephens, 2005; Bony and Dufresne, 2005). A good strategy for improving our understanding of climate mechanisms and their numerical simulation is to carry out focused studies that elucidate specific ocean-atmosphere-cloud relationships and that can inform and constrain model results. By examining the interannual variability of low-level clouds in the eastern equatorial Pacific, an area of high atmospheric and oceanic variability located on the edge of a persistent stratiform cloud deck, we aim to uncover sometimes-subtle details of marine low-level cloud processes.

Climatologically, low-level stratiform clouds are found in subtropical subsidence regions over the relatively cool eastern side of oceans, and they are most prevalent in seasons of high lower-tropospheric static stability (LTS) (Klein and Hartmann, 1993). The relationship between low-level cloud amount and LTS, or sea surface temperature (SST), found in the seasonal cycle is also apparent at other timescales. Interannual anomalies in cloud amount and SST are negatively correlated in eastern subtropical oceans (Norris and Leovy, 1994), with the maximum effect on clouds occurring 24-30 h downwind from SST anomalies (Klein et al., 1995). There is also evidence of low-level cloud variations preceding SST anomalies in daily data, though the extent, nature, and exact mechanisms involved in two-way low-level cloud-SST relationships remain to be fully analyzed (Klein, 1997; Xu et al., 2005). Low-level stratiform clouds display appreciable variability on synoptic, seasonal and interannual scales, with larger regions generally more showing variability over longer time scales (Rozendaal and Rossow, 2003), and year-to-year changes in cloud amount can be substantial relative to the climatological mean.

While most low-level stratiform clouds exist in areas of the subtropics where prevailing winds advect the atmospheric boundary layer equatorward over slowly increasing SST, one exception is the region of the eastern Pacific equatorial cold tongue. Here northward trade winds flow over climatologically decreasing SST between 5° S and 1° S and then over rapidly increasing SST as they approach the Intertropical Convergence Zone near 8° N. Previous studies have demonstrated that the boundary layer is sensitive to changes in underlying SST (e.g. Yin and Albrecht, 2000) especially on the northern side of the equatorial cold tongue, where advection over the sharp SST gradient generates large latent and sensible heat fluxes that favor development of extensive stratocumulus (Deser et al., 1993). Much less research attention has been devoted to the southern side of the cold tongue, where advection of relatively warm air over cold SST can produce shallow and stably stratified layers near the surface (e.g. Paluch et al., 1999). This is one of the very few areas of the ocean interior where cloudless boundary layers occur at non-negligible frequency (Norris, 1998b).

The southern side of the equatorial cold tongue provides a unique setting to study how advection over decreasing SST affects low-level cloudiness. The analysis is simplified since the trade winds are steady, unlike the case for extratropical latitudes. Moreover, this area lies on the northern edge of the extensive southeastern Pacific stratiform cloud region and experiences large year-to-year changes in low-level cloud amount. The present study describes and explains the driving forces behind these interannual cloud variations using satellite cloud data, ship-based synoptic reports, and soundings from two different years in the eastern equatorial Pacific region. In order to see whether the important elements of our findings are reproduced in climate simulations, we also examine output from two atmospheric general circulation models (AGCMs) run over prescribed SST and output from three coupled atmosphere-ocean general circulation models (CGCMs).

2.3 Observational data sources

The primary source of cloud information in this study is monthly mean daytime low-level cloud amount from the International Satellite Cloud Climatology Project (IS-

CCP) D2 visible-radiance adjusted cloud amount dataset (Rossow and Schiffer, 1999). These data are available on a 2.5° × 2.5° grid during July 1983-September 2001. In ISCCP, "low-level" refers to clouds whose tops are at a pressure greater than 680 hPa, and we look at combined low-level cloud coverage of all optical thicknesses. Since a satellite cannot see low-level clouds when upper-level clouds are obscuring its view, we adjust ISCCP data by assuming that low-level clouds are randomly overlapped with upper-level (middle plus high) clouds. Taking satellite-observed upper-level cloud cover, U, and satellite-observed low-level cloud cover, L, into account, we compute $L^{'}$, the corrected low-level cloud amount, from $L^{'} = L/(1-U)$, after Rozendaal et al. (1995). For convenience, the adjustment for cloud overlap is applied to monthly mean data instead of adjusting instantaneous values for cloud overlap prior to averaging them to monthly means. We found that values calculated from the two methods during July and October for the region 20°S-0°, 110-85°W had a correlation of 0.997, and in the rest of our analysis we therefore use monthly mean low-level cloud amount adjusted for overlap.

The most important large-scale meteorological parameter for our study is advection by 1000 hPa winds over varying SST: $-\vec{V}_{1000} \cdot \nabla SST$. We refer to this as "SST advection," and obtain monthly mean wind and SST data from the National Centers for Environmental Prediction/National Center for Atmospheric Research (NCEP/NCAR) reanalysis (Kalnay et al., 1996). The SST gradient used is the "upstream" gradient, i.e., composed of the finite differences centered half a grid box south and east of the corresponding point for which the advection value is indicated, in order to better approximate the temperature advection in the southeasterly trade winds of the southern tropics.

Since ISCCP cannot provide morphological cloud type information we also examine data from ship-based surface observers in the Extended Edited Cloud Report Archive (EECRA) (Hahn and Warren, 1999) from 1983-1997. Observations in the EECRA include sky coverage by all clouds and by low-level clouds, cloud type, SST, air temperature and pressure, dew point depression, and wind speed.

As a complement to the EECRA synoptic reports, we also make use of soundings by research vessels affiliated with the Eastern Pacific Investigation of Climate Processes in the Coupled Ocean-Atmosphere System (EPIC) program. Of particular interest to us are data from transects along 95° W and 110° W in November 1999 and November 2001, described in Pyatt et al. (2005), since these two years correspond to different SST advection conditions south of the Equator.

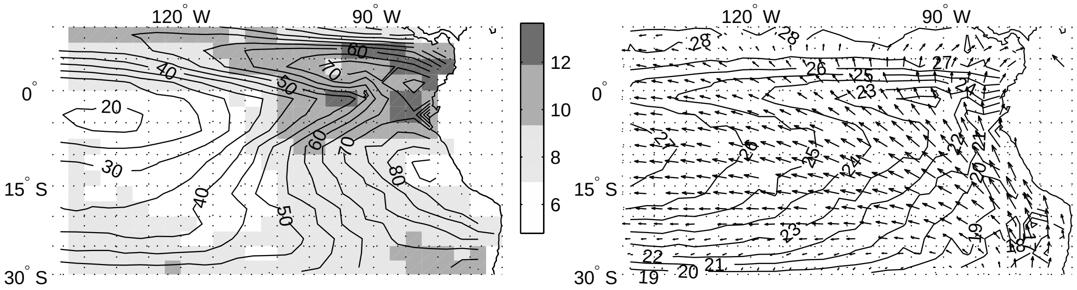

Figure 2.1: (left) June-November climatological overlap-adjusted low-level cloud amount (contours) and standard deviation of interannual monthly anomalies (shading). Units are percent-cloud-amount. (right) Climatological SST and 1000 hPa wind distribution in these months. The wind vector in the upper-right corner has a magnitude of 8 m s^{-1}.

After the treatment of observational data, we briefly examine whether modern general circulation models show a cloud-temperature advection response similar to that in observations. We examine both CGCM and AGCM simulations over the time period 1983-2001, which most nearly matches the ISCCP period.

2.4 Observational analysis and results

2.4.1 Correlation and multilinear regression analysis

Our analysis focuses on the cool-season months of June through November since that is the time of year when climatological low-level cloud amount and interannual variability are largest in the southeastern tropical Pacific, thus implying a greater potential cloud feedback on the climate system. Nonetheless, our results would be qualitatively similar if all months were included. Fig. 2.1 shows the June-November climatological low-level cloud amount and standard deviation of interannual monthly anomalies in the ISCCP data. The heart of the dense low-level cloud region aligns with areas of cooler waters off the South American coast, with a secondary area of extensive low-level cloud amount north of the equatorial SST front.

The area of the northern equatorial cold tongue exhibits high interannual variability in cloud amount due to changes in SST and SST advection associated with El Niño-Southern Oscillation (ENSO) events and tropical instability waves (Deser et al., 1993). The region of pronounced variability east of 110° W between 5° S and the Equator is a region of predominant warm SST advection. Since the sign of meridional SST gradient and climatological temperature advection reverse at or just south of 0°, the sign of SST advection south of the Equator at any time is typically opposite from that north of the front.

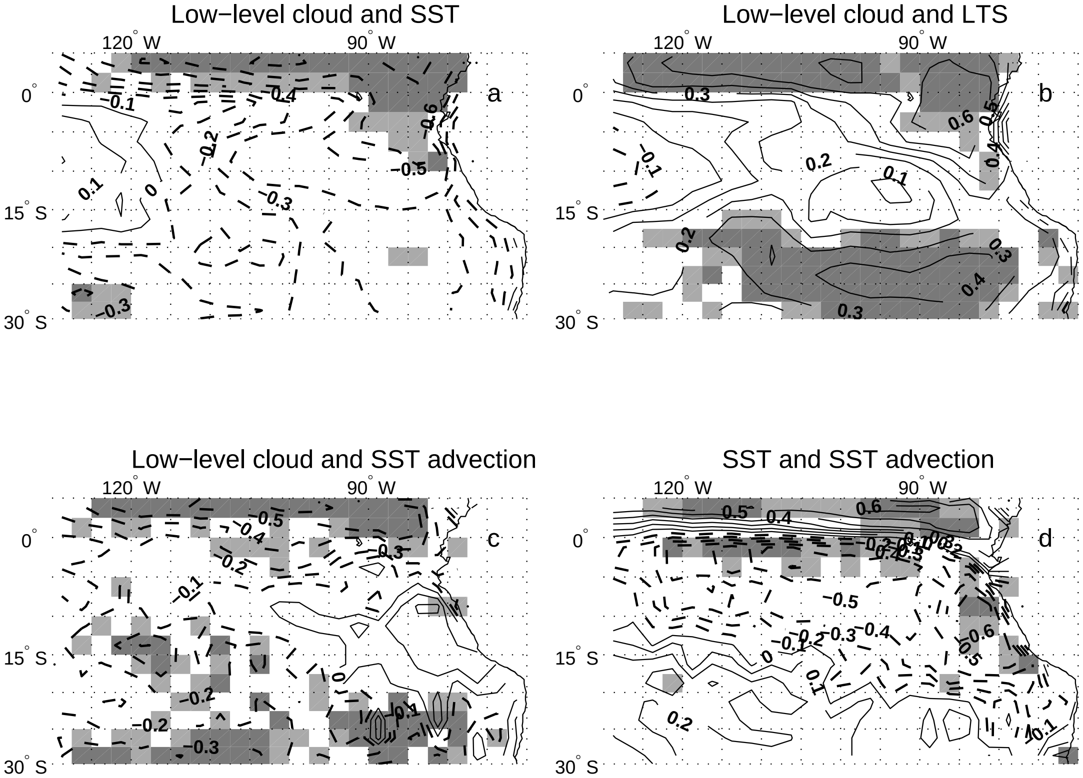

Figure 2.2: Correlation (contoured) between monthly anomalies in (a) ISCCP low-level cloud amount and SST; (b) low-level cloud amount and LTS; (c) low-level cloud amount and SST advection; and (d) SST and SST advection. Shading indicates significance at the 95% (light) and 99% (dark) confidence levels.

To investigate the conditions associated with low-level clouds in the cold tongue region, we begin with the satellite data set. From the overlap-corrected ISCCP data, we subtract 19-year (18 for October and November) averages from the monthly observations, and using the anomalies proceed with correlation and linear regression analysis at each 2.5° × 2.5° grid box. Maps of local correlations between reanalysis meteorological parameters and low-level cloud amount serve as a starting point in attributing low-level cloud variability. For such maps, we use the effective sample size and a standard t test to compute significance of linear correlations. Our method follows that of Klein (1997), but on a month-to-month basis rather than daily.

Since SST has been shown to have a close association with low-level stratiform cloudiness (Norris and Leovy, 1994), we use it as our first correlation parameter. In Fig. 2.2a, monthly anomalies in SST and cloud amount exhibit the expected negative correlation over most of the climatological low-cloud region, although the relationship is statistically significant mainly in the southern region of the stratiform deck and north of the equatorial SST front. Anomalies in SST are also negatively correlated with anomalies in low-level cloud optical thickness (not shown). Another parameter that is closely related to SST and cloudiness is LTS, defined as the difference in potential temperature between the 700 hPa level and 2 m above the surface ($\theta_{700} - \theta_{2\mathrm{m}}$) following Klein and Hartmann (1993). The statistically significant positive correlations between cloud amount and LTS anomalies on the northern side of the cold tongue displayed in Fig. 2.2b are due almost entirely to variations in SST rather than variations in 700 hPa temperature.

The sense of SST advection is another meteorological parameter that previous studies have found to be strongly related to low-level stratiform cloud amount (e.g. Klein et al., 1995; Klein, 1997; Norris and Iacobellis, 2005), and Fig. 2.2c shows that statistically significant negative correlations exist between monthly anomalies in SST advection and low-level cloud amount over the equatorial cold tongue and southwest of the climatological maximum in cloud amount. Although not shown, SST advection is also negatively correlated with low-level cloud optical thickness in these regions. The weak positive cloud-SST advection correlations occur where interannual variability is quite weak (Fig. 2.1) and consequently are less likely to be influential on the climate system. Considering that both SST and SST advection are related to variations in low-level cloud amount, it is instructive to examine how they are related to each other. Figure 2.2d presents the spatial pattern of correlations between monthly anomalies in SST and SST advection. The most prominent feature in this plot is the band of positive correlation north of the Equator and the band of negative correlation south of the Equator. This is because SST varies most strongly along the near-equatorial SST front, with lesser variability of the same sign to the North and South. Since monthly-mean SST advection anomalies in this area are mainly determined by SST variability along the largely steady wind streamlines, the latitude of greatest SST variability determines the latitude where the anomalous SST advection changes in sign. At the resolution of the grid used here,

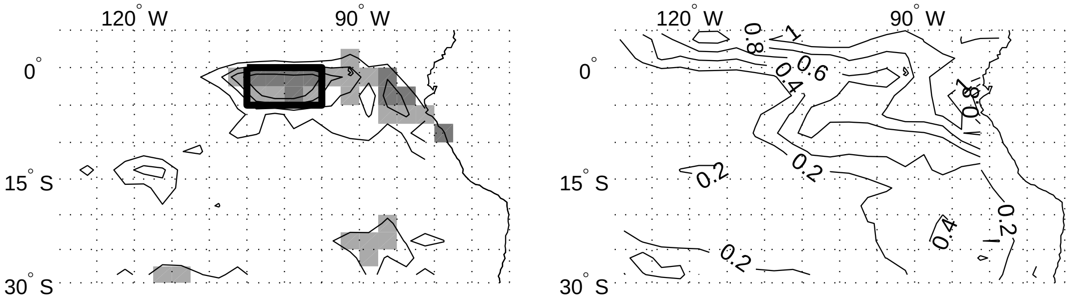

Figure 2.3: (left) Contours represent increase in variance explained (R^2) in ISCCP low-level cloud amount by regressing monthly anomalies in SST advection inaddition to monthly anomalies in SST. Contour interval is 0.1. Shading indicates significance at the 95% (light shading) and 99% (dark shading) confidence levels. Also outlined is the southern cold tongue region referred to in the text. (right) Total low-level cloud variance explained by both SST advection and SST in the multilinear regression.

that latitude is on or within a degree south of the Equator, the same as the location of the climatological SST front. On the northern side of the cold tongue, colder SST is associated with more negative SST advection, both of which favor increased low-level cloud amount. Contrastingly, on the southern side of the cold tongue, colder SST is associated with more positive SST advection, thus producing opposing effects on cloud amount.

The hypothesis that low-level cloudiness is significantly influenced by more than one meteorological factor may be tested by gauging how much additional variance (R^2 statistic) is explained by a second parameter in a multilinear regression at each grid box. To determine whether the increase in R^2 due to adding a second physical parameter is statistically significant, we employ bootstrap techniques that take into account the degree of statistical dependence of consecutive months in each grid point as well as the R^2 increase from the second parameter, described in more detail in Appendix A. Fig. 2.3 displays the amount of additional low-level cloud variance that SST advection as a second regressor accounts for when SST is the first regressor.

Although accounting for little extra variance in much of the domain, SST advection explains significantly more cloud variance than SST alone in a region on the southern side of the equatorial cold tongue (5°S - 0°, 105°-95°W), hereafter called the “southern cold tongue region.” In this region the fraction of low-level cloud amount variance explained using both regressors is around 0.5, whereas with only SST it is closer to 0.1. Very similar results are obtained if LTS is used instead of SST as the first regressor, and if climatological monthly mean winds are used instead of varying monthly mean winds. Furthermore, if we use non-overlap-adjusted low-level cloud amount (corresponding to an assumption of minimum overlap between clouds of different heights), or total ISCCP cloudiness (corresponding to a maximum overlap assumption), a very similar pattern also results. Contrastingly, other second regressor variables such as θ_{700}, vertical velocity at 700 hPa, or surface divergence do not exhibit any organized pattern that explains significantly more cloud variance.

The sensitivity of low-level cloud amount on the southern side of the cold tongue to interannual variations in advection over the SST gradient is due to the fact that absolute (not anomalous) advection changes sign from year to year. Over most subtropical stratiform cloud regions, SST advection ranges only from moderately negative to strongly negative, but in the southern cold tongue region, SST advection ranges from moderately positive to weakly negative. As listed in Table 1, monthly anomalies in SST advection averaged over the latter area are inversely correlated with anomalies in local and Niño 3.4 SST. Table 1 also shows that low-level cloud amount variability in the southern cold tongue region is more closely related to variability in SST advection than it is to variability in local SST, Niño 3.4 SST, or LTS.

2.4.2 Cold and warm SST advection composites

Compositing analysis is a useful method to illustrate changes in cloud and surface meteorological properties associated with variations in SST advection. We do this by classifying anomalous monthly SST advection values averaged over the southern cold tongue region into lower, middle, and upper terciles and then examining the cloud and meteorological anomalies associated with each tercile.

Fig. 2.4 presents mean SST and 1000 hPa wind distributions for lower and upper SST advection terciles, along with the differences between the two terciles. The very small magnitude of wind vector differences near the Equator (Fig. 2.4c) indicates that variations in SST advection are almost exclusively driven by changes in the SST gradient. The lower tercile, corresponding to cold SST advection in the anomaly sense, occurs when the equatorial cold tongue is weak and the along-wind SST gradient is nearly flat, leading to near-zero SST advection in the absolute sense (Fig. 4a). The upper tercile,

Table 2.1: Correlation coefficients for monthly-mean interannual anomalies of several reanalysis meteorological fields and ISCCP cloud fields averaged over the southern cold tongue region, 105°-95°W, 5°S-0°. Correlations significant at the 90% level are in bold and those also significant at the 95% level are in italics.

Low-level cloud amount	-	***-0.50***	0.16	**-0.41**	-0.28	0.36
Upper-level cloud amount	***-0.50***	-	0.38	-0.26	***0.76***	***-0.73***
Niño 3.4 SST	0.16	0.38	-	***-0.79***	***0.74***	***-0.62***
SST advection	**-0.41**	-0.26	***-0.79***	-	***-0.61***	***0.49***
Local SST	-0.28	***0.76***	***0.74***	***-0.61***	-	***-0.90***
$\theta_{700} - \theta_{2\mathrm{m}}$	0.36	***-0.73***	***-0.62***	***0.49***	***-0.90***	-
	Low-level cloud amount	Upper-level cloud amount	Niño 3.4 SST	SST advection	Local SST	$\theta_{700} - \theta_{2\mathrm{m}}$

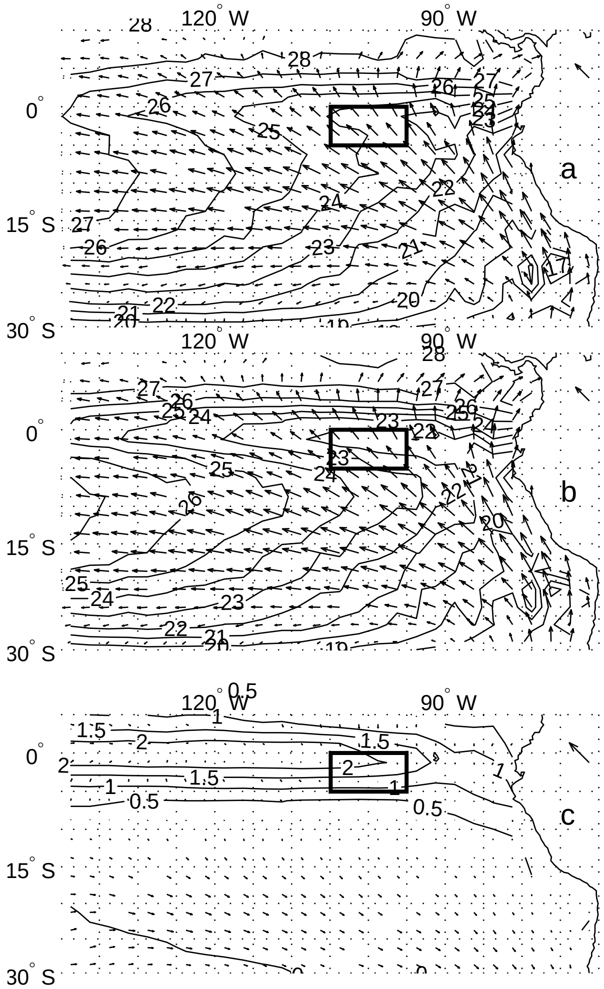

Figure 2.4: Average SST and 1000 hPa winds for cold anomalous SST advection tercile (a) and warm anomalous advection tercile (b), and for cold minus warm difference in SST and 1000 hPa wind (c). Southern cold tongue region used for compositing is outlined in each panel. The wind vector in the upper-right corner of each panel has a magnitude of 8 m s^{-1}.

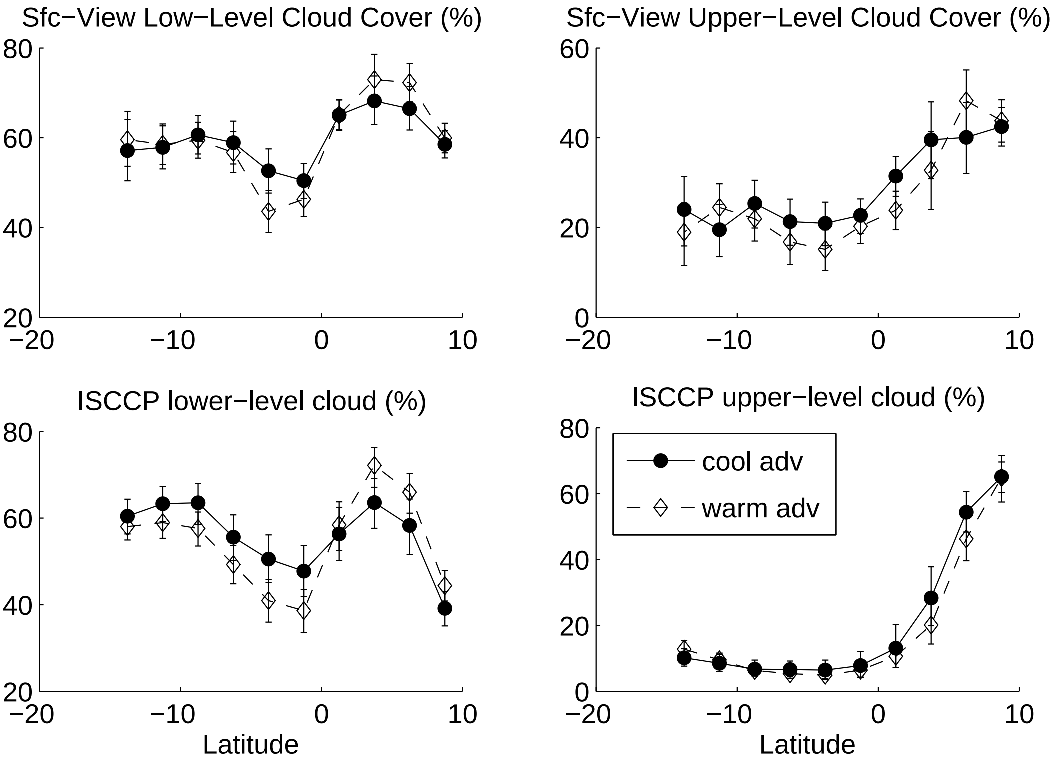

Figure 2.5: Low-level (left) and upper-level (right) cloud amount from EECRA (top) and ISCCP (bottom) datasets averaged over 105°-95° W and months belonging to terciles of cold anomalous advection (solid and filled circles) and warm anomalous advection (dashed and open diamonds). Error bars indicate 95% confidence intervals for the zonal means. ISCCP low-level cloud amount and EECRA upper-level cloud amount have been adjusted for overlapping higher and lower clouds, respectively.

corresponding to warm SST advection in the anomaly sense, occurs when the equatorial cold tongue is strong and the along-wind SST gradient is positive on the southern side of the cold tongue, leading to substantial warm SST advection in the absolute sense (Fig. 4b). The SST difference between terciles is reminiscent of the SST anomaly pattern from classic El Niño events away from the South American coast, (e.g., Rasmusson and Carpenter, 1982; Deser and Wallace, 1990), but differs from them in that it does not have strong equatorial wind anomalies or sizable SST anomalies along the coast.

Fig. 2.5 displays meridional profiles of ISCCP and EECRA cloud amount at low and upper levels for cold and warm anomalous SST advection terciles. These profiles were obtained by averaging monthly ISCCP cloud values and individual EECRA cloud observations in in 2.5° latitude increments between 105° and 95 ° W, and the error bars show the 95% confidence interval for each zonal mean using bootstrap methods described in Appendix B. South of the Equator, satellite and surface data both exhibit substantially less low-level cloud amount with warm anomalous advection and substantially more low-level cloud amount with cold anomalous advection. The decrease in ISCCP low-level cloud amount with warm anomalous advection cannot be attributed to changes in overlapping higher clouds since ISCCP upper-level cloud amount is climatologically very small in this region. North of 1.25° N, satellite and surface data both exhibit substantially more low-level cloud amount when warm anomalous advection occurs in the southern cold tongue region. The opposing changes in low-level cloud amount on southern and northern sides of the cold tongue are due to the reversal of the anomalous SST gradient along surface wind streamlines after the steady southeasterly winds cross the equatorial SST front.

One advantage of the EECRA data is that they include surface meteorological measurements and morphological cloud type observations that provide a qualitative description of boundary layer structure (e.g. Norris, 1998a). Figure 2.6 displays meridional profiles of these variables for cold and warm anomalous SST advection terciles. Warm anomalous advection is associated with the markedly more frequent occurrence of clear sky and absence of low-level cloudiness on the southern side of the equatorial cold tongue, features that are also present in the climatological mean (Norris, 1998b; Park and Leovy, 2004). The decrease in low-level cloud cover with warmer SST advection primarily results from a decrease in cumuliform cloud cover (defined as cumulus alone and cumulus mixed with stratocumulus). We attribute this implied weakening of convection to increased stratification of the atmospheric surface layer produced by advection of warmer air over cooler water, as is suggested by the near-zero air-sea temperature difference observed under these conditions.

Figure 2.6 also shows that near-surface relative humidity is larger and wind speed is smaller for warm SST advection in the southern cold tongue region, indicating that there is less upward mixing of moisture and downward mixing of momentum (e.g. Wallace et al., 1989). The enhanced stratiform cloud cover (defined as stratocumulus alone and stratus) that occurs with warm SST advection may be remnant cloudiness that has not yet dissipated even though it is no longer in turbulent communication with the ocean surface. Cold anomalous advection is associated with less frequent clear sky, more

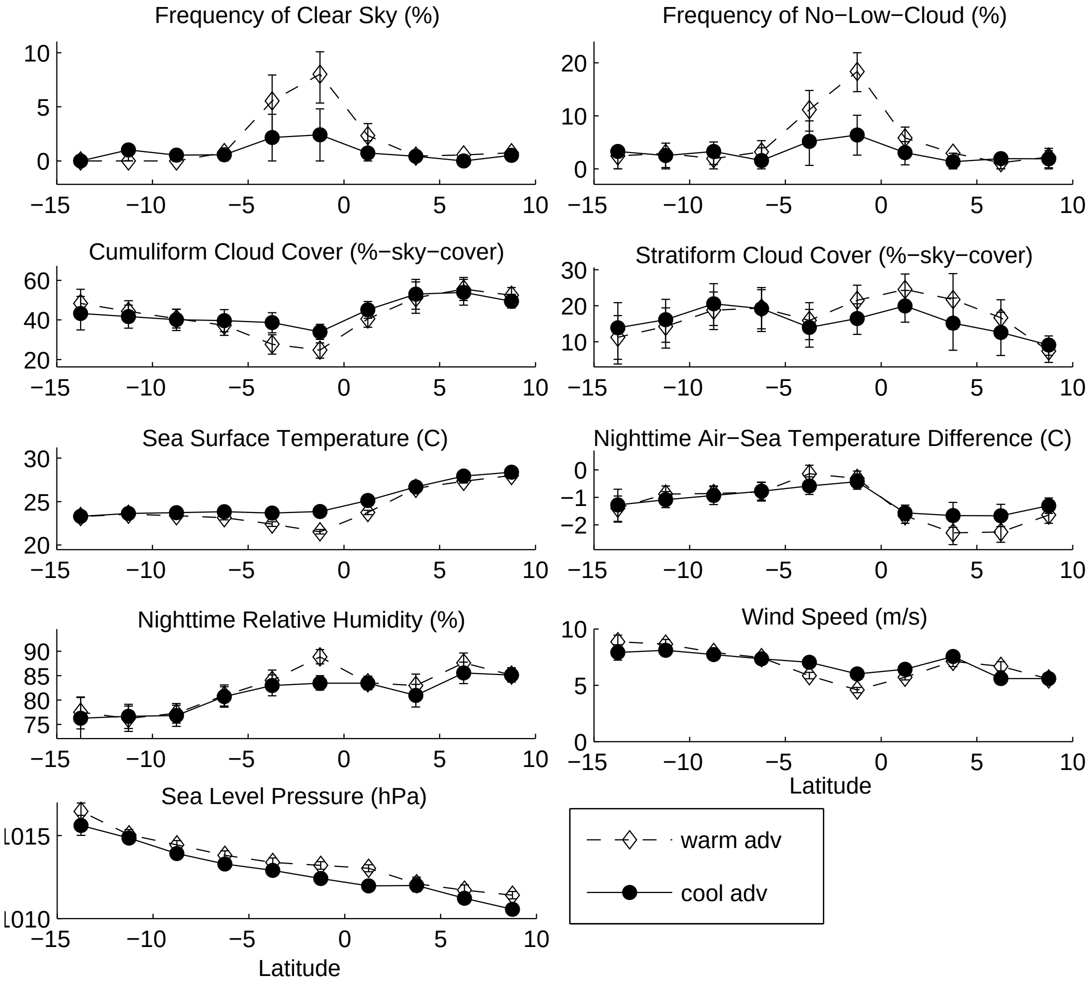

Figure 2.6: As in Fig. 2.5, except for EECRA cloud and surface meteorological parameters as labeled in the subplots.

cumuliform cloud cover, a more negative air-sea temperature difference, and a drier and windier surface layer (Fig. 2.6). All of these conditions are characteristic of the typical cloud regime downwind from major stratocumulus decks.

It is worth noting that in Fig. 2.6, the conditions in the tercile of anomalously cold temperature advection south of the Equator show more cumuliform clouds relative to the warm advection tercile all the way up to 5° N, implying that some of the additional cumulus clouds formed south of the Equator persist as they are advected northward. Likewise, the deficit in stratocumulus clouds is evident from 7.5°S to 7.5°N. The net result, shown in both the EECRA and ISCCP data (Fig. 2.5), is that the cold anomalous advection tercile relative to warm has more low-level cloud cover when averaged over the extent of the cold tongue, 5°S-5°N, in the longitude range 105°-95 ° W.

The changes in surface wind speed and relative humidity, in addition to the cloud changes, are all consistent with increased boundary-layer vertical mixing as in Wallace et al. (1989). An alternative hypothesis holds that anomalous SSTs lead to boundary-layer pressure anomalies, and that the corresponding anomalous pressure gradients cause anomalous low-level winds (Lindzen and Nigam, 1987). In the eastern tropical Pacific, Hashizume et al. (2001) and Hashizume et al. (2002) find little evidence for winds responding to such an effect. The data used in our analysis, focused as they are on boundary-layer cloud variability, are not suitable for a definitive investigation of the Lindzen-Nigam mechanism. This is particularly the case for the reanalysis winds in Fig. 2.4 since they are likely to be influenced by the boundary layer parameterization used in the model. We do note that in Fig. 2.6 the meridional pressure gradient is steadily negative over the cold tongue region and has a slope that becomes steeper in the tercile months and latitudes with anomalously cold advection and warm SST. Mean vertical profiles of wind speed from EPIC soundings (not shown) also show that in addition to the surface wind tendencies shown in the EECRA data, wind speeds in the upper parts of the boundary layer were greater over anomalously cold temperature advection and anomalously warm SST, which is consistent with Lindzen and Nigam (1987). Beyond these points, the analysis of mean values of ship reports from 15 years of EECRA data does not allow for precise calculations of momentum budgets and other methods would be required for more in-depth, quantitative evaluation of the relevant mechanisms.

Quantitative measurements of boundary layer structure are available from EPIC soundings made during November 1999, a month in the warm anomalous advection tercile, and during November 2001, a month on the cool side of the middle advection tercile. Average vertical profiles for these two months are obtained from all soundings between the Equator and 5° S along transects at 95° W and 110° W (also described in Pyatt et al., 2005). In order to preserve structure near the top of the boundary layer, soundings are scaled by the height of the base of the trade inversion prior to averaging, and the mean profile is then rescaled by the average inversion base height. The base of the trade inversion is defined as the lowest elevation where the subsequent ten data points (usually about 200 m) are warmer and the temperature increases by at least 1.5 K, and those few soundings without discernable inversions are discarded. We examine water vapor mixing ratio, saturation water vapor mixing ratio (closely related to temperature), virtual potential temperature, and equivalent potential temperature (calculated according to Bolton, 1980). While they are relevant to the structure of most of the boundary layer and the trade inversion, the soundings do not accurately depict surface-layer effects. This is due to the fact that the mean soundings miss the bottom 20 to 40 meters of the atmosphere, and moreover that the lowest recordings in many soundings are biased due to the ship's effect on the environment and the instrument sensors (C. Fairall 2006, personal communication; see also Wang et al., 2002).

Fig. 2.7 shows that strong warm SST advection during November 1999 (1.22 K d^{-1}) was associated with a boundary layer that was shallower, cooler, and drier than that observed for weak warm SST advection during November 2001 (0.50 K d^{-1}). The differences in boundary layer height in Fig. 2.7 and the cloud type in Fig. 2.6 are in agreement with previous studies noting that subtropical cumulus and cumulus-with-stratocumulus occur in deeper boundary layers than those for stratocumulus alone (Albrecht et al., 1995; Norris, 1998a). Pyatt et al. (2005) also report that south of the Equator, surface relative humidity was greater, surface wind speed was weaker, and cloud fraction was very much smaller during November 1999 than during November 2001. These observations demonstrate that stratification of the near-surface layer caused by warm air flowing over colder water inhibits the upward mixing of moisture needed to sustain cloudiness. The lower inversion height in 1999 is consistent with subsidence pushing the trade inversion further down as reduced buoyancy at the surface and cloud-top radiative cooling act to inhibit entrainment.

Further support for this stratification phenomenon is provided by the study of Paluch et al. (1999), which documented the occurrence of shallow stable surface layers

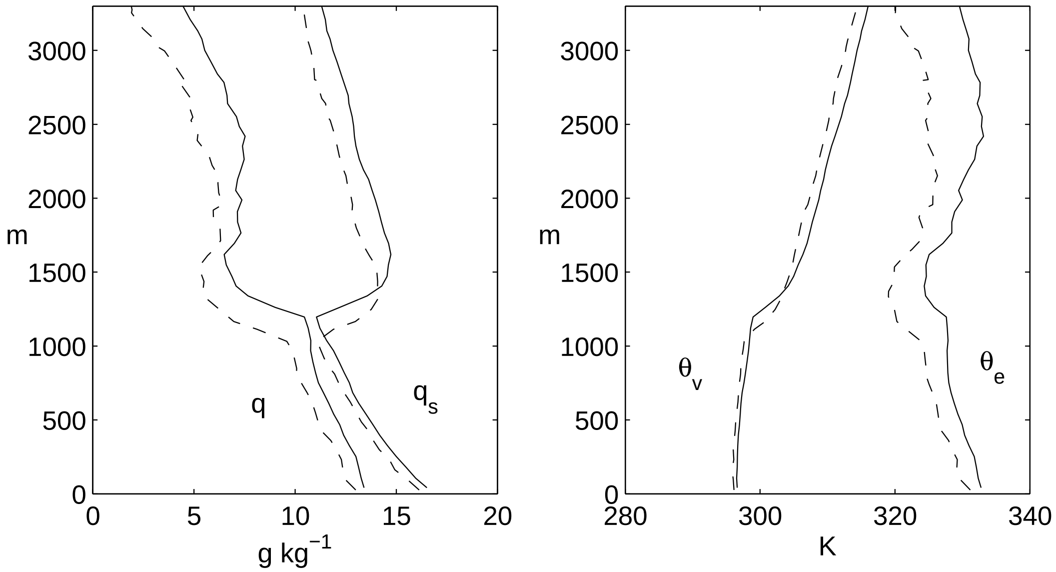

Figure 2.7: Mean EPIC vertical profiles of water vapor mixing ratio (q), saturation water vapor mixing ratio (q_s), virtual potential temperature (θ_v), and equivalent potential temperature (θ_e) averaged as described in the text over 0-5° S during November 1999 (dashed) and November 2001 (solid). November 1999 is in the warm anomalous advection tercile and November 2001 is on the cool side of the middle advection tercile.

beneath warmer layers over the southern side of the cold tongue and areas of coastal upwelling during September 1996, another month in the warm anomalous advection tercile. In contrast, measurements taken north of the Equator in the same field campaign show a deeper dry adiabatic layer starting at the surface, lying beneath a deep moist adiabatic layer with cloud all the way up to the inversion (Paluch et al., 1999). The large eddy simulation in de Szoeke and Bretherton (2004), which is forced by boundary conditions characteristic of the equatorial Pacific along 95° W, also clearly shows a stable surface layer up to the approximate latitude where the SST front is found.

2.5 Comparison with general circulation model output

Previous investigations have demonstrated that atmosphere and coupled ocean-atmosphere general circulation models produce unrealistic simulations of low-level cloudiness over the eastern tropical Pacific which contribute to large biases in the climate state (e.g. Ma et al., 1996; Yu and Mechoso, 1999). This motivates comparison of the obser-

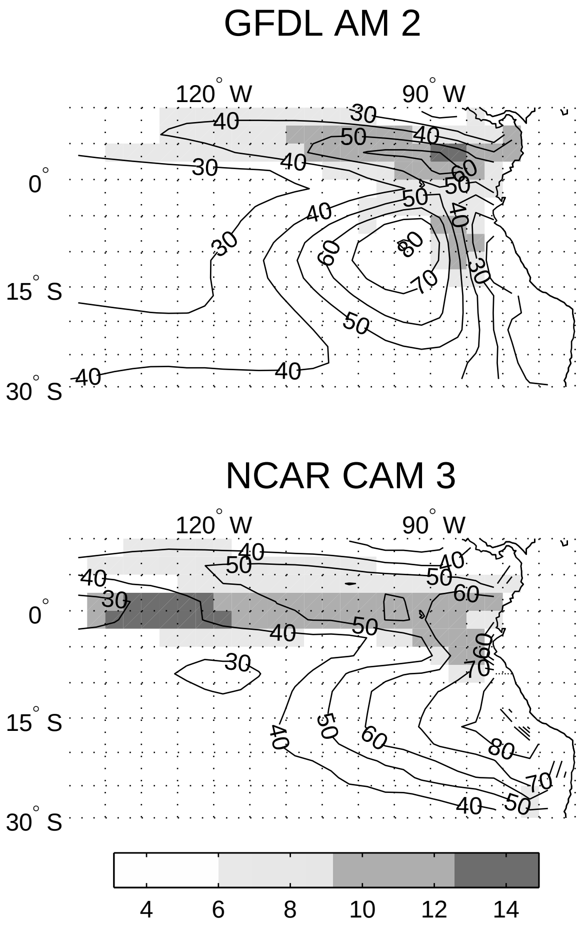

Figure 2.8: Historically-forced AGCMs' basic states. June-November low-level cloud climatology (contours) and standard deviation of interannual anomalies (shading). Top is GFDL AM2, bottom is NCAR CAM3.

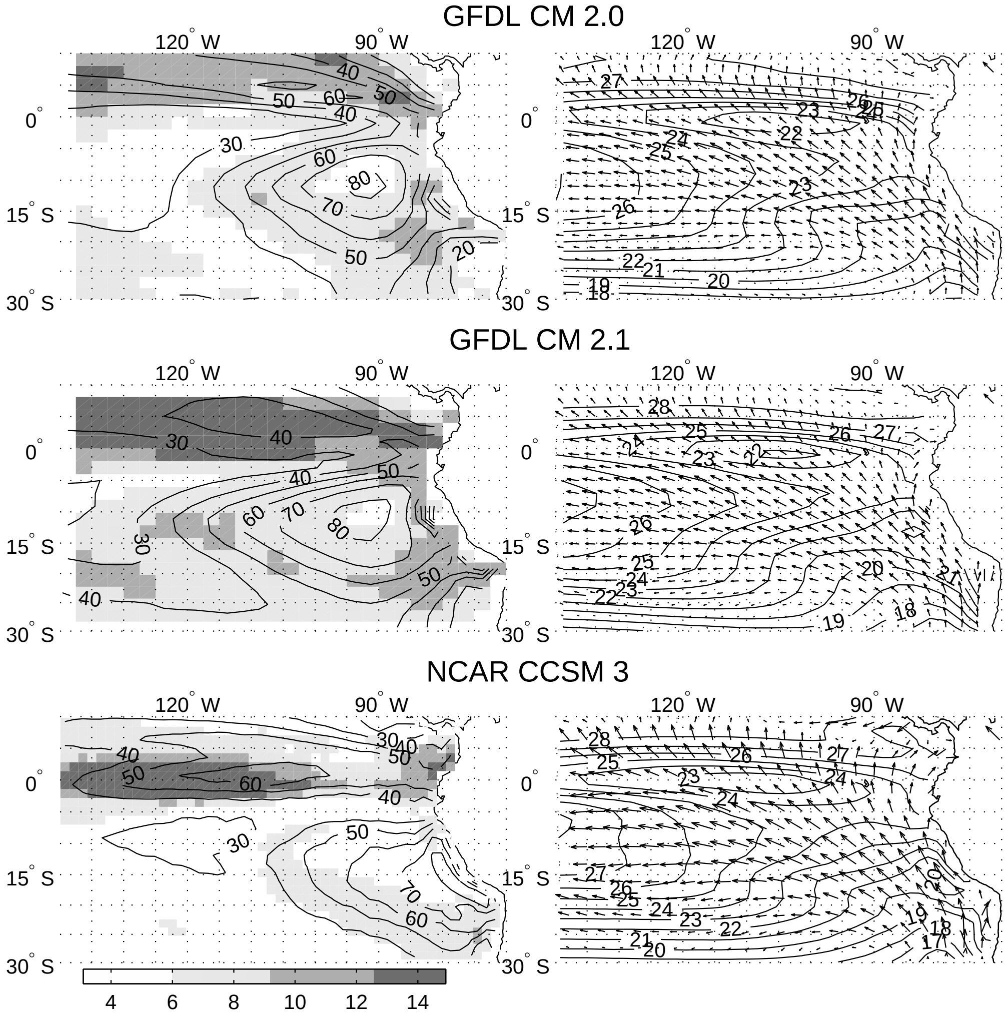

Figure 2.9: As for Fig. 2.1, but for (top) GFDL CM 2.0; (middle) GFDL CM 2.1; and (bottom) NCAR CCSM 3.

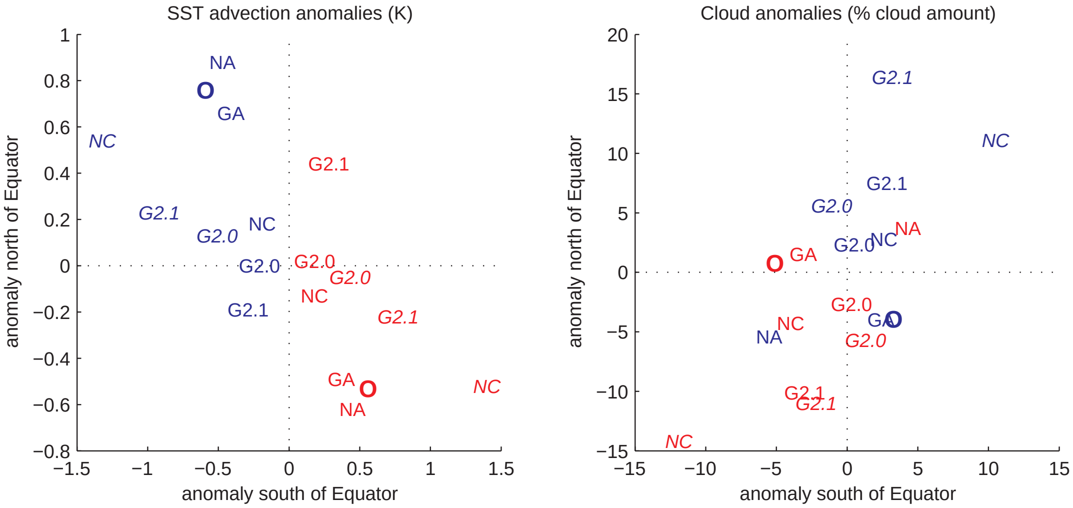

Figure 2.10: Mean SST advection (left) and low-level cloud amount anomalies (right) for the coldest and warmest SST advection terciles for observational and model output. Terciles are based on SST advection values for the 5 degrees south of the Equator: red type for anomalously warm terciles, blue type for anomalously cold. Abscissa denotes the mean anomaly value in the south of the Equator, ordinate indicates the value in the 5 degrees north of the Equator. Normal typeface denotes the longtude averaging range is 110° - 90°W, while italic indicates that the longitude range was adjusted to account for the CGCMs' detached cold tongues. "O" indicates obvservations (ISCCP cloud and reanalysis meteorology); "G" indicates GFDL models; "N" indicates NCAR models. "A" indicates AGCMS; "C" for CGCMs.

vational results of the present study to output from the two leading U.S. GCMs in order to determine whether they correctly reproduce the observed relationship between cloud amount and SST advection.

The first model is the Geophysical Fluid Dynamics Laboratory (GFDL) atmosphere-only AM2 (described in Anderson et al., 2004) and two versions of the coupled ocean-atmosphere CM2 (described in Delworth et al., 2006). The GFDL AM2 and CM2 use a prognostic cloud fraction scheme basted on Tiedtke (1993). The planetary boundary layer is modeled with a nonlocal scheme based on Lock et al. (2000). This scheme is based on results of various large eddy simulations and classifies the boundary layer as one of six types, each with a different profile of static stability, decoupling, moisture, and condensate. It determines cloud vertical extent and boundary layer depth by calculating the height of neutral buoyancy for rising and sinking parcels using conserved moist variables (Lock et al., 2000; Anderson et al., 2004). Because the AM2 was found to be unreliable in predicting cloud liquid water, the term in Lock et al. (2000) accounting for buoyancy change due to entrainment drying is omitted and the entrainment parameterization adjusted (Anderson et al., 2004). The two versions of the CM2, designated CM2.0 and CM2.1, primarily differ in their dynamical cores and particular aspects of cloud tunings. We do not expect that these differences will substantially influence low-level cloud variability over the equatorial cold tongue aside from producing dissimilar basic climate states.

The second model set is the National Center for Atmospheric Research (NCAR) atmosphere-only CAM3 (Boville et al., 2006; Collins et al., 2006b) and coupled ocean-atmosphere CCSM3 (described in Collins et al., 2006a). The NCAR CAM3 and CCSM3 use a diagnostic cloud fraction scheme based on a relative humidity threshold and an empirical relationship to LTS obtained from Klein and Hartmann (1993). The boundary layer is simulated as in Holtslag and Boville (1993). This is another nonlocal scheme that differs from Lock et al. (2000) in the derivations and values of diffusivities and velocity scales used in the parameterizations. It also lacks a built-in cloud radiative cooling term and does not define distinct boundary layer regimes with different mixing characteristics as Lock et al. (2000) do.

In order to present relevant elements of the climatology and cloud variability to illuminate the model intercomparison, the calculations for Fig. 2.1 are repeated for the AGCMs and CGCMs and presented in Figs. 2.8 and 2.9, respectively. Between the two AGCMs, the CAM3 also shows considerably greater low-level cloud variability, even though it is forced with observed SST, while AM2 levels of cloud variability more closely resemble observations. The area of low-level cloud variability in CAM3 is also concentrated in a band that straddles the Equator, while AM2 shows more variability north of 0°. Each coupled model shows a cold tongue that is (unrealistically) detached from the South American coast. They each also show the low-level June-November cloud amount variability in unrealistic places in the eastern equatorial Pacific, with CM 2.1 and CCSM3 appearing to show greatest variability over the model cold tongues.

In Fig. 2.10 the essential features of the observations and models are summarized and presented for intercomparison. The point where each label is plotted in Fig. 2.10 gives the simultaneous mean anomaly values for areas on the south side of the cold tongue (the abscissa) and the north side (the ordinate) during months in the tercile of most anomalously cold (blue label) and anomalously warm (red label) temperature advection south of the Equator. The labels identify the data set, and the two panels show cloud and SST anomalies separately. The observed values show SST advection anomalies of opposite sign across the Equator, consistent with an SST front near 1°S latitude and southeasterly trade winds in the region. Not surprisingly, the advection anomaly values for both of the AGCMs forced with actual SSTs are close to those in the observations.

The observations show a consistent negative relationship between SST advection and low-level cloud anomaly, as seen by the cool- and warm-tercile mean values falling in the upper-left and lower-right quadrants. Thus, there is a cross-equatorial dipole in cloud anomaly as well as SST advection. Of all the model sets, only the GFDL AM2 data fall in the same quadrants as the observations for cloud amount anomalies, and in fact fall relatively close to the observed values. The NCAR CAM3 falls in the lower-left and upper-right quadrants, indicating a cloud response to SST advection different from that observed in the region.

Previous studies have noted that the NCAR atmosphere model generates too much low-level cloud amount too quickly for warm SST advection conditions, presumably due to insufficient turbulent entrainment of drier air from above (Norris and Weaver, 2001; Alexander et al., 2006). Another possible reason is that the CAM3 empirical cloud-LTS parameterization forces low-level cloud amount to be large for cold SST anomalies even when they also produce warm SST advection anomalies. Although not shown, multilinear regression analysis applied to CAM3 output indicates that SST advection does not explain any additional variance in low-level cloud amount over the cold tongue. Contrastingly, multilinear regression analysis of GFDL AM2 output results in a pattern similar to that of Fig. 2.3.

Unlike the case for the atmosphere-only models, the GFDL CM2.0 and CM2.1 and the NCAR CCSM3 do not realistically simulate the north-south dipole behavior of SST advection anomalies in the 110-90° W region. Fig. 2.10 indicates that the CM2.0 and CM2.1 produce SST advection anomalies with identical sign on both sides of the Equator and that the CCSM3 produces anomalies that have the correct signs but are much smaller than observed. None of the models exhibit realistic low-level cloud behavior in the 110-90° W region.

Fig. 2.9 indicates that each model has a cold tongue significantly detached from the coast (discussed in Wittenberg et al., 2006; Deser et al., 2006). Because some features in the coupled models are merely shifted in longitude, we searched for other 20° longitude increments that exhibited both a north-south dipole in SST advection anomalies and sufficient interannual low-level cloud variability. These longitude ranges are 125°-105°W for GFDL CM 2.0 and 130°-110°W for both GFDL CM 2.1 and NCAR CCSM3 and, as shown in Fig. 2.10, also do not exhibit low-level cloud anomalies with the observed cross-equatorial sign difference and negative relationship to local SST advection anomalies. The detached cold tongues, along with trade winds south of the Equator that tend to be slightly more zonal than in observations, lead to SST advection cooler than observations (never warmer than 0.25 K d^{-1}) in each coupled model in all the averaging regions south of the Equator and all terciles. As a result, the clouds do not respond to anomalous SST advection as in the observations, where absolute advection changes more notably between the averaging terciles.

It is difficult to determine from this analysis whether the poor low-level cloud simulations in the CM2.0, CM2.1, and CCSM3 result from incorrect cloud or bounday layer parameterizations or fundamentally different SST and wind distributions. Whereas the meridional component of SST advection in the cold tongue is of primary importance in the observations, zonal advection is relatively more important in the models, even while meridional SST gradients are sharp. This difference might contribute to model inacuracies in simulating the relationship between low-level cloud and temperature advection.

2.6 Discussion and conclusions

Satellite and surface cloud observations show that the eastern Pacific south of the Equator exhibits pronounced low-level cloud variability on interannual time scales. Although SST and LTS explain some of the variance in low-level cloudiness, advection over the SST gradient plays an important role in controlling cloud type, cloud frequency and cloud amount over the equatorial cold tongue, especially in the region extending approximately 1500 kilometers west from the Galápagos Islands. When SST advection is warm, the atmospheric surface layer becomes stabilized, thus inhibiting the upward mixing of moisture from the sea surface. This is evident not only in the ensuing decrease in cloud amount and more frequent absence of low-level clouds reported by the ISCCP and EECRA datasets, but also in the greater surface relative humidity, weaker surface wind speed, and less negative air-sea temperature difference.

EECRA surface cloud observations indicate that remnant stratiform and cloudless conditions occur more frequently and cumuliform clouds occur less frequently for warm SST advection, suggesting that less moisture is being transported to the cloud layer to sustain it against subsidence and entrainment drying. EPIC soundings confirm that warm SST advection is associated with a shallower boundary layer that is drier near the top.

A question that arises is why SST advection anomalies and surface layer stability so strongly influence low-level cloud variability in the southern cloud tongue region (5° S - 0°, 105° - 95° W). Although the 5° × 10° area immediately west of the southern cold tongue region has a similar distribution of monthly SST advection values, it is climatologically warmer and less cloudy, thus restricting the potential magnitude of interannual cloud variability. Contrastingly, the 5° × 10° area east of the southern cold tongue region is climatologically colder and more cloudy, thus reducing the sensitivity of cloud amount to warm SST advection. The southern cold tongue region is distinct in that it both experiences large variations in SST advection and climatologically occupies the phase space between overcast stratocumulus conditions and sparse trade cumulus conditions.

The observed relationship between low-level cloudiness and SST advection can be used to constrain and improve the simulation of clouds in global climate models, especially since it is independent of the relationships between low-level cloudiness and SST or LTS. The GFDL atmospheric GCM (AM2) run over prescribed observed SST produces a realistic low-level cloud response to SST advection anomalies on the southern side of the equatorial cold tongue. Two versions of the GFDL coupled ocean-atmosphere model (CM2.0 and CM2.1), however, exhibit incorrect relationships between low-level cloud and SST advection. These results suggest that the necessary advection, SST, and LTS phase space observed in the southern cold tongue region simply does not occur anywhere in the CM2.0 and CM2.1 due to their large biases in the SST and surface wind distributions. The NCAR atmospheric GCM (CAM3) run over prescribed observed SST does not produce a realistic low-level cloud response to SST advection anomalies, suggesting the presence of incorrect cloud and boundary layer parameterizations. Possible sources of error are insufficient entrainment of dry air from above the cloud layer or the parameterized requirement that low-level cloud amount increase with larger LTS, irrespective of other meteorological effects. Not surprisingly, the cloud simulation in the NCAR coupled ocean-atmosphere model (CCSM3) is also unrealistic.

The observed response of low-level cloud amount to varying SST advection over the southern cold tongue region is likely to be relevant to coastal upwelling areas and extratropical oceans where advection brings warm air over cooler water. Although beyond the scope of the present study to quantify, we note that the observed inverse relationships between SST and SST advection and between cloud and SST advection imply the existence of a negative cloud feedback on and about the near-equatorial SST front. Here, a cold SST anomaly produces anomalously warm SST advection south of the front, and the decrease in low-level cloud formation south of the front leads to a net decrease in cloud cover over the equatorial region. Simultaneously, there is decreased downward mixing of momentum and dry air to the surface in the anomalously warm SST advection sector, implying a lesser wind speed and greater near-surface humidity and a decrease in latent and sensible heat fluxes. This wind-heat flux feedback acts in concert with the cloud-insolation feedback, unlike the case in Ronca and Battisti (1997), thus underscoring its potential significance. The net increase in insolation and decrease in surface fluxes is pronounced near the climatological local SST minimum, where the ocean mixed-layer depth is often less than half of its value several degrees to the north or south, thus increasing the impact of surface fluxes on SST. The incorrect representation of this feedback in coupled ocean-atmosphere models may be a contributing factor to the development of SST biases in the equatorial cold tongue.

2A Methods for calculating multilinear regression confidence intervals

The shaded areas indicating confidence levels in Fig. 2.3 come from rejecting our null hypothesis using bootstrap resampling techniques at each grid box. In this case, the null hypothesis is that the increase in cloud variance explained using the time series of SST advection in addition to SST in a multilinear regression is no greater than the increase in variance explained using a random, but physically feasible, time series in addition to SST. For the physically feasible random series, we randomly reshuffle the portion of the SST advection time series that is linearly independent of the SST series.

To extract the portion of the advection series not linearly related to SST, we use

$$\mathrm{ADV}(t) = \beta_0 + \beta_1 \mathrm{SST}(t) + \epsilon_{\mathrm{ADV}}(t) \tag{2.1}$$

where each β_i is optimally determined with a least-squares fit. We then regress low-level cloud amount (CA) against SST and a randomly reordered sequence of the residuals, $\epsilon_{\mathrm{ADV}}(t)$, obtained from equation 2.1:

$$\mathrm{CA}(t_i) = \gamma_0 + \gamma_1 \mathrm{SST}(t_i) + \gamma_2 \epsilon_{\mathrm{ADV}}(t_j) + \epsilon_{\mathrm{CA}}(t_i) \tag{2.2}$$

Here, the γ_i coefficients are again optimally determined for this equation, from least-squares fit. The sequences t_i and t_j are different series of months chosen randomly, with replacement, from all the June-Novembers over the 19-year sequence for which there are ISCCP cloud data. In each box the length of the sequences is equal to the effective sample size, N_{eff}, given by whichever is lowest among the N_{eff} values for low-level cloud amount, SST, and SST advection anomaly. For each field, $N_{eff} = -N(2\ln(\rho))^{-1}$ where ρ is the one-month autocorrelation after (Leith, 1973).

At every grid box we assemble a distinct $\epsilon_{\mathrm{ADV}}(t_j)$ and compute $\mathrm{CA}(t_i)$ 10000 times. We also find the variance explained by regressions using the complete CA, SST and ADV fields, ie.,

$$\mathrm{CA}(t) = \beta_0' + \beta_1' \mathrm{SST}(t) + \epsilon_1(t) \tag{2.3}$$

$$\mathrm{CA}(t) = \gamma_0' + \gamma_1' \mathrm{SST}(t) + \gamma_2' \mathrm{ADV}(t) + \epsilon_2(t) \tag{2.4}$$

where the primes denote optimally determined coefficients for each regression that can differ from those in equations 2.1 and 2.2. If the increase in R^2 between equation 2.3 and equation 2.4 is greater than the 9500th and 9900th largest values of the change in R^2 between equations 2.3 and 2.2, we reject the null hypothesis at the 95% and 99% confidence levels, respectively.

2B Confidence intervals for zonally averaged data

We obtain 95% confidence intervals for ISCCP data averaged over a latitude zone and tercile by calculating the mean of N_{ind} months randomly selected with replacement from months belonging to the tercile. All grid boxes in a latitude zone for a particular month are averaged together. This is repeated 10000 times, and the central 9500 values of the sequentially ordered random means determine the 95% confidence interval. An initial value for the effective sample size, N_{eff}, is determined for each latitude zone using $N_{eff} = -N(2\ln(\rho))^{-1}$, where ρ is the one-month autocorrelation (Leith, 1973). We round off the quantity N/N_{eff} and regard ISCCP values separated by this many months as independent. Months from different years are always considered independent with this method. We then count the number of independent months in each tercile to obtain N_{ind} for the ISCCP data.

Confidence intervals for EECRA data averaged over a latitude zone and tercile are determined in a similar manner, except that N_{ind} individual synoptic cloud reports are chosen with replacement from all months belonging to the tercile. Since it is very difficult to establish the degree of independence between individual synoptic reports scattered over the ocean and in time, we conservatively assume that N_{ind} for the EECRA data is half the nominal number of observations in a latitude zone and tercile.

This bootstrap resampling method does not rely on any assumptions about the probability density function of observations and is adaptable so that we can use essentially similar techniques for both the regular gridded ISCCP data and the surface observations which are irregular in space and time. It is worth noting that the zonal-mean ISCCP data show very similar error bars at almost every latitude if we simply assume a normal distribution of observations about their mean and calculate confidence intervals based on the standard deviation.

ACKNOWLEDGEMENTS

This work was supported by NSF CAREER grant AM02-38257, NASA grant GWEC NAG5-11731, and DOE grant DE-FG02-04ER63857. The first author was also assisted by a California Space Institute/Space Grant fellowship. The authors are grateful to Nick Bond of NOAA/PMEL for EPIC soundings. The ISCCP data were obtained from the NASA Goddard Institute for Space Studies (isccp.giss.nasa.gov). Reanalysis data were provided by the NOAA-CIRES Climate Diagnostics Center (www.cdc.noaa.gov).

Chapter 2 in its entirety is a reprint with no modifications to content of the article "Low-Level Cloud Variability over the Equatorial Cold Tongue in Observations and Models" that appeared in *Journal of Climate*, 2007, **20**, 1555-1570 (Copyright of the American Meteorological Society 2007). The dissertation author was the first author and primary researcher with guidance and contributions from the second author, J.R. Norris.

Chapter 3

Climatology and meteorological influences on California's wind energy resource. Part 1: General characteristics and seasonal cycle

3.1 Abstract

This study explores the climatology and low-level wind variability near three California wind farms: San Gorgonio Pass and Tehachapi Pass in Southern California, and Solano County further north. Several decades of weather reports from airfields near these sites are used. Comparisons show close, consistent relationships between proxy site wind speeds and limited data available from wind farms themselves, as well as consistency within orographic features, thus supporting the use of the nearby proxies. After adjusting for instrumental jumps these wind records show that each site has a pronounced annual cycle with highest wind speeds in the warm months: in late spring for the southern California sites, when reanalysis shows the zonal pressure gradient is greatest in magnitude, and mid-summer for the northern site. Simultaneous analysis of wind direction, wind speed, and SLP for each site and season shows a distinct signature of low pressure corresponding to stronger and more westerly winds in the winter, with moderate SLP coinciding with more light and variable flow. In contrast, summertime winds are more diurnally dependent, stronger, and show more topographic influence on direction, and SLP variability is lesser, indicating the influence of local circulations. Cool-season

variability is relevant to cut-in speeds of turbines and baseline energy production, while warm-season flow affects production when seasonal demand is often greatest. Correlation analysis among wind series and with climate indices shows that the colder months' sensitivity to synoptic forcing leads to a broad correlation in wind speed among the sites, as well as a tendency to greater wind speeds in negative phases of the Pacific-North American pattern in the cold season. Warm seasons show less pan-Californian coherence, but correlation between wind speed and nearby SST or inland soil moisture is negative, consistent with smaller-scale thermal circulations driven by diurnal heating. Correlation values with offshore buoy winds are limited, highlighting the importance of the inland processes. Monthly-mean anomaly composite maps reveal that oceanic high and coastal or inland lows broadly induce high wind speeds in the cold months, while the role of synoptic-scale forcing is less clear in April-October, when winds are more energetic and synoptic processes exert less influence.

3.2 Introduction

Electricity generation from wind has a relatively long history in California and has seen considerable renewed interest and growth in recent years (Hawkins et al., 2007; Gipe, 1995, pp.30-36). In California as in other regions, typical siting procedures usually involve a minimum of one full year of on-site high-resolution wind observations, and rarely more than a decade's worth of data (Petersen et al., 1999). The climatological literature is rich with studies discussing the effects of large-scale and regional climate variability on northeastern Pacific or western United States weather. At the same time, the question of the specific synoptic, regional, and terrain-modified meteorological conditions most strongly affecting wind speed variability in the vicinity of wind farm sites, and the likely effects of interannual climate variability and global climate change on wind at these locations, have not been thoroughly examined in the Californian context. The present work focuses on time series of winds recorded at sites representative of California's wind energy resource, their annual cycles, seasonal mean properties, and relationships with large-scale climate variability indices. A companion piece (Mansbach and Cayan, 2010b, hereinafter Part 2) examines synoptic variability and forcing of site winds, regional flows over complex terrain, and the diurnal cycles of observed winds.

Previous studies have adopted various perspectives on meteorological aspects of wind power. Research has examined wind power globally (Archer and Jacobson, 2005;

Lu et al., 2009) and internationally in regional or national overviews (ie, Haslett and Raftery, 1989; Pryor et al., 2006; Jimenez et al., 2008; Najac et al., 2009), in addition to myriad national and continental wind energy resource atlases usually put together by governmental or cooperative efforts (ie, Elliott et al., 1987). Research on meteorology and climate variability most relevant to wind power in California has ranged from modeling, large observational data sets, and nationwide perspectives (Sailor et al., 2000; Breslow and Sailor, 2002; Archer and Jacobson, 2003; Pryor et al., 2006, 2009) to more focused work on regional settings, including California's coastal resources (Jiang et al., 2008; Dvorak et al., 2010).

Despite the role that wind power already plays in California's energy infrastructure, the peer-reviewed literature does not contain a complete analysis of the climatological and meteorological processes responsible for low-level winds at the major generation sites. In addition to the wind power studies mentioned above, regional resource assessments have also been undertaken as part of national efforts (Elliott et al., 1991; Elliott and Schwartz, 2005), but it is also necessary to look to general studies of atmospheric variability affecting the region and interpret them in light of their relevance to the wind power sites. The classic modes of climate variability, among them the Pacific-North American Pattern (PNA), El Niño-Southern Oscillation, (ENSO), and Pacific Decadal Oscillation (PDO), all hold implications for California climate variability from synoptic to interannual timescales. The PNA is associated with SLP and upper-air anomalies at specified positions. Its positive phase indicates a more meridional upper-level flow over North America, while the negative phase indicates a more zonal flow (Wallace and Gutzler, 1981; Leathers et al., 1991). ENSO variability can excite a PNA pattern, and the positive phase is known to bring warmer ocean temperatures and increased storminess to Pacific North America, including impacts to the Sonoran desert in California and Arizona (Woodhouse, 1997). Its typical influences on pressure, precipitation, and wind fields are widely studied, while the PDO is often characterized as a large-scale modulation pattern of ENSO variability (Mantua et al., 1997; Gershunov and Barnett, 1998).

To more easily summarize an area's suitability for wind power development, convention often refers to the seven wind power classes defined in Elliott et al. (1991). In that study, a site with mean wind power falling in class 5 (250-300 W m^{-2} at 10m above ground level, or mean wind speed of 6.0-6.4 m/s given their wind speed distribution assumptions) or above was considered adequate for ready exploitation of the wind resource, while it was thought that wind resources down to class 3 (150-200 W m^{-2}, or 5.1-5.6 m/s at 10 m) could effectively be developed given advances in conversion technology. More recent wind energy resource maps displayed as part of the US Department of Energy's Wind Powering America initiative define the wind classes identically and describe classes 3-5 as “fair,” “good,” and “excellent,” respectively (Elliott and Schwartz, 2005). These updated maps show numerous areas in northern and southern California with class 4 or above resources, but the areas are small and spottily distributed — a sharp contrast to other areas where orography is less prominent, such as the Great Plains of the United States.

The topography of inland California and its effects on low-level wind flow are behind the patchy distributions of the areas viable for wind farms. Given an appropriate background flow, the localized amplification effects of orography can be quite large. Measurements taken with wind blowing directly toward and through well-defined mountain gaps have shown that wind speeds slightly downwind of the narrowest portion of the gap often reach 2-3 times the speed recorded further upwind, at or just before the narrowest point (Ramachandran et al., 1980). Increases in wind speed can be similar for small-scale mountain ridges, hills, and scarps as well (Barry, 2008, pp. 72-87) The diverse sites established for wind power in California include installations on the edge of the low-lying, hot Sonoran desert, the higher-elevation Mojave desert, and the Central Valley between San Francisco and Sacramento. For each of these settings, winds are particularly strong because of the channeling effect of nearby terrain. To this end, the present study analyzes wind measurements from ground meteorological stations close to, and in the same topographical setting as, major wind energy generation facilities: in the Southern California desert areas near the San Gorgonio and Tehachapi Passes, and in the Sacramento Valley north of the Straits of Carquinez.

Southern California mountain pass winds have also been the subject of interest due to their role in channeling Santa Ana winds and, in many cases, bringing increased wildfire danger. Santa Ana winds can occur from September to March and have been investigated by Raphael (2003); Westerling et al. (2004); Miller and Schlegel (2006); Hughes and Hall (2009), usually with a focus on the winds as they blow out of the Great Basin and Mojave plateaus, are channeled through mountain passes, and accelerate and warm adiabatically as they descend and move toward the coast. In contrast, the southern

California wind conversion sites examined here are on the higher-elevation side of the Tehachapi Pass connecting Mojave to the Central Valley, or on the desert side of the San Gorgonio Pass. As such, these sites are distinct from the gaps previously identified as having strong winds or and elevated fire danger during Santa Ana events, and the local wind behavior during these events has not been studied as extensively.

The objective of this study is to fill the gap in exposition of the meteorological phenomena driving low-level winds at the major California wind farms. By analyzing the seasonal cycle of winds and connection to larger-scale circulation in this paper, we address the first part of that gap. Although each site of our interest has particular characteristics, we adopt a unified framework to for all three regions in order to integrate the detailed information into a comprehensive outlook. In this paper we first describe the data used for analysis and intercomparison. We then present the methods of analysis used and our findings for individual wind time series, in long-term annual and seasonal means. We then examine the relationships among the wind time series and climate indices, considering the cold and warm seasons separately. We finally discuss our findings in a general sense, including implications for wind energy, and the most appropriate focus for further investigations of wind variability.

3.3 Data

The primary sources of site data in this study are archived METARs[1] weather reports from airports near the three wind generation sites containing hourly observations of wind speed, direction, station temperature, barometric pressure, dew-point temperature, cloud cover, cloud height, and visibility. METARs data have the advantage of being more accessible than actual on-site observations from wind farms and, in many cases, also cover a longer time period. METARs observations from Palm Springs airport, Mojave airport, Edwards Air Force Base, and Travis Air Force Base were identified as sources of relatively long records located close to major California wind energy facilities with no major topographic features separating the sites from the wind farms. Locations of observation sites are shown in Fig. 3.1. Previous studies have found neighboring wind site measurements to be a powerful aid in short-term forecasting for wind farms (Lar-

---

[1] The term METAR is derived from a French acronym and denotes a specific, concise format for reporting various meteorological variables. The reports include the fields most useful to aviators, and are widely used by airports both small and large.

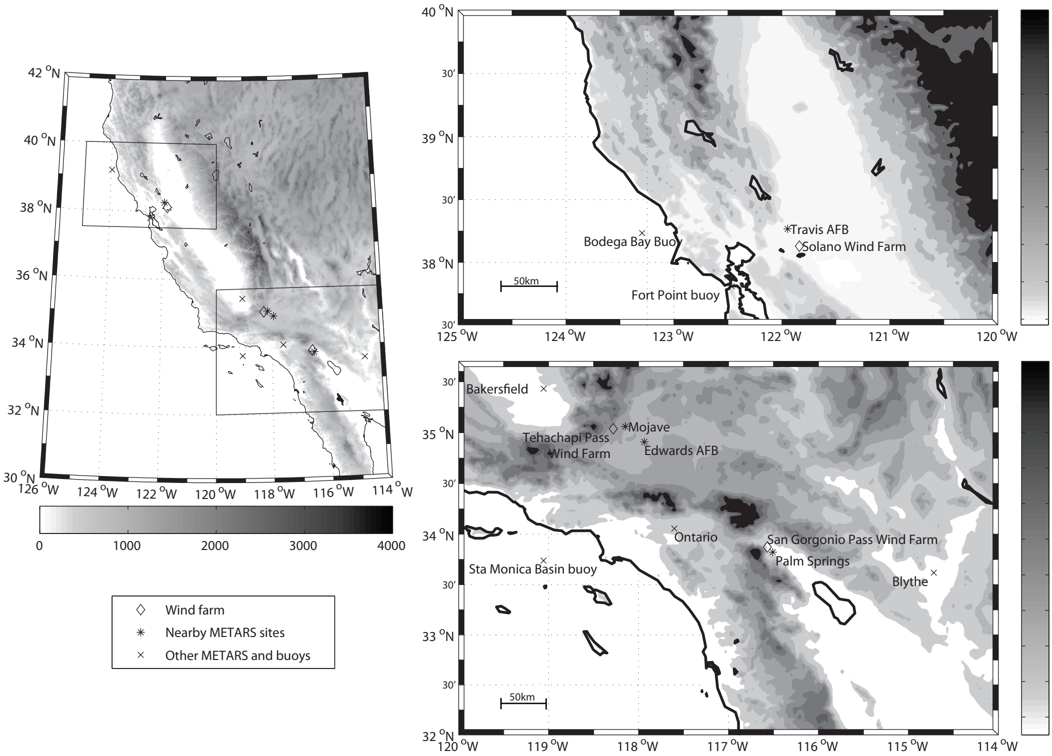

Figure 3.1: Overview and two magnified regional maps showing locations of wind power conversion facilities, nearby METARs stations, and other observation and buoy sites used in the study. The shading scheme denotes elevation, in meters, scaled separately for each projection.

son and Westrick, 2006), and in our analysis, we present additional findings to support the supposition that the METARs data from nearby locations are representative of the climatology and variability of winds at the wind energy sites themselves.

The METARs data were collected at local airports and cover different time periods for different sites. Recent data — since the late 1990s — use Automated Service Observing Systems (ASOS) and conform to current standards by reporting hourly wind as two-minute averages measured at 10 meters above the ground, 24 hours a day. However, over the several decades that measurements have been recorded, these standards were not always followed. The National Climatic Data Center provided to us a metadata listing for each METARs site denoting its history of wind measurement heights. We use this information to scale wind speed at height h, denoted V_h, to equivalent 10-meter values, V_{10} using the one-seventh power law (Peterson and Hennessey Jr, 1978):

$$\frac{V_{10}}{V_h} = \left(\frac{10}{h}\right)^{\frac{1}{7}} \tag{3.1}$$

These scaled speeds are used throughout this paper for all wind speed data derived from METARs reports.

Palms Springs airport data (METARs code KPSP) were measured on the eastern side of the San Gorgonio Pass, where the pass has begun widening out into the Sonoran Desert basin, approximately 10 km from the easternmost turbines in the San Gorgonio wind energy conversion area (Fig. (3.1)). Data are consistently present from 1973 to 2005, although observations usually were not taken at night. For data representative of winds at the Tehachapi pass wind energy sites, we use observations from two nearby locations in the Mojave desert: Mojave Airport (KMHV) near the mouth of the Pass and within 15 km of wind farm turbines, and Edwards Air Force Base (KEDW) approximately 30 km further east and south from there. While the observed wind energy at Mojave is greater than at Edwards and the site is closer to Tehachapi, the time period covered, frequency of observation, and precision of wind measurements are greater at Edwards Air Force Base. Data from Mojave are available from daylight hours mainly from 1987 to 2005, whereas Edwards data provide all-day coverage from 1942-2005.

Further north in California, Travis Air Force Base (KSUU) is located close to the wind energy production site in Solano County, near Rio Vista, and has observations from all hours of the day over 1944-2009 with no data from 1971-1972, and some months missing between 2005-2009.

METARs data are augmented by observations taken at a mast located in the currently operating wind power facility at Montezuma Hills, Rio Vista, in Solano County. The data cover 2000-2007 and were furnished by the Sacramento Municipal Utilities District (SMUD). This mast has anemometers at various heights comparable to common wind turbine hub heights of 30-60m. Whenever we make direct comparisons between SMUD and Travis data, we take the 50m sensor data and scale the wind speed to the nominal 10m value as in Eqn. 3.1.

Winds measured at the inland METARs sites are also compared to ocean surface winds at selected National Data Buoy Center and National Ocean Service weather buoys offshore California (Hamilton, 1986; Meindl and Hamilton, 1992). These buoy data are recorded hourly. The weather buoys chosen have several years of overlap with the observations from the the inland sites. The buoy wind observations are scaled to nominal

10m values from their measurement height of 5m (Hsu et al., 1994; Taylor et al., 2008). Coverage is from 1982 to 2005 for the NDBC buoys used, while the NOS buoy near Fort Point, San Francisco, covers 2005 to 2008.

We draw on SST, SLP, and 500 hPa height data from the NCEP Reanalysis gridded data, using anomalies calculated by removing climatologies based on 1968-1996 (Kalnay et al., 1996). Our intercomparison of data sets also utilizes climate indices for the PNA pattern (using the 500hPa heights-based index from Wallace and Gutzler (1981)), Niño 3.4 SST anomaly (provided by the Climate Diagnostics Center), North Atlantic Oscillation (NAO; ie, the Northern Hemisphere Annual Modes of Thompson and Wallace (2000), with rotated principal component-based indices from the Climate Prediction Center) and the PDO (principal component-based index from University of Washington/JISAO).

To examine the relationships between inland soil moisture and observed wind speed, we use output from the Variable Infiltration Capacity Macroscale Hydrologic Model (VIC; Maurer et al., 2002) over select regions of California and Nevada. The model has a horizontal resolution of 12 km and is forced with gridded daily maximum and minimum temperature, precipitation, and wind speed data from 1949-1970. The regions covered are California's Central Valley from 37 °N to 39 °N (essentially, the meridional center of the valley), the Sonoran Desert, 32.5 °N-34 °N, 114.75 °W-116 °W, the Great Basin, 36.25 °N-38.75 °N, 113.75 °W-116.25 °W, and the Mojave Desert area, a combination of the two boxes 34.5 °N-35°N, 115.75 °W-117 °W and 34.6 °N-35 °N, 117 °W-118 °W.

3.4 Time series characteristics

3.4.1 Power spectra

METARs weather observations are generally made for operational purposes, and not designed for studies of climate or interdecadal-scale variability. This problem is particularly acute for studies involving long-term variability of winds, which are very sensitive to changes in location or height of sensors, to alterations to the surface or surroundings of an anemometer, or to changes of the instrument itself when sufficient calibration is not undertaken (von Storch and Weisse, 2008; Karl et al., 1993). Discontinuities that probably can be attributed to such changes become evident from wind speed

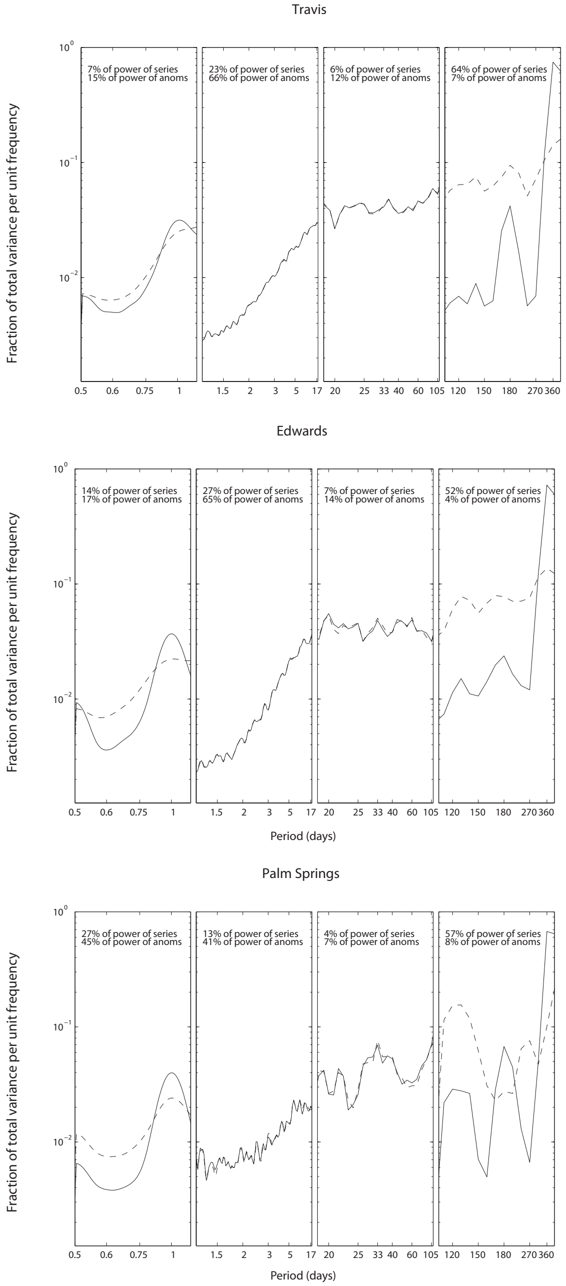

Figure 3.2: Power spectra computed from 6-hourly wind speed means and 6-hourly wind speed anomalies with the annual cycle removed at Travis, Edwards, and Palm Springs. The x-axis marks period in days, and in each of the four windows the portion of total variance contained in the corresponding range of periods is indicated. The y-axis is normalized to show variance density as a portion of total variance.

time series from Travis, Mojave, Edwards, or Palm Springs sites smoothed with 30^{-1} d^{-1} Butterworth low-pass filter (not shown). For the largest of the jumps, coincident discontinuities in mean wind direction are also apparent. Rather than an actual sudden and long-term change in wind regime, each jump is almost certainly due to a change in the anemometer and/or its location or surroundings. Within the time periods between the visible jumps, our analysis shows no inconsistencies of the wind time series behavior, power spectra, or relationships to external variables. Without ignoring the possibility of other shifts, we can make a rough correction for the obvious time series jumps by forming an "adjusted" series of daily anomaly values. We do this by taking the unadjusted anomaly series and, for the time periods between obvious wind speed jumps, recomputing each period's anomalies based on a climatology formed only from observations between those jumps. This removes the bias introduced by such jumps. Since our computation of the climatologies includes smoothing the raw means with a 10-day filter, the shape of the different climatologies used for the piecewise-constructed daily anomaly series match very closely. Thus, hereinafter when we refer to adjusted daily anomaly time series, we are describing those made by patching in anomalies computed from the following sites and time periods: at Travis, from 1944-1952, 1953-1970, 1973-1979, and 1980-1992 inclusive; at Palm Springs, from 1973-1975 and 1976-1997, and 1998-2005 inclusive; and at Edwards, from 1948-1954, 1958-1991, and 1993-2003 inclusive. Because the Mojave wind measurements contain no clear jumps, we use the un-adjusted series for this site. While the data quality limits the reliability of any analysis of interdecadal variability, they do not apparently compromise our ability to investigate variations from sub-daily to annual scales. These frequencies of variability are related to a wide variety of atmospheric states and scales of physical influences, and examination of wind behavior at these time scales should help elucidate the mechanisms responsible for interannual variability.

We begin investigating the wind series using the power spectra of 6-hourly averages and anomalies from 6-hourly climatological means. We omit the results from Mojave, where most years had no more than 13 hours a day of anemometer coverage. The spectra in Fig. 3.2 are given for both 6-hourly mean values and 6-hourly interannual anomalies. They are computed using Welch's method (Welch, 1967), normalized by the total power of the data set for periods up to yearly, and the x-axis is labeled with the time period in days aligning with the frequency (ie, 2 refers to 2 days per cycle, or a frequency of $\frac{1}{2}$ d^{-1}, etc.). For each station we present four panels allowing us to view the spectra centered on four different period ranges and the proportion of power in each, covering the whole resolved range of yearly and shorter periods. We limit our results from each site to those years when anemometer coverage was at or close to every 24 hours, and this yields a sample size of 13 years for Palm Springs, compared to 45 years for Edwards and 60 years for Travis. The issue of occasional instrumental changes does not taint these spectra, as the discontinuous changes occurred every several years and we limit the examination to annual and higher-frequency variability.

For each station, the sharpest peak in station wind speed is found near the 365-day period. Since below we describe the shape of the annual cycle in more detail, we proceed to examine the sub-annual variability by removing the mean annual cycle. This is accomplished by subtracting long-term mean wind speed of each 6-hour period. After doing so, the least total power is found in the 110-400 day band. The submonthly-to-seasonal band, covering 15 to 105 day periods, shows more power, but not as much as the shorter periods.

After removing the annual cycle, more than 80 % of the wind speed variance at each station is contained in the daily and synoptic period bands, with significant peaks around the diurnal (1 d) and longer synoptic periods(3-15 d) (Fig. 3.2). The annual cycle typically contains wind speeds that vary by 3-4 m/s (Fig. 3.7) from annual peak to trough. The 3-15 day band represents day-to-day and week-to-week wind speed fluctuations that typically vary by 1-5 m/s. The diurnal peak represents daily fluctuations, with a typical wind speed change of 2-5 m/s from the afternoon and evening peak hours to early morning wind minimum (Fig. 3.8-3.10). Our remaining investigation therefore focuses on describing the annual cycle. In the companion article we describe the patterns and analyze the atmospheric processes leading to the distinct peaks in variance density at the diurnal and synoptic scales.

3.4.2 Wind roses

To better describe the annual-mean wind characteristics and closely related station atmospheric data, we start by viewing the distributions of METARs-reported wind intensity, direction, and sea-level pressure for each site and season with the wind rose-inspired polar histograms in Figs. 3.3-3.6. These polar histograms plot dots that indicate the distribution within each season of hourly wind speeds and directions, assigning each dot a color based on the site's average sea level pressure when it was undergoing winds

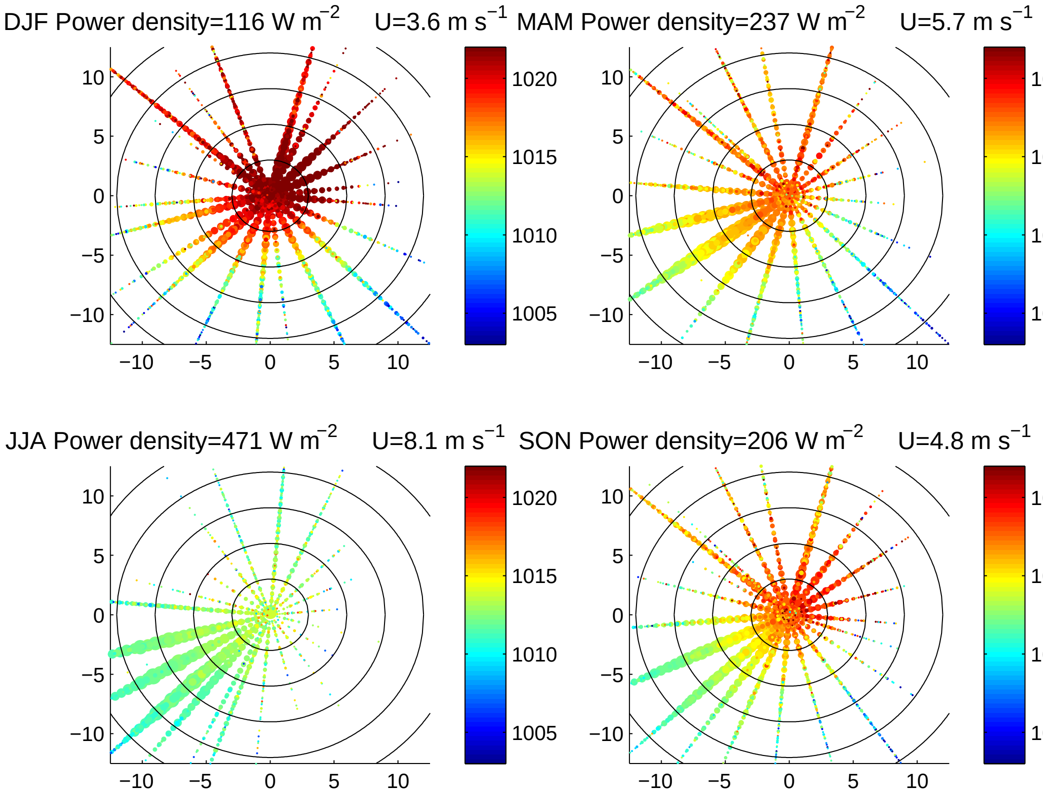

Figure 3.3: Polar histograms showing wind intensity and direction distribution at Travis for each season. In these polar histogram plots, each dot represents all hourly observations that fall within a certain direction and speed range bin for the given season and site. Each dot's angular location indicates the direction the winds were coming from, while its distance from the origin indicates the wind speed (the radial distances are marked every 3 m/s). The size of the dot indicates the frequency with which winds falling into that bin were observed, and the color of the dot indicates the mean sea-level pressure concurrent with the winds falling into each bin.

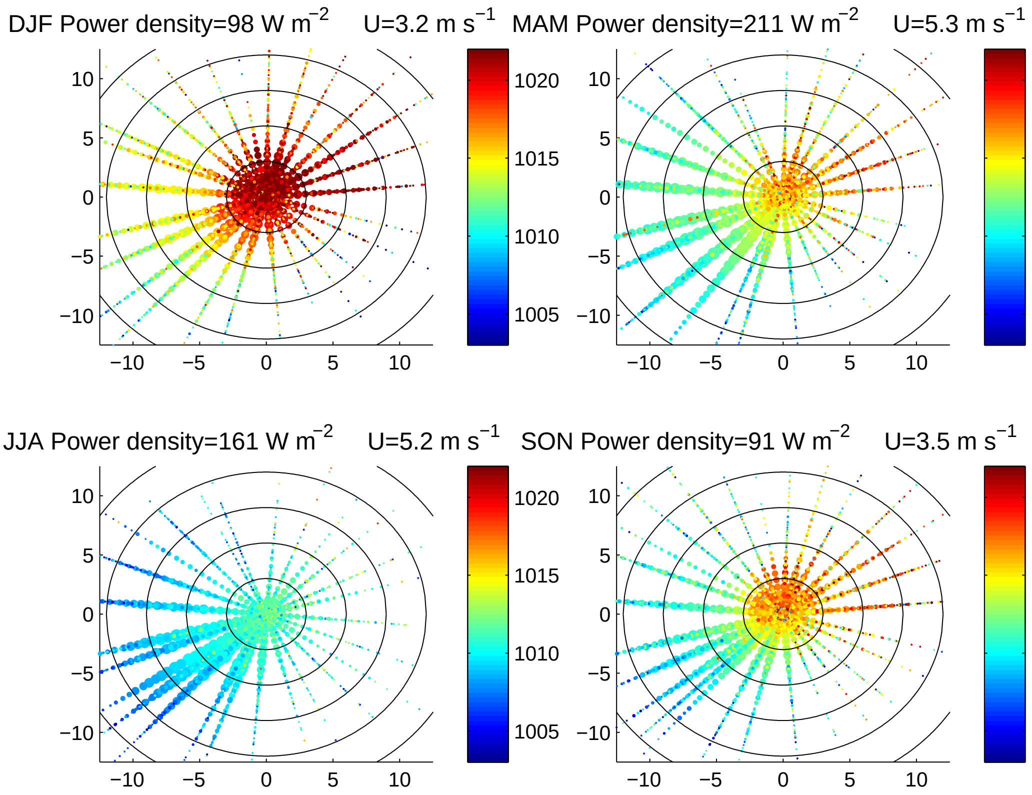

Figure 3.4: As in Fig. 3.3, but for Edwards.

in that speed and direction bin. [2] Also listed for each season is the seasonal mean wind speed and seasonal mean wind power density. Wind power density is the wind kinetic energy per unit time and unit area swept by turbine blades, taken as

$$P = \frac{1}{2}\rho_{clim}\overline{V^3} \tag{3.2}$$

where V is scalar wind speed, ρ_{clim} is the station's seasonal mean air density, the mean of hourly air density calculated from sea-level pressure, temperature, and a US Standard Atmosphere 1976 lapse rate of 6.5 K km^{-1}. Using the mean density results in variations of less than 1% from the hourly variable air density, while resulting in usable data on any hour where wind speed is reported, even in the absence of SLP or temperature readings.

---

[2] While the instrumental changes and jumps in the series at each site (described above) imply that a separate figure should have been made for each period between anemometer shifts, in practice the intensity of the recorded wind appears to have changed by less than 1.5 m/s at each shift. While this is a significant change in smoothed wind speed or wind speed anomaly time series, such a change would shift an observation's place in these polar histogram plots by at most one bin, and given the generally smooth transitions for frequency and mean SLP in adjacent bins, there would be no substantive difference realized by producing separate plots for each instrumental epoch.

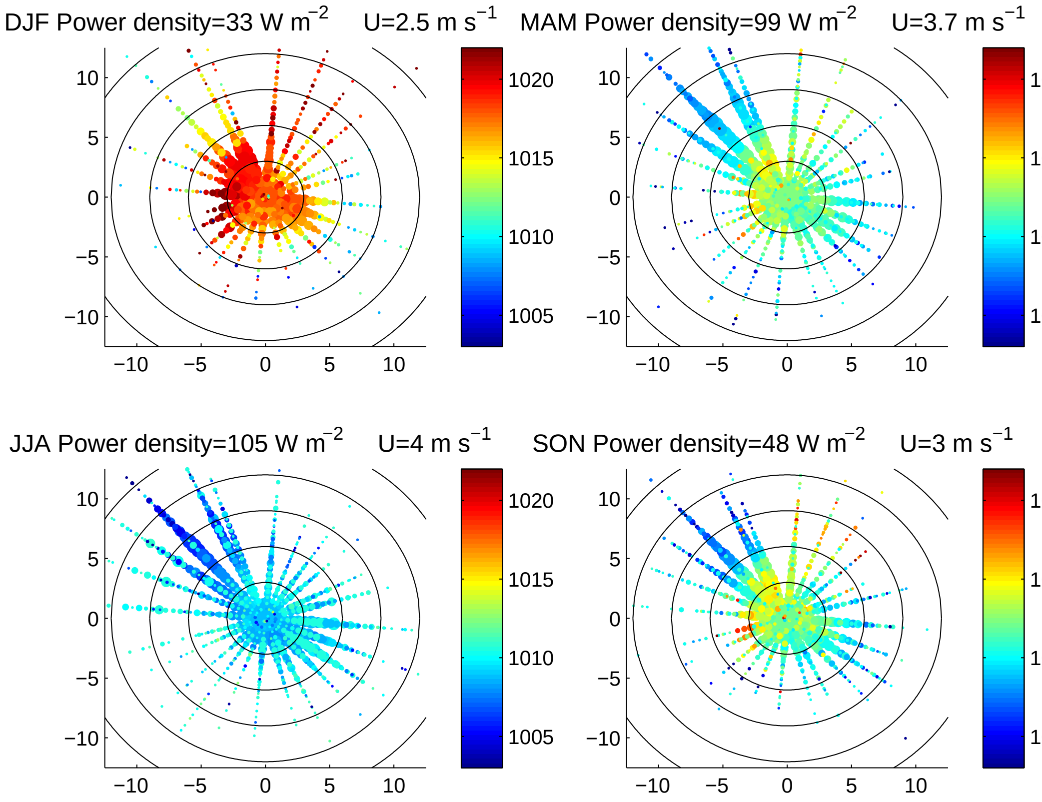

Figure 3.5: As in Fig. 3.3, but for Palm Springs.

At the Travis site in Northern California the different seasons take on fundamentally different characteristics (Fig. 3.3). Summer is the most energetic season for winds, and the dominant southwesterly direction points to an inflow from the Straits of Carquinez and, beyond that, San Francisco Bay. The generally moderate station SLP is consistent with milder summertime weather patterns, and suggests that transient synoptic processes are not a significant factor here. In contrast, winter observations exhibit a calmer mean wind, but with greater variability in terms of direction and SLP. While the variance of daily mean wind speeds is comparable for the two seasons, the relative variance (ie, the quotient of wind speed standard deviation divided by mean wind speed) is significantly greater in winter. The observations with highest station pressure are dominated by northeast breezes, while the highest wind speeds come when SLP is low.

In Fig. 3.3 spring and fall are similar to each other at Travis and are most concisely described as transition periods. Both exhibit the summerlike tendency toward

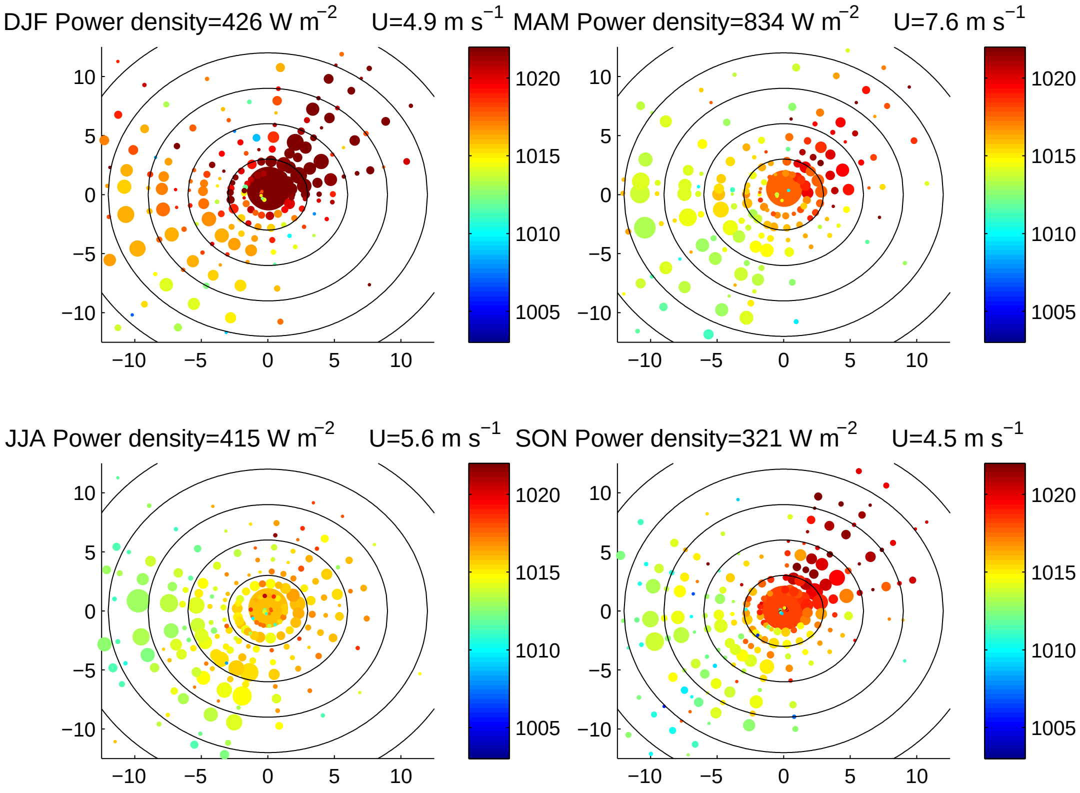

Figure 3.6: As in Fig. 3.6, but for Mojave.

SW winds greater than 5 m/s when station pressure is moderate for the period. At the same time, both also show proclivities for north or northeast winds in higher SLP conditions, as in December-February.

The polar histograms for the southern California stations (Figs. 3.4-3.6) display different characteristics from Travis. Palm Springs shows a preference for winds along a NW-SE axis, roughly the direction of the mountain ridge line close to the airport weather station. Edwards Air Force Base does also show some preferred directions, but not as strongly as Mojave, which, while located within 30 km of Edwards, is closer to the Tehachapi Pass and the SW-NE line of mountains on the western side of the Mojave Desert. Southern California sites also show some relationships between mean SLP and wind characteristics, notably in the high desert sites (Mojave and Edwards), where station pressure is notably higher in east and northerly wind conditions. Although some of this may correspond to Santa Ana conditions, especially the northeasterly winds associated with high pressure seen in winter, the presence of the pattern even in the spring months, when Santa Anas are rare, implies it is associated with common anticyclonic circulations centered on the western US and outflow from high pressure areas over the Great Basin, but not exhibiting the intense temperature, relative humidity, and gravity-driven wind speed anomalies characteristic of Santa Anas (Raphael, 2003; Hughes and Hall, 2009). The stronger and more westerly winds in these seasons are also consistent with transient eastward-moving low pressure systems centered at higher latitudes, which we examine in more detail in the Part 2. Milder mean SLPs in the summer and predominantly westerly flow are evident at each California site, although the wind is funneled very effectively into a preferred direction at Palm Springs and less so at Mojave and Edwards.

Delving further into the role of Santa Ana conditions on Southern California station climatologies, we compare the characteristics of all observations to those from days exhibiting Santa Ana conditions as defined by an index based on METARs-reported station pressure, wind, and dew point in San Diego, California and Tonopah, central Nevada, from September-March. This index is similar to previous indices used (Raphael, 2003; Miller and Schlegel, 2006) and allows us to define a day as “Santa Ana” or “Non-Santa Ana.” After removing the observations that coincide with Santa Ana days, the resulting polar histograms (not shown) still show noticeable northerly to easterly winds corresponding to higher station pressures, although their frequency is reduced. Of note is that the polar histograms of only Santa Ana days show lesser mean wind speed and wind power density at nearly all Southern California sites and applicable periods. The only exception is at Palm Springs in the wintertime, where observations on Santa Ana days show a mean wind speed of 6.0 m/s and wind power density of 52.7 W m $^{-2}$, compared to 5.9 m/s and 50.6 W m $^{-2}$ on other days. These measures all indicate that our sites have average to below average wind speeds on Santa Ana days.

The relatively slow or moderate winds in Santa Ana conditions may seem surprising. While the conditions are known for strong, warm, and dry winds, this reputation is founded in part on conditions in highly populated coastal areas and on the downslopes of mountain passes (Raphael, 2003). Each Southern California site in this analysis, however, is either on a relatively flat plane (Edwards) or on the upwind side of mountain passes where offshore flow is uphill, and thus wind speed as the dominant flow travels upslope are diminished at our sites on the Santa Ana-classified days.

The polar histograms in Figs. 3.3-3.6 also give a sense of the distribution of wind speeds at each station and season. Numerous studies have investigated the distribution of station wind speeds in general and in the wind power setting (ie Garcia-Bustamante et al., 2008; Li and Li, 2005; Celik, 2004). A variety of theoretical distributions has been proposed for wind speeds, and the Weibull distribution is often used as a first approximation that exhibits the positive skewness generally found in wind series. For the purposes of our inquiry the best theoretical PDF for each wind data set is not as important as noting the general characteristics found. First, as seen in the origin of each polar histogram, a large number of zero-wind readings were recorded at each site. These are separate from the no-value coded entries in the METARs data sets, tend to be surrounded by zero or low-wind readings, and also come from the hours of lowest climatological wind (discussed below), indicating that they are plausible, valid readings. The zero-wind hours are dispersed enough that there is a negligible number of days of zero mean wind. Although we do not here reproduce the actual PDFs, two additional points from them are relevant. The distributions have long right tails from each station and season mean, and the distributions of interannual daily-mean anomalies also display these long right tails, as this is consistent with transient systems bringing occasional strong winds. The exception to this pattern is summertime Travis winds, whose distribution is far more symmetric, and when the wind power density is greatest in both hourly data and daily means.

3.4.3 Annual cycle

To complement the polar histograms, we present each station's 10-day-smoothed annual climatology of wind speed and vector components, as well as the interannual wind speed standard deviation about the climatological mean in Fig 3.7. While the northern California site has a maximum in the summertime, with more positive climatological values of both zonal and meridional 10m wind, the southern sites peak near spring. At each site, variability rises and falls, but only slightly, roughly in phase with the climatological wind speed. This means that coefficient of variation (ie, ratio of the standard deviation to the climatological wind value) is much stronger in the calm, colder-season months, where it approaches unity, while in the warmer months it is proportionally far smaller. Figure 3.7 also shows the climatology of the zonal pressure difference, from reanalysis data in grid boxes neighboring those containing the respective stations, with the sign reversed so that higher pressure to the west is positive. At each southern California station, the annual cycle in mean wind speed roughly tracks with the annual cycle of the pressure gradient. This is not the case, however, for Travis, where the pressure gradient also peaks in late spring, but wind speeds are at their highest throughout the summer.

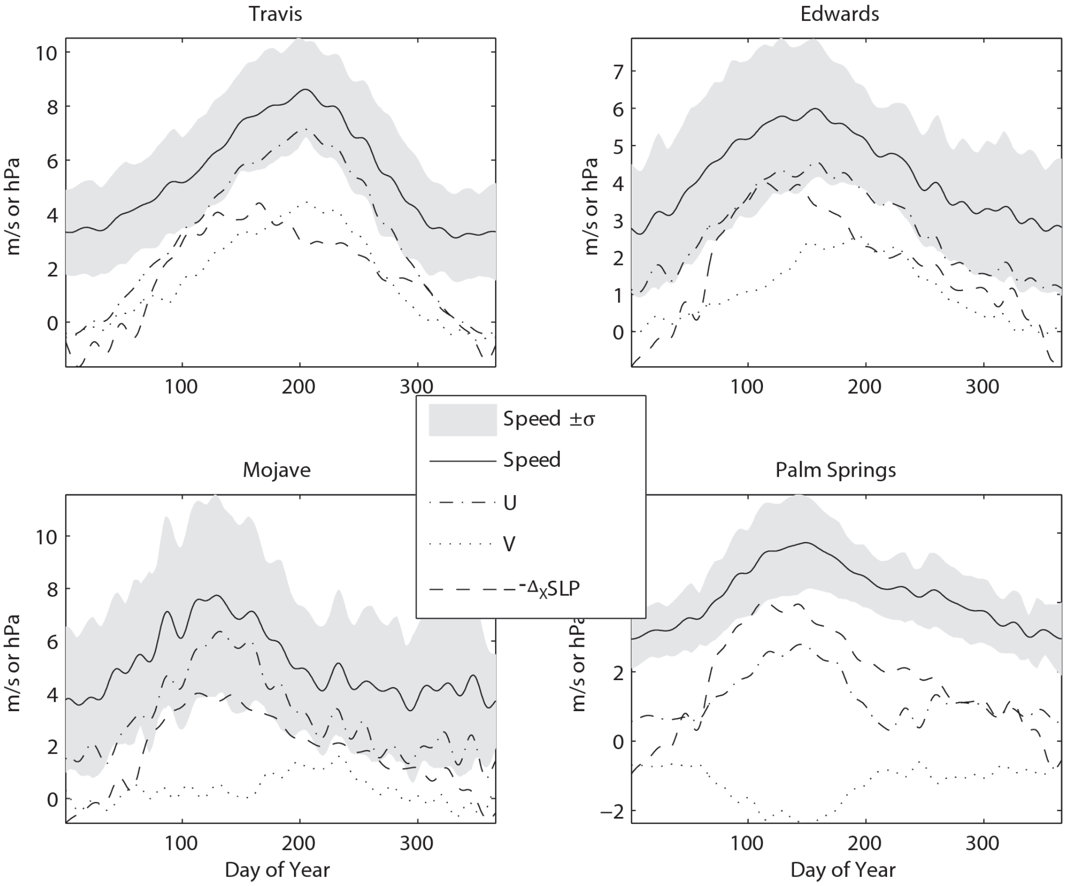

Figure 3.7: Mean annual cycle at each site of wind speed, interannual standard deviation, and zonal and meridional wind components component. Also shown is the zonal pressure difference, in hPa, between the reanalysis boxes centered directly to the west and east of each site's closest grid box center.

3.4.4 Seasonality of the diurnal cycle

In addition to the seasonal distributions of wind speed and direction, at each site there may be a considerable diurnal cycle, also suggested from the power spectra above, which itself displays variability on assorted timescales. In Figs. 3.8-3.10 the mean temperature and wind speed at each hour (local standard time) is displayed for

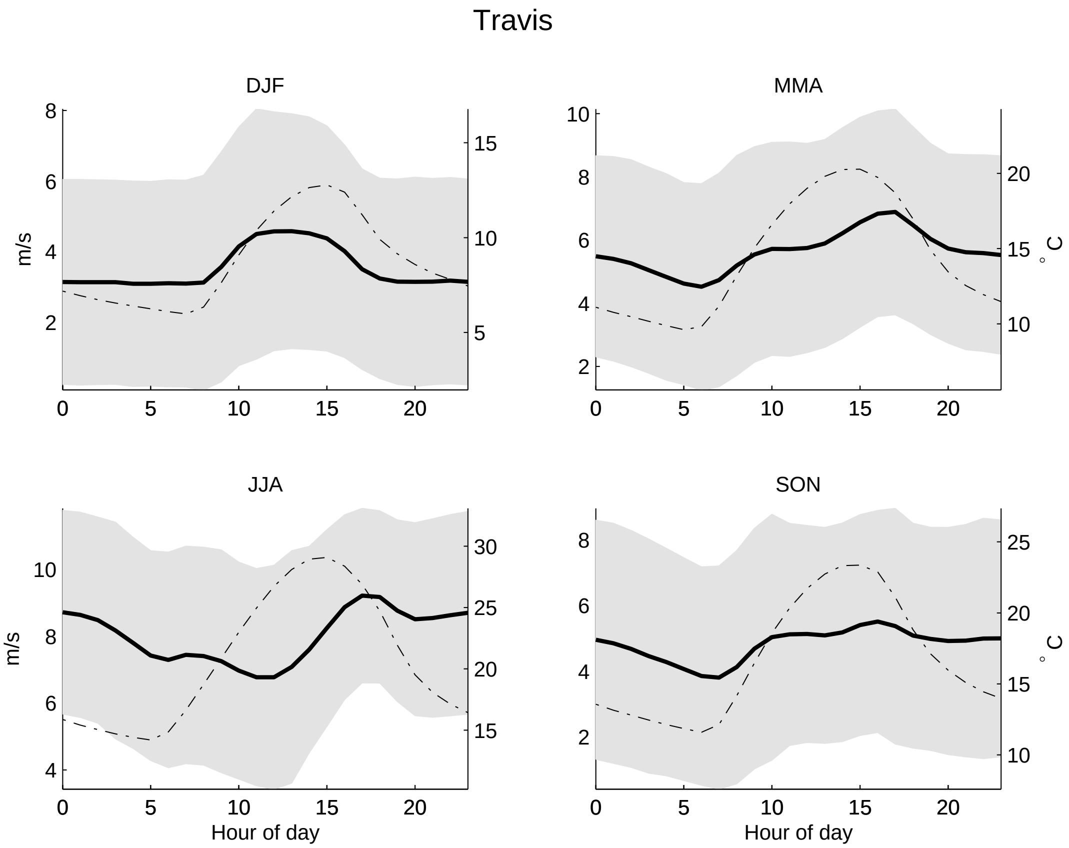

Figure 3.8: Mean diurnal cycle for each season at Travis in wind speed(solid) and temperature (dashed), with gray area about wind speed denoting ± 1 standard deviation.

each season, as well as error bars denoting ± 1 standard deviation. Edwards shows a consistent mean diurnal cycle in wind, weaker in the winter months, with calmer morning breezes giving way to stronger winds later in the day, centered near 15:00-1800 local time. These extrema are generally a few hours after the corresponding extrema in temperature, which also has a greater mean diurnal cycle in the warmer months. Given the size of the error bars, however, it seems clear that a summer day is far more likely to have a diurnal cycle such as these, and that other seasons may vary from these means significantly. Palm Springs also shows a diurnal signal that is most defined in the summer, with a winds lagging temperature by several hours and peaking near 20:00 local time. While the Travis site does not have as pronounced a diurnal cycle as the southern California locations, the spring and summer nonetheless show a discernible mean cycle, both with a maximum at 17:00 local standard time, followed by a wind speed plateau several hours

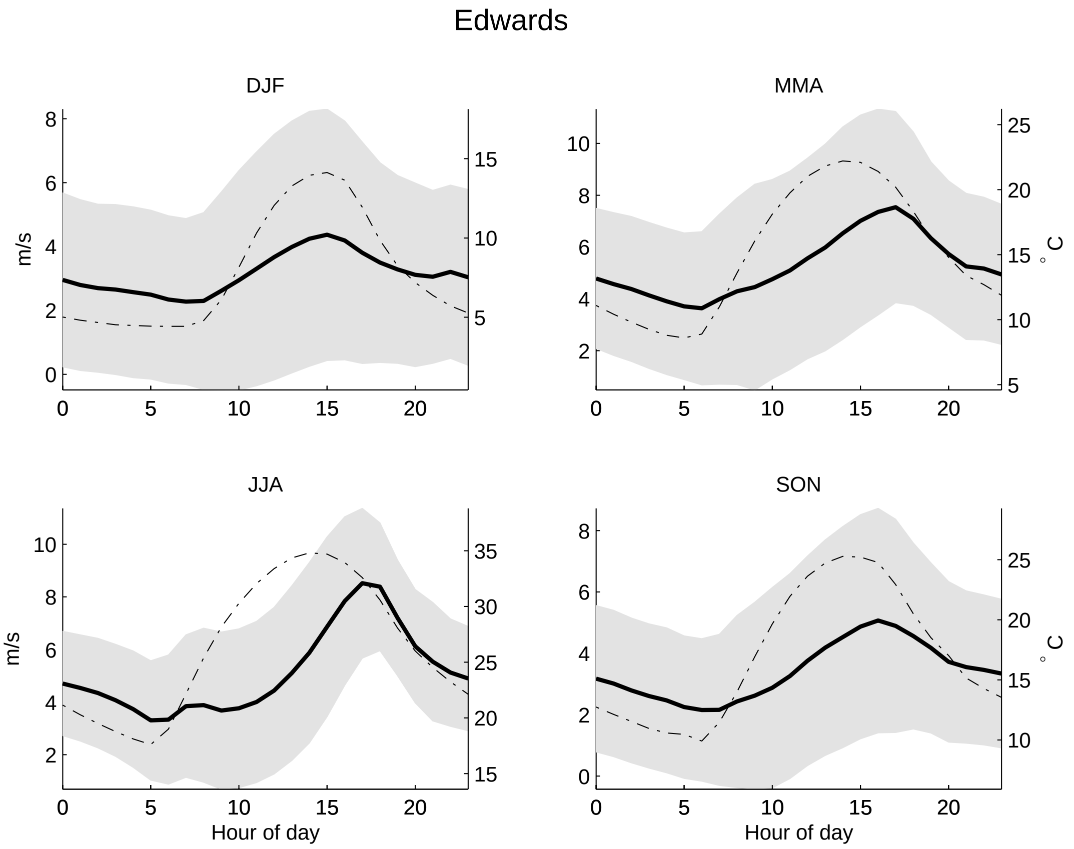

Figure 3.9: As in Fig. 3.8, but for the mean daily cycle at Edwards.

long with the wind close to this speed until past midnight. The summertime minimum wind speed time tends toward 11:00, while in the winter it is 6:00. The corresponding daily cycle in temperature is also very weak in winter, while significantly stronger in the other seasons. A wind speed peak in afternoon to early evening hours for wind energy areas would imply greater electricity generation when demand tends still to be high, a noteworthy characteristic for planning and operating such sites.

3.5 Intercomparison of wind and climate data

3.5.1 Statistical relationships between wind sites

We turn now to the relationships among the observed winds at METARs sites near wind farms, observed wind at other locations, and several common climate indices.

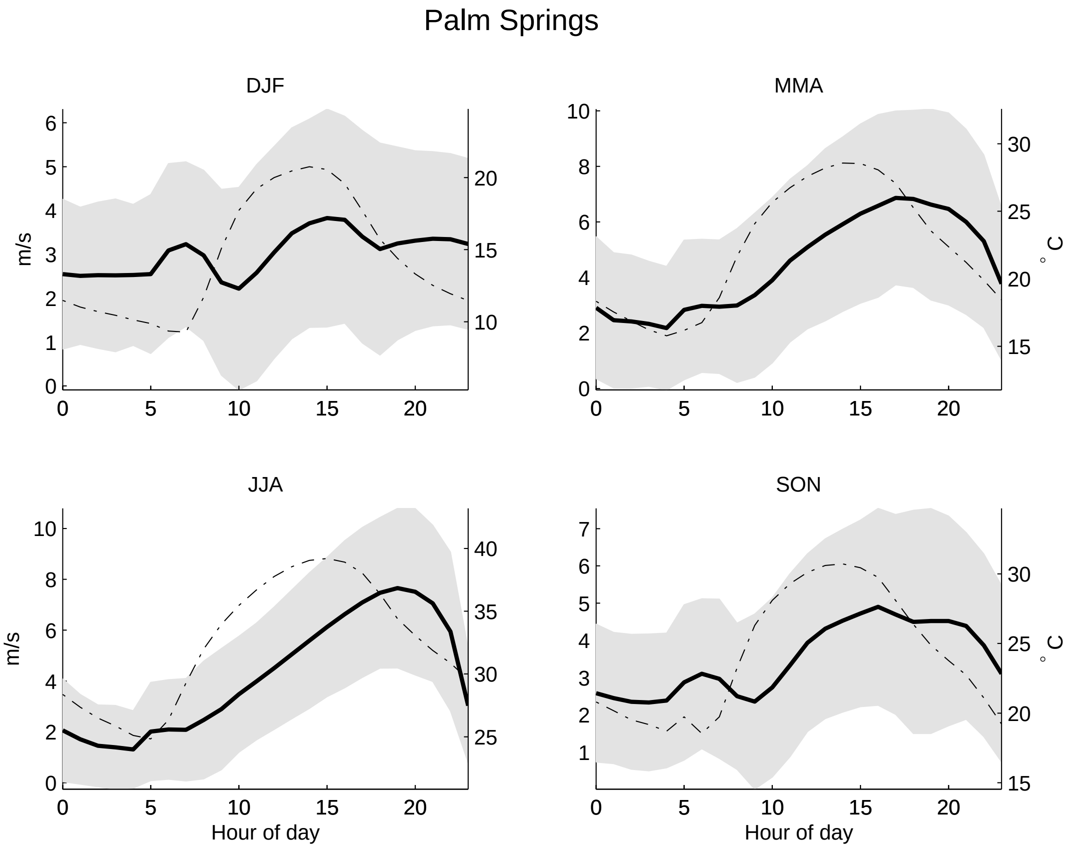

Figure 3.10: As in Fig. 3.8, but for the mean daily cycle at Palm Springs.

One goal in examining wind speed at nearby sites is to understand the degree and the limits of spatial coherence in wind patterns over various types of terrain. As a first step we present in Tables 3.1-3.4 the correlation coefficients for various wind time series, nearby SST, and climate indices for the PNA, Niño 3.4, the NAO, and the PDO. The SST is taken from reanalysis data — a combination of GISST v2.2 data before 1982 and Reynolds SST after that. The southern California SST index is based the 2.5 × 2.5 °box centered on 32.5 °N, 120 °W, while the northern California SST box is centered on 37.5 °N, 125 °W. Since the annual cycles of the wind at our sites of interest were already compared in Figure 3.7, we focus on how the time series of anomalies vary together. In addition to the four sites we examined above, we also include daily wind time series from buoy 46013 offshore of Bodega Bay, California, buoy 46025, in the Santa Monica Basin south of Los Angeles, and the Bakersfield, CA METARs site in the San Joaquin Valley northwest of the Mojave site. We examine daily-mean data in order to eliminate the effect of the diurnal cycle as well as to eliminate effects of the timing of wind patterns that might be offset by several hours between sites as weather fronts move through. For the Palm Springs, Edwards, and Travis sites, we use the series corrected for the most obvious instrumentation changes, as discussed above. Each correlation coefficient is based on all the dates where there are data available for both of the time series in question. The bold numbers in the tables indicate that we can reject, at the 95% confidence level, the null hypothesis of zero correlation, based on bias-corrected, accelerated bootstrap confidence intervals (Efron and Tibshirani, 1993). Our confidence estimations are based on that of Mudelsee (2003), who also showed the validity of these techniques for the application to climate time series. To account for serial autocorrelation in the daily time series in Tables 3.1-3.2 we use a stationary bootstrap routine that yields resampled data sets with more strings of data points that were consecutive in the original time series than would be expected from a traditional, purely random bootstrap resampling technique (Politis and Romano, 1994). We follow the formula in Mudelsee (2003) in how we relate persistence times to the stationary bootstrap's probability of selecting consecutive points. The persistence times themselves are found in two steps: first, we compute persistence times separately for each station and year's cold and warm season from $-2(\ln r_1)^{-1}$, where r_1 is the one-day lagged autocorrelation (Leith, 1973); then, we conservatively select the longest decorrelation times found for any single station and season — 2.9 days for the cold season and 2.2 days for the warm season — and use these as the persistence times for all cold and warm season data sets. We take monthly-mean wind and some climate index values to be independent, but Niño 3.4 and the PDO index are known to have persistence times longer than one month, and for these we consider values separated by more than 6 months to be independent and use the same stationary bootstrap technique as for daily data. Using the random resampling technique that accounts for serial correlation, we take 8000 bootstrap samples, compute the corrected, accelerated confidence intervals, and reject the null hypothesis if an r value of zero is outside of the central 95% confidence interval.

The highest correlation coefficients in the tables are between nearby sites, in particular the correlations between Edwards and Mojave and between Travis and the SMUD site. Several points about these pairs of stations stand out. Edwards and Mojave are close to each other as well as being located within the same topographical region. In contrast, the wind speed at Bakersfield, approximately 100 km from Mojave but in the

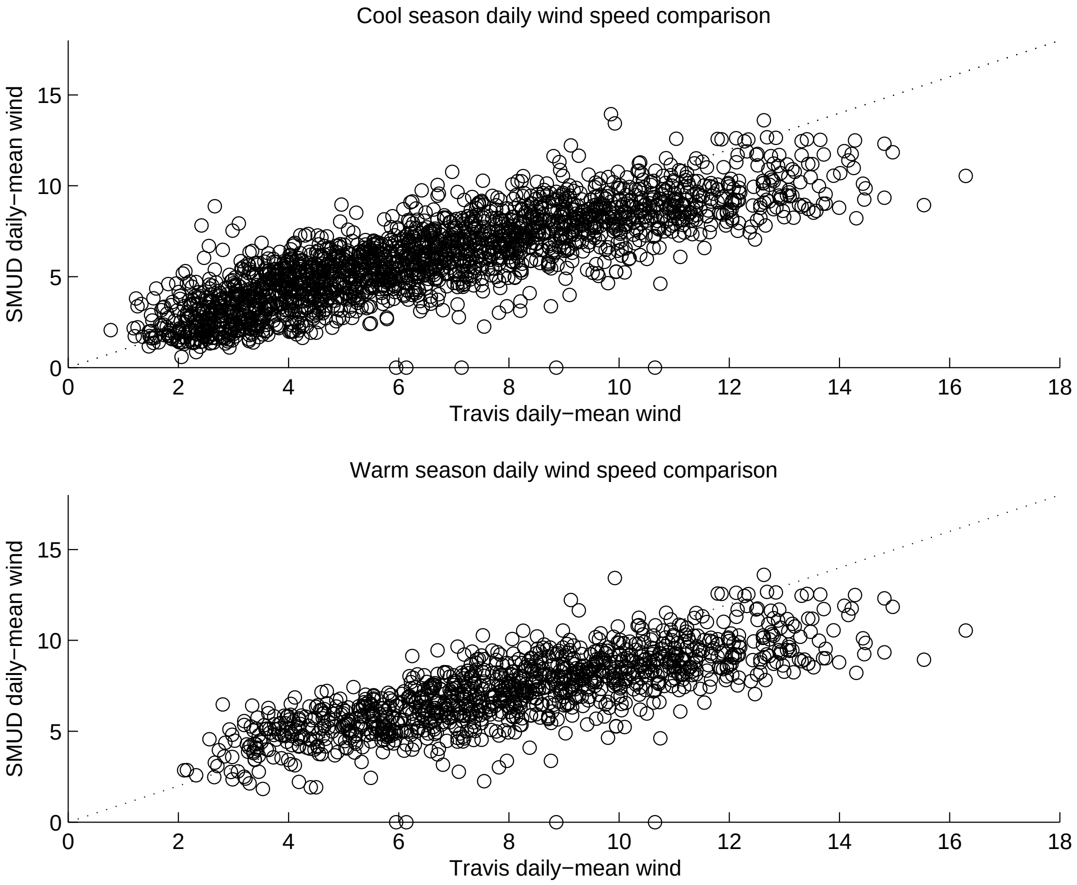

Figure 3.11: Scatterplot of Travis (x-axis) and scaled SMUD (y-axis) daily-mean wind speeds for October-March (top panel) and April-September(bottom). Data are available for both sites between 2000-2008. The dotted line is drawn along the path of x=y, ie, where points from two identical datasets would be plotted.

San Joaquin Valley west of the Tehachapi Pass, is not as highly correlated. Although Mojave consistently has more energetic winds than Edwards, the two stations exhibit strong positive correlation on daily and monthly time scales and they have similar annual cycles. This in turn reinforces our strategy of using longer and more accessible airport wind records to study the processes determining wind at wind farms. It is reasonable to extrapolate that winds at Tehachapi Pass itself are also closely related to Mojave winds but further amplified by the mountain pass, just as Mojave's proximity to Tehachapi Pass gives it higher winds than Edwards. The correlation between the sites, and similar correlation values between each site and other time series, is consistent in both warm and cold seasons, indicating Edwards and Mojave have similar responses to large winter synoptic conditions and smaller-scale summer diurnal forcing.

Daily correlation between Travis and SMUD wind speeds is higher than between Edwards and Mojave. Monthly-mean values are not shown, since the power supply to the SMUD sensors was turned off repeatedly during the overlapping data period, making for fewer than 15 separate 30-day periods of valid data in either season. The winds from the SMUD's Solano County site were measured from meteorological towers with instruments at a height of 50 meters. We have again followed common convention and scaled the winds down to equivalent 10-meter speeds using Equation 3.1. The Solano site data is available in 10-minute averages, but for this comparison we subsample these data by choosing only the average speeds covering the ten-minute period ending on each hour, and compare them directly to the concurrent Travis METARs records, which are two-minute averages taken each hour. As shown in Figure 3.11, after the power-rule scaling there is little consistent bias between the two sites in daily mean wind speeds. The major divergence is in the highest wind data, where SMUD wind speeds fall below the line of one-to-one relationship. One possible explanation is that the strongest winds occur in unstable boundary layers with vigorous vertical mixing, so that the most appropriate power-law scaling term is less than 1/7, which is most ideally suited to neutral conditions (ie, Hsu et al., 1994). More frequent data sets from high wind episodes could evaluate this further; but even while relying on Eqn. 3.1 for all wind speeds, Fig. 3.11 shows a very consistent relationship. The strong daily correlations and the generally low bias between the two sites indicates that Travis and SMUD are not just closely related in terms of timing and nature of wind fluctuations, as are Edwards and Mojave, but that Travis's long-term wind record can readily be used as a stand-in for both wind speed and wind power density values at the SMUD site itself.

Although detailed records from the San Gorgonio Pass wind farm are not available, summary seasonal data from 1977-1981 are published in Elliott et al. (1987, Appendix E). These give the mean wind speed and wind power at an observation site directly at the exit of San Gorgonio Pass. The mean wind speed values for winter, spring, summer, and fall (defined by the same months as in our study) at a mast height of 9.1m were 4.2, 7.7, 7.8, and 5.2 m/s. These compare with 10m-height mean wind speeds at our Palm Springs site of 3.0, 4.9, 4.7, and 3.8 m/s from the same period. The mean wind power density measurements for each season in San Gorgonio were 153, 526, 489, and 230 W m^{-2}, compared with 40, 162, 145, and 84 W m^{-2} in Palm Springs Airport METARs. Almost all Palm Springs METARs reports from this period did not have data between local 0:00 and 5:00, while cold-season days also tended to have no data for 23:00 and 06:00. The typical daily cycles calculated from years with 24-hour coverage indicate that the peak wind was centered on 19:00 local time, with the lowest value of the day at or close to 04:00 (Fig. 3.10). This indicates that the missing data likely came from both high and low points of the daily cycle, and their absence does not greatly affect the daily or seasonal means. Thus we also highlight that in comparing measured values at the Pass itself to our METARs wind speeds, the relative seasonal cycle in wind power density was very similar, and the ratio of Pass seasonal mean wind speed to METARs seasonal mean wind speed was not below 1.4 or above 1.7. While we are not able compare daily or interannual variability between the two nearby sites, the close relationship in seasonal cycle, and in seasonal wind distribution implied by the similarities in wind speed and wind power tendencies, supports the premise of using the high resolution METARs data to diagnose the behavior at the more energetic neighboring location. At the same time that the cycles appear closely related, the San Gorgonio Pass site is sufficiently more energetic that its seasonal means fall in greater windpower classes than does Palm Springs. San Gorgonio Pass 10m winds place it in classes 3, 7, 7, and 4 for winter-fall, respectively and an annual mean wind power density value corresponding to class 6, “outstanding.” Nearby Palm Springs seasonal values, in contrast, would only fall in windpower classes 1, 3, 2, and 1, with an annual average wind power density in class 2, “marginal” (Elliott and Schwartz, 2005).

Other, less local relationships are also evident from Tables 3.1-3.4. We highlight the positive correlation between Travis and the Southern California METARs sites.

These are greater (r=0.24 to 0.41, which are statistically significant) in the daily cold season table (Table 3.1), presumably because this is when synoptic events are strongest and could affect both regions simultaneously. The relationship between Travis and Edwards remains strong throughout the year, on both daily and monthly time scales. It is also interesting to note that throughout the cold months Travis wind speeds are positively correlated with the nearest ocean winds, at Bodega Bay, but during the the warm season they exhibit a weak negative correlation. This again reflects more dominant synoptic forcing in the cold season, while the rest of the year is more given to local circulations and the regional Delta Breeze that affects the Sacramento Valley.

The positive correlation observed between Buoy 25 off of Santa Monica and the Southern California sites also indicates a relationship between the coastal ocean wind speed and the orographically-influenced site recordings scores of kilometers away. Since the buoy is located south and east of the corner-like feature of Point Conception, it is sheltered from the climatological along-coast winds dominant north of Point Conception, especially in the summer (Dorman and Winant, 2000; Taylor et al., 2008). Rather, the wind speeds at Edwards and Palm Springs reflect weather patterns that may extend or propagate from the Southern California Bight inland to the wind farm areas.

3.5.2 Relationships to surface forcing

In addition to relationships among wind sites, it is natural to investigate relationships to surfacing forcing in the area. SSTs near the region provide a starting point, and their generally negative correlations with site winds are consistent with a circulation driven by the contrast of cool coastal waters with solar heating at inland locations (Tables 3.3-3.4). To investigate modulations on the other side of that process, we look at the correlations between wind speeds and soil moisture in the top 10 cm of the land surface in several arid regions near the sites, as reconstructed by the VIC model. Tables 3.5-3.6 show the correlations between monthly-mean wind speed anomalies at each site and soil moisture anomalies over the Central Valley, Great Basin, Mojave, and Sonoran deserts from the VIC model (Maurer et al., 2002). These monthly mean data are once again separated into warm and cool seasons, with bias-corrected, accelerated stationary bootstrap techniques used to estimate the correlations' statistical significance assuming a characteristic soil moisture decorrelation time of 3 months (Efron and Tibshirani, 1993; Politis and Romano, 1994; Mudelsee, 2003).

Table 3.5 shows that while many of the wind speed anomaly series are essentially uncorrelated with moisture, cool season Palm Springs wind speed shows a negative correlation with soil moisture in the neighboring Sonoran Desert as well as in the Great Basin and Mojave regions. Lower soil moisture would allow for more effective solar heating of these areas and development of stronger thermal circulations, as previously shown in observations and models (Ookouchi et al., 1984; Yan and Anthes, 1988; Segal et al., 1988, 1989). In contrast, we suggest a combination of mechanisms for the positive correlation between Edwards winds and Central Valley soil moisture. Since Edwards displays increased wind speeds with increased tendency toward continental cyclonic activity (Fig. 3.12 as well as Part 2) the same moisture-bearing low pressure anomalies that bring precipitation to the Central Valley would also tend to produce strong winds at Edwards. This is supported by the fact that, if we make monthly soil moisture and wind speed means only from daily means that were separated by at least two days from measurable precipitation (using the same data that formed the forcing fields for the VIC model, at the nearest grid point to each station), the correlation between Edwards wind speeds and Central Valley soil moisture drops to 0.15. However, the other notable changes in correlation when we remove precipitation events from the averages are that correlation between Edwards wind speeds and soil moisture in each of the other three regions drops from near zero to approximately -0.15. While these indicate that Central Valley soil moisture and Edwards winds may be affected by the same forcing mechanisms, as opposed to the former directly forcing the latter, they also suggest that in the cool months, moist Central Valley land surface and dry surfaces in the other regions imply stronger winds, just as seen with Palm Springs.

In the warm season, the wind versus soil moisture correlations reveal different mechanisms. The negative correlation between Travis winds and soil moisture in the Central Valley is consistent with a thermally-induced circulation, as in Zhong et al. (2004). The dominant flow in the warm months is from San Francisco Bay into the Central Valley in response to the thermally-induced SLP gradient between Sacramento and San Francisco; this is described in Part 2. A month or season with a moister land surface would tend to heat less in response to solar insolation, setting up a lesser temperature difference and SLP gradient between the coast and valley. The opposite is true for periods with low soil moisture, and previous studies have also shown the sea breeze strength and penetration to depend on the neighboring land soil moisture levels

(Yan and Anthes, 1988; Physick, 1980). In further analysis, we find that the relationship is higher for spring than summertime months; correlation for the time series from months of April alone is -0.51. The springtime maximum correlation is interesting in that spring is a period when soil moisture anomalies could be quite wet or quite dry. This is also possible in winter, but this period does not have the same strong insolation as spring. In summer, the magnitude of soil moisture anomalies is likely to be small. The same argument applies to the relationship between Palm Springs winds and soil moisture in the Sonoran and Mojave areas, much as was seen in the cool season. In contrast to that season, however, the Great Basin area shows very little correlation to Palm Springs winds, while the Central Valley shows the opposite, a positive relationship. The positive correlation between Central Valley moisture and southern California site winds, while mild, is consistent with the relationships between mesoscale station SLP differences and observed winds found in Part 2, in that greater soil moisture would tend to produce lesser warming on the western side of our wind sites, and thus allow the temperature and SLP differences on opposite sides of the sites to increase as the sun heats the regions to the east.

3.5.3 Links to monthly climate indicators

While we reserve analyzing the details of local regional circulations until Part 2, it is natural to investigate surrogates of some of the longer-scale processes that may reasonably be thought to modulate such processes here. While wind speeds at the wind farm sites exhibit a modest linkage to wind speeds along the California coast, it is not clear if, or to what extent, they reflect the fluctuations of large-scale atmospheric circulation, as represented by well-known climate indices. While Conil and Hall (2006) find that neither the PNA nor other major modes of atmospheric variability strongly affect the the three southern California wind regimes that they identify from high-resolution MM5 simulations, our study is focused on the wind speed at particular sites in the state, not the overall flow patterns in the southern region. While their weather regimes are not inconsistent with our analysis, the emphasis we place on specific in situ wind speed observations suggests that it may be instructive to perform a separate comparison with indices of large-scale atmospheric variability.

Regarding the four climate indices examined (Tables 3.3-3.4), the cold season displays significant correlation between monthly-mean wind speeds and several indices.

Each of our three principal sites with long data records shows a negative correlation with the PNA index, somewhat weak but significant at the 95% level. This indicates that during the negative phase of the PNA, increased westerly flow from the North Pacific and onshore over California favors higher-than-average wind speed, while during the positive phase a more meridional flow and anomalous 500 hPa ridging over the continent tends to provoke a decrease in wind speeds (Leathers et al., 1991). In Part 2, we show in detail that the common synoptic patterns most associated with stronger than average winds at the METARs sites in the cold season closely resemble the negative phase of the PNA, and that the common patterns with weak winds resemble the positive-phase PNA. The PNA linkage is also a good starting point to understand the relationship between other climate indices and station winds. ENSO's extratropical Pacific influences are often discussed in terms of exciting a PNA or PNA-like pattern (Straus and Shukla, 2002; Yu, 2007), as well as influencing SSTs off of western North America. In turn the PDO can be viewed as a modulation of ENSO impacts (Gershunov and Barnett, 1998), or in its positive phase, the large-scale SST pattern in which upper-air patterns preferentially exhibit the positive PNA pattern, and vice-versa for the negative phase (Mantua et al., 1997). This is consistent with the observed negative and statistically significant correlations between station wind speed series and PDO or Niño 3.4. Although none of these climate variability indices comes close to explaining a majority of the wind speed variance, the PNA in the cold season is the best available index to serve as a summary statistic or infer wind speed behavior over long reconstructed or projected future periods.

A more direct illustration of the common atmospheric state in different station wind regimes is provided in Fig. 3.12, showing the composite mean 500 hPa height and SLP anomalies for October-March months whose mean wind speed was in the slowest and fastest quartiles for the cold season at each site. At Travis and Edwards, the patterns from the fastest wind months each show an anomalous 500 hPa trough centered over the northern Rocky Mountain area and extending off the Pacific Northwest coast. In contrast, a similarly located anomalous ridge is evident in the slowest months' patterns, although these also contain an offshore negative anomaly on the northwestern edge of the plotted domain. Mojave's composite patterns are similar, but displaced so that the northerly anomalous trough in the windy months is accompanied by a subtropical oceanic ridge and the edges of a ridge well inland and poleward. These composites resemble the negative and positive phases of the PNA, respectively, of Wallace and Gutzler (1981), which are historically defined based on winter months. The 500 hPa patterns for windy months are consistent with increased cyclogenesis over the western portion of the continent and the lower mean continental SLP in Fig. 3.12, as well as increased subsidence over the North Pacific and development of anticyclones which support the tendency to higher mean oceanic anomalous SLP also evident in the figure. The anomalous ridge in the calmest months supports continental subsidence and anticyclonic development over the continent, associated with the anomalously high continental SLP anomalies seen, but cyclonic activity and storminess over the oceanic portion.

At Palm Springs, however, the windy and calm-quartile cold-season months show a different pattern. The composite from the least windy months contains a distinct anomalous trough offshore that extends just to the coastline, and a mean anomalous ridge centered further north and east over the continent. For Palm Springs, the composite SLP anomalies exhibit a narrower pattern of contrasting high and low pressures than for the other sites. Rather, the important contrast appears in a more local area about the site. The low-wind months show decreased SLP in the Southern California Bight and directly east of the wind farm, with neutral to slightly increased SLP to the west and south, in the grid boxes approximately covering the Sonoran Desert plain into which the predominantly westerly site winds blow. This positive anomalous zonal pressure gradient contrasts with the high-wind days, where the lack of such a pressure gradient force allows increased westerly wind acceleration. At the same time, the weak local SLP anomalies allow for the development of smaller-scale circulations at the site.

The warm season station winds are not as consistently or strongly related to the PNA as the cool months (Table 3.4). The PNA index is defined in the same manner as for the cold months, even though the PNA pattern is only weakly expressed during summertime (Barnston and Livezey, 1987; Wallace et al., 1993). Composite-mean 500 hPa anomalies from the slowest wind speed quartile months in April-September at each southern California station (Fig. 3.13) contain anomalous ridges over the western coast of North America and eastern North Pacific. Just as in winter, their presence would tend to inhibit cyclonic development over the continent, and the positive SLP anomalies over the continent, while not as strong as for the more synoptically active cold season, reflect this. In the warm season high wind speed monthly means, only Edwards shows a well organized anomalous trough and negative continental SLP anomalies. The composite for winds at Mojave shows scattered negative SLP anomalies without an extensive sup-

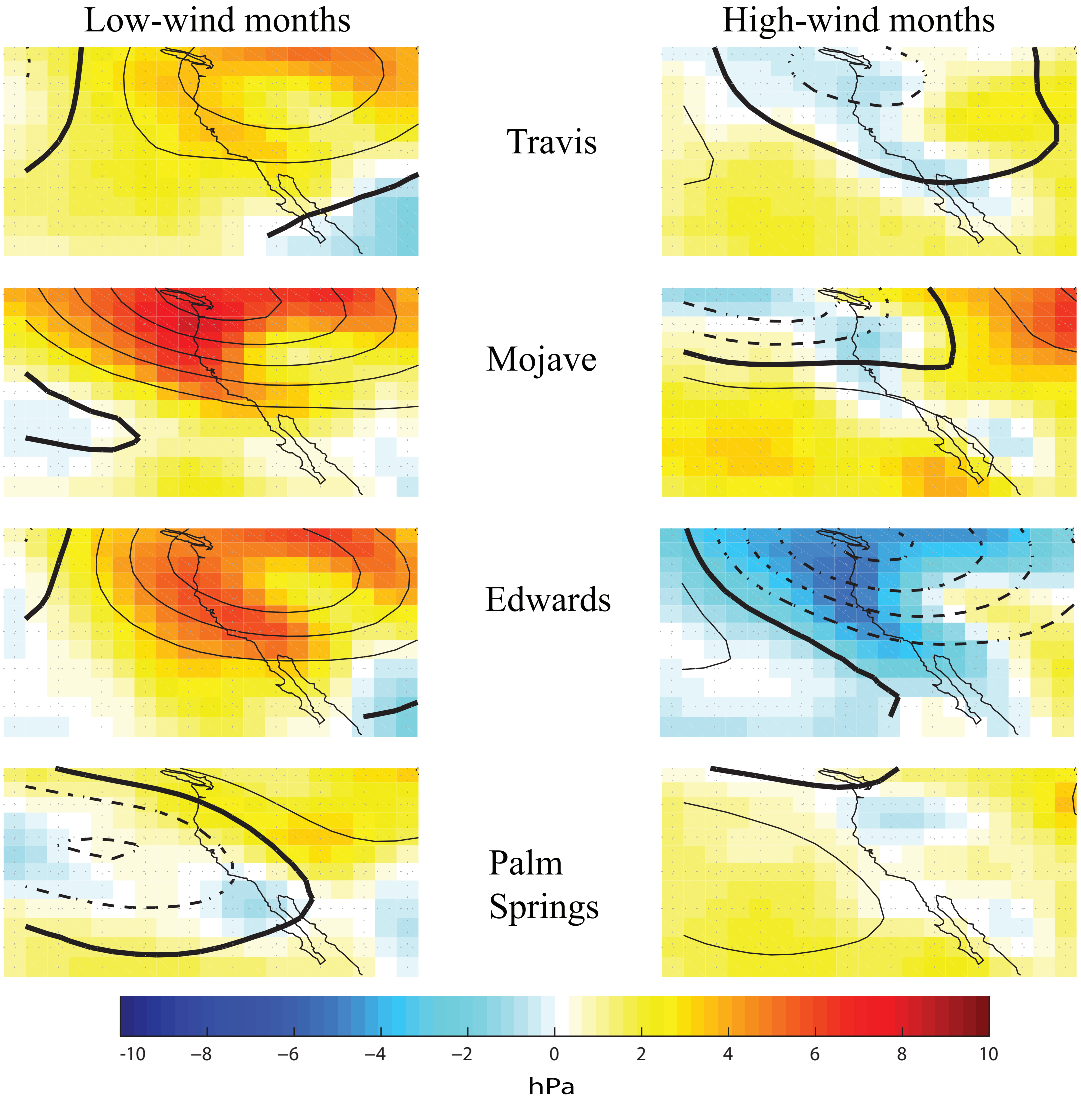

Figure 3.12: Composite mean of monthly-mean 500 hPa height (contoured, m) and SLP (color, hPa) anomalies from months when each station was in the lowest-wind quartile (left column) and highest-wind quartile (right) in October-March. Shown from top to bottom are maps based on Travis, Mojave, Edwards, and Palm Springs monthly wind speed anomaly quartiles. Height contour interval is 10m, the zero contour is bold and negative contours are dashed.

porting anomaly pattern, indicating that smaller-scale transient systems contribute to the windier months, although its shorter data record might exclude some periods when larger-scale storms with upper air support made for strong site winds. Palm Springs SLP anomaly patterns whose resulting low-level winds, if geostrophic, would translate to increased westerlies in high-wind months and decreased westerlies in calm months.

Importantly, although the monthly-mean anomalous circulation patterns are weaker in the warm months than in the cold season, the mean wind speed in the warm season is significantly greater and wind variability from the climatological mean is somewhat greater. This suggests the influence of more local processes, on scales up to hundreds of kilometers in extent, that drive wind behavior in the warm months but do not show up clearly in reanalysis monthly means.

For the warm season months with fastest and slowest wind speeds at Travis the composite 500 hPa anomaly means do not exhibit a similar proclivity to support cyclonic and anticyclonic development as for the cold season. A weak anomalous ridge in the windiest months is evident, with its edge directly over the site location; its presence would prevent synoptic forcing from reaching Travis. However, given the small magnitude and lack of organization of the mean SLP anomalies as well as anomalous large-scale vertical motion or 850 hPa temperature (not shown), this analysis does not reveal other major large-scale influences on warm-season Travis winds at the monthly time scale.

In Part 2 we explore more detail of the summertime circulation here and also show how summertime wind is found to depend strongly, in differentiated ways for each station, on mesoscale pressure gradients, boundary-layer stratification, and local circulations that can develop in a variety of synoptic states. In light of this it is also germane that in the warm season, Edwards, Palm Springs and Travis each have negative correlation to sea surface temperature off the coasts of southern and northern California(Table 3.4). This is consistent with cooler coastal temperatures allowing for greater thermal contrast with the daytime inland areas, leading to low-level pressure adjustment and down-gradient flow at these sites. The water's high thermal inertia provides a counterpoint to the inland desert areas and their strong variability on diurnal periods. To the extent that coupled global models display skill in simulating east Pacific circulation and SST, the changes in SST compared to inland heating may provide an important estimate, both conceptually and quantitatively in downscaling studies, for warm-season wind power density changes under climate change.

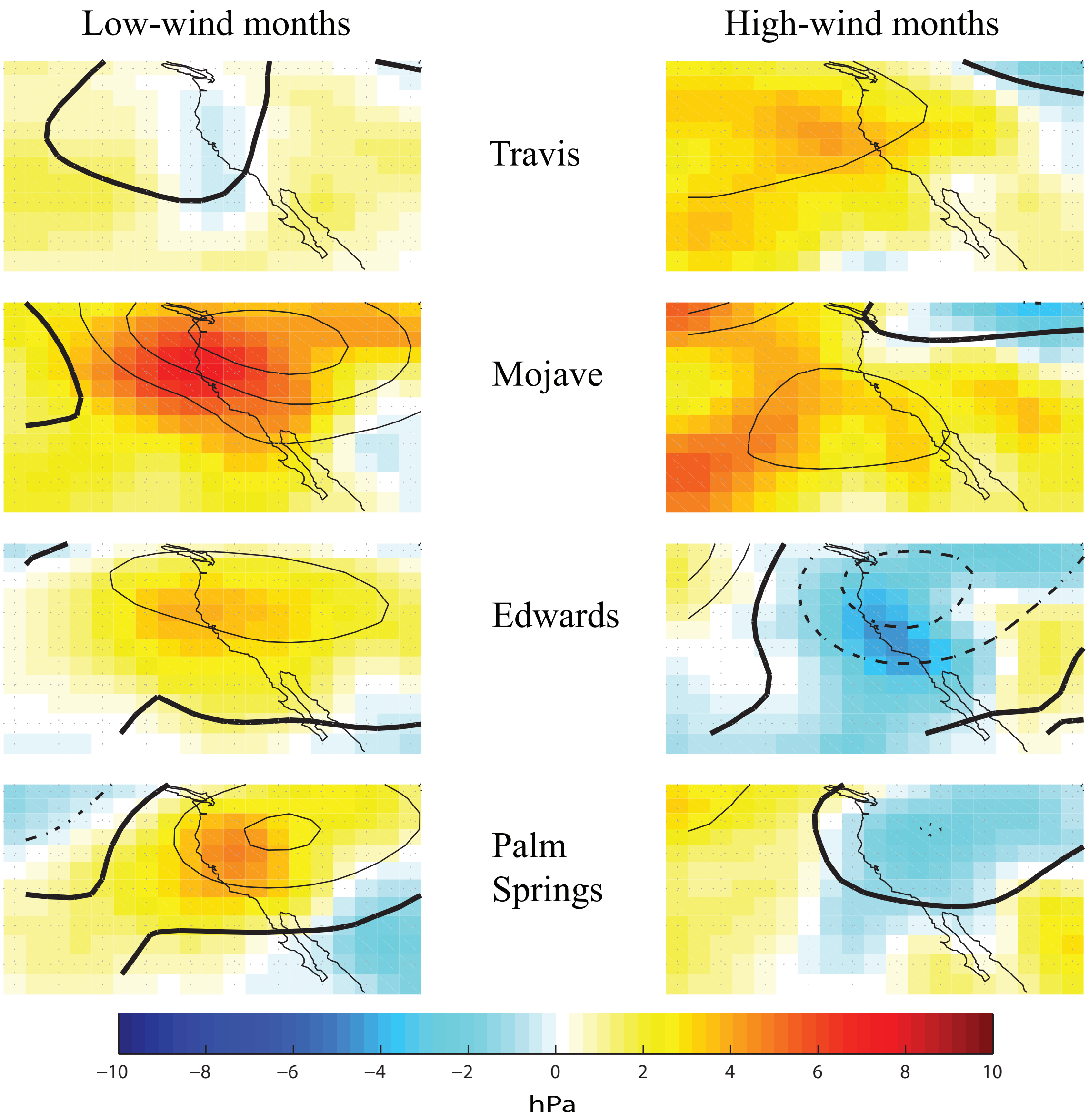

Figure 3.13: As in Fig. 3.12, but for April-September.

3.6 Summary and Discussion

We have used instrumental records from four sites near wind farms in California to analyze the climatology of the wind at these locations, its seasonality, its variability, and the relationships among various wind time series and indices of climate variability. Each of the sites is located near one of three established large-scale wind energy conversion facilities. A cross-comparison of wind time series, including direct analysis of available, shorter wind records from one such wind farm and seasonal means from another, indicates that site-recorded wind speeds and wind power density from nearby locations in the same basin are closely related to each other in terms of climatology, and variability over a range of scales. Thus, we believe that our findings from the wind records at Travis, Palm Springs, and Mojave and Edwards are readily applicable to the Solano County, Palm Springs, and Tehachapi Pass wind power sites, respectively.

Each site displays a clear annual cycle. Mean wind speeds at the southern California sites peak in the spring time, in phase with peak seasonal SLP gradients from reanalysis, but those of Travis peak in the summer when inland temperatures are greater. The records also reveal that variability about the climatological mean has a somewhat greater magnitude in the warm months, but the increase in this variability is not commensurate with the increase in the seasonal cycle – the ratio of standard deviation about the climatological mean to climatological mean wind speed itself on each day of the year, is highest in the winter. The significance of these different measures of variability likely depends on the demand, expectations, and integration strategy for any wind power plant. If the site is needed to maintain a minimum baseline amount of production year-round, such as to supply electricity for seasonally invariant, general energy use, then the high wintertime relative variability is of greater concern. Total wind power density is lesser at these times, and meeting the installed turbines' cut-in speeds might be an issue on relatively calm days in the calmer cold season months. On the other hand, if a site is relied on to cover increased seasonal demand, such as to provide for air conditioning use in the summer, then the increased variability (in absolute terms) coinciding with the warm season will be of greater importance to site planners and operators.

Atmospheric flow at the sites in our study area are significantly influenced by the complex terrain nearby. This is evidenced by the similarities between preferred wind directions at Palm Springs, Mojave, and Travis and nearby orographic orientation, and by the stronger winds at San Gorgonio compared to Palm Springs or Mojave compared to Edwards. These latter two sites show a strong correlation in wind speed over all the seasons and time scales examined, but speeds are consistently higher at Mojave airport, which is closer to Tehachapi Pass. Flows during maximum winds at each of the sites are oriented from the coast toward the interior. Santa Ana flows, when winds reverse and blow toward the coast, do not result in unusually strong or persistent wind episodes at the sites.

The more pronounced diurnal cycle in the spring and summer months for each station is consistent with the progression of solar intensity. In the spring and summer at Travis, Edwards, and Palm Springs, maximum wind speed lags the afternoon maximum temperature by a few hours in the seasonal mean. Mojave data coverage is insufficient to form a mean 24-hour cycle, and while late afternoon winds are generally the highest during the hours of observation in the warm months, we are not able to say the exact hour of peak climatological wind speed. Although even in these seasons individual days can have a wind speed maximum at any hour, the fact that the cycle is much more consistent in the seasons when wind power is at its greatest means that significant amounts of electricity are consistently available in the afternoon and evening hours from these sites. The fact that the timing of wind power peaks is less consistent in the seasons with lesser insolation and diurnal cycles points to a topic undertaken in Part 2, that of diagnosing the weather patterns important to variations in site winds.

In the cool season, correlations indicate a modest tendency for the wind speed variation at the four observational sites to be modulated by the large scale atmospheric circulation.The negative phase of the PNA pattern favors strengthened wind speeds over all. Other modes of modes of climate variability examined — ENSO, the NAO, and the PDO — exhibit correlations that have statistical significance but it is not clear if this represents mechanisms independent of their excitation of the PNA pattern. Many of the monthly-mean 500 hPa patterns corresponding to extreme winds for different stations and seasons clearly project onto a classical PNA pattern, and likewise imply clear tendencies for increased cyclonic development over the continent and support of the oceanic anticyclone in windy months. While the PNA and monthly-mean synoptic anomaly patterns are stronger in the cool season than warm, it is in the warm months that climatological wind speeds peak at each site of our analysis, and variability of daily-mean wind speeds about the climatological mean is also somewhat greater in these months. This strongly suggests the presence of local processes, on scales too small to be evident in the reanalysis data, that drive strong low-level flow and contribute to the diurnal and synoptic-scale peaks in the power spectra.

In the summer season, no tested climate index shows a broad, statistically significant relationship to site wind speeds in the region. However, monthly SST anomalies in the vicinity do show significant relationships to warm-season station winds. This could indicate a direct role of SSTs in determining land-sea thermal and SLP contrasts, as well as reflecting larger-scale oceanic and atmospheric anomalies. The SSTs analyzed were from reanalysis grid boxes containing only ocean, and came only within scores of km of the coastline. Actual SST measurements from within 50 km of the coast might exert more influence on summertime winds, and these of course are more rapidly variable due to coastal upwelling processes, as well as harder to reproduce in large-scale models.

In addition to SSTs and their influence over coastal atmospheric temperatures, correlation analysis demonstrates a significant association of inland soil moisture on site wind speeds over monthly time scales. This is particularly pronounced at Palm Springs and in the warm months at Travis, sites where basin-wide pressure patterns here and in Part 2 indicate direct synoptic forcing is secondary to more local circulations. The process that seems most likely to underlie this relationship is the role of soil moisture in moderating the inland-coastal temperature contrasts, whereas a drier land surface would allow for greater average solar heating and pressure adjustment over the course of a month or longer time periods. The longer time scales of variability of SST and soil moisture fields together suggest them as starting point for any investigation of processes governing seasonal variability. Beyond this general discussion of seasonal variability, however, the underlying nature of our observational data becomes a concern, since the occasional changes in sensor and/or surroundings at most sites only allow for a handful of reliable, independent data points in assessing seasonal variability before long-term spurious data trends become a potential problem, even with the first-order homogenization performed here. Although this does not rule out a more detailed focus on longer time-scale variability, the results indicate that the quality of the long-term record is less of an issue for the shorter time scales that form the focus of the companion study.

The 500 hPa anomaly patterns common to the most and least windy months indicate that warm-season Travis winds are driven almost entirely by local and regional processes, and that the synoptic scenario most favorable to strong winds is of very weak surface and 500 hPa anomalies over the region, allowing the smaller-scale processes to proceed unimpeded. This contrasts with the other sites examined, which still show half-height anomalies conducive to increased large-scale flow near the site in the warm season as in the cold.

Overall, our analysis brings out some defining characteristics of wind energy used for electricity generation in California. The locations of sites which produce winds sufficiently strong to support wind farms are largely a reflection of particular topographic features. These locations exhibit strong seasonal cycles, as within each season there is a different mixture of local and large-scale meteorological influences driving the wind. No single large-scale climate variability index is found to explain the temporal variability of the wind speed at these sites. However, the wind speed at the sites do reflect some essential features and important time scales so that the processes driving diurnal and synoptic events can each be used to detail the variability about the seasonal means.

ACKNOWLEDGEMENTS

The first author completed part of this work while supported by a NASA Earth System Science Fellowship, NASA Grant NNX07AN73H. Additional funding was provided by the NOAA RISA program through the California Applications Program, and by the California Energy Omission through the California Climate Change Center. We are indebted to M. Tyree for obtaining and furnishing METARs data and to T. Das for the VIC hydrological data. J. Buck Cutting and the Sacramento Municipal Utility District were extremely helpful in providing in situ wind farm meteorological data.

Chapter 3, in full, is a reprint with minor modifications of the article "Climatology and meteorological influences on California's wind energy resource. Part 1: General characteristics and seasonal cycle," to be submitted for publication. The author of the dissertation is the first author and primary researcher, and contributions were also made by the scond author, D. Cayan.

Table 3.1: (below and left of main diagonal): pairwise correlation coefficients for October-March cold season observed daily-mean wind speed anomalies (using adjusted time series for Travis, Palm Springs, and Edwards, as described in the text). Boldface indicates significance at the 95% level using the bootstrap tests, accounting for persistence, as described in the text. Coefficients are calculated within the season and for each pair of time series all of the overlapping dates of observations in these months are used. Columns correspond to the same data sets as corresponding rows, but abbreviated labels are used. (above and right of main diagonal): number of valid overlapping daily observations used for calculating the correlation coefficients.

	B13	**KSUU**	**SMUD**	**KBFL**	**KMHV**	**KEDW**	**KPSP**	**B25**
Bodega Bay buoy	–	**3718**	**625**	**3808**	**2507**	**3634**	**3808**	**3400**
Travis	**0.29**	–	**935**	**5740**	**2718**	**9371**	**5740**	**3790**
SMUD	**0.35**	**0.74**	–	**623**	**530**	**599**	**623**	533
Bakersfield	**0.21**	**0.26**	**0.27**	–	**2874**	**5724**	**5922**	**3882**
Mojave	**0.30**	**0.34**	**0.26**	**0.23**	–	**2733**	**2874**	**2670**
Edwards	**0.28**	**0.41**	**0.29**	**0.33**	**0.69**	–	**5724**	**3716**
Palm Springs	**0.12**	**0.24**	**0.12**	**0.09**	**0.25**	**0.33**	–	**3882**
Santa Monica buoy	**0.23**	**0.24**	0.09	**0.40**	**0.37**	**0.49**	**0.34**	–

Table 3.2: As in Table 3.1, but for the April-September warm season.

	B13	**KSUU**	**SMUD**	**KBFL**	**KMHV**	**KEDW**	**KPSP**	**B25**
Bodega Bay buoy	–	**4000**	884	**3981**	**2556**	**3814**	**4002**	3555
Travis	**-0.09**	–	**1171**	**5894**	**2789**	**9522**	**5914**	3903
SMUD	-0.04	**0.74**	–	820	**708**	**810**	841	717
Bakersfield	**-0.08**	**0.14**	0.08	–	**2837**	**5721**	**5956**	**3936**
Mojave	**0.17**	**0.18**	**0.09**	**0.27**	–	**2666**	**2843**	**2541**
Edwards	**0.13**	**0.23**	**0.13**	**0.40**	**0.63**	–	**5741**	**3833**
Palm Springs	**0.04**	**0.10**	0.04	**0.29**	**0.29**	**0.44**	–	**3936**
Santa Monica buoy	-0.01	-0.01	-0.05	**0.28**	**0.23**	**0.33**	**0.29**	–

Table 3.3: Pairwise correlation coefficients among monthly-mean October-March wind speeds and monthly climate indices in the cold season.

	B13	**KSUU**	**KBFL**	**KMHV**	**KEDW**	**KPSP**	**B25**	**PNA**	**N3.4**	**NAO**	**PDO**	**N SST**	**S SST**
Bodega Bay buoy	–	**126**	129	**86**	**124**	129	**117**	129	132	132	132	132	**132**
Travis	**0.44**	–	189	**91**	**310**	**189**	**126**	**315**	330	335	335	**330**	**330**
Bakers-field	0.16	0.13	–	97	**190**	195	**129**	**195**	195	195	195	**195**	**195**
Mojave	**0.44**	**0.54**	-0.17	–	**93**	**97**	**90**	97	**97**	97	97	97	**97**
Edw-ards	**0.26**	**0.37**	**0.17**	**0.50**	–	**190**	**124**	**328**	**328**	**328**	**328**	**328**	**328**
Palm Springs	0.08	**0.28**	0.00	**0.33**	**0.25**	–	**129**	**195**	195	195	**195**	195	195
Santa Monica buoy	**0.40**	**0.28**	**0.29**	**0.35**	**0.45**	**0.29**	–	129	129	129	129	129	**129**
PNA	-0.18	**-0.18**	**-0.19**	-0.12	**-0.30**	**-0.18**	0.04	–	**333**	333	**333**	**333**	**333**
Niño 3.4	-0.00	0.03	0.01	**-0.20**	**-0.14**	-0.11	0.23	**0.30**	–	348	**348**	**348**	**348**
NAO	0.02	0.02	-0.01	-0.16	**-0.13**	0.03	-0.10	-0.06	0.01	–	354	348	**348**
PDO	-0.12	-0.15	-0.18	-0.06	**-0.26**	**-0.18**	-0.01	**0.52**	**0.41**	0.03	–	**348**	**348**
North Cal SST	-0.08	**-0.12**	**-0.26**	-0.02	**-0.28**	-0.08	-0.10	**0.64**	**0.34**	0.10	**0.59**	–	**348**
South Cal SST	**-0.16**	**-0.20**	**-0.21**	**-0.24**	**-0.39**	-0.14	**-0.21**	**0.57**	**0.35**	**0.15**	**0.49**	**0.86**	–

Table 3.4: As in Table 3.3, but for the April-September warm season.

	B13	**KSUU**	**KBFL**	**KMHV**	**KEDW**	**KPSP**	**B25**	**PNA**	**N3.4**	**NAO**	**PDO**	**N SST**	**S SST**
Bodega Bay buoy	–	130	129	**82**	125	130	116	131	132	**132**	132	**132**	132
Travis	-0.11	–	193	**91**	**313**	194	128	321	334	340	**340**	**334**	**334**
Bakers-field	-0.13	0.02	–	92	188	195	129	195	195	195	195	195	195
Mojave	**0.24**	**0.22**	-0.03	–	**87**	**93**	**82**	93	93	93	93	93	93
Ed-wards	0.09	**0.16**	0.04	**0.56**	–	**189**	**126**	**327**	327	327	327	327	**327**
Palm Springs	-0.07	0.12	0.10	**0.33**	**0.24**	–	**129**	196	196	**196**	196	**196**	**196**
Santa Monica buoy	0.04	0.03	0.17	**0.43**	**0.46**	**0.19**	–	129	129	**129**	129	129	**129**
PNA	-0.10	0.04	0.09	-0.14	**-0.16**	0.01	-0.09	–	**335**	335	**335**	**335**	**335**
Niño 3.4	-0.12	-0.02	-0.12	-0.02	-0.03	0.10	-0.03	**0.17**	–	348	**348**	**348**	**348**
NAO	**0.22**	-0.08	0.03	-0.10	-0.11	**-0.25**	**-0.35**	0.08	-0.00	–	354	348	**348**
PDO	0.02	**-0.24**	-0.08	0.01	-0.16	0.01	0.04	**0.23**	**0.48**	0.03	–	**348**	**348**
North Cal SST	**-0.17**	**-0.14**	-0.09	-0.03	-0.03	**-0.17**	-0.07	**0.26**	**0.29**	0.03	**0.35**	–	**348**
South Cal SST	0.10	**-0.30**	-0.09	-0.07	**-0.20**	**-0.26**	**-0.18**	**0.17**	**0.22**	**0.12**	**0.47**	**0.67**	–

Table 3.5: Pairwise correlation coefficients between monthly-mean site wind speed anomalies and simultaneous monthly soil moisture anomalies in the top 10cm of the land surface, for the October-March cool season. Correlations significant at the 95% level using bootstrap methods are shown in bold .

	Central Valley soil moisture	**Great Basin soil moisture**	**Mojave Desert soil moisture**	**Sonoran Desert soil moisture**
Travis wind	0.09	-0.00	0.06	0.03
Edwards wind	**0.35**	0.01	0.01	-0.03
Palm Springs wind	-0.02	**-0.19**	**-0.26**	**-0.29**

Table 3.6: As in Fig. 3.5 but for the April-September warm season.

	Central Valley soil moisture	**Great Basin soil moisture**	**Mojave Desert soil moisture**	**Sonoran Desert soil moisture**
Travis wind	**-0.28**	**-0.21**	**-0.19**	-0.10
Edwards wind	**0.15**	-0.05	**-0.15**	-0.10
Palm Springs wind	**0.22**	-0.08	**-0.22**	**-0.28**

Chapter 4

Climatology and meteorological influences on California's wind energy resource. Part 2: Synoptic and diurnal characteristics

4.1 Abstract

Decades' worth of observations, reanalysis, and regional model data are used to examine the variability in atmospheric circulations affecting three major California wind farms. Self-organizing maps (SOM) reveal that from October-March the common occurrence of oceanic high SLP and continental low SLP centers are the main large-scale factors leading to increased wind speeds at wind farms near San Gorgonio and Tehachapi passes in southern California and Solano County further North. Ocean low/continental highs have the opposite effect. In addition, Palm Springs is especially sensitive to the SLP difference between the California Bite and the Sonoran Desert that the site borders.The reanalysis and in situ SLP gradients (at 100km separation) are strongly correlated to cotemporaneous site wind speeds, indicating the principal mechanism relating SOM patterns to wind speeds. Dynamically downscaled reanalysis data at 10km resolution reveals that the strong down-gradient summertime flow at the northern site commences at the coast and propagates inland in a distinct packet that is modulated by large scale conditions and by boundary-layer structure, as revealed by nearby sounding data. Similarly, summertime flow over Tehachapi Pass and the Mojave desert is seen to merge

with incoming southerly flow from coastal Los Angeles and accelerate toward the Nevada Great Basin area on windier days. While the 10km reanalysis does not resolve the Palm Springs flow, experiments over select days with the Weather Research and Forecasting model validate very well when run at 2.5km resolution, and additional experiments show that the essential behavior is not captured when only solar or only lateral boundary focing is used. These regional flow patterns illustrate processes accounting for several statistically significant relationships between reanalysis fields and site winds.

4.2 Introduction

As wind power grows and takes a more prominent position in the energy infrastructure, the detailed behavior of the wind at existing and potential future conversion sites grows in importance. This is especially true in California, where wind power developed before many other locations in the United States (Gipe, 1995), and where the strong synoptic, diurnal, and orographic forcings combine to influence wind climate and variability. Site design and operation, as well as market integration mechanisms and energy policy all benefit from a firm understanding of the underlying energy source, its general characteristics, and the causes of its variability. In Part 1 of this study (Mansbach and Cayan, 2010a) we use hourly wind measurements from meteorological stations near three of California's principal wind farms as well as select observations from wind farms and other data to diagnose the annual cycles, relationships to large-scale climate indices, and seasonal-mean wind behavior in these areas. We also show that sites located close to and within the same orographic settings as each other have very closely related wind behavior on hourly to annual timescales, verifying that our results are applicable to wind farms themselves. In this paper we expand on these findings by relating wind observations to synoptic forcing patterns, diurnal cycles, and local flow as channeled by terrain for the three areas: Palm Springs, near the San Gorgonio Pass wind farm; Mojave Airport and Edwards Air Force Base, near Tehachapi Pass wind farm; and Travis Air Force Base, near the Solano County wind farm in northern California.

Electricity demand has secular and long-term variability as well as annual, weekly, and diurnal cycles (ie Martin-Rodriguez and Caceres-Hernandez, 2005; McSharry et al., 2005). Importantly, the supply of wind-generated electricity, via the wind forcing, has significant variations too. In Part 1 we find that wind variability at the sites of interest has spectral peaks around the annual, synoptic (3-15 day), and diurnal periods. As such, an understanding of the synoptic and diurnal forcing, drawn as needed from observations, analysis, and models, can serve important operational needs. These include matching likely timing of supply and demand and producing wind and wind power density forecasts with lead times of hours to days (Giebel et al., 2003). As we have detailed the annual cycle in Part 1, we proceed now to examine the meteorological processes behind the synoptic and diurnal wind behavior.

Although peer-reviewed discussions of the meteorological processes specifically driving California's inland wind resource variability are not known to us, general studies of climate variability and meteorological processes affecting the area are highly pertinent. Conil and Hall (2006) used a 6-km resolution model over southern California to diagnose cold-season weather types. They found that winds were largely dominated by the interplay between regimes of common northwesterly flow, onshore events, and Santa Ana wind regimes, and that SLP over the Great Basin area (centered on Nevada) was strongly related to these variations.

Winds adjacent to the California coast are also pertinent to our study subject. Coastal wind studies have been motivated largely by the relevance to ocean upwelling and productivity, but at the same time these winds form the boundary forcing for the inland circulations that impact wind farms. The balance of North Pacific High and continental low pressure creates a sharp SLP gradient over California in the summer. Subsidence over the ocean and the thermal low driven by daytime heating in the Southwestern US lead to strong, nearly geostrophic climatological along-coast winds that are punctuated by occasional synoptically driven high wind events, as well as modifications to the flow due to interactions between the marine boundary layer, the coastline, and the coastal mountains (Dorman, 1987; Winant et al., 1988; Dorman and Winant, 1995; Winant and Dorman, 1997; Taylor et al., 2008). While the large-scale factors remain important to inland winds, the breakdown of geostrophy with surface drag and the complex terrain in the region strongly modify the flow from that offshore.

Santa Ana wind events have also been examined in multiple studies, much of the interest stemming from their relation to fire weather in southern California. Although Conil and Hall (2006); Raphael (2003); Miller and Schlegel (2006); Hughes and Hall (2009) have shown the importance of these winds to southern California climate, in Part 1 we find that their role in shaping seasonal wind characteristics at the sites of our principal interest, which in Santa Ana conditions lie upwind of major mountain passes, has been minimal. Still, Santa Ana winds provide another relevant example of the importance of terrain channeling, small-scale thermal variations, and Great Basin pressure on the region.

The complex topography surrounding the established wind energy sites, the juxtaposition of the ocean, temperate coastal areas, and more arid inland expanses, and the strong summertime insolation in California would suggest that locally forced circulations might play a significant role, even as synoptic conditions exert some control. The classic local, orographically induced circulations include daytime upslope and nighttime downslope winds, forced by pressure gradients resulting from hydrostatic adjustment to insolation and longwave cooling, respectively (Barry, 2008, pp. 176-196). Recent observations in the Intermountain West have shown these processes occurring regularly, along with the related, larger-scale up-valley and down-valley winds (Stewart et al., 2002; Ludwig et al., 2004). In California these processes intermingle with effects of the sea breeze and land breeze, which can be pronounced when inland temperatures sharply contrast with upwelling-cooled coastal waters, and which when fully developed may extend as far inland as the wind farms in question (Miller et al., 2003).

Given the importance of several different scales of wind circulation, this study makes use of observational records as well as large- and regional-scale model data to determine the development of common flow patterns, the resulting winds at the wind farms, and what conditions lead to strengthening or weakening of these circulations. In this work we first review the data sources from Part 1 and introduce new ones to help understand synoptic and diurnal processes. We then introduce a powerful and flexible methodology to identify synoptic patterns, which we apply to gridded weather information from distinct seasons as well as specially selected subsets therein. We then examine in more detail several relationships suggested by the synoptic classifications, including mean hourly regional circulation patterns and their relationship to the larger scale as well as to station observed winds. We conclude with a discussion of our results.

4.3 Data

Archived METARs observations again serve as the primary source for wind observations, as in Part 1. We use data from Travis Air Force Base in the Sacramento Valley as a proxy for wind behavior at the Sacramento Municipal Utilities District's (SMUD) Montezuma Hills wind farm in Rio Vista, Solano County. The two sites were shown to be highly correlated (r>0.7) at all times of the year over the approximately 5 years for which we have coincident data. Edwards Air Force Base and Mojave Airport represent the winds at Tehachapi Pass wind energy site. Edwards and Mojave, 30 km apart in the high desert, are very closely related to each other, and we treat them as representative of winds at Tehachapi Pass, which is another 15 km from Mojave on the edge of the desert. Palm Springs airport winds were recorded where the San Gorgonio Pass begins to widen into the Sonoran Desert, about 10 km to the east of the wind farm located directly in the pass. The available data showed that the seasonal cycles of wind and wind power density are very similar at the two sites. Palm Springs data are present from 1973 onward, Mojave from 1987, and Travis and Edwards since the 1940s. Coverage at the latter two sites was 24 hours a day most years, while Mojave has only daytime recordings, and Palm Springs has mostly daytime observations, with 13 of 24 hour coverage. We also make use of additional METARs stations for SLP and wind data in the vicinity of these sites, as well as wind data from buoys along the California coastal ocean provided by the National Data Buoy Center and National Ocean Service buoys, as we did in Part 1 (Hamilton, 1986; Meindl and Hamilton, 1992). Wind speed observations are scaled using the one-seventh power law to their nominal 10m value using a history of METARs anemometer heights provided to us by the National Climatic Data Center. For the longer wind series some instrumental shifts resulted in several obvious jumps spread over the decades, and so we have made a first approximation at homogenization by calculating a separate mean annual cycle for each period between jumps, and subtracting these from the observations to produce a corrected anomaly data series.

Larger-scale meteorological conditions, including sea level pressure, 500 hPa height, surface temperature, and upper-air winds are taken from the NCEP Reanalysis daily and six-hourly data on a $2.5\,^{\circ}\times\,2.5\,^{\circ}$grid (Kalnay et al., 1996). Daily anomalies are computed by subtracting climatologies calculated over 1968-1996.

The California Reanalysis Downscaling at 10km (CaRD10) regional dataset described in Kanamitsu and Kanamaru (2007) provides regional-scale circulation and other meteorological information. This is an hourly, California-centered, 10 km resolution hydrostatic dynamical downscaling of the global reanalysis data that covers the same time period as the global reanalysis. The data are found to replicate land winds better than the global reanalysis, and also show improvement over the coarser-scale data assimilation North American Regional Reanalysis (NARR; Mesinger et al., 2006), particularly in reproducing complex wind patterns such as in Santa Ana and Catalina Eddy events (Kanamitsu and Kanamaru, 2007; Kanamaru and Kanamitsu, 2007). Because of this skill in capturing flow over terrain, we use the data set to span the divide between the directly-measured station data and the gridded reanalysis data available.

4.4 Analysis using self-organizing maps

4.4.1 Cold season

The broad peak in the spectral analysis of daily-mean and daily interannual anomaly wind speed around the 3-15 day period, shown in Part 1, suggests the importance of propagating extra-tropical weather systems. To examine atmospheric conditions associated with site wind variability, we examine the synoptic-scale patterns common to the western US/eastern North Pacific area, their progression, and the station wind speed response.

Using NCEP reanalysis data, we seek to organize the gridded meteorological data in realistic ways that are instructive to the analyst. Basic dynamical concerns suggest that this could take the form of a geographic arrangement of pressure fields, mandatory level heights, and/or wind fields in a region about the sites of interest. For this study we employ self-organizing maps (SOMs) (Kohonen, 2001), which we find stably illustrate the commonly observed patterns as well as showing connections to site data.

Self-organizing maps are a well-established tool in biostatistics and other sciences, and are gaining traction in atmospheric and climate science as well (Kohonen, 2001; Hewitson and Crane, 2002; Cavazos, 1999). Rather than forming patterns based solely on eigenvectors or partitioning the sample space of data (ie, the set of weather maps from a certain region and period) into separate clusters, a self-organizing map is an unsupervised learning and classification system that describes the extent of the sample space by representing its characteristic common states with a specified number of patterns, referred to as nodes.

In this study we use maps of anomalies from daily climatological values. In the SOM algorithm, a region's two-dimensional anomaly map of any given day is concatenated into a vector and if the map contains multiple fields – such as a 500 hPa height map overlying a sea-level pressure map – the elements belonging to each field are divided by their collective standard deviation to normalize across the multiple variables displayed on the map. Each day's scaled, concatenated vector now represents a point in a space whose dimensionality is determined by the number of gridpoints in the original anomaly maps. The SOM analysis identifies nodes that best summarize the cloud of points in this space. The analysis starts with an initial guess as to what these nodes might be, and this guess for each of the m × n nodes is a different linear combination of the first two principal component eigenvectors of the sample space. (Random initial states could also be used with similar results, but are computationally inefficient, according to Kohonen (2001)). In the next step, each node is then re-positioned based on the locations of the sample points within a certain vicinity of it, with the nearby points weighted to exert a greater influence than the more distant ones over the node's new location. This step is carried out repeatedly, with the size and weight of the hypersphere of influence shrinking at each step. Once the influence of all points near a node has shrunk to zero, the nodes are considered to be determined for this subspace.

Each resulting node is re-scaled and can be plotted as a weather map. There are several advantages to computing such maps, as became clear in this analysis as well as discussed in Hewitson and Crane (2002) and Kohonen (2001). A point that is close to multiple nodes at any step in the process contributes to all of the nodes' subsequent positions. In practice this often leads to final maps with less abrupt transitions between nodes than with k-means clustering, and less chance of qualitatively different final maps due to variations in the initial guess or due to changes in a small number of sample points. The resultant nodes can represent differences in one part of the map domain while other areas are similar, and with appropriate grid dimensions can display a smooth transition in conditions from node to node and across the grid of final maps. Thus, a self-organizing map (really a map of several weather maps, in our case) represents the continuum of possibilities spanned by the weather over the period and region in question. Even a large SOM (for instance, a grid of 5 × 5 nodes) will often display a smaller and more easily understood number of key patterns or weather systems, while also allowing the analyst to easily classify any given day by its place in that continuum.

In Figs. 4.1 and 4.2 we present cool season (October-March) and warm season (April-September) SOMs for an area extending approximately 1500 km zonally and approximately 1000 km meridionally from the outline defined by the Travis, Palm Springs, Edwards, and Mojave METARs sites. The maps show, for each season, the characteristic patterns of SLP anomaly and 2-day change in 500 hPa height anomaly from

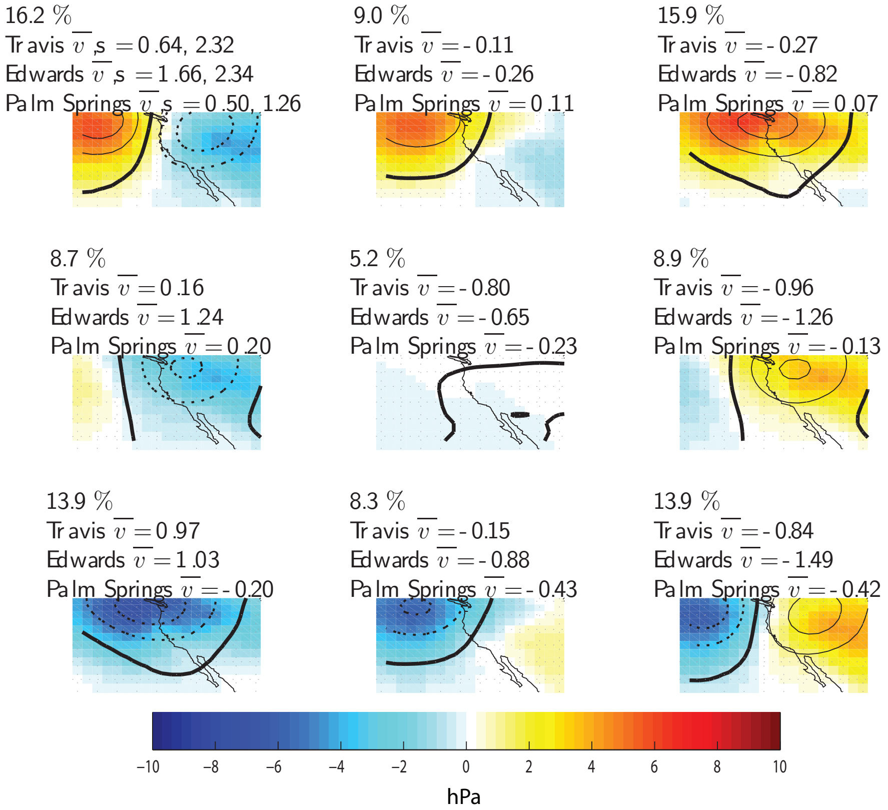

Figure 4.1: Self organizing map for October-March. Colors are composite anomalous SLP; contours are composite anomalous 2-day change in 500 hPa height. Dashed contours indicate anomalous troughing. Contour interval is 25m. Listed above each node is the frequency of days most closely matching that pattern, the mean wind speed anomaly values and for the first node, the wind speed standard deviation for all days examined, at Travis, Edwards, and Palm Springs.

1968-1996, as well as the frequency with which these patterns occur and the composite mean daily wind speed anomaly at each of the three best-sampled sites, adjusted for instrumental jumps, in the days that best match that map pattern. The corresponding seasonal climatological states are presented in Fig. 4.3. Also computed, and used later in our analysis, are the nine SOM time series corresponding to the Euclidean distance (in scaled SOM hyperspace) between each day's reanalysis weather pattern and each of the nine node patterns. Above each node is the wind speed anomaly from all days whose weather map most nearly resembled that node, at each of the Edwards, Palm Springs, and Travis sites. Because the Mojave values mirror the trends at Edwards, but are made up of fewer observations, given the shorter period of years and limited hours of the day that Mojave reported wind speeds, we have omitted the mean anomalous wind speeds at Mojave from Figs. 4.1 and 4.2.

Focusing first on the cool season, several patterns are worth noting. The maps display the push and pull between the patterns of oceanic anomalous high/continental low and oceanic anomalous low/continental high in SLP anomalies (upper-left to lower-rightmost maps). The site wind speed anomalies in southern California are most positive in the oceanic high/continental low SLP cases, and most negative in oceanic low/continental high scenarios. The corresponding 500 hPa ridging/troughing anomalies (ie, solid or dotted contours, respectively) generally align to support the sustenance and propagation of the sea-level disturbances, through lower-tropospheric vertical motions implied by quasi-geostrophic dynamical considerations. In addition to anomaly patterns with contrasting SLP anomalies over the oceanic and continental areas, there is also a node showing a broad area of low pressure straddling the coast near the Pacific Northwest, and one showing the same with anomalous SLP high (lower-left and upper-rightmost panels).

While the Travis wind speed anomalies vary with weather patterns in the same way as the southern California sites in the upper-left, middle, and lower-rightmost nodes, this does not seem to be the mode of variability most influential to Travis mean wind speeds. Rather, the pattern most strongly corresponding to anomalously high winds at Travis is that of widespread low SLP (the lower-left node), with some 500 hPa troughing activity downstream to the East of it. In contrast, along the bottom row of the cold-season SOM, the middle pattern's SLP depression that is not directly overlying the site shows near-neutral mean conditions at Travis, and the rightmost node, with a continental high, shows a negative wind speed response. Higher-density SOM grids (not shown) display a smooth transition between patterns where the depression squarely overlies Travis, to those where it lies to the east and forms a dipole opposite a continental high, with commensurate smooth transition from positive to negative mean wind speed anomaly.

In the cool season, the oceanic high SLP pattern, as characterized by the SOMs, serves to expand the climatological area of North Pacific high pressure northward, while anomalous continental highs and lows collocate with the climatological high centered from the Great Basin to the southern Rocky Mountains (Fig. 4.3). The end result is that the upper-leftmost pattern in the SOM superimposed on the climatology is a negative zonal sea-level pressure gradient across California. In the opposite case, the continental high and oceanic SLP depression decrease or weakly reverse such a gradient. In addition to the ocean-continent dipole pattern of variability, the characteristic sea-level patterns identified by the SOM algorithm also include oceanic and continental highs and lows in isolation. Broad disturbed areas covering the greater western U.S. and eastern North Pacific (the upper-right and lower-left nodes) are visible in the SOM. Conil and Hall (2006) find that cold-season Southern California winds react to a monopole of SLP centered over the western US. The composite means of Edwards and Palm Springs station data show a relationship to such a monopole, particularly along the middle row of the SOM grid. Here, for over one fifth of the days examined, wind speeds at both stations show an inverse relationship with Great Basin area SLP anomaly. On the other hand, the southern California composite anomalies consistently become more negative as one progresses down any column of the grid, where the major change is a suppression of the oceanic high or development of the low, indicating that in many cases the station winds are not varying solely in reaction to a monopole pattern. This pattern is found for both Palm Springs and Edwards, but the SOMs indicate that Edwards overall has a stronger response than Palm Springs to these synoptic forcings.

The presentation of the overlying 2-day 500 hPa heights in Fig. 4.1 may at first seem superfluous, as the centers of downward and upward vertical motion implied by the ridging and troughing tend to align themselves ahead of the surface highs and lows, respectively, as one would expect for propagating midlatitude systems. Further examination, however, shows that they are indeed relevant to the station winds. When SOMs are used to form patterns and find best-matching days solely based on SLP information (not shown), very similar SLP distribution patterns are found, but the corresponding

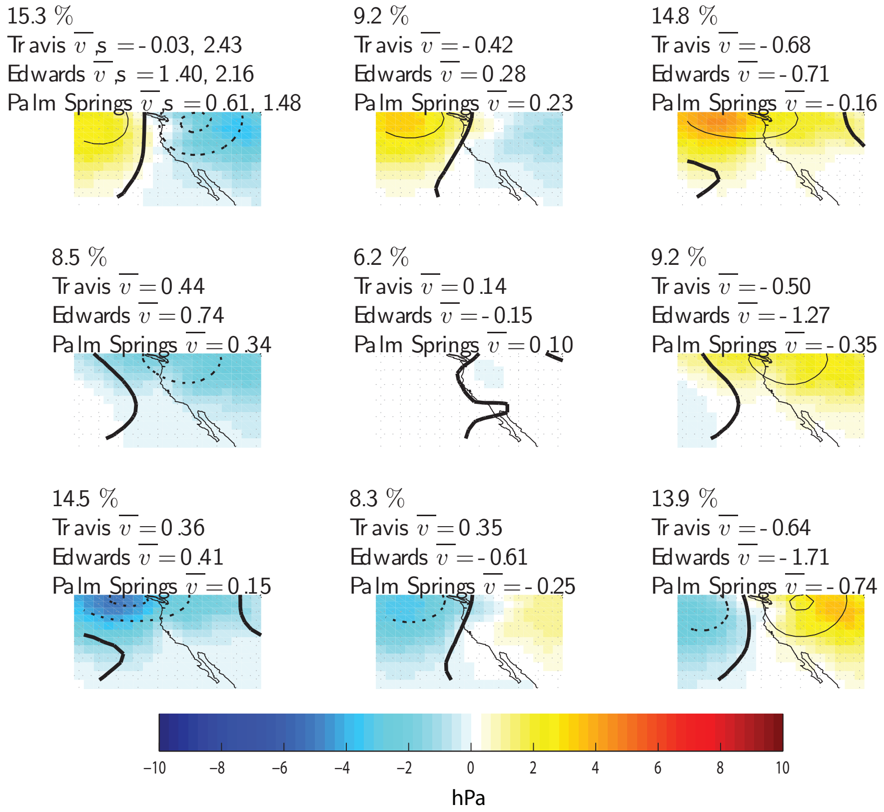

Figure 4.2: As in Fig. 4.1, but for April-September.

wind speed mean anomaly values at each station are generally lesser in magnitude and the standard deviation of wind speed anomalies in each group are greater than in the bivariate SLP/Z_{500} SOMs presented here. The value of using the Z_{500} information is even more evident when we compute SOMs with larger grids (not shown). When using as many as 25 nodes to find patterns from SLP and Z_{500}, the differences between adjacent nodes are often largely due to differences in the upper-air patterns. In turn, the SOMs calculated without using 500 hPa patterns often do not provoke as clear a response in station wind speeds. This suggests that when upper-level support is present to sustain and develop anomalous near-surface highs (through 500 hPa ridging activity east of the SLP high) and lows (through troughing), the station winds have a more consistent response.

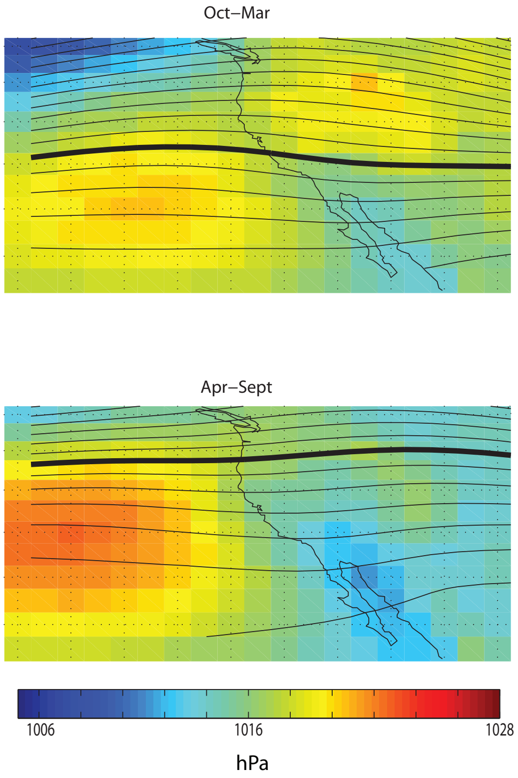

Figure 4.3: Climatological SLP distributions in hPa (colors) and 500 hPa height (contours, 5700 contour weighted and interval is 25 hPa) for October-March and April-September.

4.4.2 Warm season

For the warm season, the self-organizing map of anomalous SLP (Fig. 4.2) exhibits similar but weaker versions of the cold season patterns, with some northward displacement. Anomalies are smaller than in Fig. 4.1, indicating lesser synoptic activity in the warm months, while the 500 hPa levels show little organization or support for the surface disturbances. Although the nodes exhibit essentially the same, but weaker, anomalous weather patterns, these occur within a different climatological distribution of pressure (Fig. 4.3). The summertime eastern North Pacific has a stronger high pressure center that extends further north than the cold months' anticyclone, while the continental high has largely dissipated and the low-lying desert areas of the southwest show considerably lower pressure. This results in an enhanced zonal sea-level pressure difference across California in the mean, whose seasonal timing coincides with or has a slight offset from the mean maximum wind at each station (Part 1).

Considering all three sites, the main difference in the warm season compared to the cold is in the Travis composite mean wind speed response. Mean speed anomalies are negative for the upper-left node, and the slowest winds correspond to the pattern of high SLP in the northwestern part of the domain (upper-right node). Although there is some difference in the mean wind speeds corresponding to each pattern, a clear relationship between synoptic forcing and site winds is not apparent. In fact, for this station and season, a domain of this size might be bigger than we need. Close examination suggests a consistent relationship between the meridional SLP gradient near the site and wind speeds, a topic we explore in section 4.6. In addition to the SLP gradients near the lower limit of scales resolved by reanalysis, the diminished wind response at Travis leaves open the possible role of smaller-scale circulations (section 4.7).

While we have utilized SOM analysis to diagnose the forcings of site wind speed on variability synoptic time scales, the SOMs presented do not explicitly describe the time development of the synoptic states. There are several other lines of evidence, however, showing that the large-scale patterns evolve from day to day in concert with the site wind speed anomalies and as one would expect from general extratropical synoptic meteorological theory. First, we found the best-matching node for each day's reanalysis conditions over many years, and calculated the likelihood of transitioning from any given node pattern to each other pattern over one, two, or three days' time. In general, persistence — having the same SOM node best describe two consecutive daily patterns — was the most common transition over one day's time. For days matching the node indicating broad high pressure (upper-right), for instance, in the cool season there was a 50% probability that the next day would also best match that node. For the days when there was a transition to a different node, and for the common two-day changes, the transition was generally to a neighboring SOM node. For instance, continental high pressure (the center node on the rightmost column) has a tendency to transition to oceanic low/continental high (lower-right), with a 60% probability of that transition in one or two days' time in the cool season. Transitions to non-neighboring nodes are not frequent over one or two days' time, but the likelihood of day 3 matching a node not neighboring the day 0 node is much greater.

In addition to this analysis, we used SOMs to find the most common patterns in 4-day wind speed anomalies at every site and season (not shown). The results show that the common higher-wind events tend to last one or two days before winds go back down to climatological values, at each site and season. Pronounced low wind events can also end after one or two days, although negative anomaly and near-zero anomaly events are also seen at each site that last as long as 4 days. The only site that shows a tendency toward 3 or 4 day long high wind events is Travis in the summertime, when a pattern of four continuous days of 2 m/s anomalous daily-mean wind speed is one of the principal patterns. Moreover, when we look at the mean SOM synoptic classification for the days contributing to each of the identified common 4-day patterns, we see that there tends to be a close relationship between synoptic state and wind speed on each day. For example, at Edwards and Mojave, one common multi-day wind speed anomaly pattern is two days of strong winds (2 m/s or more above climatology) followed by two days of near-zero anomaly wind speeds; these usually occur when the first two days best match the upper-left and upper-middle SOM nodes, and the next two are weak versions of the center-bottom and lower-left nodes. Overall, these results provide a useful confirmation that the SOM patterns do match up with the synoptic variability found in the time series analysis, as well as illustrating the linkage between synoptic patterns and wind speed variability across days.

4.5 Synoptic patterns from select windy and calm days

Although the SOM nodes in Figs. 4.1 and 4.2 indicate the station composite mean wind speed anomaly corresponding to each common synoptic pattern, more detail about the relevant forcings is evident from separating the windiest from the calmest quartile days for each station and examining the dominant synoptic patterns in each set. Figs. 4.4-4.7 show these for the synoptically active months of December-January. Separate maps (not shown) have shown that similar patterns hold in other seasons, albeit with weaker anomalies that are somewhat offset northwards. Fig. 4.4 reveals that for Travis, stronger winds are forced by anomalously high oceanic SLP with 500 hPa ridging overlying it, much as implied from Fig. 4.1. In addition, however, the low pressure center associated with stronger winds need not be a purely continental low; strong winds are often excited when a depression straddles the coastal northeast Pacific and the Pacific Northwest, especially with anomalous upper-level troughing ahead of it. This might be a coastal storm approaching the area from the west or north, and the geostrophic component of the flow around a low-level disturbance such as this would bring westerly winds toward San Francisco Bay and the anemometer at Travis. For low-wind Travis h

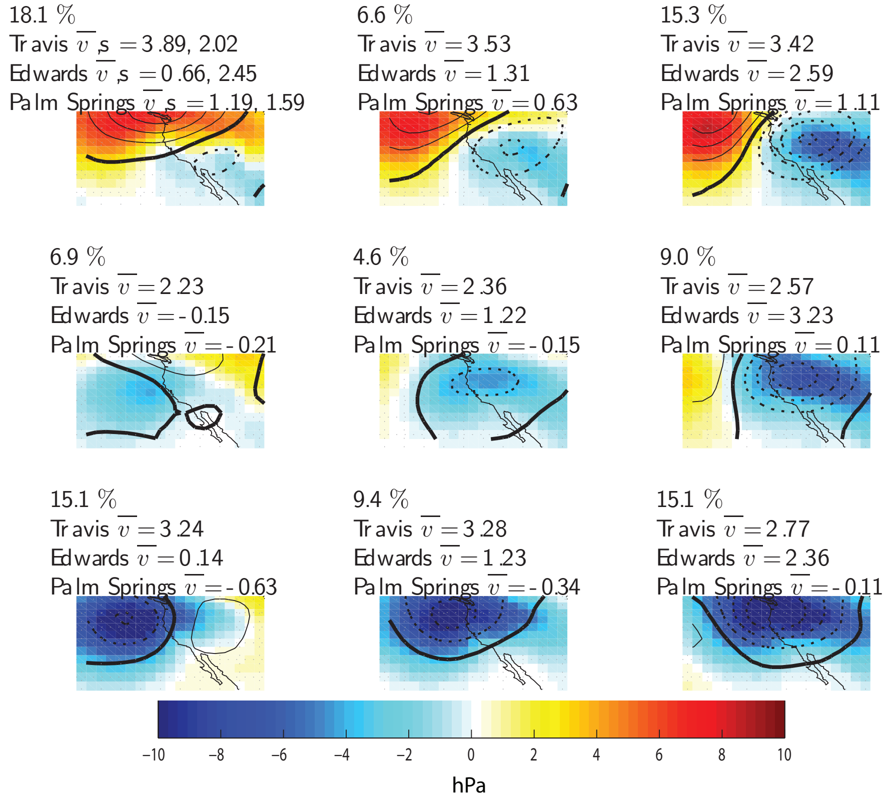

Figure 4.4: As in Fig. 4.1, but only examining conditions from days in the windiest quartile of December-January days at Travis.

days, the opposite patterns occur (Fig. 4.5): each pattern shows anomalous high SLP over the western US and northern California. The top and bottom rows of nodes show that this pattern corresponds to lower station winds whether accompanied by oceanic high or developing low pressure centers. The top row also shows that a more positive meridional pressure gradient over California corresponds to weaker circulation at Travis, in addition to the oceanic/continental contrast identified in the earlier figures.

For Edwards, which shows the strongest response to the patterns identified from all days in the cold season, the SOM patterns corresponding to calmest and windiest days are similar to those found in the group of all cool-season days in Fig. 4.1. Fig. 4.6 shows that in addition to the oceanic highs and continental low SLP disturbances, Edwards also is windy when a coastal low has come onshore and dipped southward toward southern California. The windiest days contain stronger 500 hPa ridging supporting a high and troughing over a low than the patterns from all days in Fig. 4.1. Similarly, Fig. 4.6 shows that strong winds at Edwards are found when there is an oceanic high SLP anomaly and/or continental SLP low, with organized 500hPa ridging and troughing leading the high or low, respectively. The SLP patterns associated with weak Dec-Jan winds at Edwards in Fig. 4.7 are strikingly inverse symmetric to those for the high wind cases in Fig. 4.6, although the upper-air anomaly means are lower. Every node in Fig. 4.7 shows anomalously high SLP over the continental region. The consistency of this feature with a variety of states of oceanic SLP supports the findings by Conil and Hall (2006) of a monopole-like center of action for these days in the calmest wintertime quartile. At the same time, the high wind cases in Fig. 4.6 show that this SLP monopole does not account for all of the wind response at the site: the mean wind speed anomaly is about 1 m/s greater for days corresponding to the nodes in the rightmost column of the SOM than it is in the lower-left and lower-middle nodes. The negative SLP anomaly over the Great Basin area is comparable in these five nodes, but the anomaly maps along the rightmost column also show a positive oceanic SLP feature, while the other two do not. The role of Great Basin pressure is also explored in section 4.7, where we investigate the daily cycle at Edwards.

We have also examined the SOM patterns characteristic of Dec-Feb high and low wind days at Palm Springs (not shown). The oceanic high/continental low are present in some windy quartile nodes, as well as inverse symmetric SLP distributions showing oceanic low SLP anomalies in nodes for the calmest quartile days. In addition, however, other windy-quartile patterns are dominated by SLP highs over the western US, and the central node from the low-wind SOM shows very little anomalous SLP or 500 hPa heights. Furthermore, several windy-day patterns resemble calm-day patterns, and the significant differences between patterns found and the most commonly occurring ones in the cold season (Fig. 4.1) are symptoms of why Palm Springs overall has a less clearly defined cold season response to synoptic forcing than the other sites (Fig. 4.1). While we have omitted reproducing or detailing all the features of the Palm Springs composites, some points are worth comment. The low-wind quartile continental lows that do appear do not extend as far south as the Palm Springs site itself or the approximate latitude of the rest of the Sonoran desert, while the continental SLP depressions on high-wind days extend much further south, well into Mexico. Likewise, continental SLP highs for low wind composites extend well south and to the eastern limit of the domain, as do the

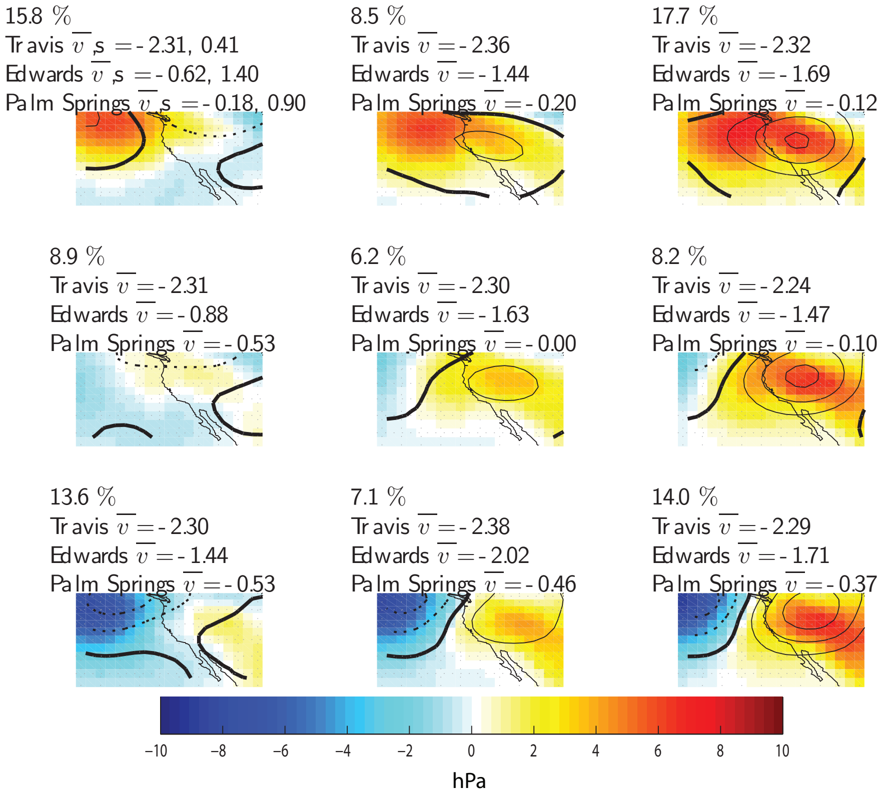

Figure 4.5: As in Fig. 4.1, but for days in the least windy quartile of December-January days at Travis.

continental lows on windy days.

4.6 Role of SLP gradients

Several of the SOM nodes in Figs. 4.1 - 4.7 imply that the common synoptic patterns affect station winds by setting up anomalous sea-level pressure gradients. The exact zonal and meridional pressure anomaly gradients, $\frac{\partial p'}{\partial x}$ and $\frac{\partial p'}{\partial y}$, can be approximated by the bulk differences, $\frac{\Delta p'}{\Delta x,y}$ as can the non-anomalous gradients, $\frac{\Delta p}{\Delta x,y}$. We calculate these from daily reanalysis SLP located one grid box west and east or north and south of the reanalysis boxes closest to the stations. The southern California sites are closest to 35°N, 117.5°W, while Travis is closest to 37.5°N, 122.5 °W. This results in approximate values of 450 km for Δx and 550 km for Δy.

Tables 4.1 and 4.2 show the relationships between bulk zonal and meridional

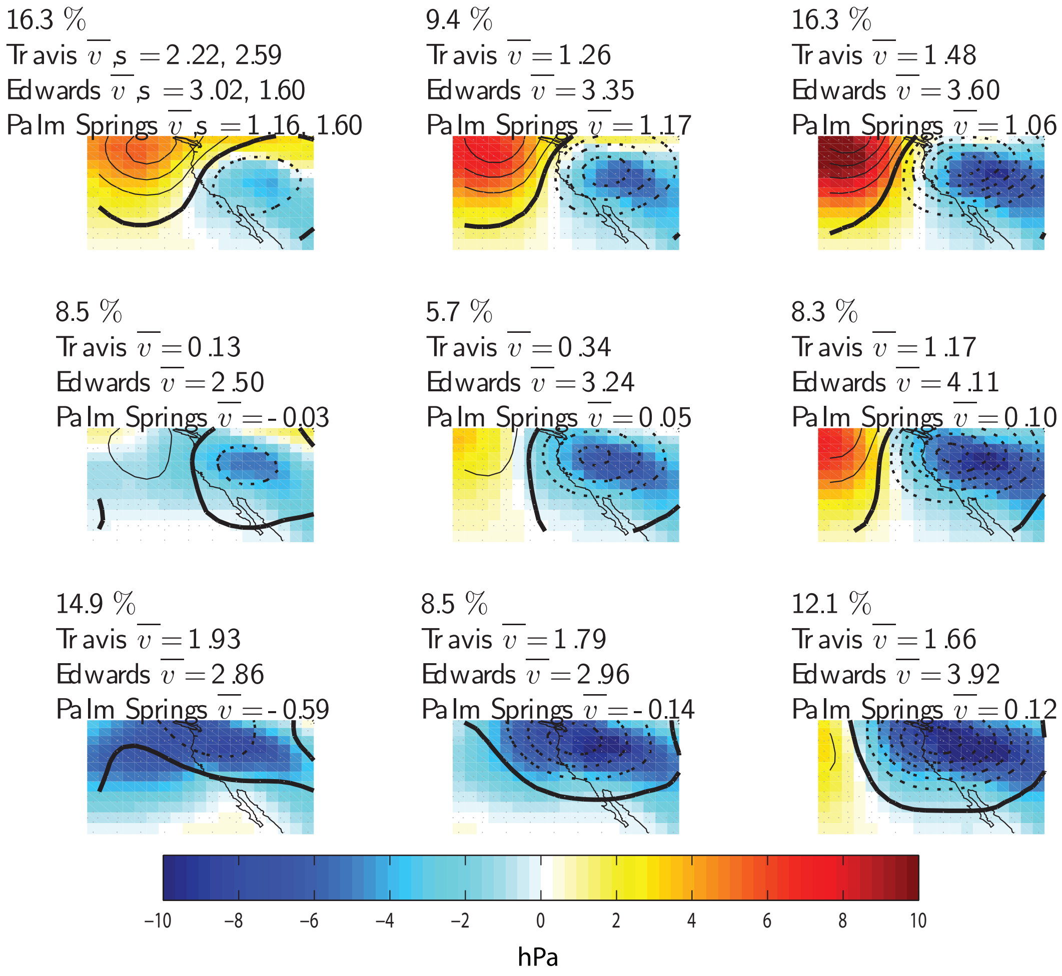

Figure 4.6: As in Fig. 4.1, but for days in the windiest quartile of December-January days at Edwards.

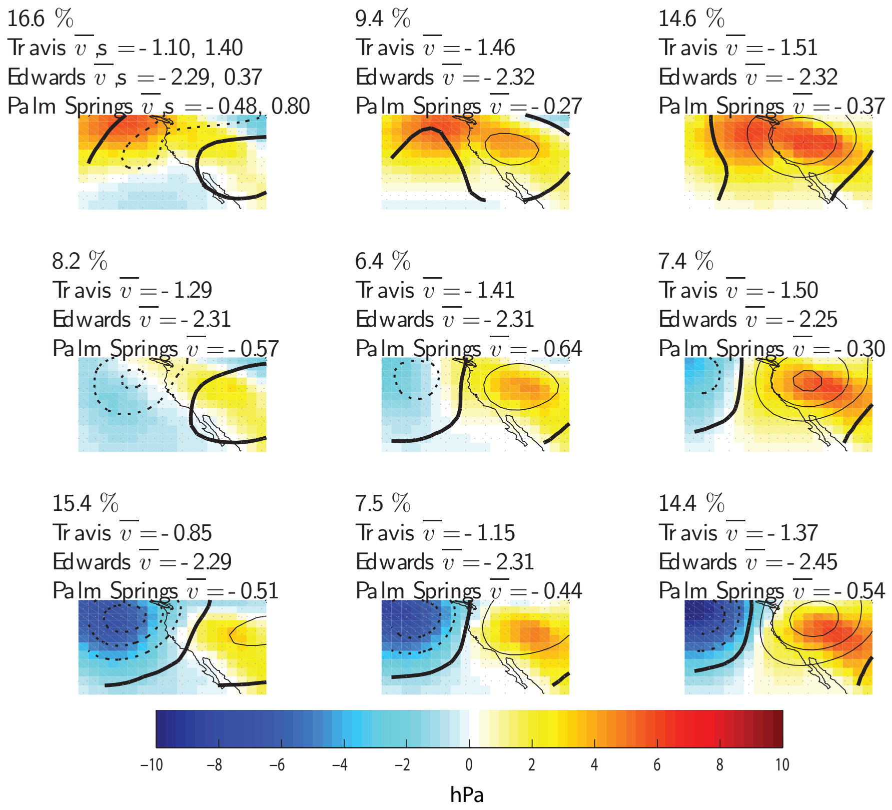

Figure 4.7: As in Fig. 4.1, but for days in the least windy quartile of December-January days at Edwards.

Table 4.1: Pairwise correlation coefficients for zonal SLP difference over 450 km (from reanalysis) and wind speeds at the station labeled in the leftmost column. The left two columns of r values cover cold and warm seasons, using daily-mean data, while the two rightmost columns use daily interannual anomalies for wind and pressure data. Every correlation shown is significant at the 95% level using the bootstrap methods described in the text and Part 1.

	cold season daily data	**warm season daily data**	**cold season daily interannual anomalies**	**warm season daily interannual anomalies**
Travis	-0.21	-0.08	-0.16	-0.16
Edwards	-0.52	-0.54	-0.50	-0.50
Mojave	-0.48	-0.48	-0.45	-0.40
Palm Springs	-0.43	-0.55	-0.33	-0.46

Table 4.2: As in Table 4.1, but pressure differences are over a meridional spacing of 550 km.

	cold season daily data	**warm season daily data**	**cold season daily interannual anomalies**	**warm season daily interannual anomalies**
Travis	-0.27	-0.25	-0.24	-0.29
Edwards	-0.51	-0.60	-0.49	-0.58
Mojave	-0.40	-0.42	-0.38	-0.35
Palm Springs	-0.07	-0.45	0.05	-0.37

pressure differences and station winds for Travis, Edwards, Mojave, and Palm Springs. The range of correlations was quite broad, but since all available daily mean wind speeds in each season were used, it is not surprising that all correlations were significant at the 95% confidence level using bias-corrected, accelerated bootstrap methods, with stationary bootstrap to account for serial dependence (Efron and Tibshirani, 1993; Politis and Romano, 1994; Mudelsee, 2003, detailed further in Part 1). In general, the correlation values are similar whether for observed daily mean or interannual daily anomaly values. Correlations were all negative, indicating that increased pressure gradient in the direction to reinforce the mean westerly to northwesterly wind flow is associated with increased wind speed. Edwards winds are the most negatively correlated to pressure gradients, which is also consistent with Table 4.3. Travis winds are least correlated to zonal pressure differences in the warm season (correlation actually goes to zero when $\Delta x \approx 1350$ km). Although the reanalysis grid is too coarse to resolve the narrow topography within California, the stronger correlation between Travis wind speeds and meridional pressure gradient indicates that reanalysis-scale SLP differences do reflect the along-Sacramento Valley mesoscale SLP patterns found in Zhong et al. (2004), where lower SLPs further north in the Sacramento Valley correspond to stronger winds at Travis.

It is worth noting that the highest-magnitude r values in tables 4.1 and 4.2 are comparable to those between the observed daily wind anomalies and the best-fit line formed from a multilinear regression using nine SOM time series as the only predictors in addition to the intercept. In that sense, any one of the high-correlation SLP gradients from reanalysis essentially explains as much of the wind's variance as the set of SOM synoptic types. However, the SOMs are still more valuable in understanding the meteorological patterns involved and addressing the combinations of factors that affect wind behavior. They also lead to efficient and objective selection of days with similar synoptic forcing for compositing and other uses. Furthermore, all of these correlation coefficients are diagnostic of observed past relationships; determining the relative merits of using SOM time series versus simple SLP differences for forecasting winds or downscaling use would necessitate additional experiments and independent validation.

We next compute the mesoscale pressure difference recorded between Bakersfield and Edwards and its correlation to Mojave winds. This is following Green et al. (1992), who showed a strong relationship between the wind on the Mojave desert side of Tehachapi Pass and the SLP difference between stations in the southern San Joaquin Valley and the Mojave Desert, on the opposite side of Tehachapi Pass. In our data, the wind is indeed closely related to this gradient, showing negative correlation (pressure difference is defined as negative when SLP at Edwards is lower than at Bakersfield) in hourly data over all months of the year, with r values ranging from -0.48 in January to -0.22 in August. Green et al. (1992) found that while the mesoscale pressure difference across Tehachapi Pass was closely related to San Joaquin Valley-Mojave Desert SLP difference at most hours, local noontime winds did not exhibit such a relationship. They ascribed this to diabatic slope heating, noting that Tehachapi Pass data were taken on the desert side of the pass, and morning insolation could heat the pass, creating pressure perturbations or slope winds. This is worth noting in relation to the winds at the Tehachapi Pass wind energy conversion facility, although our data from Mojave Airport, near Tehachapi but on the generally horizontal desert floor, shows the correlation between SLP difference at noontime is just as strong as at other times. Correlation between wind speed and pressure gradient on daily timescales is similar to that on hourly timescales, reaching -0.50 and -0.36 in January and August, respectively, and -0.39 and -0.20 in these months for interannual anomaly daily means. The data are summarized for warm and cold seasons in Table 4.3.

The observations indicate that the anomalous flow is mainly down-gradient, modified by topography. While the Mojave airport lies close to the roughly northwest-southeast line between Bakersfield and Edwards, flow is mainly along the southwest-northeast axis parallel to the nearby mountains (Part 1). The correlation between zonal wind and the mesoscale pressure gradient in each month is slightly more negative than that between wind speed and the gradient, indicating westerly flow when Bakersfield SLP is higher than Edwards. Scatterplots (not shown) of anomalous SLP gradient versus anomalous wind direction show that when the SLP difference is negative, direction is predominantly between 200 and 290 degrees, and between 30 and 100 when it is positive. This also fits well with the patterns found from the network of observation stations in Green et al. (1992).

Similarly, Zhong et al. (2004) showed that the pressure difference between Sacramento and San Francisco, lying on either side of Travis, has a strong mean daily cycle and becomes most negative near midnight, in phase with Travis winds and a few hours after the peak in mean temperature difference between Sacramento and San Francisco. Our results using San Francisco and Sacramento airport METARs data is consistent with this, as shown in Table 4.3 and Fig. 4.11. The correlation table indicates that the Sacramento-San Francisco pressure gradient plays a role both in hourly and in daily data with annual cycle removed. While we see reanalysis SLP differences in Table 4.2 begin to approximate the role of measured in-valley $\frac{\Delta SLP}{\Delta y}$ shown in Zhong et al. (2004), the zonal width of the valley is far too small to be resolved by the global reanalysis; consequently, the correlation coefficients in Table 4.1, which uses coarse reanalysis SLP fields for Travis $\frac{\Delta SLP}{\Delta x}$ are much lower than using values from sites separated by smaller distances, presented in Table 4.3.

Along similar lines, we can examine the role of a mesoscale pressure gradient across the San Gorgonio Pass on the Palm Springs station winds. The available observational records, using the best sites available to determine the pressure gradient — METARs from Blythe Airport in the low desert and Ontario Airport west of Palm Springs — have data only from 1995-1997. While this observed correlation suggests that the relationship between observed wind speed and mesoscale pressure difference is strong, the limited data availability means that this relationship has not formally been observed over a wide range of climate states.

Zonal pressure gradients at both mesoscale and the lower end of reanalysis-resolved scales have spectral peaks at the diurnal period, as do the wind time series, and these have daily and annual timing in phase with the low-level thermal low pressure centered over Arizona (Rowson and Colucci, 1992), stronger winds coinciding with deeper thermal lows and stronger pressure gradients. Time series of warm season wind speed and six-hourly reanalysis zonal pressure difference band-pass filtered to focus on subdaily signals (not shown) show correlation of greater magnitude than those in Table 4.1. While these features seem to indicate that southern California winds simply accel-

Table 4.3: Pairwise correlation coefficients for station-observed wind speeds and mesoscale SLP differences at points on opposite sides of each station (ie, Edwards and Bakersfield for Mojave winds, Blythe and Ontario for Palm Springs winds). Hourly data used are differences from the daily climatological value, and daily data are interannual anomalies. Every correlation shown is significant at the 95% level using the bootstrap methods described in the text and Part 1.

	Observations, cold season	**Observations, warm season**
Travis, hourly difference from climatological day means	**-0.17**	**-0.47**
Travis, daily interannual anomalies	**-0.11**	**-0.35**
Mojave, hourly difference from climatological day means	**-0.38**	**-0.35**
Mojave, daily interannual anomalies	**-0.35**	**-0.37**
Palm Springs, hourly difference from climatological day means	**-0.15**	**-0.31**
Palm Springs, daily interannual anomalies	**-0.19**	**-0.36**

erate down the SLP gradient in response to the deepening thermal low centered over Arizona, the topography of the region, and past studies (Conil and Hall, 2006; Green et al., 1992), suggest that there is actually fine-scaled structure to the low-level flow. This is confirmed by the results of the detailed examination in the following section.

4.7 Local circulations and diurnal variability

4.7.1 Northern California

In this section we investigate the regional flow regimes relevant to wind energy sites, and examine variations therein. While the SOM analysis gives a starting point for synoptic-scale flow, the combination of topography and smaller-scale processes can lead to significant variability not directly explained by these patterns. We start with the warm season wind behavior at Travis, which shows the weakest response to SOM-classified synoptic systems, and is the season having the most energetic winds (Part 1). In order to zero in on the pertinent local phenomena, we exclude the spring and fall months, which

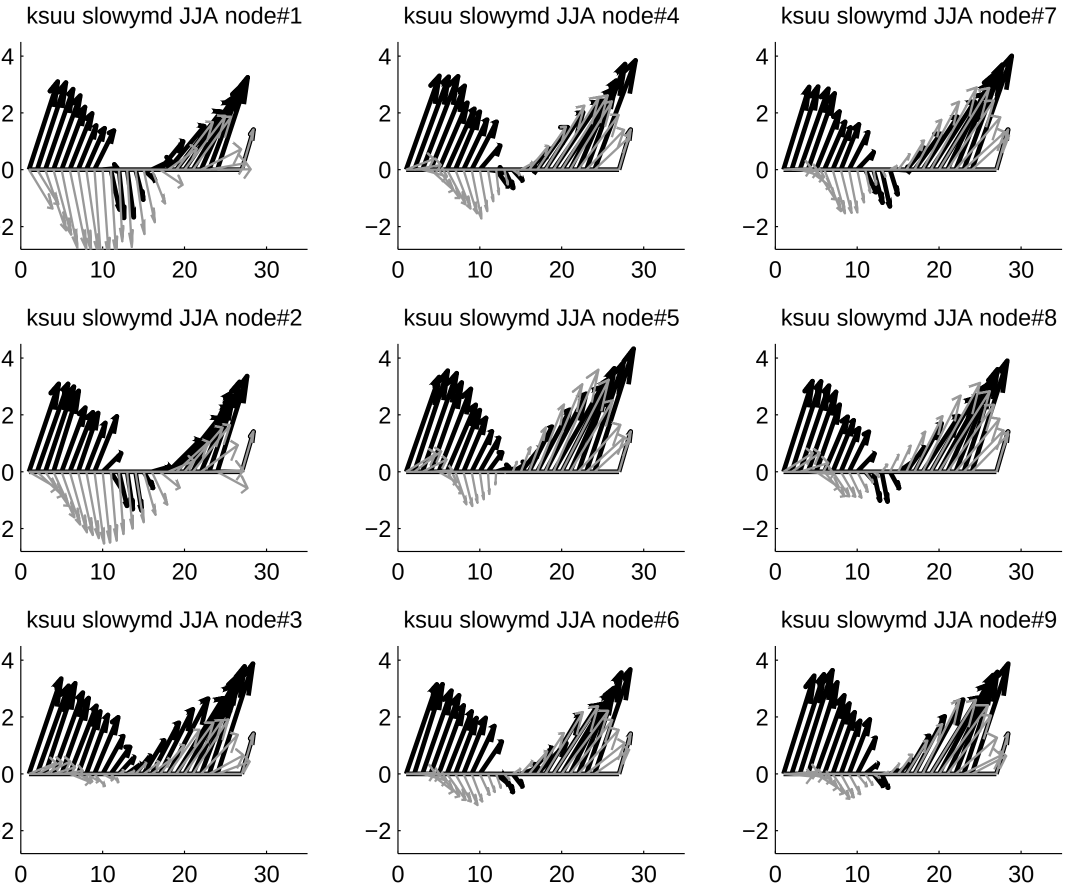

Figure 4.8: Mean hourly wind vectors for days in the slowest wind quartile in June-August corresponding to each of the SOM patterns in Fig. 4.2 for KSUU station data (black) and nearest corresponding CaRD10 point (grey). The mean winds for local hour 0-23 are presented. For scale, the last, offset vector represents a southwest wind at 2 m/s .

have some characteristics of the large-scale cool-season flow (ie, in the polar histograms in Part 1), and instead focus on June-August. We divide the summertime days from 1968-1996 into quartiles based on daily-mean wind speed anomaly and compare the fastest and slowest quartiles. Because the Travis wind speed response to SOM patterns are weak, a substantial amount of days from each SOM synoptic type are represented in every wind speed quantile. To avoid averaging together days of dissimilar meteorology that nonetheless have a similar station mean daily wind speed response, for each of the fastest and slowest wind quartile days we first separately examine the composite mean daily cycle corresponding to each SOM pattern, and compare these cycles to the CaRD10 composite means for the same days. We reproduce a representative sample of one such set of composite means, for slow-wind days at Travis, in Fig. 4.8.

Two patterns stand out in Fig. 4.8. In each wind speed quartile, there is little variation in observed hourly composite mean patterns among different SOM nodes. These low wind speed days, for all SOM patterns, show weak southwest winds in the early morning and afternoon-evening hours, and around midday the winds slacken and on many days turn lightly northwest. High wind speed days — not shown here — are characterized by stronger, persistent southwest to west-southwesterly winds, with a diminution in speed around noon and an acceleration in the late afternoon, local time. Another salient feature regards the CaRD10 simulated winds. For late nights, morning, and midday hours, the model winds show a more negative meridional component than the observations. For the calm day composites in Fig. 4.8, the model often shows winds from the north or northwest even when observed winds are from the south or southwest. This bias appears in the windy days as well (not shown), where the simulated morning southwesterly winds are weaker in the meridional component than those observed. The model does faithfully simulate the afternoon southwesterly acceleration of the winds for both groups of days, however.

Noting these shortcomings in local CaRD10 winds, we proceed to examine the regional CaRD10 flow. Since variation is minimal between SOM types, we consider the hourly composite means of all high or low wind speed quartile days in Figs. 4.9 and 4.10. In both figures, a downslope to down-valley flow is evident at local 0:00 to 8:00 on the eastern (inland) side of the coastal mountains north of San Francisco Bay. While downslope winds are characteristic of mountain-valley systems in the cooler hours, this CaRD10 flow coincides quite closely with the spurious northerly v component in the wind described above. Comparison with the station observations in a typical summer found in Fig. 2 of Zhong et al. (2004) also suggests that the CaRD10 downslope and down-valley winds persist too late in the morning and extend too far south. In discussing the hydrostatic Regional Spectral Model that produced the CaRD10 data we refer to slope flows. In nature or in nonhydrostatic models, slope heating produces a vertical pressure gradient force when the low-level air in contact with the heated surface leads to an anomalous vertical pressure gradient. This comes in addition to the horizontal pressure gradient force where the surface heating leads to adjustment in the atmospheric column and horizontal pressure gradient compared to a point on the same surface in the free atmosphere, not in contact with a heated surface. Slope longwave cooling has analogous effects for the horizontal and vertical cases (Barry, 2008). Slope winds in a hydrostatic model are excited only by this horizontal pressure gradient force, which combines with mass continuity to result in terrain-following flow, but it has been shown that such a hydrostatic case can accurately reproduce orographically forced flow (Mahrer and Pielke, 1977; Johnson and Uccellini, 1983), and it is understood that this is the case when we refer to slope winds under the hydrostatic assumption. The CaRD10 downslope flow nearly totally subsides after noontime, after which upslope flow begins to develop. The observed and CaRD10 winds at Travis begin to accelerate, and the model's hourly mean bias decreases. The CaRD10 simulation indicates that, by noon, a sea breeze has already commenced at the coast but the leading edge of the packet of stronger west-southwest winds has still not moved far inland. These winds penetrate the Travis area by 16:00, and dominate the areas around Travis and the SMUD wind farm with the strongest flow of the day by 20:00. The vestiges of this wind pulse are still evident south and east of the sites at 0:00, although, in the model, down-slope flow is beginning to develop at Travis by this time. Thus, while the mean daily wind speed cycle at Travis is found to be in phase with pressure gradients between the eastern edge of the valley and the coast (Fig. 4.11; cf.Zhong et al. (2004)), and correlates with the mesoscale pressure gradient in Table 4.3, the model indicates that more than just pressure gradients across the Sacramento Valley are driving the wind. Rather, a propagating feature occurs consisting of a distinct front of stronger onshore winds which originate at the coast and move inland, funneling through the Straits of Carquinez, and results in the rapid afternoon acceleration.

For the least windy days, the CaRD10 composite also exhibits a pulse of accelerated southwesterly wind, but it is weaker than that for the high-wind case (Fig. 4.10

compared to Fig. 4.9). By 12:00, onshore winds have developed and are blowing across the Bay, but the leading edge has not extended as far inland as in Fig. 4.9. By 16:00 and 20:00 the pulse of faster southwesterly winds is impacting the airfield and wind energy sites, although the wind is not as fast as in the strong wind composite (Fig. 4.9). The packet of accelerated west-southwest to southwesterly winds later in the day is also weaker and less defined.

The pressure difference across the Central Vally, between Sacramento and San Francisco, is a strong driver of the wind at Travis, and the CaRD10 data show the patterns and timing of the wind's development. Additional sub-reanalysis-scale processes in addition to across-valley SLP difference may also be involved, both in the creation and in the dissipation of boundary-layer momentum. Zhong et al. (2004) and Bao et al. (2008) provide evidence that the along-valley pressure gradients play an important role, by causing the flow to split and accelerate along the valley once it has entered from the coast. Additionally, to examine dissipation, we use time series of upper-air and surface data indicative of the strength of the capping inversion above the planetary boundary layer in the valley. Iacobellis et al. (2009) use twice-daily radiosonde data from Oakland airport to assess inversion strength by comparing 850 hPa potential temperature to surface potential temperature. They argue that since 850 hPa temperatures show very little spatial variation over the region, 850 hPa potential temperature from Oakland compared to surface potential temperature at observing stations in the Central Valley yield a good indicator of inversion strength at these locations. We adopt this methodology, utilizing a time series of soundings from Oakland at 12Z (4:00 local solar time) and simultaneous surface measurements from selected stations in the Sacramento Valley to find $\Delta\theta_{850}$, indicating the strength of the inversion in this basin. The surface measurements come from the same network of stations as used in Iacobellis et al. (2009) and, as in that report, corrections have been made to smooth out obvious jumps in the temperature record, although the stations were selected in part because minimal corrections were necessary. The surface stations used are Orland, Chico, Marysville, Davis, and Vacaville, all in the Sacramento Valley.

We examine the effect of $\Delta\theta_{850}$ on wind at Travis, but take care to separate out, as much as possible, the interrelated factor of San Francisco-Sacramento pressure difference, ΔSLP. We focus on changes in mean Travis wind speed after 2:00 local time, and consider whether different regimes of $\Delta\theta_{850}$ show different values of late night-early morning mean wind deceleration, in groups of days with little variation in the hour-by hour SLP difference pattern. The results are shown in Fig. 4.11, where we plot the proportional change in hourly-mean wind speed from the 2:00 value, plotting separately the days in each $\Delta\theta_{850}$ tercile within each ΔSLP tercile. Analysis of the CaRD10 regional 850 hPa flow (not shown) reveals no discernible difference in the composite-mean circulations in low and high $\Delta\theta_{850}$ days within any ΔSLP group. Plotting the proportional, rather than actual, change in wind speed relative to 2:00, we essentially make a linear correction to account for the increased drag that is expected of higher-speed boundary layer winds, since drag depends on wind speed, and thus come closer to isolating the effects of $\Delta\theta_{850}$ on 10m wind.

Fig. 4.11 shows that, after controlling for ΔSLP, nights with higher Sacramento Valley $\Delta\theta_{850}$ see greater decrease in Travis wind speed than days with weaker inversions. The 95% confidence intervals around the plots in the first and third tercile in each panel are calculated using the bootstrap percentile method (Efron and Tibshirani, 1993). They show that high-$\Delta\theta_{850}$ conditions experience significantly more deceleration than low-$\Delta\theta_{850}$ days, for every ΔSLP regime. While plots of actual decrease in wind speed from 2:00 (not shown) show that the difference in deceleration is significant at this level for every ΔSLP regime, in the plots showing proportional decrease — incorporating the increased surface drag due to increased wind speed — the difference is still significant at the 95% level except for a few hours in the highest ΔSLP tercile (Fig. 4.11).

The inversion-strength linkage is another mechanism by which large-scale conditions affect wind speed at the wind farm sites, since inversion strength is largely controlled by the vertical velocity and temperature advection caused by broad scale highs and low pressure systems (Iacobellis et al., 2009). Several factors likely explain why greater $\Delta\theta_{850}$ corresponds to greater boundary-layer wind deceleration in the Sacramento Valley basin. Although in the daytime, surface heating tends deepen the boundary layer while decreasing $\Delta\theta_{850}$ (Tennekes, 1973), at night radiative cooling will cut off the thermal mixing supporting the daytime boundary layer and allow the inversion base height to fall. Thus, an increase in $\Delta\theta_{850}$ can be thought of as indicating a stronger temperature inversion to cap the planetary boundary layer, as well as a shallower boundary layer. The momentum confined to a shallower boundary layer will then be affected more by drag at the surface or, in the cases where radiative cooling has caused the lower portion of the boundary layer to become stably stratified, the air up to anemometer height will likely feel the effects of surface drag and see wind speed decrease, but have minimal momentum mix in from above.

The eastward-propagating diurnal pulse of accelerated wind shown in CaRD10 data also fits with observed hourly buoy wind data in San Francisco Bay. Fort Point Buoy lies just inside the Bay, while the Richmond buoy lies further northward, cut off from the open ocean and approximately one third of the distance from Fort Point to the gap at the Straits of Carquinez. The Fort Point Buoy provides the clearest signs of the sea breeze expanding inland to cause the afternoon wind acceleration at Travis and, by extension, the Solano wind farm. Over the years 2005-2008 for which Fort Point data are available, the overall correlation for its hourly summertime wind speed with simultaneous winds at Travis is 0.21, while that where Travis lags Fort Point is 0.26. These correlations are based on wind speeds as recorded at the sites, without removing the mean diurnal cycle, since the phase difference between these diurnal cycles may reflect the propagating winds we are interested in. In days in the strongest quartile of $\Delta\theta_{850}$, however, the instantaneous Travis -Fort Point wind speed correlation is -0.13, while the correlation with Travis lagging Fort Point by 7 hours is 0.19, with the significant difference in correlation presumably due to more pronounced hours of accelerating and decelerating wind under the stronger inversion and less developed boundary layer. The Richmond buoy is influenced both by wind flowing from the mouth of San Francisco Bay and that flowing over the Petaluma Gap in the coastal mountains, further north. Because of this, it generally shows little increase in correlation when leading Travis wind speeds. Only on days when both Richmond and Fort Point are in their slowest quartile of wind speed, is there an appreciable increase in correlation, in this case from 0.16 to 0.29 when at 9 hours lag. This relatively modest difference is not significant at the 95% level (but is at the 85% level), in contrast to the correlation increase at Fort Point, using bias-corrected, accelerated bootstrap methods, where the set of days of interest are resampled and the difference in lagged and instantaneous correlation computed for each bootstrap realization.

While the lag relationship between wind speeds at Travis and Fort Point has clear implications for hours-ahead wind energy predictions, especially when soundings and surface stations show high $\Delta\theta_{850}$, the occasional and weaker lag correlation with wind speed at the Richmond buoy shows that the inland progression of the wind seen in CaRD10 does not uniformly fill the San Francisco Bay enough to be evident at all observation sites. The day-time up-slope winds on the western side of the hills just east of the Bay may also be exaggerated in CaRD10, since it has shown such biases within the Central Valley, and these may be contributing to the appearance of a very broad, distinct climatological sea breeze. Higher-resolution modeling and inspection of more in situ wind records, including land-based ones located roughly between Fort Point and the Straits of Carquinez, will likely reveal more details of the conditions under which the pulse of accelerated winds is best defined. These can then be analyzed with respect to optimal observation locations and quantitative relationships with Travis or SMUD wind, as would benefit operational forecasting.

4.7.2 Southern California

Palm Springs

Similar to Travis, the southern California sites also show a weaker warm season response to SOM synoptic patterns than in the cold season. This suggests that we might gain insight from the same methods of using CaRD10 to investigate regional circulations. While not reproduced here, our initial comparison of hourly composite-mean wind vectors for each SOM type, from high-wind quartile days at Palm Springs, shows significant differences from the observed winds at the site. In the observations, the wind is mainly from the Northwest with occasional southeasterly periods, while the CaRD10-simulated winds include a large amount of southwesterly surface winds. This direction is rarely observed at Palm Springs, almost certainly because the orographic setting of San Gorgonio Pass and downward slope into the low desert channels the winds along a northwest-southeast direction. While the model does capture some of the afternoon acceleration, the model-observation similarity is not as tight as in the case of Travis. The low wind speed quartiles (not shown) reveal similar bias and unrealistic wind direction. This is a case where the 10km horizontal spacing is clearly too coarse to model some of the important details around the wind farm and airport. Because of these inaccuracies, we do not here reproduce CaRD10 regional 10 m composite wind fields for Palm Springs. In our inspection of them, however, there is a diurnal circulation beginning at the coast (which faithfully reproduces the climatological sea-breeze cycle observed at locations in coastal Long Beach and Los Alamitos) and a pulse of accelerated winds that propagates toward Palm Springs. As this pulse moves eastward over complex topography it becomes less distinct, and the wind vectors near Palm Springs seem more dominated by a very local circulation of midday winds upslope San Gorgonio Peak, northwest of the site. This is reminiscent of the exaggerated model slope winds near Travis. While this pulse might be a realistic element in the Palm Springs summertime wind behavior, the overall complicated terrain and exaggerated slope winds warrant simulations of horizontal resolution of only a few kilometers in future investigations.

As an initial step in examining the region through higher resolution modeling, we conducted several mesoscale experiments around the Palm Springs area. We chose the days of 19-21 July 1999, which display a moderate-to-strong 10m wind speed in the climatologically preferred direction at Palm Springs, and a well-defined diurnal cycle. Two questions guided the work: Does increasing model horizontal resolution result in substantially better simulation of Palm Springs 10m winds than CaRD10 in these summertime conditions? And, what is the relative importance of differential diabatic heating in the region compared to lateral boundary conditions and advection into the region?

While many factors other than resolution affect the accuracy of a mesoscale model, and there are often limited gains by going to meshes finer than 5 km, the complexity of topography around Palm Springs makes it a strong candidate to show superior results with higher resolution (Mass et al., 2002). Thus, two sets of model data addressed the question of horizontal resolution. The first were higher-resolution runs of the same hydrostatic Regional Spectral Model that created the CaRD10 data, at equivalent horizontal resolutions of 5km and 2.5km in two separate runs. Model setup and physics were unchanged from Kanamitsu and Kanamaru (2007), but atmospheric state and topography were treated at the higher spectral resolutions. The second model used was the Advanced Research WRF (Weather Research and Forecasting, Skamarock et al., 2008) model, version 3.1. WRF was run in its default nonhydrostatic mode, with resolutions of 10, 5, and 2.5 km, using topography based on 30-second USGS data to resolve the features around San Gorgonio Pass.

In every case the outermost WRF domain was forced by 3-hourly NARR data at 32 km resolution (Mesinger et al., 2006). The 10km data presented in the figures was a single domain case, and the 5km data was from a two-way nested domain inside the 10km domain. The 2.5km case, as well as every experiment with modified boundary conditions or physics, was from a two-way nested domain of 2.5 km inside the 10 km domain (Fig. 4.12). (Initial results showed no substantive difference when an additional intermediate-resolution domain of 5 km was used, other than the increased cost of a third domain.) All domains and WRF runs used the same 35 vertical levels, with more levels in the bottom kilometer of the atmosphere, and the lowest two eta levels at $\sigma = 1.0, 0.993$. Since the focus of the exercise was to see if this model captures the site winds in a gross sense when run at a horizontal resolution that resolves the topography, little effort was made to compare physics parameterization options. The boundary layer parameterization was the Yonsei University (YSU) non-local scheme and the Kain-Fritsch cumulus parameterization was used in all domains coarser than 2.5 km. Numerical diffusion was along coordinate surfaces, which may have led to unphysical diffusion along eta levels in the steep topography.

We summarize the resulting 10m winds from both sets of models at the grid point nearest the Palm Springs site in Fig. 4.13. We display hours 25-72 of the 3-day period; the first day served largely for model spin-up and adjustment. From the figures it is clear that while RSM captures correctly the time of highest wind speeds near the observation site, the nature of the flow is inaccurate: modeled flow is southerly and considerably slower than observations, and these problems only increase as model resolution becomes finer. WRF, on the other hand, shows improvement as model resolution is increased. The winds from the 10 km model show top speeds on par with those in the observations, but timing and direction of these winds is wrong. At 5 km resolution, the daily cycle is captured much better, with a south-southeastward acceleration of winds in the afternoon and light and variable winds overnight. Only in the 2.5 km model run, however, does the simulation roughly capture the timing, direction, and magnitude of the observed wind behavior. Although the modeled winds still show some bias in direction, and the modeled transition in the daily cycle of winds is not as abrupt as was observed, WRF at 2.5 km shows vast improvement over the other models and bears a striking resemblance to ground truth.

While these hourly wind summaries give a nominal answer to the question of the potential improvement and amount of horizontal resolution necessary to capture the Palm Springs flow, a fuller picture of the low-level flow near the mountain gap emerges from Figs. 4.14-4.15. The site of the observational station in Palm Springs apparently makes for a very demanding test: several of the models agree with the highest-resolution and best-validated WRF model regarding the important feature of jetlike low-level flow between the two mountain peaks in the domain, leading to consistent and strong westerlies there, but most of the models do not realistically capture the flow at the airport site itself just outside the main jet. Both the WRF 2.5 km and RSM 5 km models show a jet through the pass, capturing the existence of the feature that allows for the wind farm northwest of the airport to be practical in the first place. The WRF 5 km model in particular shows a strong and well-defined jet flowing through San Gorgonio Pass and also shows oscillations between northwest and southwest winds in the outflow after emerging from the pass, in the same manner as the 2.5 km WRF runs. However, none of these models shows the edge of the jet reaching the airport site during the simulation, which explains their inaccuracy in Fig. 4.13. One additional problematic feature of the RSM runs is the opposing southeasterly flow coming up the desert plain and meeting the southern leeward extent of the mountain gap jet in both 2.5 km images. This flow, on the easternmost edge of the plotted domain, rarely appears in any of the WRF runs, but over the course of the two days it tends to flow upslope in morning hours in the RSM. In contrast, a distinctive feature of the 5 km and 2.5 km WRF runs is the meandering of the jet downwind of the mountain gap. Animations (not reproduced here) show that an extended area of winds with speeds of 8 m/s or greater largely flows northeastward out of the gap, but on both days of the model this strong flow turns southeastward at some point between 22:00 and 7:00 local time, emptying into the the low desert. Part of this flow is visible in the bottom-rightmost panel of Fig. 4.15. The winds blowing up the desert plain in the 2.5 km RSM model, combined with the model's tendency to exaggerate diurnal upslope and downslope flows discussed above, likely figure in the discrepancies between all RSM simulations and observations at the demanding validation point of Palm Springs.

Another set of model intercomparisons addresses our second motivating question, regarding the relative importance of domain-boundary forcing versus local differential heating. We conduct two more runs of the WRF model at 2.5 km. The first one is altered so that initial and lateral boundary conditions on the outer domain are quiescent and constant, and thus only insolation and longwave cooling are present to excite the flow. The second experiment uses the WRF 2.5 km model with full initial and lateral boundary conditions, but the land surface is constrained to its diurnal mean temperature and radiative transfer is turned off. Figure 4.18 shows two frames from each of these experiments at the same times of day as in Figs. 4.14-4.15. The experiment with no large-scale forcing but radiative transfer turned on was spun up for four days before the period examined, to compensate for the effects of quiescent initial conditions. Although each experiment shows an area of strong westerly winds blowing through San Gorgonio pass, both in these images and in the full animations (not reproduced here), the jets are not as strong, wide, or extensive as in the full-physics WRF 2.5 km model (Fig. 4.15). The terrain-following flow upstream of the pass at local 16:00 on 20 July in the insolation-driven model (upper-left of Fig. 4.18) is very similar to in the full model, but the outflow downwind is much less extensive. Similarly, at 4:00 the next morning the heating-driven model again agrees with the full one that the outflow will be blowing southeastward toward the low desert, although it is much weaker in the reduced-physics experiment. Analysis of the full model period shows that the flow out of the pass seldom blows northeastward, unlike the fully forced model. The experiment with radiative transfer turned off and full boundary and initial conditions shows a more consistent jet at the eastern end of San Gorgonio Pass, but one that mainly blows W-WSW and does not extend as far downwind as in the fully forced model.

Since the meandering jet downwind of San Gorgonio Pass is a striking characteristic of the WRF 2.5 km model data, which validates the best at our wind site, but is not consistent across all models, we make a simple quantitative summary of its behavior in Fig. 4.17. By comparing the difference in speed over the box in the northern pathway for the jet minus that in the southern pathway, we produce a time series that summarizes the path at every hour: positive when the jet is flowing northward, negative when it is flowing southward toward the low desert, and zero when it is effectively split. The first salient feature of the figure is the regular nature of the jet's changes in direction in the WRF 2.5 km model. The jet flows northward each day from morning (local 8:00-9:00) until approximately 16:00, when it veers southward. In addition to the repetition of this cycle over the three days of the simulation, evidence that the cycle is excited by local insolation comes from the regular daily uptick in the northward flow in the insolation-driven WRF model (second from bottom). Here the northward flow increases around midday and tops out near 20:00, in a peak that is more concentrated and occurs later than the full-physics model's. Although the insolation-driven model's time series is rougher and does not capture all of the cycle found in the WRF 2.5 km model, the boundary-condition-driven model fares worse, showing no resemblance to the full model in this metric. It is the full model dynamics that lead to the WRF 2.5 km results, not a simple combination of the results of discrete sets of processes. Also in the figure, the WRF 5 km model shows the same principal downwind jet behavior as the 2.5

km model. While data is not available to validate the jet meandering over the desert area, this shows how much the data sets from the 5 and 2.5 km resolution runs have in common, while those models where solar-driven effects are explicitly separated show markedly different behavior.

Another summary of the limited-physics experiments is seen in Fig. 4.18, where the hourly wind vectors for each of the experiments as well as the hourly vector sum of winds from the two are compared to the full WRF 2.5 km model at two locations near San Gorgonio. The left-hand column shows winds at the point closest to Palm Spring airport, while the right-hand column is from the point approximately 15km northwest, at 33.94 °N, 116.64 °W and directly in the center of the mountain gap jet. Examining first the hourly vectors corresponding to the observational site, the model forced only by insolation clearly has a greater mean wind speed and is closer to the fully forced model, although the timing of the daily wind acceleration is notably off. Wind speeds of each of the partially forced models do not capture that of the fully forced model, either individually or in sum. For the wind time series at this grid point the vector sum of the model winds resembles those of the insolation-forced model, with notably smaller wind speed and incorrect phase of the acceleration compared to the full model. The situation is largely reversed for the point in the center of the low-level jet, in that the model forced exclusively by initial and boundary conditions has wind speeds closer to those of the full model, while the insolation-only model simulates a much slower wind regime. These patterns generally hold if one examines any point or area in the core of the jet (not shown). Still, the fully forced model has more steady wind and, over these two days, a smoother and more organized daily cycle. Neither of the partially forced models nor the vector sum of their winds matches these aspects.

These mesoscale experiments and analysis could be expanded on in several ways. More runs over a wider variety of summertime conditions would be necessary before drawing any final conclusions about the physics governing the flow. With more data to work with, an explicit accounting of the momentum budget around the pass would probably also be very helpful and allow us to separate the effects of pressure gradients, converging low-level flow, and vertical momentum mixing in the acceleration of wind near the gap. Nonetheless, the present experiments they address our motivating questions. Regarding model resolution, the WRF 2.5 km case does a far superior job of simulating the wind at Palm Springs and resolving sharp circulation features near San Gorgonio

Pass than the CaRD10 data. At the same time, the WRF 5km and RSM 2.5 km data also resolve the mountain gap jet and show many of the same prominent features as the WRF 2.5 km model, implying that for many applications in the area these models would likely suffice.

Regarding the importance of local diabatic versus boundary condition forcing, the experiment realized does not show one set of processes dominating over the other; rather, comparing the low-level flow at separate points indicates that neither one consistently captured more of the fully forced model's behavior than the other. Both differential heating and boundary conditions, and the interactions between the two sets of processes, appear fundamentally important to an accurate simulation.

One additional point does emerge, with implications to wind speed prediction. The WRF model at 5 km and 2.5 km, the RSM model at 2.5 km, and the partially forced WRF experiments all show a low-level convergence zone directly upwind of San Gorgonio Pass, inland and behind the Santa Ana foothills, in the vicinity of Perris, California (Figs. 4.14, 4.15, 4.18). In more detailed hour-by-hour examinations (not shown), the convergence zone becomes pronounced around midday, after an onshore breeze at the coast splits, flows around the foothills, and merges again on the inland side of the mountains. The distance of 30 km separating this area from San Gorgonio Pass implies that sustained surface wind speeds of 5-8 m/s are 1-3 hours upstream of the pass. If further modeling studies confirm the consistency of the convergence zone and a lagged relationship to momentum at the wind site, it could hold promise for short term hours-ahead prediction of power production and ramp events, with lead times slightly shorter than those at which Fort Point shows potential predictability for Travis. It would then be beneficial to examine the historical record for any weather stations in the convergence zone area, or even to look into the use of broader-coverage wind measurement systems such as Doppler lidar, to improve short-term forecasts.

Edwards

The agreement between the simulation and observations is better near Edwards, which we use to describe the regional circulation near Tehachapi Pass. The fewer years and shorter typical hours of observation at Mojave do not allow for many points of observation-model comparison, making Edwards the preferred observational record. Using the same technique of examining each SOM type and wind speed quartile composite hourly mean wind vector series separately, as in Fig. 4.8, we assess the main observed and simulated patterns. At Edwards, for SOM types calculated from fastest and slowest wind speed quartile days, CaRD10-simulated composite mean hourly winds closely replicate observations. The best agreement is for the model vs. observed means on the days in the lightest wind quartile at Edwards (Fig. 4.19). This, and the relative similarity in daily mean cycle among different nodes, justifies an examination of the mean wind fields every four hours on all fastest and slowest wind speed days. Figs. 4.20 and 4.21 show that two CaRD10-simulated patterns of circulation away from the sites are similar between the fastest and slowest composite daily cycles. For instance, the wind in the San Joaquin Valley, west and north of the sites, is very similar in both composite means, even though Mojave, downwind of the valley, sees stronger wind in the fastest quartile days. Among the differences present, we note that southerly flow through the mountains on the southern edge of the desert, especially Cajon Pass south and east of the site, is greater on windy days and also continues over the desert plain, rather than dissipating soon after emerging from the pass as it does on calm days. While the wind over the ocean west of the coast is very similar on both days and is similar as it turns more westerly and bends around the Southern California Bight in the morning hours, by the afternoon the ocean winds south of the sites are noticeably stronger and more westerly on the high wind days. These in turn feed the stronger southerly circulation through Cajon Pass and the surrounding mountains. Perhaps the biggest difference between the two composite mean days is the strength and extent of the southerly and southwesterly circulation across the Mojave desert and through the northern and eastern borders of the pictured domain. No such southerly flow is apparent in the slowest quartile days. The stronger and more prolonged winds near Mojave and Edwards feed into this southerly flow, which is also consistent with the low SLP anomalies over the Nevada desert in the SOM nodes for the warm season. To determine explicitly if the reanalysis SLP patterns are similarly related to observed site winds, we calculate the correlation between the reanalysis SLP in the gridbox centered immediately northeast of the sites, in the Great Basin, and the site winds. Correlation coefficients over all days in the April-September warm season between this quantity and Edwards wind speed anomalies is -0.61, while with Mojave winds the value is -0.46.

4.8 Summary and Discussion

While California has long been a leader in wind power development, an in-depth treatment of the meteorological and climatological aspects of the wind resource has heretofore been lacking. In Part 1 we detailed the annual cycle in the winds at three major wind farm sites, as well as showing there are spectral peaks in wind speed variability at the synoptic and diurnal scales, which we have analyzed in this work. This variability holds implications for matching wind power supply with demand, producing wind energy forecasts, and developing an electrical grid that optimally incorporates intermittent renewable resources.

This analysis has drawn on self-organizing maps (SOM) to classify the weather patterns driving the peak in wind speed variability in the 3-15 day band that was identified in Part 1. While similar meteorological patterns might be determined through principal component or clustering techniques, the SOM is attractive in that its pattern-identifying abilities are intuitively understandable, it avoids restrictions about orthogonality between modes or symmetric positive and negative variability about the mean state, and it yields results that are generally stable with regard to parameter adjustment. Our SOM analysis reveals the most common anomalous SLP and 500 hPa anomaly patterns in the region about our stations, but these patterns are more strongly influential on wind speed at Edwards and cold-season Travis than at Palm Springs. In the warm season the SOM association at Travis weakens considerably, an indication that local circulations dominate. The essential elements of the general SOM-identified patterns are large-scale fluctuations in oceanic SLP and in continental SLP. A large positive oceanic SLP anomaly encourages higher station wind speeds, and a large negative continental SLP anomaly also corresponds to positive wind speed anomalies. The reverse is true for oceanic lows and continental highs. Anomalous 2-day change in 500 hPa height shows anomalous ridging activity over positive SLP anomalies and anomalous troughing over low SLP disturbances, which implies vertical motions that propagate and support the surface features. These patterns are not identical to classical PNA patterns or centers of action such as in Wallace and Gutzler (1981); Leathers and Palecki (1992), but are related enough to begin to illustrate the significant negative cold season correlation with the PNA index in Part 1.

The diagnostics of observations and regional model composites near Mojave, Edwards, and Tehachapi Pass also illustrate circulation consistent with the statistical finding that the SLP in the Great Basin is one larger-scale factor that consistently influences wind speed at these sites. This is true even while the flow in the Mojave desert interacts with other basins through several mountain passes, including the San Joaquin Valley and coastal Los Angeles. Although Great Basin pressure in the warm months depends largely on a thermal low with a strong diurnal component, the area is large enough to be well represented by reanalysis, and it, as well as its contrast to SST and SLP in the Southern California Bight, serves as a powerful starting point for describing the sites' winds from larger-scale meteorology. While observational stations and recording hours over the Mojave desert itself are sparse compared to the San Francisco-Central Valley area, and Iacobellis et al. (2009) do not provide a $\Delta\theta_{850}$ time series immediately applicable to the area, the observational analysis used here for Northern California provides a clear blueprint for observational analysis of such regional flows. Given sufficient observed data it could easily be applied to diagnose the conditions governing dissipation and the specifics of low-level SLP gradients for Mojave, Edwards, and Tehachapi Pass.

Palm Springs has a weaker wind response to synoptic weather type variability than Edwards. The basin wide surface and 500 hPa anomaly patterns in certain subsets of very windy days at Palm Springs resemble the synoptic state in some of the least windy days in Dec-Feb. While this makes it harder to succinctly diagnose Palm Springs wind response to synoptic forcing, it is worth emphasizing that the SLP patterns and gradient over region immediately adjacent to the site, from the Southern California Bight to the Sonoran Desert, influence site winds more consistently than the those over the basin as a whole. The weak response still suggests that even in winter, local circulations whose main forcing mechanisms are not resolved in the reanalysis can be vital to the wind behavior at Palm Springs. This, combined with the trouble the CaRD10 model has in resolving the topography around Palm Springs, point to the need to better understand the interaction between synoptic-scale and finer-scale, orographically influenced processes in determining the flow at Palm Springs. Future investigations could use mesoscale simulations down to several km horizontal resolution to further probe Palm Springs meteorology.

The CaRD10 regional atmospheric reanalysis convincingly explains summertime observations at Travis. The major feature in summertime at Travis is the strong westerly wind that occurs in the afternoon, which is broadly exhibited by observations and replicated by CaRD10. It is excited by the thermally induced San Francisco-Sacramento SLP difference, but is initiated in a propagating packet of westerly wind that emanates from the coast. On mean strong wind days, this flow is observed to persist through the next morning, although CaRD10 has an exaggerated diminution of the wind corresponding to unrealistically strong nighttime downslope winds on the western side of Sacramento Valley. However, we find the modeled flow of accelerated westerly winds beginning midday at the coast and flowing eastward to be a coherent explanation for the observed afternoon wind behavior. This modeled flow is further consistent with the time-lag correlation between buoy winds at the coast and at Travis, and the cooling tendency of the afternoon winds. This leads us to conclude, since weak-wind days generally have much calmer winds in the local AM hours, that the variability of summertime Travis winds depends also on persistence or falloff of winds in the late night and early morning hours. This nighttime falloff was found to be closely related to the strength of the inversion, represented by $\Delta\theta_{850}$, as well as to the near equilibration of temperatures and pressures between coast and valley and, to a lesser extent, downslope winds in the valley. Thus, several specific processes are key to the wind speed variability, including the Sacramento Valley diabatic heating, nearshore SST, along-valley SLP gradient, longwave nighttime cooling, large-scale subsidence, inversion strength, and vertical mixing, in determining the exact strength of the warm-season winds affecting Travis and the SMUD site.

While the sensor network in San Francisco Bay and the Sacramento Valley, including data from air pollution transport measurement campaigns, may be able support purely observational studies focused on this issues, the present results indicate the need for higher-resolution modeling, including Bay surface temperatures and non-hydrostatic effects of the diabatic heating patterns.

Together with the findings in Part 1, this diagnosis of the climatology and variability of California's inland wind energy resource has several implications for future study and applications. For instance, on the smaller scale, the mean diurnal circulations we have analyzed for Edwards and Travis can be used to analyze other sites' suitability for wind conversion facilities in the Mojave Desert and Central Valley. The areas enjoying similar exposure to orographic and meteorological forcing include Tejon and Cajon passes north of Los Angeles, and several ridge lines directly between the Straits of Carquinez and Sacramento. The pressure and temperature cycles found important to determining the strength of these circulations can be compared to factors influencing electricity demand and needs. The CaRD10 data also suggest that comprehensive regional simulations would need to simulate the daily variability at Palm Springs with more finely resolved topography and without unrealistically strong slope winds in the extremely sharp Gorgonio Pass. In the bigger picture, although complex terrain plays a major role in determining what sites are adequate for wind farms, we have also identified larger-scale influences that can be used for examinations of wind power capacity under climate change. The PNA and SST indices found to be significant in Part 1 are a rough approximation of these. SOM analysis of GCM output, combined with specific time series of SLP, low-level temperature, and upper-air fields would likely show even greater fidelity than these rough indices, and could be used directly to estimate site wind behavior corresponding to a simulated climate from relatively low-resolution data.

ACKNOWLEDGEMENTS

The first author completed part of this work while supported by a NASA Earth System Science Fellowship, NASA Grant NNX07AN73H. Additional funding was provided by the NOAA RISA program through the California Applications Program, and by the California Energy Commission through the California Climate Change Center. M. Kanamitsu furnished and provided helpful discussions of CaRD10 data. M. Tyree was invaluable in obtaining METARs data. S. Iacobellis provided data for lower-tropospheric stratification metrics and he and J. Norris contributed details and discussions regarding these data.

Chapter 4, in part, is a reprint with minor modifications of the article "Climatology and meteorological influences on California's wind energy resource. Part 2: Synoptic and diurnal characteristics," to be submitted for publication. The author of the dissertation is the first author and primary researcher, and contributions were also made by the scond author, D. Cayan.

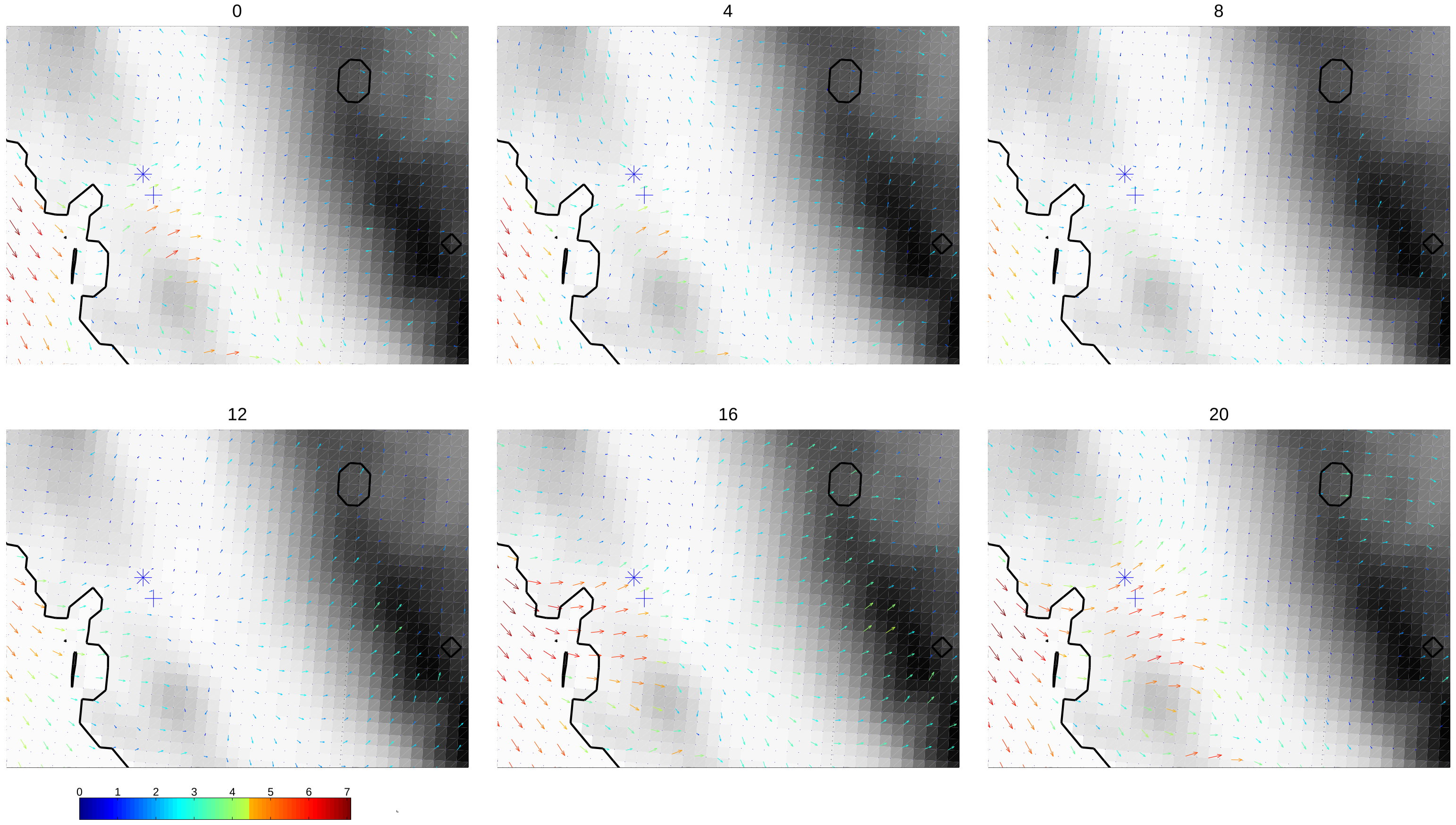

Figure 4.9: Progression of winds at 10 meters at 0:00, 4:00, 8:00, 12:00, 16:00 and 20:00 local time from the CaRD10 downscaling for composite-mean day constructed from days in the windiest quartile at Travis from June-August 1968-1996. Model topography is in grayscale, the extents of oceans and lakes as resolved by the model are indicated by black contours, and wind speeds in m/s are shown by arrow colors. Locations of Travis and SMUD wind energy site are indicated by asterisks and crosses, respectively. Local hour of day is above each panel. For clarity, the wind vectors are omitted for every other zonal and every other meridional point.

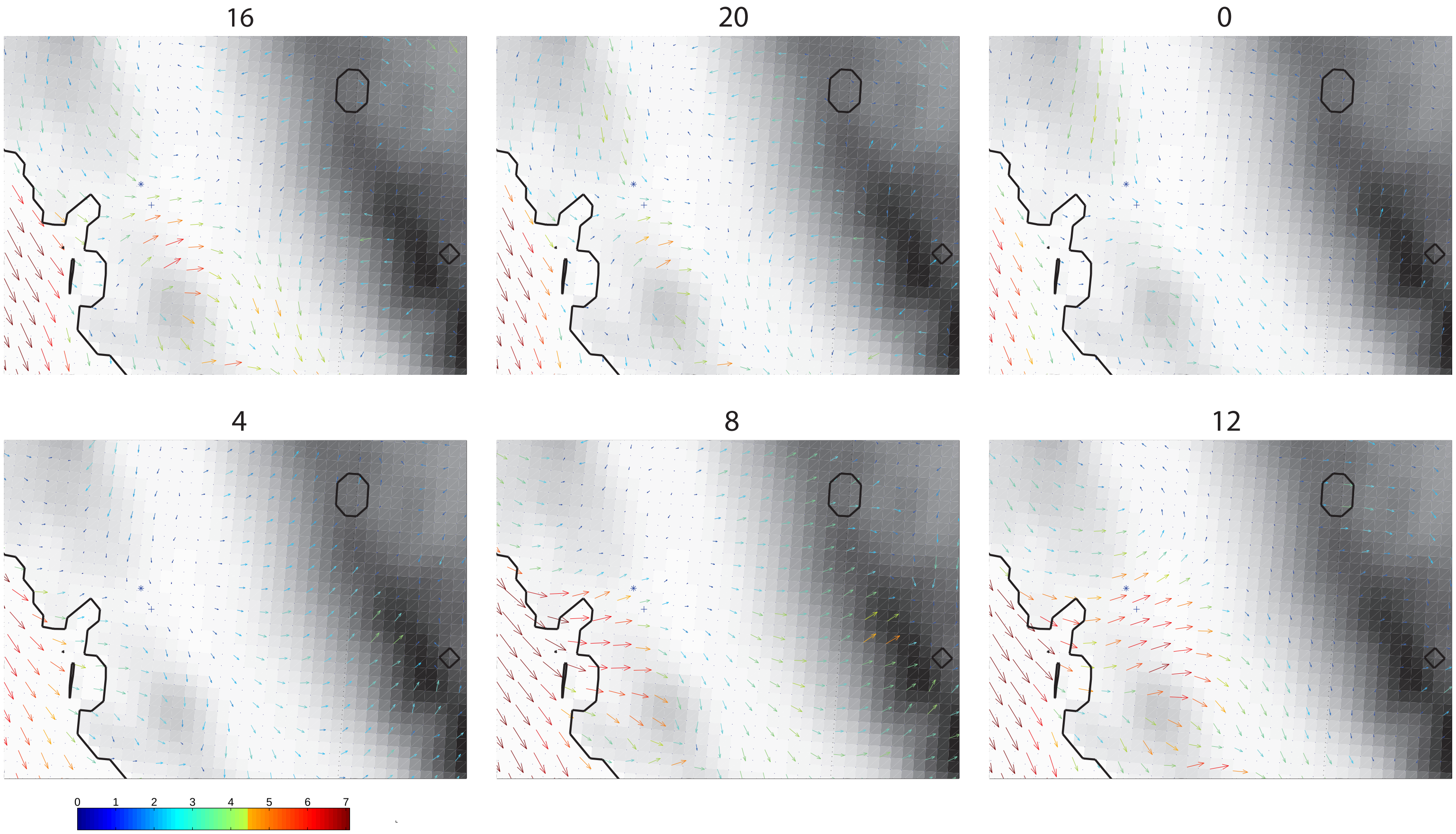

Figure 4.10: As in Fig. 4.9 but the composite mean is from days in the least windy quartile at Travis.

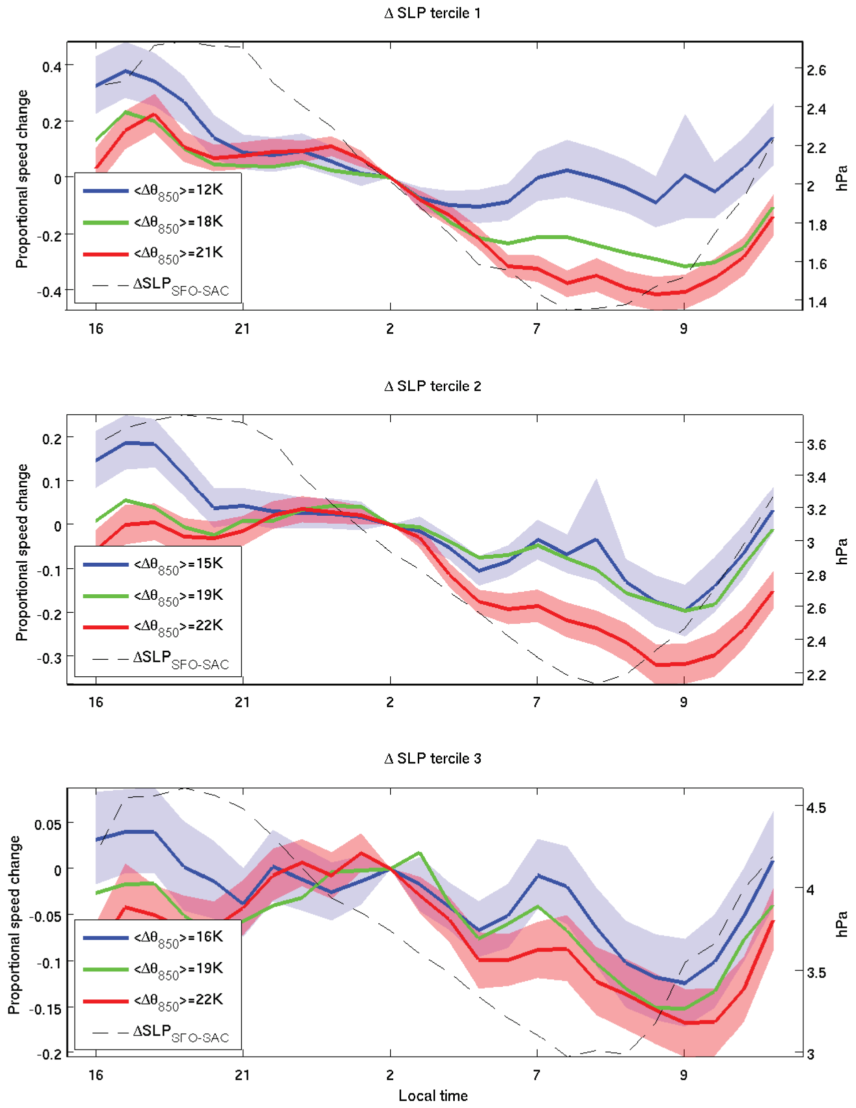

Figure 4.11: Mean proportional change in wind speed from its 10GMT (2:00 local time) value in different regimes of observed summertime mesoscale pressure gradient and $\Delta\theta_{850}$. Each panel displays mean wind speed, expressed as proportional change from its 10 GMT value, within a tercile of the June-September San Francisco-Sacramento daily-mean pressure difference (hourly values are plotted on the right-hand scale). Within each ΔSLP tercile the days are further divided into terciles based on $\Delta\theta_{850}$, using Oakland soundings and local surface data, and these proportional wind speed changes are plotted. Also plotted are the 95% bootstrap confidence intervals for the lowest and highest $\Delta\theta_{850}$ tercile mean hourly values of proportional change in wind speed.

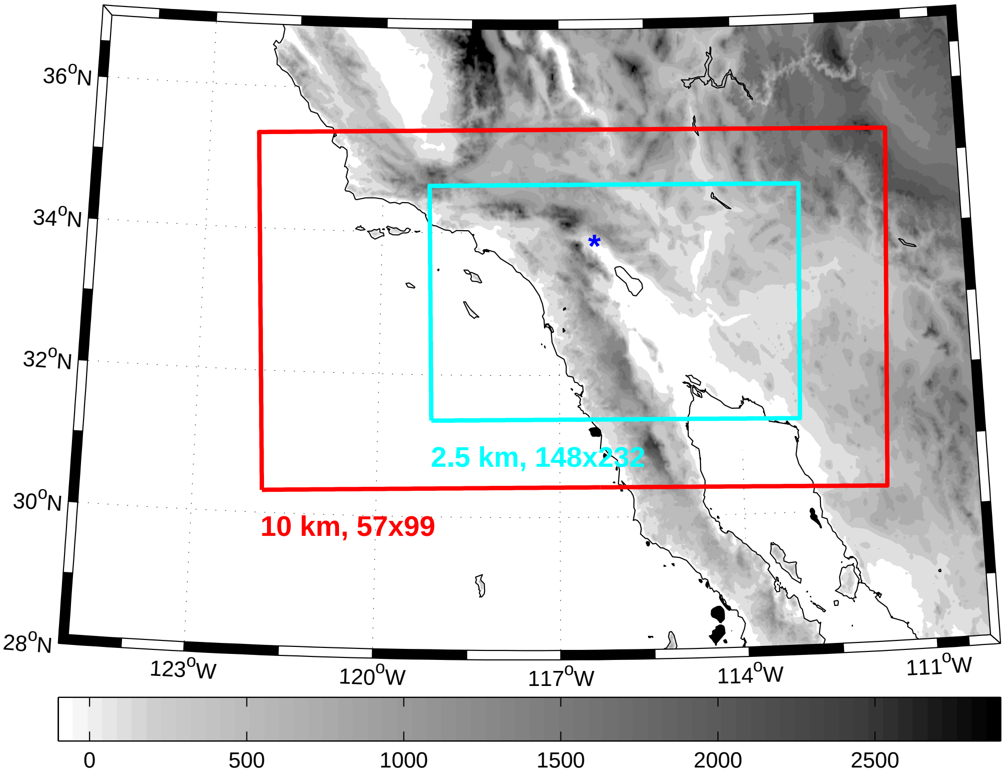

Figure 4.12: The area around southern California, with shaded elevation in meters, and the domains used for the WRF 2.5 km simulations. The 10 km domain for the 5 and 10 km resolution scenarios was considerably larger, equivalent to the CaRD10 domain in Kanamitsu and Kanamaru (2007). The Palm Springs site is marked with a blue asterisk.

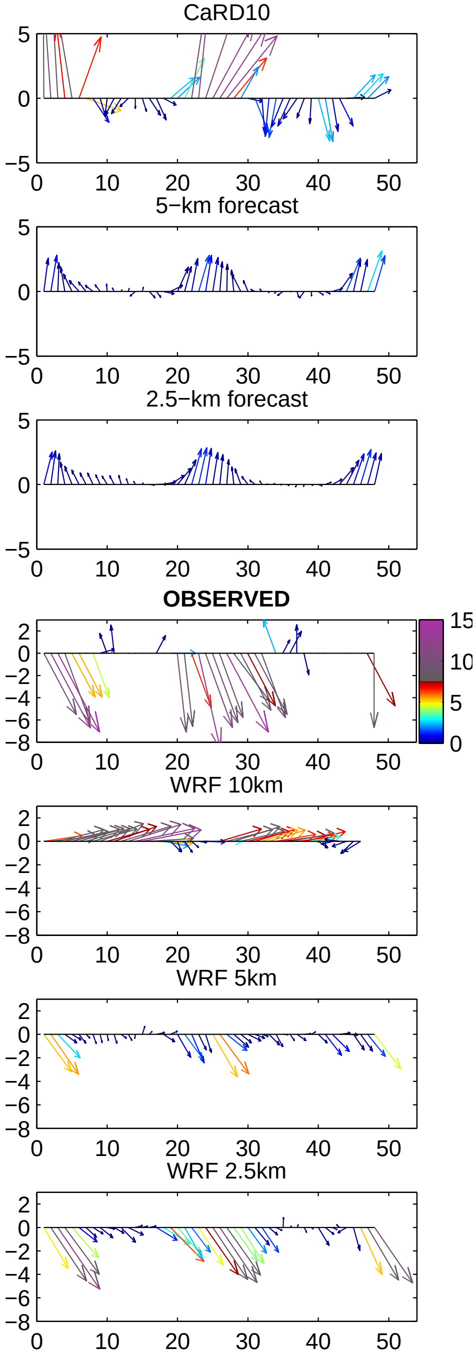

Figure 4.13: Hourly wind vectors as observed at Palm Springs (center), as well as from the nearest grid boxes in three different resolutions of RSM (top rows) and WRF simulations (bottom rows), covering 20-21 July 1999, GMT. The color key indicating wind speed in m/s is the same for every panel. Hours with no vector in the observations have zero wind speed.

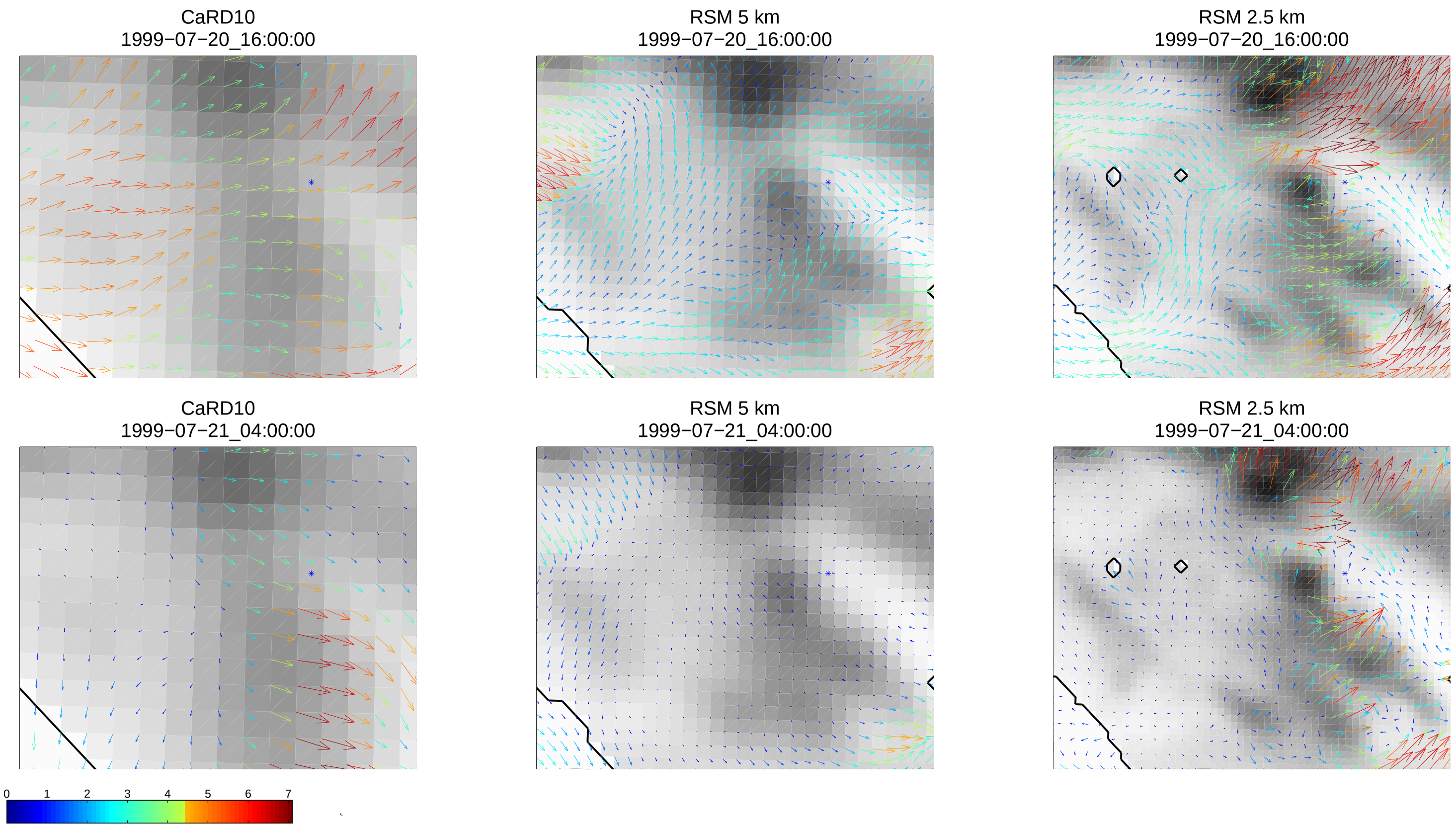

Figure 4.14: 10m winds in each of the three RSM model runs, at one afternoon and one early morning hour. Local solar time and model resolution is noted above each panel, and Palm Springs airport is a blue asterisk. For clarity, the wind vectors are omitted for every other zonal and every other meridional point in the 2.5 km panels.

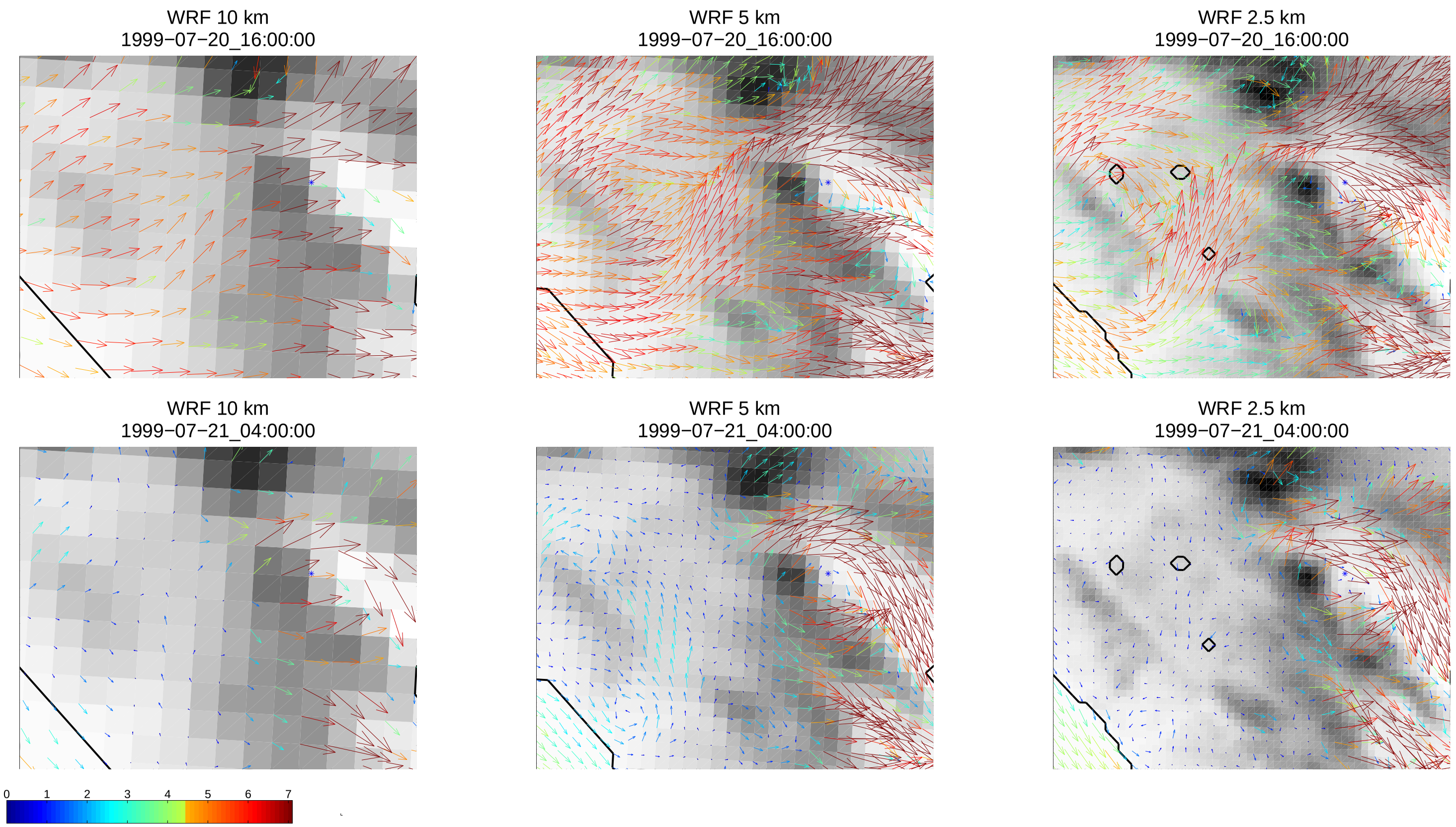

WRF 10 km
1999−07−20_16:00:00

WRF 5 km
1999−07−20_16:00:00

WRF 2.5 km
1999−07−20_16:00:00

WRF 10 km
1999−07−21_04:00:00

WRF 5 km
1999−07−21_04:00:00

WRF 2.5 km
1999−07−21_04:00:00

Figure 4.15: As in Fig. 4.14, but for three different resolution runs of the WRF model.

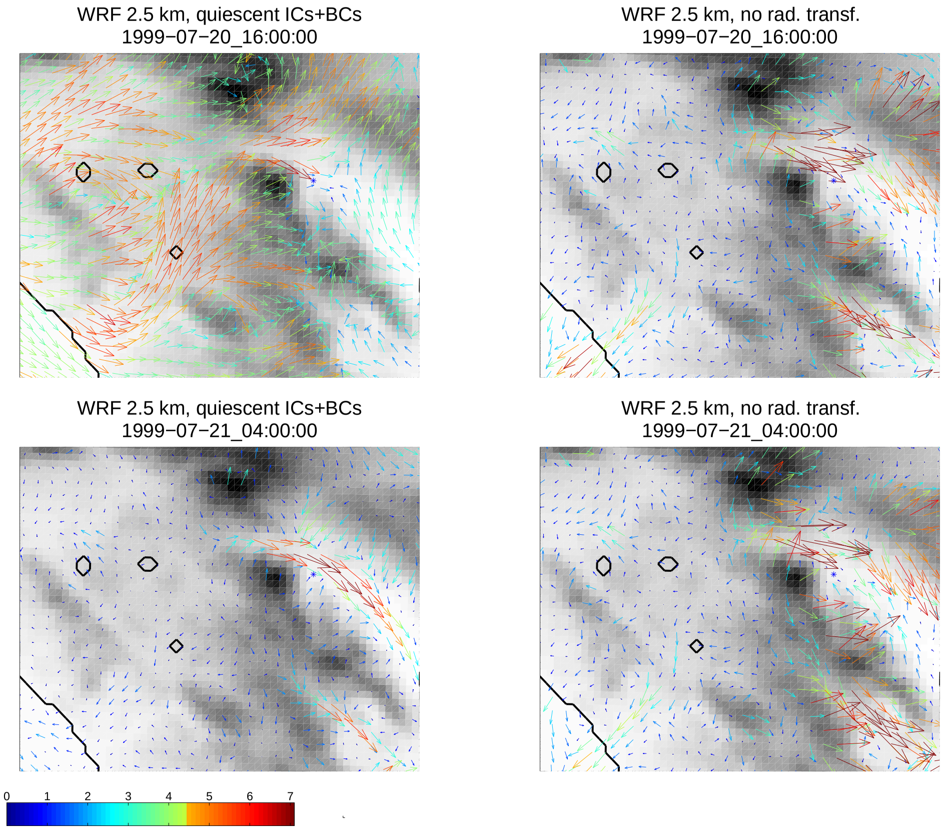

Figure 4.16: As in Fig. 4.14, but for two different experiments with the WRF model at 2.5 km resolution. The left column shows results when initial and boundary conditions were quiescent and constant, and solar heating and longwave cooling excited the flow. The second column shows results when radiative transfer was turned off, but the surface was fixed at its diurnal mean temperature and full initial and boundary conditions were used. For clarity, the wind vectors are omitted for every other zonal and every other meridional point.

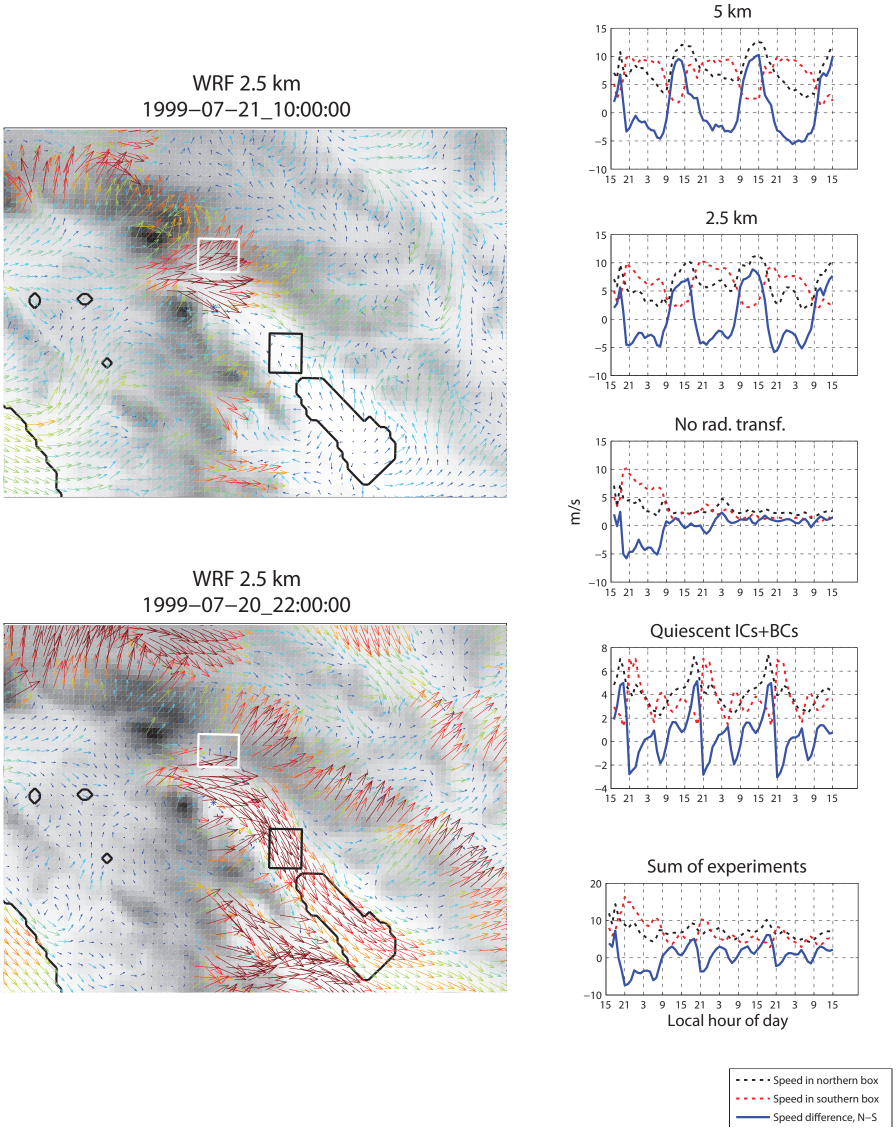

Figure 4.17: At left are two 10m wind fields at different times from the 2.5 km WRF model, illustrating the northward and southward states of the low-level jet downwind of San Gorgonio Pass. The thick black line to the lower left is the coast and further to the east is the Salton Sea. Also shown are the two rectangular boxes, with side lengths from 15-20 km, used to calculate the jet direction time series. At right is the jet direction time series for five different mesoscale model runs, with the thick blue line indicating the average speed in the northern box minus the average speed in the southern box at every hour. All 72 hours of the time series are plotted to show the repeated signals better, although the first 24 were intended to be spinup. The x axis shows local time of day over the three days of simulation, with the last 48 hours corresponding to those plotted in Fig. 4.13

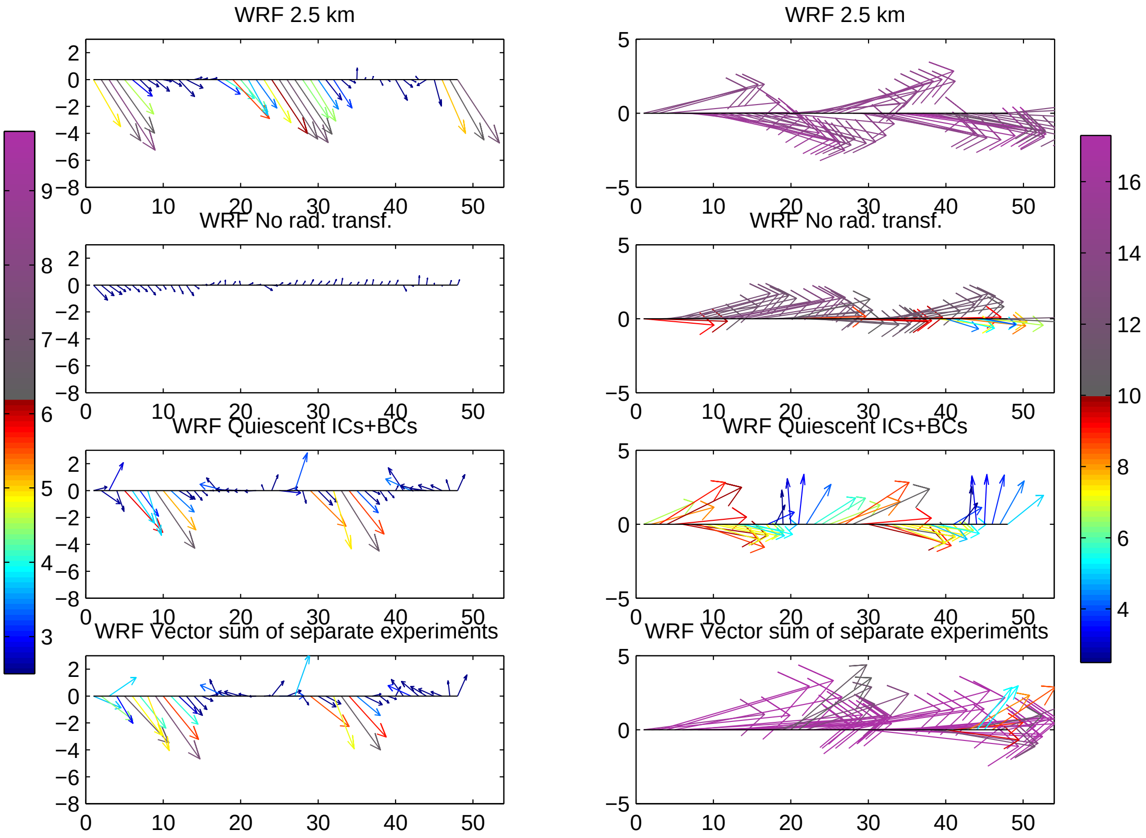

Figure 4.18: Hourly 10m wind vectors for the fully forced WRF model and each of the partially forced WRF experimental runs at 2.5 km, as well as the vector sum of winds from the two experiments. The left column is from the grid point closest to the Palm Springs airport, the same as for Fig. 4.13, while the right column is for a point approximately 17 km away, in the center of the inter-mountain low-level jet.

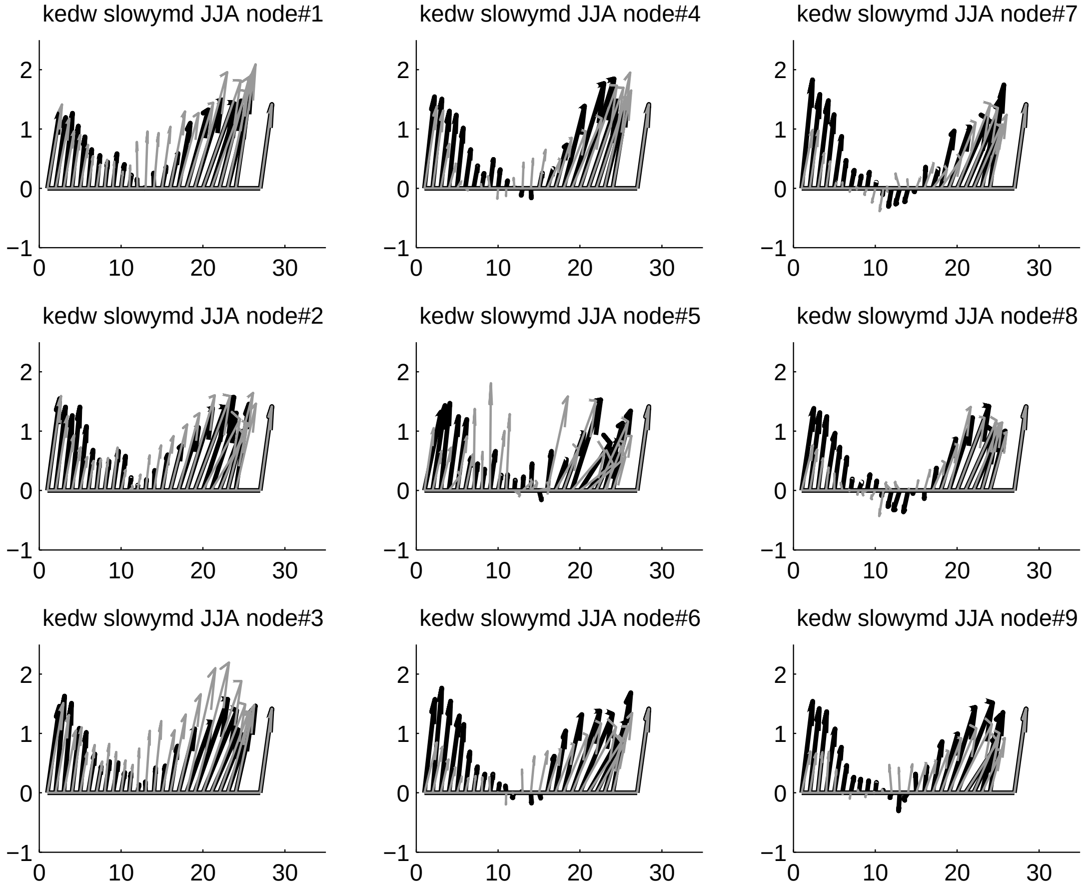

Figure 4.19: As in Fig. 4.8, but for days in the slowest mean wind-speed anomaly quartile at Edwards.

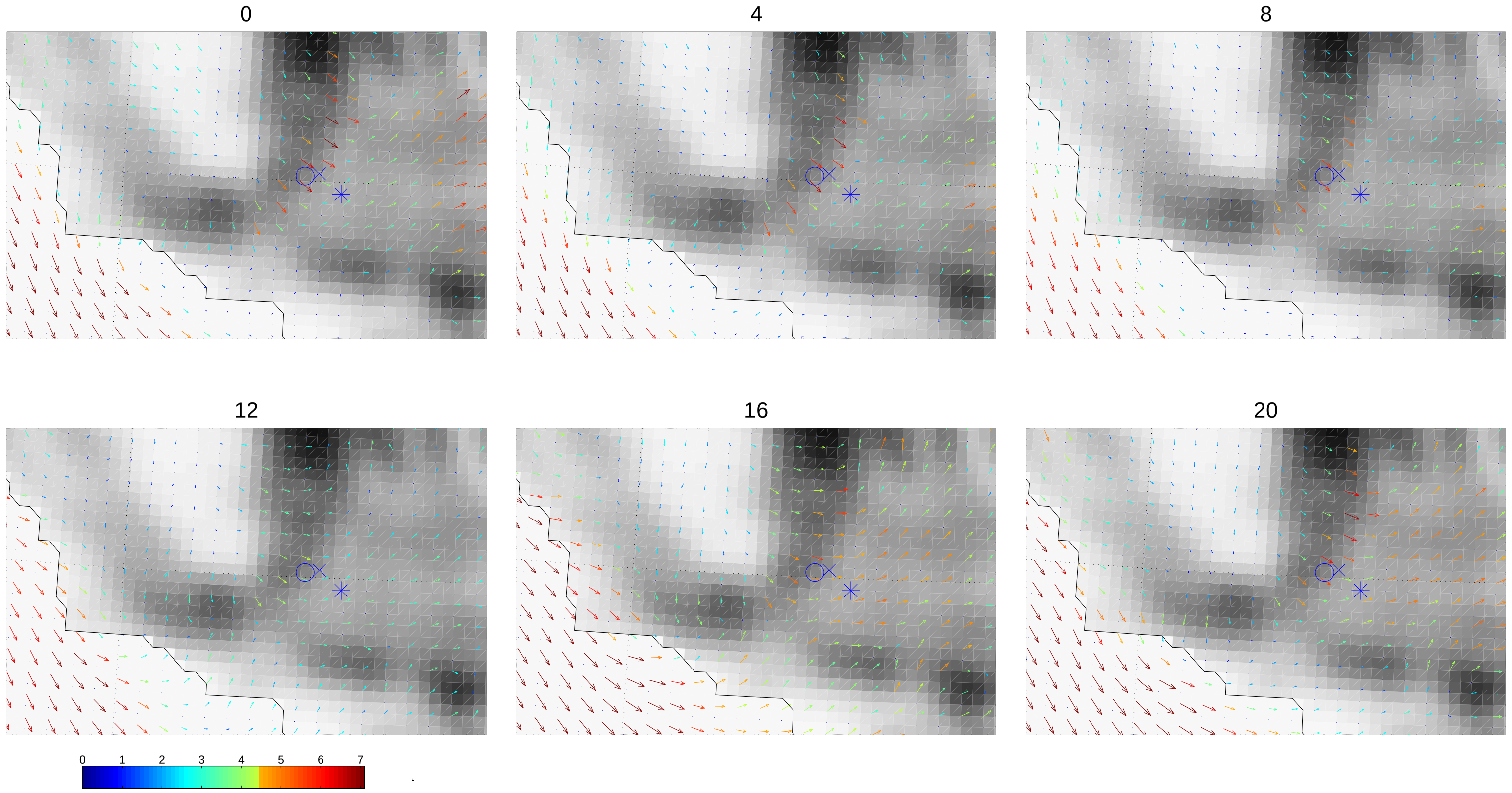

Figure 4.20: As in Fig. 4.9 but the composite mean is from days in the windiest quartile at Edwards. Edwards, Mojave, Tehachapi, and Palm Springs are shown by asterisks, x's, circles, and diamonds, respectively.

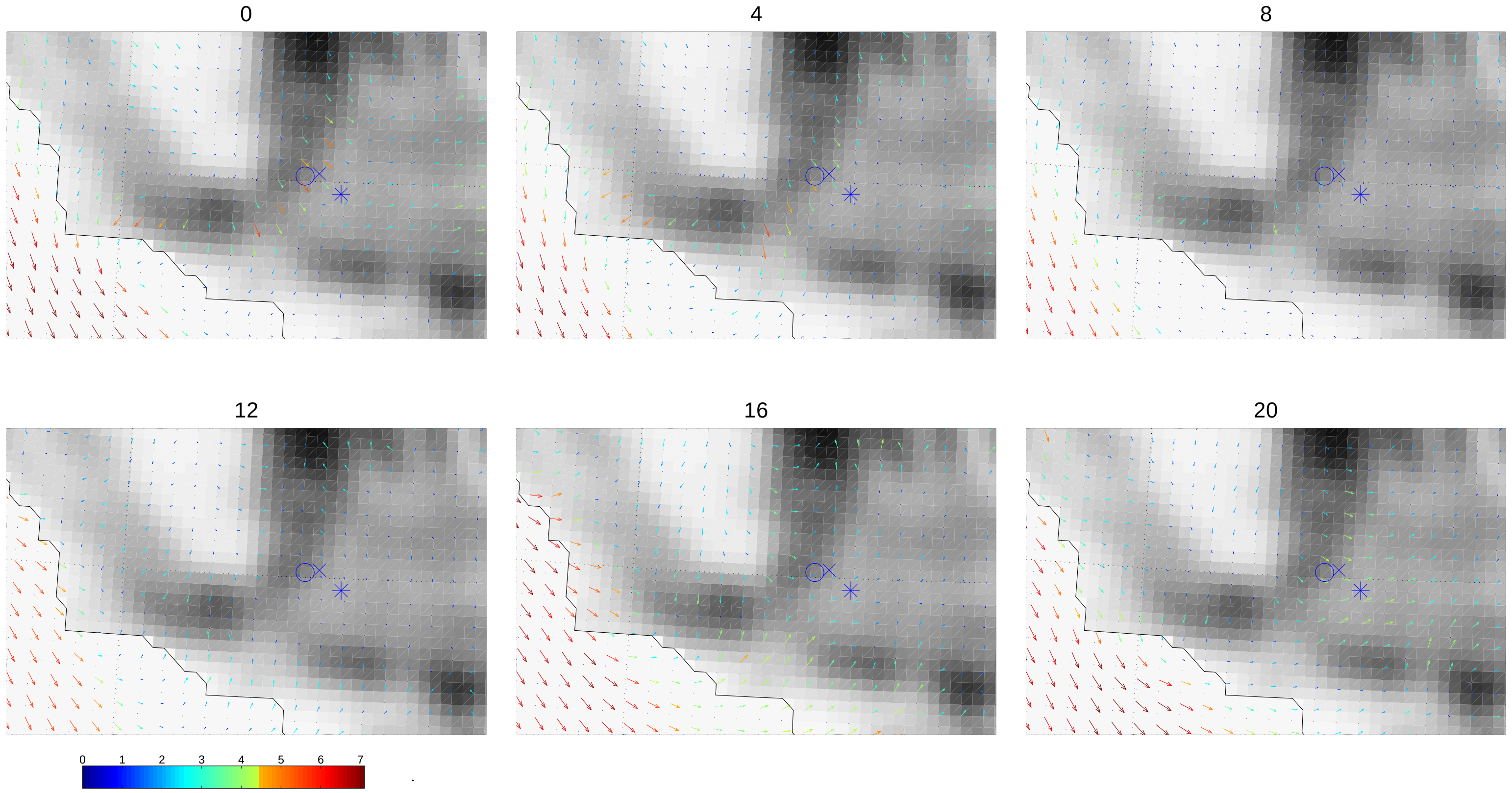

Figure 4.21: As in Fig. 4.9 but the composite mean is from days in the least windy quartile at Edwards. Edwards, Mojave, Tehachapi, and Palm Springs are shown by asterisks, x's, circles, and diamonds, respectively.

Chapter 5

Formulation of a statistical downscaling model for California site winds, with an application to 21st century climate scenarios

5.1 Abstract

The present study describes a statistical downscaling scheme for relating GCM output to site winds, covering the model's formulation, validation, and application to 21st century climate. The multilinear regression model integrates weather type information as well as the results of previous observational analysis of low-level winds near the California wind farms at Solano County, Tehachapi Pass, and San Gorgonio Pass, in order to reproduce wind speeds with a fidelity that the direct output of GCMs or global reanalysis do not capture. Validation by comparing downscaled reanalysis data to an independent period of observed wind speeds in the 20th century shows that the model has skill for both monthly and daily data. It also has correlation coefficients with observed speeds that are comparable to those of several higher-resolution mesoscale models. After applying it to the output of three coupled climate models for 20th and 21st data under IPCC emissions scenario A1b, it is seen that some monthly and seasonal mean wind speed changes are implied of up to 0.6 m/s in the summertime. However, the discrepancies between climate models prevent any definitive consensus, and other seasons see wind speed changes of smaller magnitudes. The model facilitates analysis and physical

interpretation of the disparate processes affecting wind speed at each site. Analysis of the principal summertime inter-model discrepancies reveals an important pattern: while in one model the area of major western North American surface heating coincides with a decrease in SLP, consistent with direct local adjustment response to the heating, other models have compensating processes that lead to increased continental SLP and opposite effects on downscaled site winds. Other seasons also exhibit differences in distribution of the SLP and temperature changes that are milder, but do affect site wind speeds. The importance of the coupled models' representation of these regional patterns and the value of the downscaling scheme as an overview for greenhouse gas-forced climate simulations is discussed.

5.2 Introduction

While the effects of climate change are often discussed in terms of impacts to ecosystems or natural resources traditionally used by humans, there is also a need to examine the effects on the renewable energy resources that are only recently being consumed on large scales. Solar and wind energy production clearly require appropriate atmospheric conditions, and more specifically require that sites currently displaying those conditions can be relied on to do so in the near future. However, the means to evaluate this are not always straightforward. For wind power, areas of sufficiently energetic low-level flow are often not well simulated in the general circulation models (GCM) used to evaluate greenhouse gas-forced climate scenarios, and for areas such as California, the sub-grid scale topography is also key to the flow near wind farms. At the same time, dynamically downscaling a GCM can be computationally and logistically demanding, and by extension impractical for application to multiple emissions scenarios or multiple GCMs. This points to the need for a downscaling technique for orographically forced sites that relates large-scale conditions in a GCM to site wind speeds, without the computational expense incurred by dynamical downscaling. The present study applies previous observational analysis results to formulate, assess, and apply a statistical downscaling scheme that inexpensively estimates the effects of climate change on three prominent wind development areas in California.

The question of climate change's effect on wind power is not a new one, and has been addressed in various ways. Breslow and Sailor (2002) analyzed changes in wind energy in the 10m wind speed field of 2 GCMs, while Sailor et al. (2008) used treestructured regression to downscale GCM data for several sites in the Pacific Northwest, and Sailor et al. (2000) employed neural-network downscaling of GCMs for three wind speed sites. Regarding northern Europe, including Scandinavia, Pryor et al. (2005a) used a regional atmospheric model to dynamically downscale climate change scenarios. While the downscaling was found to have skill over the historical run, it produced conflicting results with different 21^{st} century forcings, leading to an overall high uncertainty in wind speed changes. Pryor et al. (2005b) used a statistical scheme for stations that showed a Weibull wind speed distribution in observations. Their results detected more wind speed changes in the period 2081-2100 than 2046-2065, suggesting that for other regions as well, end-of-century conditions hold more promise to indicate first-order wind speed changes due to climate change. Najac et al. (2009) combined observational analysis of numerous wind stations over France with weather typing and analog downscaling methods to assess the impacts of climate change in 14 different greenhouse gas-forced models, finding regional and seasonal tendencies in 21^{st} century behavior for both the centers and tails of wind speed distributions. In contrast, analysis of past wind speed changes can also inform the question of wind power under climate change. Pryor et al. (2009) analyzed a combination of wind observations, regional, and global models, and found discrepancies between data sets regarding long-term trends in the continental US. Pryor and Barthelmie (2003) examined the low-level flow over the Baltic from global reanalysis data and found increases in wind speed, especially due to stronger wind events driven by synoptic systems.

Prior downscaling studies for predictands other than wind speed are also highly relevant to ours. Temperature is a societally important field with sub-grid-scale variability, but generally shows more spatial coherence than wind. This is consistent with the large amount of variance explained in multilinear regression models such as Wigley et al. (1990) and Solman and Nuñez (1999). These models are constructed in a more automated process than the one we develop, in that each station is downscaled based on a small selection of possible predictors, such as the large-scale temperature and coincident and nearby pressure fields. Other, more, complicated methods can also be used, and often have been for downscaling precipitation. While it is another field of great interest, precipitation is in may ways more complicated to downscale than temperature and perhaps wind speed as well, in that it is vary spatially inhomogeneous, tends to have a very long-tailed probability density function, and often depends on highly nonlinear, small-scale processes (atmospheric convection). The variety of approaches to statistically downscaling precipitation include linear and nonlinear regression as well as weather typing and stochastic methods (Wilby and Wigley, 1997).

This study makes use of observed linear relationships between site winds and large-scale atmospheric conditions to downscale several global climate models. It is most similar to the work of Najac et al. (2009), with the important difference that it integrates atmospheric fields and weather type time series into a multivariate regression model, and eschews analog methods completely. The methods used to formulate the present model could also be applied to other settings or other data sets down to intermediate resolution (ie, regional reanalysis), while potential applications include historical reconstructions of wind resources or operational large-scale overviews of wind power availability on daily to seasonal timescales. After verification and error analysis of the downscaling model, we apply it to downscale several coupled climate models under greenhouse gas forcing. We analyze the projected 21st century wind changes in each model in terms of the specific physical mechanisms responsible for the changes, as well as the important differences they reveal between models.

5.3 Setting and data sources

The downscaling model relates conditions resolved by the NCEP reanalysis (Kalnay et al., 1996) to interannual anomalies in observed winds at Travis Air Force Base, Edwards Air Force Base, and Palm Springs Airport. These in situ wind data come from archived METARs reports and, as shown in Mansbach and Cayan (2010a) (hereinafter MC1), after being processed with a simple homogenization procedure, they are found to be representative of winds at the Californian wind farms at Solano County, Tehachapi Pass, and San Gorgonio Pass, respectively. After the model is trained and validated, it is straightforward to replace NCEP global reanalysis with publicly available output from GCMs under historical and climate-change runs. Thus, although our understanding of the processes affecting the site winds draws on other model and in situ data sets described in MC1 and in Mansbach and Cayan (2010b) (hereinafter MC2), the time series used to train the model are not drawn from these in situ and higher-resolution data sets because they have no 21^{st} century analogs.

The 21^{st} century climate data we consider correspond to specific greenhouse gas emissions scenarios laid out in the Intergovernmental Panel on Climate Change (IPCC)

Special Report on Emissions Scenarios (IPCC, 2000) under storyline A1b. This describes a 21^{st} century world of economic expansion, decelerated population growth, international cooperation, and a balance between renewable and fossil-fuel based energy sources. From multimodel mean data, this scenario has a predicted level of21^{st} century global-mean surface warming and sea level rise in the higher range of the scenarios evaluated, but is not the highest (Solomon et al., 2008). The A1b GCM output emissions scenario analyzed were from those submitted to the Climate Model Intercomparison Project Phase 3 in support of the fourth IPCC Assessment Report (Solomon et al., 2008). Although over a dozen sets of model output were submitted, this study uses the results from downscaling three of those models, in order to give sufficient focus to the regional patterns and physical processes affecting site winds. The models are GFDL 2.1 (Delworth et al., 2006), ECHAM5 as run by the Max Planck Institute (Roeckner et al., 2003; Marsland et al., 2003), and CNRM (Guérémy et al., 2005). Data was obtained through the Lawrence Livermore National Laboratory portal.

5.4 Model formulation and verification

5.4.1 Atmospheric predictors

The downscaling scheme is a a multivariate linear regression model trained with NCEP Reanalysis data. It is impractical to use model-resolved surface wind speeds as directly representative of the sites because of the low resolution of the model, the complex physics affecting boundary-layer winds, and the complex topography of the region. For instance, as shown in MC1, the Palm Springs and Edwards wind sites in southern California (representative of winds at San Gorgonio and Tehachapi Pass wind farms, respectively) correspond to the same grid box in the reanalysis, yet their daily wind speed correlation with one another is not above 0.45 for any time of year. To construct the model, we assemble a large number of possible predictors and use a selection routine and training data to assemble the optimal model subset from these and assign the regression coefficients for each predictor. We then assess the skill of the model on an independent verification data set, adjust selection parameters, and re-train and validate until settling on the final model. This processes is illustrated schematically in Fig. 5.1.

The general aim of the model is to approximate as best is possible a site's daily

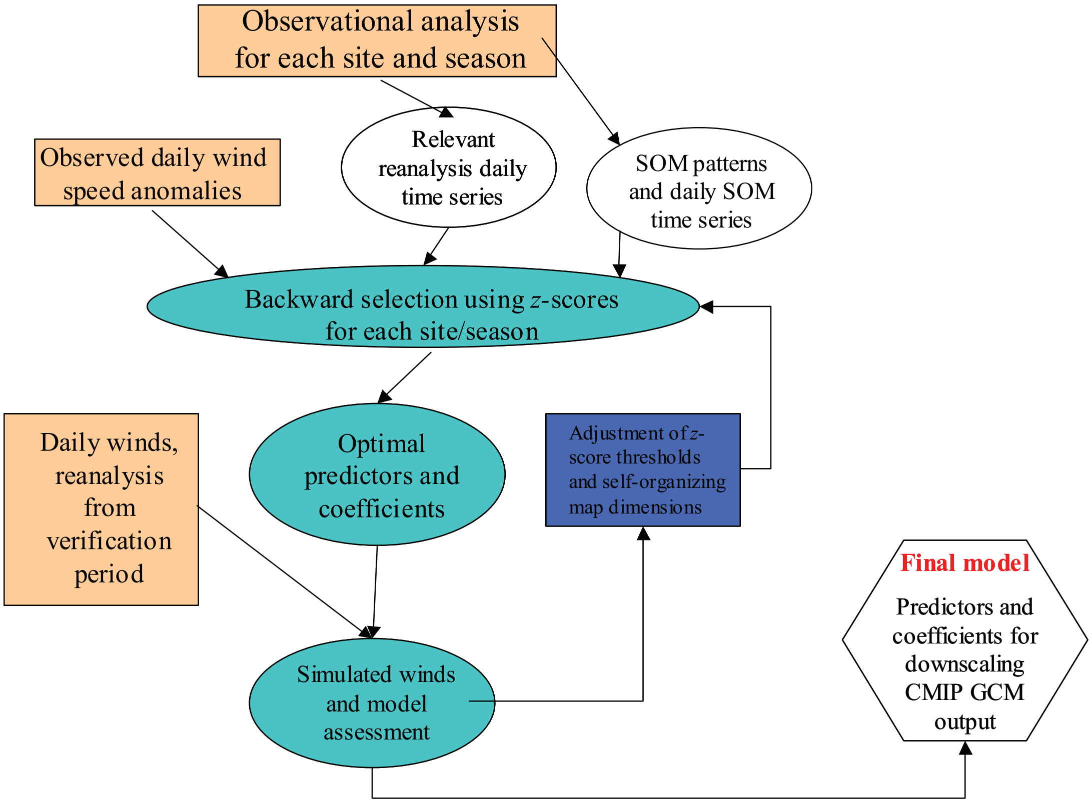

Figure 5.1: Schematic representation of the downscaling model formulation and selection process.

wind speed time series, $Y(t)$, with a least-sum-of-squares estimate, $\hat{Y}(t)$. The basic form of the model is

$$\hat{Y}(t) = \beta_0 + \sum_{i=1}^{N} X_i(t)\beta_i \tag{5.1}$$

, where each predictor X_i is a time series from reanalysis data. The optimal time series used are chosen by an objective backward selection process from a large pool of possible predictors, and the number of total predictors, N, is determined in the training and verification phases. Because of the different seasonal patterns of variability at each site, as described in MC1 and MC2, we select and verify a separate set of X_i and β_i for each site and each of the seasons Dec-Feb, Mar-May, Jun-Aug, and Sep-Nov.

The first step is to summarize the basin-wide synoptic state into several time series X_i. This is accomplished with self-organizing maps (Kohonen, 2001). For each day used in training the model we examine the anomalies of SLP and 500 hPa zonal and meridional wind over the region. For the southern California sites, the domain's extents are 18.75 °- 51.25 °N, 93.75 °- 151.25 °W. For Travis, they are 23.75 °- 41.25 °N, 93.75 °- 151.25 °W. Self-organizing maps are an unsupervised learning and pattern classification technique that identifies the common, distinct patterns from a large number of weather states (Kohonen, 2001). SOM patterns describe the major modes of variability in the region, without the requirements of orthogonality imposed by EOFs or the high sensitivity to parameter adjustment found in k-means clustering. As shown in MC2, for instance, an SOM of the northeast Pacific and western United States finds that the principal patterns found, called nodes, describe a center of action in anomalous SLP over the ocean and a separate one over the continent, with support from 500 hPa ridging and troughing anomalies. These SLP patterns can vary separately, leading to conditions with broad areas of high or low pressure, or of opposing patterns over the ocean as over the continent. (In referring to the figures in MC2 to illustrate the SOMs used internally in our model, the 500 hPa anomaly contours generally describe streamlines of the anomalous 500 hPa flow.) At the same time, it can also be instructive to examine the SOM patterns found in only certain subsets of a given season. Our tests have indicated that for some stations and seasons, the model has greater downscaling skill when it uses the SOM patterns based on only the windiest and least windy quartile of days in the training period at that site, such as those seen in MC2.

To integrate SOM-defined patterns into the model, we include the time series of the SOM quantitative error as predictors. The quantitative error for each day and SOM node is the magnitude of the vector difference between that day's observed SLP-500 hPa anomaly map and the pre-defined SOM node, after both are concatenated into vectors (Kohonen, 2001). Thus, a low quantitative error indicates a high similarity to the given node, and the β_i coefficient for the time series corresponding to a pattern that tends to excite a positive site wind speed response will be more negative than the β_i coefficient for a pattern that tends to excite a negative wind speed response.

The n_{syn} synoptic-summary time series from SOM analysis are automatically included in the model and not subject to the backward selection routine. In numerous tests this has greater skill in downscaling as it allows the subsequent backward selection process to choose X_i series that correspond to specific, more local conditions, since the general background synoptic state is already captured by the SOM series. Thus, after taking the synoptic-summary time series into account, the model becomes

$$\hat{Y}(t) = \beta_0 + \sum_{i=1}^{n_{syn}} X_i(t)\beta_i + \sum_{i=n_{syn}+1}^{N} X_i(t)\beta_i \tag{5.2}$$

The value of n_{syn} is varied in the training process along with the grid dimensions of the SOM, and depends on whether the synoptic summary time series are based on a single SOM from all days in the season, or on two separate SOMs formed from the windiest and least windy days at the site and season in question. One further aspect of the SOM series integration is varied. The 2-dimensional SOMs used in this and previous studies intend to map the set of all synoptic states most nearly to a plane, with each of the m×n nodes demarcating a point on that plane that represents a large number of states from the training data set. If the nodes were perfectly contained on a plane, then only three time series of quantitative error would be sufficient to map any subsequent point to its best-matching location, and the other series could be neglected with no loss of information. Although in practice that is not observed, most SOMs used here, like those shown in MC2, do have smooth transitions between adjacent nodes, indicating they are close to being mapped to a plane. Thus, including only the series of quantitative errors corresponding to the corner nodes of each SOM results in fewer X_i series and less risk of overtraining the model, while providing nearly as much information and skill in reproducing the training data.

The time series that are then made available to the model are built on the results of MC1 and MC2 regarding what physical fields are observed to relate to site wind speeds. Complete lists of the fields from which the backward selection model chooses are in Tables 5.1-5.2, and we here describe reasons for making each group of fields available to the model.

It is intuitive to use reanalysis-simulated surface wind speed in the grid box covering each site as a possible predictor. While issues of resolution, complex topography, and model physics mean that it is not always an accurate predictor of observed wind speed, it nonetheless often shows a significant and positive correlation to many observed site-season wind speed series.

Winds at 700 hPa are generally above the heights of the orography in the region, and may be expected to be better simulated by the GCM. The accurately simulated 700 hPa winds may then be thought of as mixing downward to affect the site wind speeds. The observed 10 m winds may be most related to total momentum (700 hPa wind speeds)

Table 5.1: List of the time series that the backward selection model chose from to to be included, along with the synoptic type information, for the Travis downscaling model. The time series that were chosen are indicated by a superscript that denotes the season of the year (DJF=1, SON=4) and the sign of the corresponding β_i least-sum-of-squares coefficient in that season. If the the backward selection model retained the 1- or 2-day lagged version of the series, that is also denoted in the superscript by ‘lagX’, where X is the number of days by which it is lagged.

Ncal Zonal SLP gradient at 1 boxes^{1+}
NCal Meridional SLP gradient at 1 boxes
Ncal Zonal SLP gradient at 2 boxes
NCal Meridional SLP gradient at 2 boxes$^{2-,3-,4-}$
Ncal Zonal SLP gradient at 3 boxes
NCal Meridional SLP gradient at 3 boxes
Ncal Zonal SLP gradient at 4 boxes^{2-}
NCal Meridional SLP gradient at 4 boxes
Ncal Zonal SLP gradient at 5 boxes
NCal Meridional SLP gradient at 5 boxes
SLP at 40, 110 (incl Ely, NV)$^{3-}$
Site 200 mb U wind (Ncal site:37.5, 122.5)
Site 200 mb V wind (Ncal site:37.5, 122.5)
Site 700 mb U wind (Ncal site:37.5, 122.5)$^{(1lag1+),(3lag1-)}$
Site 700 mb V wind (Ncal site:37.5, 122.5)$^{1-,(2lag1-),4-}$
Site 700 mb wind speed (Ncal site:37.5, 122.5)
Site 200 mb wind speed (Ncal site:37.5, 122.5)
SLP at 27.5, -112.5 - Sonora/Sea Cortez
SLP 55 -122.5 (BC)
mean SLP in 7.5degx7.5 deg centered over KSUU
SLP 40 122.5 (KSUU)$^{1-,3+}$
LTS (850-sfc) at 37.5 122.5
Site (KSUU) - offshore temp$^{(2lag1+),(3lag1+),(4lag2+)}$
SST at 37.14, 125.6
SW wind at 925 mb West of SF Bay

Table 5.2: List of the time series that the backward selection model chose from to to be included, along with the synoptic type information, for the Edwards and Travis downscaling models. The time series that were chosen are indicated by a superscript that denotes site the series was chosen for (Edwards/Palm Springs), the season of the year (DJF=1, SON=4) and the sign of the corresponding β_i least-sum-of-squares coefficient in that season. If the the backward selection model retained the 1- or 2-day lagged version of the series, that is also denoted in the superscript by 'lagX', where X is the number of days by which it is lagged.

Zonal SLP gradient at1boxes$^{\text{E1-,E2-,E4-,P2-,P3-,P4-}}$
Meridional SLP gradient at1boxes$^{\text{E1-,P3-}}$
Zonal SLP gradient at2boxes
Meridional SLP gradient at2boxes
Zonal SLP gradient at3boxes
Meridional SLP gradient at3boxes
Zonal SLP gradient at4boxes
Meridional SLP gradient at4boxes
Zonal SLP gradient at5boxes
Meridional SLP gradient at5boxes
U 700 at 35N, 117.5W$^{\text{E2+,E3+,E4+}}$
V 700 at 35N, 117.5W
U 200 at 35N, 117.5W
V 200 at 35N, 117.5W
SPD 700 at 35N, 117.5W$^{\text{E1+}}$
SPD 200 at 35N, 117.5W
SPD sfc at 35N, 117.5W$^{\text{E1+,E2+,(E2lag1-),E4+,P1+,P4+}}$
Southern California site SLP (35N 117.5w)$^{\text{P1+}}$
SLP 1 grid box south and east of southern California site (ie, 32.5N, 115W)$^{\text{E3+,P3-}}$
Southern California site temperature
Temperature 1 SE of Southern California site (32.5N, 115W)
SLP SSE of Southern California (27.5 N 112.5W)
SLP NNW of Southern California (55N -112.5W)
SLP at 35 N 115 W (1 E of Southern California site)$^{\text{P1-}}$
SLP at 40 N 135 W (Well offshore CA/OR, near summer Pac high center)
Southern California LTS (700 hPa-sfc pot temp)
LTS LTS (700 hPa-sfc pot temp) 1se of SCal site (32.5N 115W)
SLP in Great Basin (ie, 3 box avg: 37.5 115; 40 115; 40 117.5$^{\text{E2-,E3-,E4-,P1+}}$
California Bight SLP (32.5 122.5)$^{\text{(P1lag1+),P2-,(P2lag1+)}}$
Temp diff between Great basin and Cal Bight (ie, 3 box avg: 37.5 115; 40 115; 40 117.5)-(32.5 120)$^{\text{E1-,P3-}}$
2m air temp at 32.5 112.5 - California Bight T2m (32.5 120)$^{\text{E2-,P2-,(P2lag1+),P4-,(P4lag1+)}}$
2m air temp at 32.5 115 - California Bight T2m (32.5 120)$^{\text{E2-,P2-,P4-}}$

or to the meridional or zonal components, depending on the mixing mechanisms and the geometry of the basins in which the sites lie.

In contrast, 200 hPa winds, from the grid boxes containing the sites, are included as possible predictors, but not because they are thought to directly represent or mix downward and affect low-level winds. Rather, they form part an important aspect of the large-scale dynamics of the free atmosphere that can have profound effect on the low-level flow through quasigeostophic motions. In this sense the separate zonal, meridional, or total speed anomalies at 200 hPa have a different interpretation than at 700 hPa. Total and zonal momentum may reflect a more well-developed subtropical jet stream over the area, for example, while meridional 200 hPa momentum reflects strong troughing or ridging over the sites – providing more specificity and detail than the general matching of upper-air patterns from the SOM time series.

Air temperatures at 2 m above ground are also used as possible predictors in the model due to their relationships to differential heating and important local-scale circulations (MC2), particularly in the arid inland regions of southern California and the Great Basin. The grid box containing San Francisco and the Sacramento Valley is also included because it may roughly approximate the overall heating of the area, even though in the observations it is actually the sub-grid scale contrast between the inland heating and the cool marine temperatures at the coast that drives the circulation (MC2 and Zhong et al., 2004).

One note is in order regarding the temperature time series, which in the final model are always differences in 2m temperature between two grid boxes. The mesoscale dynamical circulations in the region largely depend on the contrast in temperature and SLP, which in turn are dictated by diurnal heating and cooling. But, when our model selection routine, using daily data, tests temperature time series, it tends to find much more predictive skill in the continental temperature time series, which vary more rapidly than the oceanic ones. This would result in a model that downscales based on the continental temperature time series but not the oceanic ones, which in turn would lead to extreme downscaled wind speed change predictions for a warmed 21$^{\mathrm{st}}$ century scenario. To avoid such spurious predictions we pass to the selection algorithm time series of temperature differences between land and nearby ocean.

SLP at select locations found to be important in the observations are natural candidate fields for integration into the downscaling model. Since MC2 found relationships between observed wind speed for many sites and seasons and reanalysis-resolved zonal and meridional pressure gradients, these are the first predictor candidates. The gradients are computed over separations of 1-4 grid boxes on either side of the site, but the selection algorithm is constrained to choose at most one zonal and one meridional SLP gradient time series for each station and season. Other locations whose SLP is a predictor candidate include the Great Basin area (comprising three grid boxes), the Southern California Bight, the Sonoran Desert, and the grid boxes over the sites themselves, as follows from MC1, MC2, and Conil and Hall (2006). In contrast to the case for 2 m temperatures, the objective selection algorithm tends to retain SLP time series in pairs, usually with β_i values of the same order of magnitude, indicating that the statistically skillful predictors tend to correspond to the physically meaningful SLP gradients, and also assisting the interpretation of the final model.

Lower-tropospheric stability is another predictor candidate, for the importance it is found to play in boundary-layer momentum dissipation in the Sacramento Valley (MC2). In this case LTS is defined based on potential temperature at 850 hPa and the surface, $LTS \equiv \theta_{850} - \theta_{sfc}$. When measured by nearby radiosondes and surface stations in the Sacramento Valley, this quantity generally is large when the low-level temperature inversion is strong and when the planetary boundary layer is shallow (Iacobellis et al., 2009). However, our initial comparisons of LTS time series from observations, covering 1960-2007, compared to LTS time series from reanalysis, show fundamentally different seasonal cycles and no correlation between interannual anomalies in the two sets, perhaps explaining why the selection algorithm tends not to choose LTS to downscale winds from reanalysis data.

Missing from this pool of predictor candidates are several fields whose inclusion would provide increased downscaling skill. SOM time series based on SLP and 500 hPa height anomaly patterns would be a natural extension of the SOMs in MC2, and in downscaling reanalysis they indeed show at least as much skill as those based on 500 hPa wind components, but are not included here. Likewise, time series of 500 hPa heights at select grid boxes and of vertical velocity at 700 and 850 hPa were found to improve the ability of the model to downscale reanalysis for local winds, judging by an independent verification period. All these were omitted from this study because geopotential height and vertical velocity are not included for most of the CMIP models whose output is posted at the Lawrence Livermore/PCMDI data portal that we used as a source for our

GCM data, and hence it was necessary to construct and train the model only with the reanalysis fields that are available for CMIP models as well.

In addition to these $X_i(t)$ predictor candidates, we also make available to the selection algorithm the above time series at one and two days lag. The inclusion of $X_i(t-1)$ and $X_i(t-2)$ allows comparing values of a field on successive days, such as for instance, the one-day change in 2m temperature, which might indicate thermal excitation of winds at the sites. It could also, for instance, show the two-day change in 200 hPa meridional winds, indicative of upper-air longwave passing over the area. The lagged SOM time series, however, are not included as potential predictors. It is worth clarifying that this model is not capturing autoregressive behavior or Granger causality. It is simply allowing the selection algorithm to recognize when certain elements of the atmospheric state on day t-2 or t-1 consistently show skill in predicting the observed winds on day t. Thus, the final model becomes

$$\hat{Y}(t) = \beta_0 + \sum_{i=1}^{n_{syn}} X_i(t)\beta_i + \sum_{i=n_{syn}+1}^{n_0} X_i(t)\beta_i + \sum_{i=n_0+1}^{n_1} X_i(t-1)\beta_i + \sum_{i=n_1+1}^{N} X_i(t-2)\beta_i \quad (5.3)$$

.

5.4.2 Backward selection phase

The model is chosen via a backward selection algorithm where the time series whose scaled z-scores fall below a specified threshold magnitude are removed from the model at every iteration, until all remaining predictors have a satisfactory score. The scaled z-scores are given as (Hastie et al., 2001):

$$z_j = \frac{\beta_j}{\hat{\sigma}\sqrt{v_j}} \quad (5.4)$$

where, if $\mathbf{X}$ is the $N \times p$ matrix of all X_i not yet eliminated from the model, then v_j is jth diagonal element of $(\mathbf{X}^T\mathbf{X})^{-1}$ and $\hat{\sigma}$ is the estimate of the variance, $\hat{\sigma}^2 = \frac{1}{N-p-1}\sum_{i=1}^{N}(y_i - \hat{y}_i)^2$. Since the variance-covariance matrix of the regression parameters is given by

$$Var(\beta) = (\mathbf{X}^T\mathbf{X})^{-1}\sigma^2 \quad (5.5)$$

, (Hastie et al., 2001), the scaled z-scores essentially compare the value of each least-squares parameter β_j to the estimated variance of that parameter, and reject the corresponding candidate X_j when the magnitude of the ratio is below a fixed threshold.

In the model training process, the size of the SOMs, subset of days they are based on (whether an SOM for all days or on each from the calmest and windiest days; subsection 5.4.1), and number of SOM time series used, are tuned and directly affect n_{syn}. The z-score threshold for eliminating a predictor is also tuned, which affects the number of total predictors retained, N. For this study, the goal in tuning these parameters is to achieve high correlation values and low model mean absolute error (MAE) with verification data independent from the training data, while still maintaining a manageable number N of model predictors that can be examined and interpreted for their corresponding physical mechanism. Although there is some some subjectivity in the tuning process, we have found these goals overall to be mutually compatible. The final model selection and coefficients for each site and season reflect a balance of these three goals.

At this point it is possible to view the results of the model formulation and training stages. For every case and season it is straightforward to take into account the time series retained (shown in Tables 5.1-5.2) and the sign and magnitude of the corresponding regression coefficients, and group these into a smaller number of more physically meaningful terms — for instance, combining the individual SLP time series into SLP gradients, grouping lagged and simultaneous fields as single terms describing the temporal change in the quantity, etc. These groups are shown in Tables 5.3-5.5 and are also discussed concurrently with the downscaling results in Section 5.6.

While for the most part the groups and their associated regression coefficients are consistent with the observational findings in MC1 and MC2 and the discussion in the previous subsection, there is one predictor where the time series' role in the model is not as straightforward and merits explanation. The anomalous Southern California Bight minus Great Basin 2 m temperature predictor is somewhat counterintuitive in that its correlation with observed Edwards winds is negative (ie, calmer winds when Bight is anomalously warm and Great Basin temperature cold), but its β coefficient in this model is positive (ie, more energetic winds when Bight is anomalously warm and Great Basin temperature cold). In fact, when the regression is carried out over the training period with the meridional and zonal pressure difference predictors removed, the resulting coefficient is negative, just like its correlation coefficient. However, when the meridional and zonal components of SLP gradient are explicitly included in the regression model, the β_i value changes sign, reflecting the component of the temperature-difference time series that is independent of the SLP gradients. Thus, the temperature difference term is effectively a correction to the SLP gradients' contribution to the estimated wind speed. While a scenario such as this, where β_i is of the opposite sign as the correlation coefficient, is possible in any multivariate regression, with the present model it happens seldom, and more commonly is seen in the cases where two separate SLP time series are retained in the model to effectively form a SLP difference-based predictor.

Table 5.3: Physically motivated groupings and titles of the fields chosen by the backward selection phase of the model for each season at Edwards. Quantities without a minus sign contribute positively to wind anomalies when they are themselves anomalously positive; quantities that have a negative regression coefficient are proceeded by a minus sign and enclosed in parentheses.

Travis DJF predictor groups	**Travis MAM predictor groups**	**Travis JJA predictor groups**	**Travis SON predictor groups**
-(Zonal SLP gradient)	-(Meridional SLP gradient)	-(Meridional SLP gradient)	-(Meridional SLP gradient)
-(700 hPa V)	-(Zonal SLP gradient)	Site-Nevada SLP	-(700 hPa V)
-(Site SLP)	Prev day negative 700 hPa V	-(Prev day 700 hPa U)	2 Days previous site-offshore temp diff
Prev day 700 hPa U	Prev Day site-offshore temp diff	Prev Day site-offshore temp diff	

Table 5.4: As in Table 5.3, but for downscaling predictors for Edwards.

Edwards DJF predictor groups	**Edwards MAM predictor groups**	**Edwards JJA predictor groups**	**Edwards SON predictor groups**
-(Zonal SLP gradient)	Zonal SLP	700 hPa speed	Zonal SLP
-(Meridional SLP gradient)	700 hPa U	Southern Sonoran - Great Basin SLP diff	700 hPa U
700 hPa speed	Sfc speed		Sfc speed
Sfc speed	-(Great Basin SLP)		-(Great Basin SLP)
Bight-Great Basin Temp	Sonoran temp-CA Bight temp		

Table 5.5: As in Table 5.3, but for downscaling predictors for Palm Springs.

Palm Springs DJF predictor groups	**Palm Springs MAM predictor groups**	**Palm Springs JJA predictor groups**	**Palm Springs SON predictor groups**
Sfc speed	-(Zonal SLP gradient)	-(Zonal SLP gradient with broadened continental center)	-(Zonal SLP gradient)
Site - Sonoran SLP	CA bight 1-day SLP decrease	Meridional SLP	Decrease in desert-Bight temp. difference
Great Basin - Sonoran SLP	Temp drop in Sonoran Desert	CA Bight-Great Basin temp	Temp drop in Sonoran Desert
CA BIght prev day - Sonoran SLP			

5.5 Model skill assessment

The model downscales daily data, whose longer-term statistics we are also interested in, and the decades of data from each site leave ample room for comparing output to independent observations for error analysis. Numerous different measures could be used to examine downscaling skill, but here we concentrate on MAE, Pearson product-moment correlation coefficients, and classification of wind speed terciles from daily time scales as well as monthly means.

Tables 5.6-5.8 give r and MAE values for daily and monthly-mean wind speeds, as well as the mean of the absolute value of the anomalies in the data sets as a measure of variability. Since wind speed anomalies at most sites and seasons display a long right tail, mean absolute values are displayed instead of root-mean squared error (RMSE) and standard deviation, so that a relatively small number of extreme positive outliers does not have a large influence on the skill scores. However, the interpretation is fundamentally similar to that of the RMSE and standard deviation statistics.

Whereas, in numerical weather prediction, model skill is often defined as increased accuracy over a forecast of persistence, for longer-term forecasting and hindcasting skill can be defined as increase in accuracy over climatology. Climatology in this case means zero anomaly values, ie, $\hat{Y}(t) = 0$ for every station and season. In this sense, the model may be said to have skill if the MAE is less than the mean absolute value of the observed anomalies (MAVO), which would be equal to the MAE if $\forall t, \hat{Y}_i(t) = 0$. Another way to determine skill is by how often the model correctly classifies any period of time as calm, normal, or windy. If the model correctly identifies periods as being in the lowest, middle, or highest wind-speed anomaly tercile more than one-third of the time (which would be the result of guessing all $\hat{Y}_i(t) = 0$), then the model has demonstrated skill over climatology. This test, as applied here, uses the tercile threshold values for each season separately based on the respective model or observational data for each season, averaged over the time scale of interest, and hence removes any consistent biases in the model data. While this in some ways is less stringent than comparing MAE to MAVO, which penalizes consistent bias compared to verification data, given that our primary application of this model is in comparing 20^{th} to 21^{st} century greenhouse-gas forced GCM output, any consistent bias will be subtracted out anyway, and the tercile-classification measure is quite relevant.

Tables 5.6-5.8 show several measures of the model skill, both over the daily time scale on which the model operates, and aggregated into monthly mean data as an indicator of how well they capture longer-term variability. In the daily data, almost every site and season shows MAE<MAVO, and all show skill in classifying the wind speed anomaly tercile of daily-mean winds (proportion correct>0.33). The bold numbers in columns 2 and 3 of the tables indicates that the difference between MAE and MAVO is significantly different at the 90% level based on bias-corrected, accelerated bootstrap resampling, with 10000 bootstrap iterations for each difference, after Efron and Tibshirani (1993). The vast majority of sites and seasons, as well as yearly averages based on daily data, show that MAE is significantly less than MAVO. The exceptions to this come at Palm Springs. Here, both Dec-Feb and Jun-Aug seasons show that MAE is not less than MAVO, with the difference statistically significant in winter. This is also the site where synoptic forcing was found to have the least direct influence on wind speed, similar synoptic scenarios showed multiple corresponding wind regimes, and few factors from large- or regional-scale scale models were found to explain the overall wind speed and small-scale circulation contributions to it, all in MC2. Even in these seasons, however, the model correctly simulates the wind speed anomaly tercile for 40% of all days, indicating skill and practical utility in these seasons as well.

The statistics based on monthly means in Tables 5.6-5.8 present a more mixed assessment. For several sites and seasons, monthly MAE<MAVO, and this is found to be statistically significant for spring and fall months at Travis. In others, the MAE

and MAVO quantities are statistically equivalent, while in some cases the MAVO is significantly greater than MAE. This is the case for winter at Edwards, for example, even though though 63% of monthly wind speed terciles are correctly diagnosed and r=0.74 here, which indicates the downscaled time series explains more than half of the intermonthly variance and is higher than the r value in many cases where monthly MAE<MAVO. Since the model selection and least-sum-of-squares coefficient estimation was performed on daily data, it is not surprising that r values tend to be lower on monthly scales, while the smoothing effects of taking longer-term statistics also decrease the magnitude of model error and internal variability of model and observational data sets. For monthly data, the model shows definite skill in classifying calm, normal, or windy periods, often more than with daily data.

To put some of the skill statistics in context, we note that the r values for observations and daily cold-season wind speed anomalies in the 6km mesoscale modeling study of Conil and Hall (2006) were generally between 0.4 and 0.75, but less than 0.6 for stations in inland and more complex terrain. We also compared output from the California Reanalysis Downscaling at 10km (CaRD10; Kanamitsu and Kanamaru, 2007) dynamically downscaled data set to site winds kanarsm1. Our analysis shows that the r values for daily CaRD10 mean wind speed anomalies, separated by seasons, at our three main sites range from 0.27 to 0.59, and most were under 0.5. The inland winds in CaRD10, in turn, were shown to be superior to those in NARR in Kanamaru and Kanamitsu (2007). The monthly r values, broken down by season, for CaRD10 are mainly between 0.2 and 0.4. Thus, as far as indicated by Pearson correlation coefficients, our specific downscaling model has skill comparable to that of these higher resolution regional and mesoscale models.

Although the error statistics for downscaled reanalysis indicate that any application of the model must be interpreted with care, the skill shown in different metrics suggest that it is still worthwhile to examine the changes in downscaled site winds under climate change, as this would likely detect any major shifts in wind speed. With that in mind we apply the model to downscale several GCMs under the SRES A1b emissions scenario after integration over the 21st century.

Since the error analysis, for daily and monthly means and at each site, shows that the variability of the downscaled data is consistently less than the variability of the observed anomalies, we will not examine the modeled output for extreme episodes. We found, for example, that the model largely fails to identify extreme quintiles or more exacting classifications of wind speed behavior. Rather, the discussion will be restricted to time means, terciles, or 25th and 75th percentile values of monthly wind speed.

5.6 21st century downscaling results

Bearing the model error results for downscaling reanalysis in mind, we present the findings from applying the downscaling model to the CNRM, ECHAM5, and GFDL 2.1 models, comparing values within each model from the historical period 1961-2000 to the period 2081-2100. The overall predicted changes in monthly-mean wind speed and mean monthly 75th percentile of daily wind speed are summarized for each of the sites, seasons, and GCMs examined in Fig. 5.2. The fact that the monthly means (horizontal axis on each panel) and mean monthly 75th percentiles of daily wind speeds (vertical axis) largely track together indicates that each wind speed distribution, to the extent it is reproduced by the model, mainly retains its shape under the 21st century climate change. A preponderance of points in the first quadrant above the line $y = x$ or in the third quadrant below this line would indicate a widening of the distribution, with more frequent events that are extreme by 20th century standards; points below $y = x$ in the first quadrant or above $y = x$ in the third quadrant would mean a narrower distribution. Since most points are close to this line, for these GCMs, what wind speed changes do occur are primarily due to an overall shift in the location of the distribution. More detailed examination of the downscaled wind speed distributions (not shown) confirm this.

Examining first the December-February results, Fig. 5.2 shows that most wind speed changes implied by the model are modest. All three GCMs show a wind speed decrease for Travis on the order of 0.2 m/s, compared to the climatological value of 3.1 m/s in its annual cycle (Table 5.9). The downscaled models disagree about the sign of wind speed changes for both Edwards and Palm Springs, although none are very substantial. Spring presents another agreement between the downscaled CNRM and GFDL models, showing accelerated winds Travis, while the GFDL 2.1 model shows minimal change. Summer, which has the highest climatological (20th century) wind speed at Travis (Table 5.9) and which is on par with spring climatological wind speed values at the other sites, shows the greatest changes, but also the greatest model disagreement. The maximum magnitude of monthly-mean wind speed change of 0.6 m/s is in the range

Table 5.6: Skill of the statistical model in downscaling reanalysis for Travis. The model was trained on observations from 1985-1995 inclusive, and the statistics are based on 1961-2000, excluding the training years. The first two columns present Pearson correlation coefficient and mean absolute error, followed by the mean absolute value of the observed anomalies. When these two quantities are different at the 90% confidence level, both are displayed in bold. The mean absolute value of the simulated anomalies are then presented to show the variability of model output, followed by the proportion of time that the model-output wind speed anomaly tercile is the same as the observed wind-speed anomaly tercile. The statistics for monthly-mean quantities are presented in the first five rows, followed by the daily-mean data from which the monthly quantities were derived.

	r value	**MAE**	**Mean abs. anomalies, obs**	**Mean abs. anomalies, model**	**Proportion of terciles correct**
DJF monthly means	0.53	0.63	0.67	0.49	0.51
MAM monthly means	0.45	**0.70**	**0.78**	0.31	0.42
JJA monthly means	0.37	0.85	0.84	0.47	0.41
SON monthly means	0.41	**0.63**	**0.68**	0.29	0.45
Monthly means, entire year	0.40	**0.71**	**0.74**	0.39	0.45
DJF daily means	0.49	**1.55**	**1.70**	1.02	0.49
MAM daily means	0.44	**1.51**	**1.76**	0.88	0.53
JJA daily means	0.60	**1.53**	**1.95**	1.32	0.48
SON daily means	0.43	**1.72**	**1.91**	1.05	0.41
Daily means, entire year	0.49	**1.58**	**1.83**	1.07	0.48

Table 5.7: As in Table 5.6, but with observed anomalies and model-downscaled data for Edwards Air Force Base near Tehachapi Pass.

	r value	**MAE**	**Mean abs. anomalies, obs**	**Mean abs. anomalies, model**	**Proportion of terciles correct**
DJF monthly means	0.74	**0.82**	**0.64**	0.85	0.63
MAM monthly means	0.56	0.58	0.62	0.56	0.54
JJA monthly means	0.44	0.73	0.65	0.59	0.48
SON monthly means	0.52	**0.76**	**0.53**	0.76	0.49
Monthly means, entire year	0.44	**0.72**	**0.61**	0.69	0.53
DJF daily means	0.77	**1.37**	**1.84**	1.39	0.60
MAM daily means	0.77	**1.26**	**2.10**	1.55	0.62
JJA daily means	0.70	**1.11**	**1.52**	1.08	0.58
SON daily means	0.74	**1.30**	**1.72**	1.33	0.62
Daily means, entire year	0.72	**1.26**	**1.80**	1.34	0.60

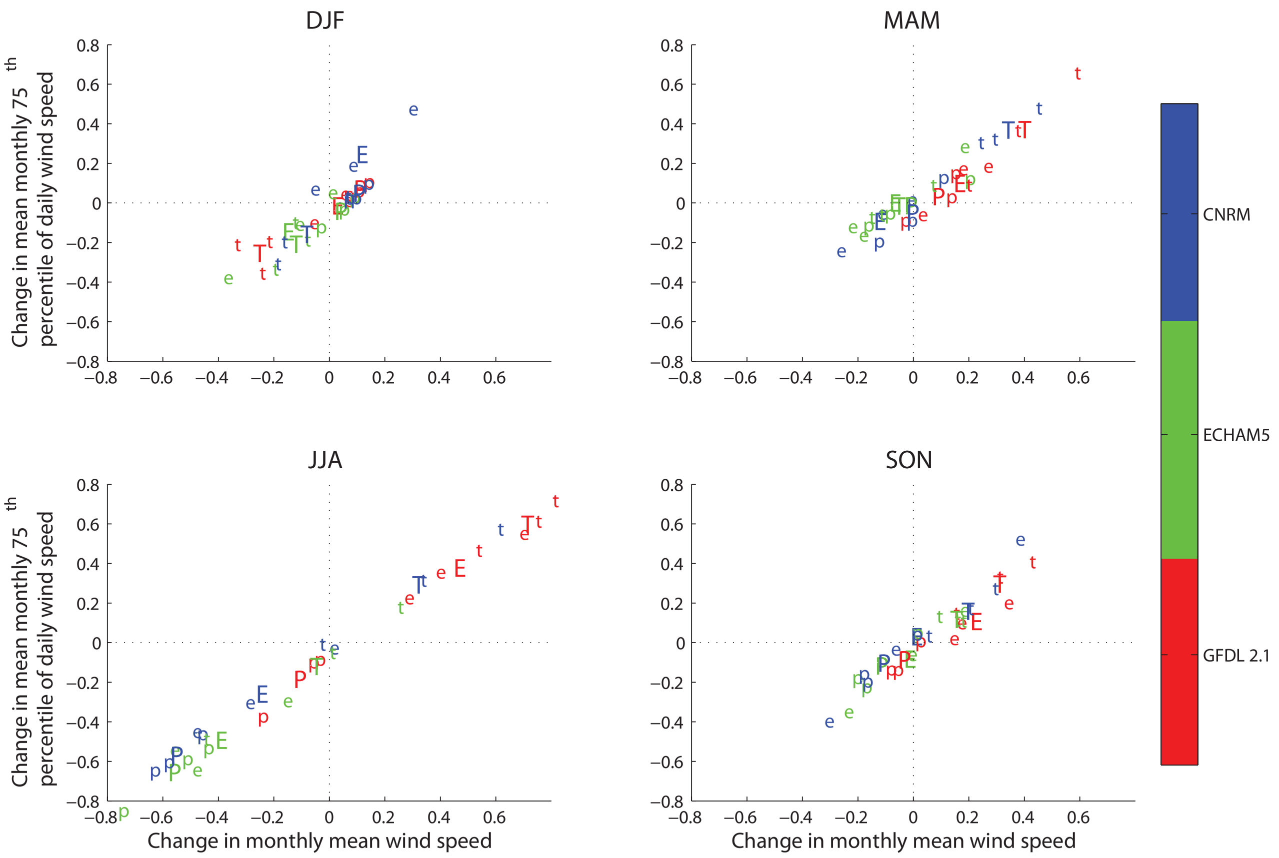

Figure 5.2: Summary of the changes in wind speed for 2081-2100 compared to 1961-2000 under emissions scenario A1b. For each season, the x-axis indicates the change in mean monthly wind speed, while the y-axis shows the change in mean monthly 75th percentile of daily-mean wind speeds. The position of the large capital letters indicates the seasonal average of these changes for each model and site, while the small lowercase letters correspond to the three separate months within that Season. T indicates data for Travis, E for Edwards, and P for Palm Springs, while the color key indicates which of the three downscaled GCMs is represented by each letter.

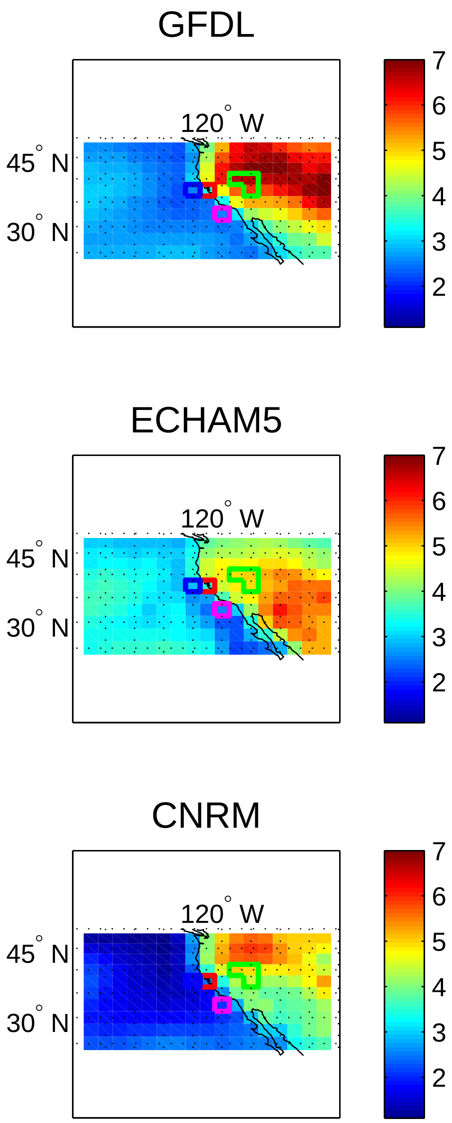

Figure 5.3: Mean June-August changes in 2m temperature for 2081-2100 compared to 1961-2000 in each of the GCMs examined. The effect of this field on Travis wind speeds is based on the difference between the value outlined in red and the value outlined in blue. The effect of this field on Palm Springs wind speeds is based on the difference between the value outlined in magenta and the value outlined in green.

that the downscaling model resolves with skill, but the discrepancies between GCMs calls for closer examination. Autumn again has inter-GCM agreement regarding Travis, but with smaller predicted changes and no consensus for the other sites.

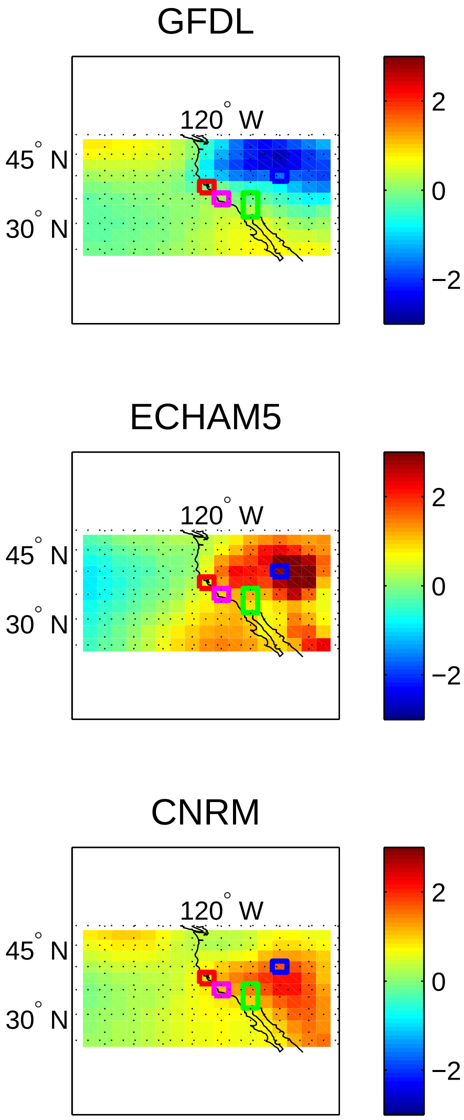

Figure 5.4: Mean June-August changes in SLP for 2081-2100 compared to 1961-2000 in each of the GCMs examined. The effect of this field on Travis wind speeds is based on the difference between the value outlined in red and the value outlined in blue. The effect of this field on Palm Springs wind speeds is based on the difference between the value outlined in magenta and the value outlined in green.

Focusing on the Jun-Aug changes, we examine the spatial distribution of 2 m air temperature and SLP changes over the 21st century in Figs. 5.3 and 5.4, as well as the points contributing to each site's downscaled wind speed. While each model shows warming overall and greater warming over the ocean than over the continents, the specific patterns differ. The warming over western North America in GFDL 2.1 is strong and very widespread, while ECHAM5 shows more in the US Southwest into Mexico and CNRM more in the northern Rockies and Great Plains. Comparing this to the changes in the SLP patterns in Fig. 5.4 reveals striking differences. The area of greatest warming in GFDL 2.1 coincides with lower SLPs, consistent with a direct thermal adjustment process in response to heating. The other two models show a general increase in SLP. Whereas the decreased SLP in GFDL 2.1 would merge with the 20th century thermal low in the Southwest US (ie, Rowson and Colucci, 1992) and lead to a broad area of low SLP in the summertime western US, the warming in CNRM would effectively coincide with an elimination of the thermal low. Whether this is because of large-scale circulation changes, different treatment of the daily timing of the warming and SLP adjustment processes, or other factors, remains to be investigated. Similarly, ECHAM5 shows a large area of increased SLP in the late 21st century, centered slightly north and east of that of CNRM, which would reduce the thermal low. These patterns sharply contrast with GFDL. Taking these two figures together it is clear why pressure effects combine with thermal effects in influencing summertime Travis GFDL 2.1 wind speed changes but oppose one another in the other models, as well as producing discrepancies in wind speed changes for Palm Springs and Edwards.

In light of these maps, it is also illuminating to investigate the Dec-Feb changes in downscaled wind speeds and in SLP and 2 m temperature distributions. As seen in Figs. 5.5-5.6, the discrepancy in downscaled wind speed changes implied by each model is not large in absolute terms for the winter, although taking the lower climatological mean wind speed into account (Table 5.9) shows that it still considerable in relative terms. Moreover, the distributions themselves in Fig. 5.8 and 5.9 show sharply different patterns the summer patterns in Figs. 5.3 and 5.4. GFDL 2.1 shows only a relatively moderate degree of continental warming in Dec-Feb, while ECHAM5 is greater in both continental and oceanic warming in the plotted domain, and CNRM roughly resembles GFDL 2.1. The corresponding distribution of mean 21st century SLP changes for GFDL 2.1 is a very broad increase in pressure, covering the entire domain but strongest in

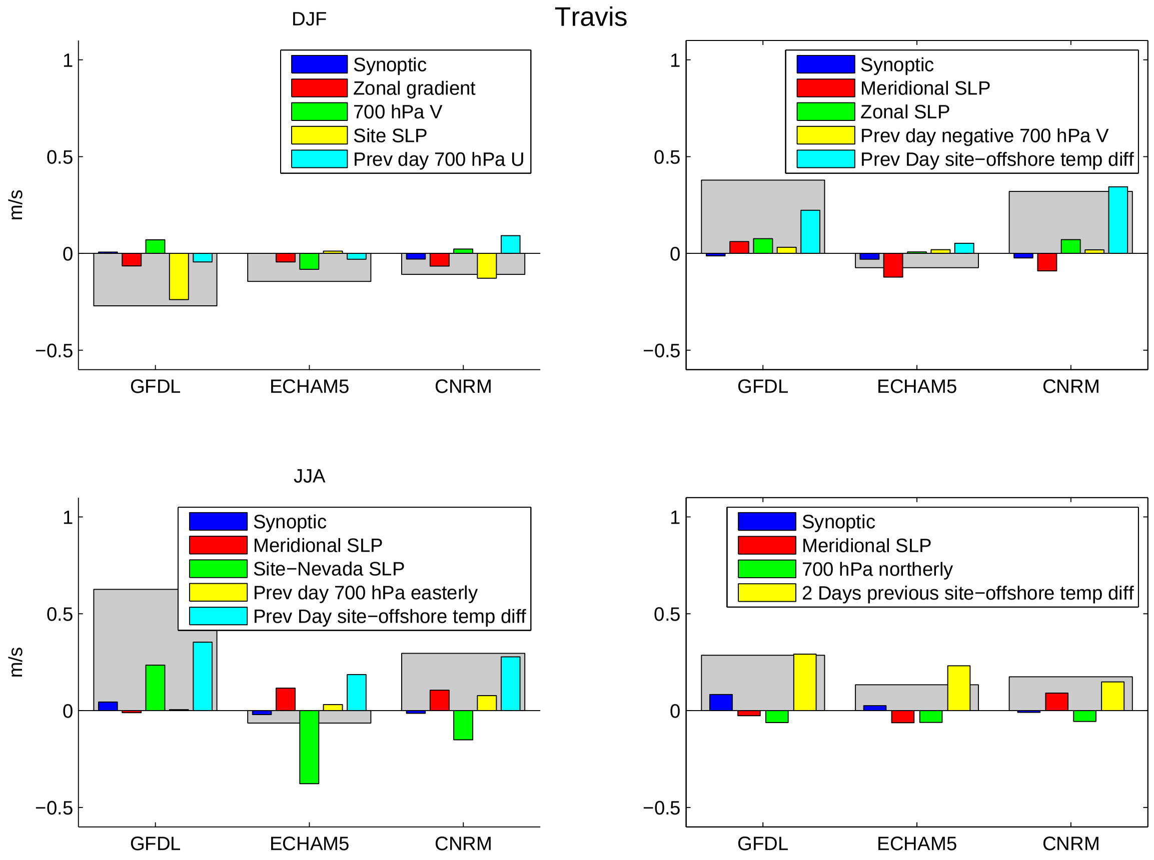

Figure 5.5: Downscaled wind speed changes and component contributions for Travis. For each season, the large gray bars indicate the net change in downscaled monthly-mean wind speed change in 2081-2100 compared to 1960-2000 for each GCM examined. The colored bars within the gray bars indicate the changes in the components examined to calculate the changes, which are the predictors used by the model, labeled here and in Table 5.3. The values indicated by the colored bars sum to that of the gray bar they are plotted within.

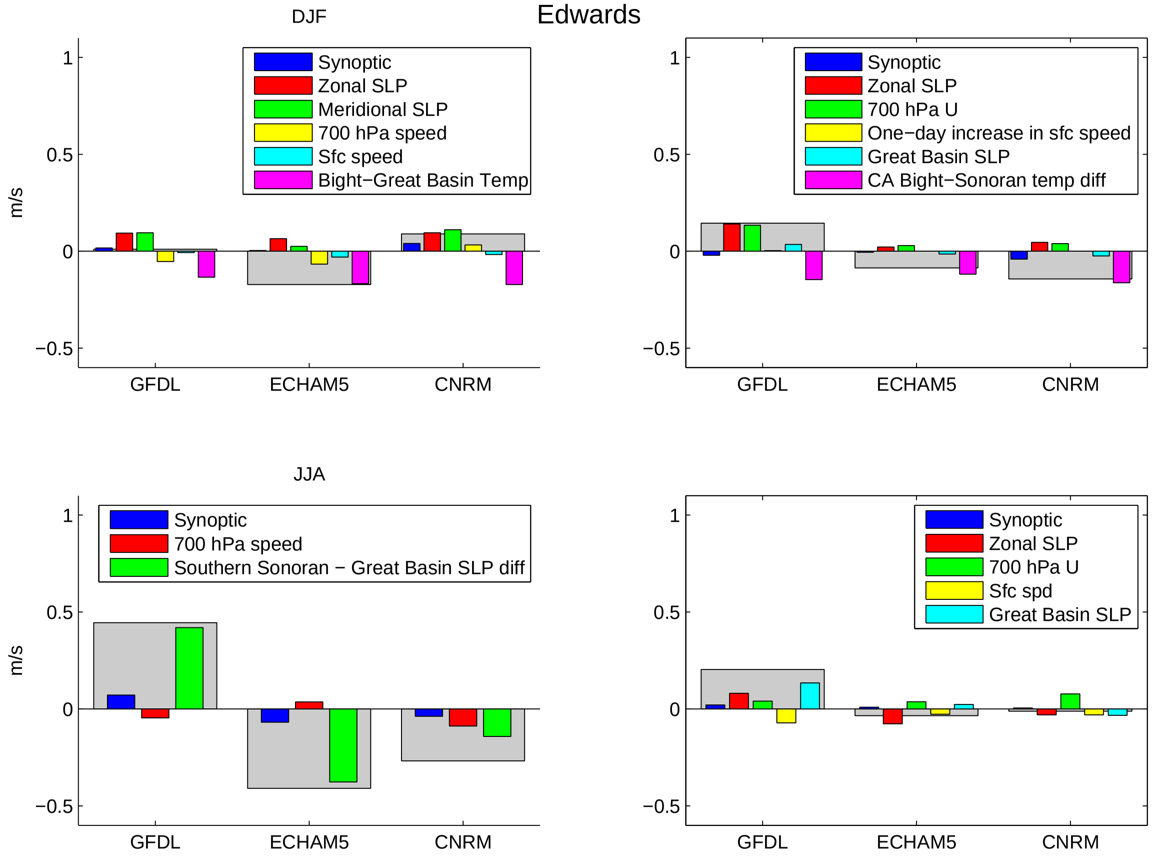

Figure 5.6: As in Fig. 5.5, but for Edwards.

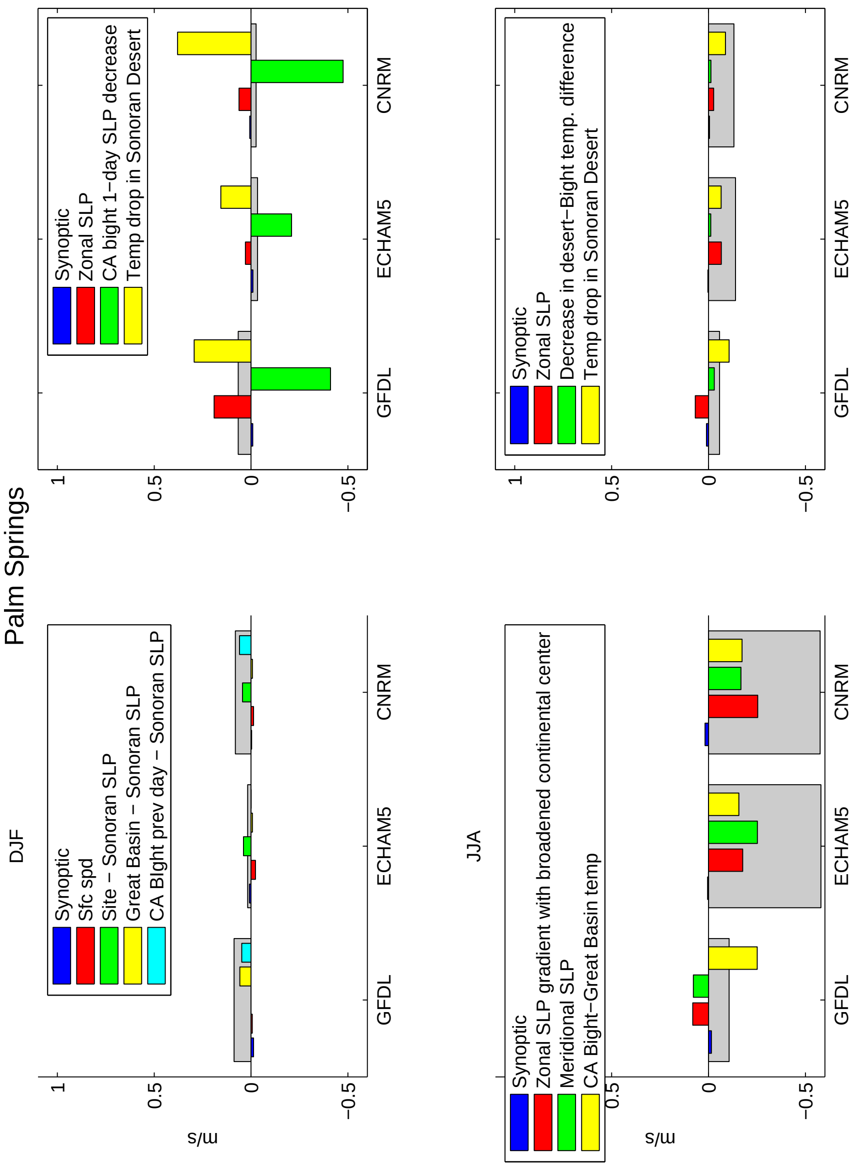

Figure 5.7: As in Fig. 5.5, but for Palm Springs.

the oceanic center near the US Pacific Northwest. This contrasts with the extensive, apparently thermal continental low in the GFDL summertime changes (Fig. 5.4), but once again it is the broadest and strongest SLP change pattern from among these three GCMs. The ECHAM5 SLP change pattern, in contrast, is quite mild in Dec-Feb, unlike in the summertime, and does not show any direct relationship to its spatial pattern of warming. CNRM shows a broad area of increased oceanic SLP but this is centered further offshore than GFDL's and is not accompanied by increased continental pressure. While none of these SLP and 2 m temperature patterns can be explained just by the presence of simple local thermal relationship between the two fields, as with summertime GFDL 2.1, they still do show significant discrepancies in the amount of near-surface warming, the oceanic-versus-continental warming, and the circulation effects that lead to SLP changes. Thus, they again point out key differences among the three models on the regional level, and the corresponding changes implied for site wind speed show impacts of the regional-level discrepancies.

At Travis, the downscaled models all show a decrease in mean Dec-Feb wind speeds. All the models show the zonal pressure gradient across the site becoming more positive over the 21^{st} century, which contributes to the wind speed decrease (Fig. 5.5). At the same time, in each model one or both components of the 700 hPa vector winds weakly compensate for this, just as there is discrepancy regarding the sign of the 700 hPa wind speed change, which affects Edwards surface winds. At the Edwards site, although zonal and meridional SLP gradients are consistently seen to become more negative, implying a net acceleration of winds, the dominant term in the downscaling for each model is the anomalous temperature difference between the Southern California Bight and the Great Basin (Fig. 5.6). This predictor has a regression coefficient of the opposite sign as its correlation coefficient to the observed data. In Section 5.4 it is argued that in this multivariate model it essentially acts as a correction term to the effects of zonal and meridional SLP gradient on the predictand, and for every downscaled GCM it does in fact oppose the effects of these gradients on site winds. The continental warming in each case makes this quantity more negative, compensating for the SLP gradient changes, and in the case of ECHAM5 leading to a predicted wind speed decrease of nearly 0.2 m/s. Palm Springs winter time wind speed changes are governed by a variety of factors. One of them, for both this site and Edwards, is the GCM-resolved large-scale surface wind speed, but the changes this metric implies for the local site changes are small compared to the changes implied by the GCM-simulated SLP distribution changes. The predictors retained for Palm Springs winter essentially focus on the Sonoran Desert area SLP as compared to SLP in the grid boxes containing the site, the Southern Californian Bight, or the Great Basin. Although the sign of the changes for these SLP differences varies among the three different GCMs, the overall implied wind speed change for the site is weakly positive (Fig. 5.7).

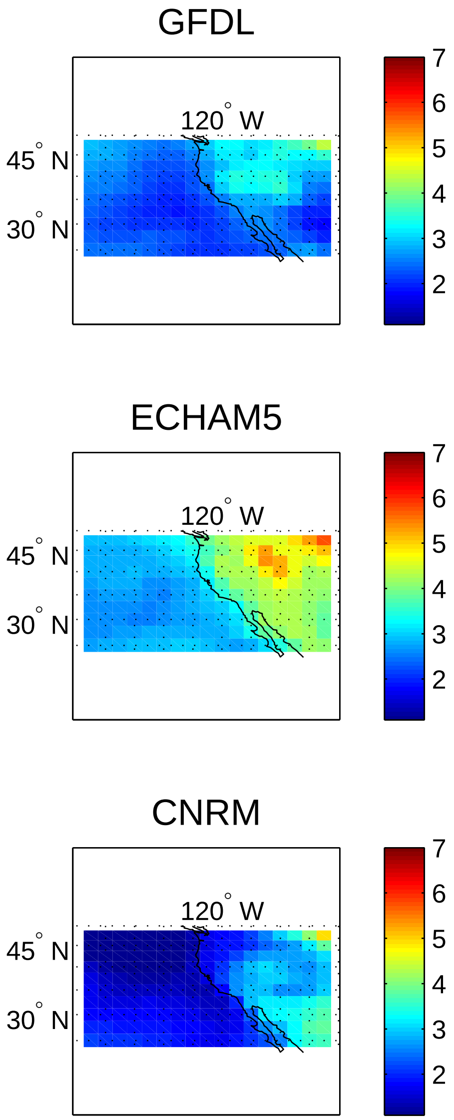

Figure 5.8: Mean December-February changes in 2m temperature for 2081-2100 compared to 1961-2000 in each of the GCMs examined.

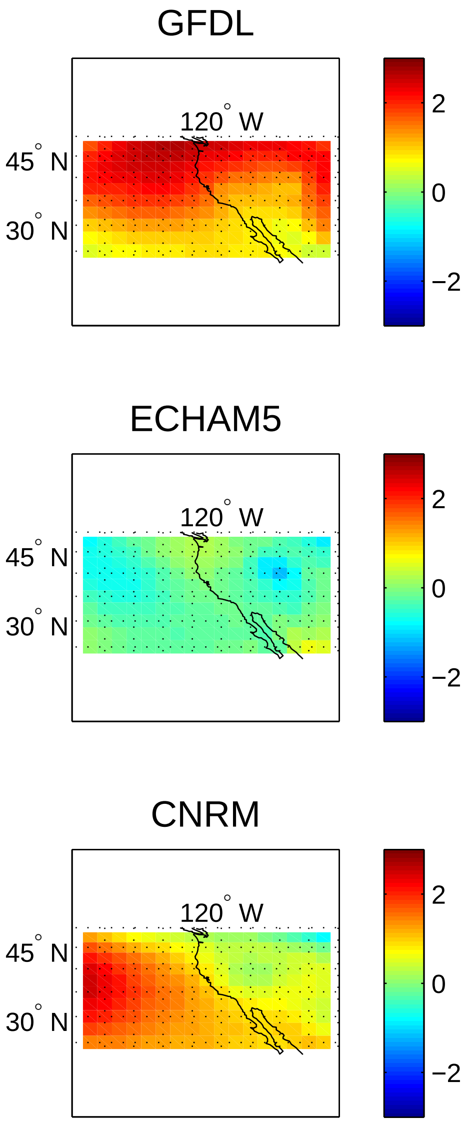

Figure 5.9: Mean December-February changes in SLP for 2081-2100 compared to 1961-2000 in each of the GCMs examined.

Table 5.8: As in Table 5.6, but for Palm Springs Airport near San Gorgonio Pass. Statistics are from the verification period 1973-2000, excluding the training years of 1985-1995.

	r value	**MAE**	**Mean abs. anomalies, obs**	**Mean abs. anomalies, model**	**Proportion of terciles correct**
DJF monthly means	0.47	**0.49**	**0.33**	0.46	0.50
MAM monthly means	0.38	0.41	0.39	0.32	0.51
JJA monthly means	0.44	0.39	0.40	0.30	0.43
SON monthly means	0.37	**0.47**	**0.35**	0.42	0.50
Monthly means, entire year	0.39	**0.44**	**0.37**	0.37	0.49
DJF daily means	0.56	**0.87**	**0.84**	0.65	0.40
MAM daily means	0.56	**1.09**	**1.30**	0.88	0.49
JJA daily means	0.52	**0.86**	**0.94**	0.63	0.40
SON daily means	0.49	0.92	0.92	0.66	0.45
Daily means, entire year	0.53	**0.93**	**1.00**	0.71	0.44

5.7 Conclusions

We have detailed a statistical method to downscale winds for three sites in California. Reanalysis and current GCMs do not approach the resolution required to resolve the nearby topography at these sites, and so use of GCMs for direct diagnosis of the winds is not accurate. Self-organizing map quantitative error time series incorporate weather type information into the multilinear regression model with no use of analog methods, instead assigning positive or negative wind speed anomalies to any given day's similarity to several different weather types. Every potential predictor submitted to the selection algorithm has a basis and rationale from the observational analysis in MC1 and MC2, and hence the predictors that the backward selection algorithm retain in the final model represent the most statistically important factors in determining a site's wind speed anomaly. By avoiding analog methods we rely less on the assumption of stationary in wind speed-weather type relationships than Najac et al. (2009), yet retain the ability to view the component processes responsible for wind speed changes in a way generally unavailable from a neural network approach to downscaling (ie Sailor et al., 2000). Considering the considerable sub-synoptic scale aspects of the circulations at each site, as shown in MC2, this could be considered an important quality for downscaling this region.

The trained model was used to downscaled 20^{th} century reanalysis data and compared to observations. For the raw, daily-mean downscaled output, each site and season of the model showed significant skill over climatology in the sense of having MAE<MAVO, a large proportion of the days classified in the correct tercile, or correlation coefficients between 0.45 and 0.75. It therefore compares well with the corresponding r values of mesoscale models (Conil and Hall, 2006; Kanamitsu and Kanamaru, 2007) compared to inland California wind speeds on a daily basis. Its skill scores with these metrics are generally comparable or slightly worse than those in Najac et al. (2009), but the downscaled versus observed internal variance as measured by RMSE or mean absolute deviation within either data set is considerably worse. This is not a surprise in that our method relies on linear regression in place of analog relationships and uses no inflation to try to capture the sub-grid scale variability not reflected in GCMs (Zorita and Von Storch, 1999).

The validation over monthly time scales reveals that the model still has skill over longer averaging periods, although MAE approaches MAVO. While a decrease in skill scores may be expected for a model trained and validated on daily data, it still raises the question of what methods of formulation could result in a model with greater skill over long averaging periods, as would be desired for application to long-term climate change. A regression model that predicts monthly-mean statistics such as mean, median, 25th and 75th percentile of daily-mean wind speeds, could be constructed with largely the same methods as the present model. Our initial endeavors (not shown) did not, however, result in significant improvement in monthly-mean wind speed downscaling using the monthly-mean predictors. The limited reliability of the observational data sets over interannual to decadal time scales (MC1) may be an explanation, as well as the simple fact that few independent samples and a lesser sampling of possible atmospheric states are available to train a model operating on monthly or longer time scales with finite training data. In this case, a hybrid model be worth exploring, where monthly-mean statistics are characterized by a weighted average of results from models operating on different time scales. Such a model might also enjoy the benefits of capturing lower-frequency variability related to terms like SST or soil moisture (MC1) while also taking into account higher-frequency atmospheric variations and a more accurate aggregate response to any fields which have a nonlinear relationship to wind speed anomalies. Such a hybrid model would entail new questions as well and ample uncertainties in formulation and tuning, and would require an in-depth investigation of its own.

The results of applying our model to 20th and 21st century GCM output show mostly weak to moderate changes in monthly-mean and 75th percentile wind speed, but little consensus regarding those cases where stronger wind speed change may be implied. One clear pattern is that GFDL 2.1 differs from CNRM and ECHAM5 in the summertime SLP change over the continental areas where significant warming is found. If specific analysis of the underlying models could lend support to the GFDL model's simulation of 21st century SLP response to warming, or the other models' simulated compensation and increase in SLP, then a more definitive statement could be made. In the case that the GFDL model processes governing the continental summertime SLP were diagnosed found credible, it would lend more confidence to the findings of increased wind speed at Travis and Edwards in the summertime. On the other hand, if further study lent more support to the distributions of SLP changes found in CNRM and ECHAM5, this would support the predictions of notable decrease in summertime Palm Springs winds.

The fact that the range of possible long-term wind speed changes by season roughly tracks with the present climatological seasonal cycle, with larger possible changes in the more energetic months, holds implications similar to those arising from the to the seasonal cycle of variability about the climatological mean discussed in MC1. Namely, if meeting minimum baseline power demands or turbine cut-in wind speeds is of primary concern, then the small changes implied for the winter seasons will nonetheless be of importance as they come at the time of year of low wind speeds. Conversely, if meeting demand in the more energetic wind times of year, or keeping pace with long-term changes in demand or wind generation facilities is a concern, then the high discrepancies but potential for greater wind speed changes — increases or decreases — in the summer cannot be overlooked.

Even beyond the present application to wind speeds, our results show both the power and limitations of current GCMs. While factors such as greater continental than oceanic warming are common in greenhouse gas-forced 21$^{\text{st}}$ century simulations, spatial temperature and pressure change patterns still show great inter-model discrepancies (Solomon et al., 2008). Ours is another argument for increased emphasis on regional climate change, to help identify uncertainties and devise research priorities to overcome them (ie, Council, 2009). An in-depth study of the type necessary to determine the credibility of GFDL's regional summertime results compared to other models', for instance, is beyond our present scope but would have powerful implications for any investigation of climate change in the area. Moreover, development of publicly available dynamically downscaled data sets through initiatives such as the North American Regional Climate Change Assessment Program (NARCCAP) could allow dramatic improvements for future studies in the vein of our own.

Although the statistical downscaling model is built on multilinear methods that have clear physical interpretations, it still relies implicitly on various assumptions of stationarity in the relationships between atmospheric predictors and site winds. In addition to those relationships already discussed, it is worth mentioning that there is an implicit assumption of stationarity regarding the change in continental 2 m air temperature and SLP distribution in the greenhouse gas-forced models. Many of the summertime relationships between site winds and temperature or pressure are based on the dominant 20$^{\text{th}}$ century patterns of strong daytime signals in temperature and SLP, which dominates the daily-mean reanalysis data used to train the model Rowson and Colucci (1992). Thus, if 21$^{\text{st}}$ warming in the US Southwest and Great Basin areas is mainly due to daytime temperature increases then the relationships based on 20th century observations and reanalysis can be expected to hold true for 2081-2100. If 21st century summertime continental warming is not concentrated in the daytime, however, then this would have a forcing effect on site winds that is weaker than or even opposite what is implied by our downscaling model. So, in addition to the gains that a model such as ours might enjoy from forcing data at a higher spatial resolution, inclusion of a higher temporal resolution for forcing data could also help resolve this problem. This also it underscores the need for reliable diurnal cycles in GCMs for the output any such statistical downscaling scheme to be accurate. In our initial experiments using 6-hourly reanalysis data to predict 6-hourly mean site wind speeds, constructing separate multilinear regressions for the anomalies centered at hours 0, 6, 12, and 18Z, overall skill in reproducing verification data was no better than with the daily model detailed above, over the same averaging periods. This does not contradict our comments about the value of a higher temporal resolution for forcing data, however. Since the diurnal circulations we would hope to capture, and the separation of areas heated differentially on these scales, are mostly smaller than the 2.5 °spatial resolution of the 6-hourly reanalysis of our experiments, it simply indicates that the benefits are more likely to come when higher spatial resolution for forcing data comes together with higher temporal resolution.

A next-generation statistical downscaling model that relies on a data set such as those being produced through NARCCAP would enjoy higher-resolution data and a broader selection of model fields to downscale future climate, leading to improvements in both skill and scope over GCM-based approaches. In that sense, works such as the present bring to light important issues for climate change adaptation at the same time that they inform discussion on one means of mitigation.

Table 5.9: Climatological daily mean wind speeds for each site and season.

	DJF	**MAM**	**JJA**	**SON**
Travis	3.37	5.34	7.68	4.60
Palm Springs	3.36	5.30	5.16	4.02
Edwards	3.09	5.28	5.02	3.42

ACKNOWLEDGEMENTS

Chapter 5, in full, is a reprint with minor modifications of the article "Formulation of a statistical downscaling model for California site winds, with an application to 21$^{\text{st}}$ century climate scenarios," to be submitted for publication. The author of the dissertation is the sole author.

Chapter 6

Conclusions

The studies in this dissertation have examined boundary-layer meteorological processes, whether for their importance to global climate and climate change, as with marine clouds, or for their importance to human electricity generation, consumption, and long-term resource stability, as with wind power. Regarding marine boundary-layer clouds, variability in monthly-mean cloud amount on the southern edge of the equatorial Pacific cold tongue was related to low-level temperature advection by wind, referred to as "SST advection." The physical mechanism relating SST advection to low-level cloud cover is straightforward: when cool air blows over increasingly warm water, as in equatorward flow over an eastern subtropical ocean, the thermal instability of the surface layer increases sea-air fluxes and vertical atmospheric boundary layer mixing. When downwind SST is cold, however, these fluxes and mixing are inhibited. As it is well established that boundary-layer clouds are poorly simulated in GCMs, with major consequences for the modeling of cloud-climate feedbacks (Bony and Dufresne, 2005), it is entirely possible that multiple aspects of physics, thermodynamics, and turbulence closure model components must be remedied for more realistic atmospheric and atmosphere-ocean GCM simulations. Nonetheless, chapter 2 shows that several GCMs do not capture the observed relationships between SST advection and low-level cloudiness, and the chapter provides both a suggestion for improving cloud parameterizations and a test for the fidelity of any such parameterization.

Regarding the studies of interior low-level winds, chapter 3 reveals several broad similarities among three wind farm areas in California. All three peak in the warm months in the climatological mean, which generally coincides with the climatological period of the year when large-scale zonal SLP gradient is most negative. Additionally, all three show greater directional consistency and a more regular diurnal cycle in the summer months, whereas winter tends to be more dominated by synoptic-scale forcing. The implications of these tendencies depend on the requirements of the wind farm developer, much in the same way that the possible changes to wind speed under greenhouse gas emissions scenario A1b, explored in chapter 5, do. Namely, the variability about the annual mean values in the cold months, while smaller in terms of m/s, can be significant to the question of meeting baseline power needs or turbine cut-in wind speeds in the colder months. The warm-season variability is larger in terms of m/s, both for 20th century variability about climatology and for 21st century wind speed changes, and this is most pertinent for meeting increased seasonal power demands such as air conditioning use.

Conclusions based on chapter 3 also include likely promising starting points for any inquiry into seasonal summaries or prediction of wind speed at the sites, namely the PNA, nearshore SSTs, and inland soil moisture. Chapter 4 helps elucidate the physical mechanisms for these statistical relationships: the role of oceanic high SLP anomalies and continental lows in exciting increased cold-season station windiness, and the role of differential heating and coast-inland thermal contrasts for warm-season flows. One method used to show the larger-scale patterns — the use of self-organizing maps — is found to be more adaptable than traditional EOF analysis while being more stable and usable than k-means clustering, and this method holds promise for many aspects of atmospheric and climate science.

The regional and mesoscale model results in chapter 4, overall, provide more detail than previously available in the published literature regarding the “Delta Breeze” in northern California. They simultaneously point out observational sites that could aid in wind energy prediction as well details of the circulation relevant to Central Valley air pollution. The WRF model results in southern California provide an estimate of the horizontal resolution needed to properly capture Palm Springs winds, and while they do not resolve all questions regarding synoptic influence on Palm Springs winds and interactions between scales, they do provide a degree of specificity not available from the CaRD10 data or the in situ and reanalysis data collections.

Chapter 5 provides the the first known site-specific estimates of wind speed changes under global climate change for the California wind farm areas in question. At the same time, however, it highlights several important questions regarding GCMs used to model climate change under greenhouse gas forcing, and underscores the uncertainties in regional patterns in the set of models examined. Thus, the details of the methodology used to formulate the model are of as much interest as the results themselves, and could serve to guide future studies even when the current dependence on global reanalysis and GCMs is replaced with higher-resolution regional historical and future data sets.

Besides viewing the effects of climate change on wind power as done here, it is logical to ask what the effects of extensive wind power conversion on global climate and weather patterns may be. Although the specifics depend as much on policy, economics, engineering, and population dynamics as they do on atmospheric science, some scenarios have been evaluated from the meteorological perspective. In particular, Keith et al. (2004) examined several scenarios of widespread large wind turbine deployment, simulating the effect of the wind power conversion facilities by adjusting the roughness length or by adding an extra drag term to the boundary layer schemes of two different GCMs. Although the models indicate negligible net overall effect on global-mean surface temperature, the study authors did find regional effects on temperature and wind patterns. Simulated extensive wind farm development in the central US, Europe, and East Asia were found to lead to warming tendencies in the northern subtropics and cooling further north, although one model also showed cooling to the east of the wind farm areas in the central US. More evenly distributed global deployment of wind power facilities led to weaker but broader versions of these patterns, as well as some warming in Southern Hemisphere subtropical areas. Keith et al. (2004) found that regional climate patterns induced directly by wind farms might be detectable under some scenarios in the 21st century, but could not be expected to be strong or consistent enough to provoke meaningful research into two-way interactions between wind farm deployment and climate change.

Overall, the work in the present dissertation addresses several important issues by investigating atmospheric boundary layer processes, mainly through observational analysis while still conscious of theory and modeling concerns. While the subjects of marine boundary layer flow, inland winds, and effects of climate change all still contain numerous unanswered questions, the foregoing has established several important new findings regarding boundary layers in different settings. Besides methodological contributions, the results are valuable for understanding the climate system and climate feedbacks, for efficiently harvesting a valuable atmospheric resource, and for planning about that resource through understanding it over the long term with climate change scenarios.

References

Albrecht, B. A., Bretherton, C. S., Johnson, D., Schubert, W. H., and Frisch, A. S., 1995: The Atlantic Stratocumulus Transition Experiment - ASTEX. *Bulletin Am. Meteorol. Soc.*, **76**, 889–904.

Albrecht, B. A., Randall, D. A., and Nicholls, S., 1988: Observations of marine stratocumulus clouds during fire. *Bulletin Am. Meteorol. Soc.*, **69**, 618–626.

Alexander, M., Yin, J., Branstator, G., Capotondi, A., Cassou, C., Cullather, R., Kwon, Y., Norris, J., Scott, J., and Wainer, I., 2006: Extratropical Atmosphere–Ocean Variability in CCSM3. *Journal of Climate*, **19**(11), 2496–2525.

Anderson, J. L., Balaji, V., Broccoli, A. J., Cooke, W. F., Delworth, T. L., Dixon, K. W., Donner, L. J., Dunne, K. A., Freidenreich, S. M., Garner, S. T., Gudgel, R. G., Gordon, C. T., Held, I. M., Hemler, R. S., Horowitz, L. W., Klein, S. A., Knutson, T. R., Kushner, P. J., Langenhost, A. R., Lau, N. C., Liang, Z., Malyshev, S. L., Milly, P. C. D., Nath, M. J., Ploshay, J. J., Ramaswamy, V., Schwarzkopf, M. D., Shevliakova, E., Sirutis, J. J., Soden, B. J., Stern, W. F., Thompson, L. A., Wilson, R. J., Wittenberg, A. T., and Wyman, B. L., 2004: The new GFDL global atmosphere and land model AM2-LM2: Evaluation with prescribed SST simulations. *J. Climate*, **17**, 4641–4673.

Archer, C., and Jacobson, M., 2003: Spatial and temporal distributions of US winds and wind power at 80 m derived from measurements. *Journal of Geophysical Research*, **108**(D9), 1–20.

Archer, C., and Jacobson, M., 2005: Evaluation of global wind power. *Journal of Geophysical Research-Atmospheres*, **110**(D12).

Bao, J., Michelson, S., Persson, P., Djalalova, I., and Wilczak, J., 2008: Observed and WRF-simulated low-level winds in a high-ozone episode during the Central California Ozone Study. *Journal of Applied Meteorology and Climatology*, **47**(9), 2372–2394.

Barnston, A., and Livezey, R., 1987: Classification, seasonality and persistence of low-frequency atmospheric circulation patterns. *Monthly Weather Review*, **115**(6), 1083–1126.

Barry, R., 2008: *Mountain weather and climate.* Cambridge University Press.

Bolton, D., 1980: The computation of equivalent potential temperature. *Monthly Weather Rev.*, **108**, 1046–1053.

Bony, S., and Dufresne, J. L., 2005: Marine boundary layer clouds at the heart of tropical cloud feedback uncertainties in climate models. *Geophysical Research Lett.*, **32**(20).

Boville, B. A., Rasch, P. J., Hack, J. J., and McCaa, J. R., 2006: Representation of clouds and precipitation processes in the Community Atmosphere Model (CAM3). Submitted, *J. Climate*.

Breslow, P., and Sailor, D., 2002: Vulnerability of wind power resources to climate change in the continental United States. *Renewable energy*, **27**(4), 585–598.

Cavazos, T., 1999: Large-scale circulation anomalies conducive to extreme precipitation events and derivation of daily rainfall in northeastern Mexico and southeastern Texas. *Journal of Climate*, **12**(5), 1506–1523.

Celik, A., 2004: A statistical analysis of wind power density based on the Weibull and Rayleigh models at the southern region of Turkey. *Renewable energy*, **29**(4), 593–604.

Collins, W. D., Bitz, C. M., Blackmon, M. L., Bonan, G. B., Bretherton, C. S., Carton, J. A., Chang, P., Doney, S. C., Hack, J. J., Henderson, T. B., Kiehl, J. T., Large, W. G., McKenna, D. S., Santer, B. D., and Smith, R. D., 2006a: The community climate system model: CCSM3. Submitted, *J. Climate*.

Collins, W. D., Rasch, P. J., Boville, B. A., Hack, J. J., McCaa, J. R., L.Williamson, D., Briegleb, B. P., Bitz, C. M., Lin, S.-J., and Zhang, M., 2006b: The formulation and atmospheric simulation of the Community Atmosphere Model: CAM3. Submitted, *J. Climate*.

Conil, S., and Hall, A., 2006: Local regimes of atmospheric variability: a case study of Southern California. *Journal of Climate*, **19**(17), 4308–4325.

Council, N. R., 2009: Restructuring Federal Climate Research to Meet the Challenges of Climate Change.

de Szoeke, S. P., and Bretherton, C. S., 2004: Quasi-lagrangian large eddy simulations of cross-equatorial flow in the East Pacific atmospheric boundary layer. *J. Atmospheric Sciences*, **61**, 1837–1858.

Delworth, T. L., Broccoli, A. J., Rosati, A., Stouffer, R., Balaji, V., Beesley, J. A., Cooke, W. F., Dixon, K. W., Dunne, J., Durachta, K. D. J. W., Findell, K. L., Ginoux, P., Gnanadesikan, A., Gordon, C. T., Griffies, S. M., Gudgel, R., Harrison, M. J., andR. S. Hemler, I. M. H., Horowitz, L. W., Klein, S. A., Knutson, T. R., Kushner, P. J., Langenhorst, A. R., amd S. J. Lin, H. C. L., Lu, J., Malyshev, S. L., Milly, P. C. D., Ramaswamy, V., Russell, J., Schwarzkopf, M. D., dn J. J. Sirutis, E. S., Spelman, M. J., Stern, W. F., Winton, M., Wittenberg, A. T., Wyman, B., Zeng, F., and Zhang, R., 2006: GFDL's CM2 global coupled climate models – Part 1: Formulation and simulation characteristics. *Journal of Climate*, **19**, 643–674.

Deser, C., Bates, J. J., and Wahl, S., 1993: The influence of sea-surface temperature-gradients on stratiform cloudiness along the equatorial front in the Pacific Ocean. *J. Climate*, **6**, 1172–1180.

Deser, C., Capotondi, A., Saravanan, R., and Phillips, A. S., 2006: Tropical pacific and Atlantic climate variability in ccsm3. *J. Climate*, **19**, 2451–2481.

Deser, C., and Wallace, J. M., 1990: Large-scale atmospheric circulation features of warm and cold episodes in the tropical Pacific. *J. Climate*, **3**, 1254–1281.

Dorman, C., 1987: Possible role of gravity currents in northern California's coastal summer wind reversals. *Journal of Geophysical Research*, **92**(C2), 1497–1506.

Dorman, C., and Winant, C., 1995: Buoy observations of the atmosphere along the west coast of the United States. *Journal of Geophysical Research*, **100**, 16029–16044.

Dorman, C., and Winant, C., 2000: The structure and variability of the marine atmosphere around the Santa Barbara Channel. *Monthly Weather Review*, **128**(2), 261–282.

Dvorak, M. J., Archer, C. L., and Jacobson, M. Z., 2010: California offshore wind energy potential. *Renewable Energy*, **35**(6), 1244–1254.

Efron, B., and Tibshirani, R., 1993: *An introduction to the bootstrap*, volume 57. Chapman & Hall, Boca Raton, FL.

Elliott, D., Holladay, C., Barchet, W., Foote, H., and Sandusky, W., 1987: Wind energy resource atlas of the United States.

Elliott, D., and Schwartz, M., 2005: Development and Validation of High-Resolution State Wind Resource Maps for the United States. Technical report, NREL/TP-500-38127, National Renewable Energy Lab., Golden, CO (US).

Elliott, D., Wendell, L., and Gower, G., 1991: An assessment of the available windy land area and wind energy potential in the contiguous United States. Technical report, PNL-7789, Pacific Northwest Lab., Richland, WA (United States).

Garcia-Bustamante, E., Gonzalez-Rouco, J., Jimenez, P., Navarro, J., and Montavez, J., 2008: The influence of the Weibull assumption in monthly wind energy estimation. *Wind Energy*, **11**(5).

Gershunov, A., and Barnett, T., 1998: Interdecadal modulation of ENSO teleconnections. *Bulletin of the American Meteorological Society*, **79**(12), 2715–2725.

Giebel, G., Brownsword, R., and Kariniotakis, G., 2003: The state-of-the-art in short-term prediction of wind power. A literature overview. *Risoe National Laboratory.*

Gipe, P., 1995: *Wind energy comes of age.* John Wiley Sons., Inc.

Green, M., Myrup, L., and Flocchini, R., 1992: A method for classification of wind field patterns and its application to Southern California. *International Journal of Climatology*, **12**(2).

Guérémy, J., Déqué, M., Braun, A., and Piedelièvre, J., 2005: Actual and potential skill of seasonal predictions using the CNRM contribution to DEMETER: coupled versus uncoupled model. *Tellus. Series A: Dynamic Meteorology and Oceanography*, **57**(3), 308–319.

Hahn, C. J., and Warren, S. G., 1999: Extended edited synoptic cloud reports from ships and land stations over the globe, 1952-1996. Numerical Data Package NDP026C, Carbon Dioxide Information Analysis Center, Oak Ridge National Laboratory, Oak Ridge, TN 37831-6335.

Hamilton, G., 1986: National Data Buoy Center Programs. *Bulletin of the American Meteorological Society*, **67**(4), 411–415.

Hashizume, H., Xie, S., Fujiwara, M., Shiotani, M., Watanabe, T., Tanimoto, Y., Liu, W., and Takeuchi, K., 2002: Direct observations of atmospheric boundary layer response to SST variations associated with tropical instability waves over the eastern equatorial Pacific. *AGU Fall Meeting Abstracts*, D8+.

Hashizume, H., Xie, S.-P., Liu, W. T., and Takeuchi, K., 2001: Local and remote atmospheric response to tropical instability waves: A global view from space. , **106**, 10173–10186.

Haslett, J., and Raftery, A., 1989: Space-time modelling with long-memory dependence: assessing Ireland's wind power resource. *Applied Statistics*, 1–50.

Hastie, T., Tibshirani, R., and Friedman, J., 2001: *The elements of statistical learning: data mining, inference, and prediction: with 200 full-color illustrations*. Springer, New York.

Hawkins, D., Blatchford, J., and Makarov, Y., 2007: Wind Integration Issues and Solutions in California. In *IEEE Power Engineering Society General Meeting, 2007*, 1–9.

Hewitson, B., and Crane, R., 2002: Self-organizing maps: applications to synoptic climatology. *Climate Research*, **22**(1), 13–26.

Holtslag, A. A. M., and Boville, B. A., 1993: Local versus nonlocal boundary-layer diffusion in a global climate model. *J. Climate*, **6**, 1825–1842.

Hsu, S., Meindl, E., and Gilhousen, D., 1994: Determining the power-law wind-profile exponent under near-neutral stability conditions at sea. *Journal of Applied Meteorology*, **33**(6), 757–765.

Hughes, M., and Hall, A., 2009: The dynamics of the Santa Ana winds. *Clim. Dyn.*

Iacobellis, S., Norris, J., Kanamitsu, M., Tyree, M., and Cayan, D., 2009: Climate variability and California low-level temperature inversions. Technical Report CEC-500-2009-020-D, California Climate Change Center.

IPCC, 2000: Emissions Scenarios. A Special Report of Working Group II of the Intergovernmental Panel on Climate Change.

Jiang, Q., Doyle, J., Haack, T., Dvorak, M., Archer, C., and Jacobson, M., 2008: Exploring wind energy potential off the California coast. *Geophysical Research Letters*, **35**(20), L20819.

Jimenez, P., Gonzalez-Rouco, J., Montavez, J., Garcia-Bustamante, E., and Navarro, J., 2008: Climatology of wind patterns in the northeast of the Iberian Peninsula. *International Journal of Climatology.*

Johnson, D., and Uccellini, L., 1983: A comparison of methods for computing the sigma-coordinate pressure gradient force for flow over sloped terrain in a hybrid theta-sigma model. *Monthly Weather Review*, **111**(4), 870–886.

Kalnay, E., Kanamitsu, M., Kistler, R., Collins, W., Deaven, D., Gandin, L., Irdell, M., Saha, S., White, G., Woollen, J., Zhu, Y., Chelliah, M., Ebisuzaki, W., Higgins, W., Janowiak, J., Mo, K. C., Ropelewski, C., Wang, J., Leetmaa, A., Reynolds, R., Jenne, R., and Joseph, D., 1996: The NCEP/NCAR 40-year reanalysis project. *Bulletin Am. Meteorol. Soc.*, **77**, 437–471.

Kanamaru, H., and Kanamitsu, M., 2007: 57-Year California Reanalysis Downscaling at 10km (CaRD10) Part II. Comparison with North American Regional Reanalysis. *Journal of Climate*, **20**, 5553–71.

Kanamitsu, M., and Kanamaru, H., 2007: 57-Year California Reanalysis Downscaling at 10km (CaRD10) Part I. System Detail and Validation with Observations. *Journal of Climate*, **20**, 5527–52.

Karl, T., Quayle, R., and Groisman, P., 1993: Detecting climate variations and change: New challenges for observing and data management systems. *Journal of climate*, **6**(8), 1481–1494.

Keith, D., DeCarolis, J., Denkenberger, D., Lenschow, D., Malyshev, S., Pacala, S., and Rasch, P., 2004: The influence of large-scale wind power on global climate. *Proceedings of the National Academy of Sciences*, **101**(46), 16115–16120.

Klein, S. A., 1997: Synoptic variability of low-cloud properties and meteorological parameters in the subtropical trade wind boundary layer. *J. Climate*, **10**, 2018–2039.

Klein, S. A., and Hartmann, D. L., 1993: The seasonal cycle of low stratiform clouds. *J. Climate*, **6**, 1587–1606.

Klein, S. A., Hartmann, D. L., and Norris, J. R., 1995: On the relationships among low-cloud structure, sea-surface temperature, and atmospheric circulation in the summertime northeast Pacific. *J. Climate*, **8**, 1140–1155.

Kohonen, T., 2001: *Self-Organizing Maps.* Springer-Verlag, New York, third edition.

Larson, K., and Westrick, K., 2006: Short-term wind forecasting using off-site observations. *Wind Energy*, **9**.

Leathers, D., and Palecki, M., 1992: The Pacific/North American teleconnection pattern and United States climate. Part II: Temporal characteristics and index specification. *Journal of Climate*, **5**(7), 707–716.

Leathers, D., Yarnal, B., and Palecki, M., 1991: The Pacific/North American teleconnection pattern and United States climate. Part I: Regional temperature and precipitation associations. *Journal of Climate*, **4**(5), 517–528.

Leith, C., 1973: The Standard Error of Time-Average Estimates of Climatic Means. *Journal of Applied Meteorology*, **12**(6).

Li, M., and Li, X., 2005: MEP-type distribution function: a better alternative to Weibull function for wind speed distributions. *Renewable energy*, **30**(8), 1221–1240.

Lilly, D., 1968: Models of cloud-topped mixed layers under a strong inversion. *Quart. J. Roy. Meteor. Soc*, **94**, 292–309.

Lindzen, R. S., and Nigam, S., 1987: On the Role of Sea Surface Temperature Gradients in Forcing Low-Level Winds and Convergence in the Tropics. *Journal of Atmospheric Sciences*, **44**, 2418–2436.

Lock, A. P., Brown, A. R., Bush, M. R., Martin, G. M., and Smith, R. N. B., 2000: A new boundary layer mixing scheme. Part I: Scheme description and single-column model tests. *Monthly Weather Rev.*, **128**, 3187–3199.

Lu, X., M.B., M., and Kiviluomac, J., 2009: Global potential for wind-generated electricity. *Proceedings of the National Academy of Sciences*, **Published before print, 22 June**, 1–6.

Ludwig, F., Horel, J., Whiteman, C., Dreveton, C., Guillou, Y., Pezzoli, A., Tedeschi, G., Resch, F., Nesbitt, S., Zipser, E., et al., 2004: Using EOF Analysis to Identify Important Surface Wind Patterns in Mountain Valleys. *Journal of Applied Meteorology*, **43**(7).

Ma, C.-C., Mechoso, C. R., Robertson, A. W., and Arakawa, A., 1996: Peruvian Stratus Clouds and the Tropical Pacific Circulation: A Coupled Ocean-Atmosphere GCM Study. *Journal of Climate*, **9**, 1635–1645.

Mahrer, Y., and Pielke, R., 1977: A numerical study of the airflow over irregular terrain. *Beiträge zur Physik der Atmosphäre*, **50**(1), 98–113.

Mansbach, D., and Cayan, D., 2010a: Climatology and meteorological influences on california's wind energy resource. part 1: General characteristics and seasonal cycle.

Mansbach, D., and Cayan, D., 2010b: Climatology and meteorological influences on california's wind energy resource. part 2: Synoptic and diurnal characteristics.

Mantua, N., Hare, S., Zhang, Y., Wallace, J., and Francis, R., 1997: A Pacific interdecadal climate oscillation with impacts on salmon production. *Bulletin of the American Meteorological Society*, **78**(6), 1069–1079.

Marsland, S., Haak, H., Jungclaus, J., Latif, M., and Roske, F., 2003: The Max-Planck-Institute global ocean/sea ice model with orthogonal curvilinear coordinates. *Ocean Modelling*, **5**(2), 91–127.

Martin-Rodriguez, G., and Caceres-Hernandez, J., 2005: Modelling the hourly Spanish electricity demand. *Economic Modelling*, **22**(3), 551–569.

Mass, C., Ovens, D., Westrick, K., and Colle, B., 2002: Does increasing horizontal resolution produce more skillful forecasts? *Bulletin of the American Meteorological Society*, **83**(3), 407–430.

Maurer, E., Wood, A., Adam, J., Lettenmaier, D., and Nijssen, B., 2002: A long-term hydrologically based dataset of land surface fluxes and states for the conterminous United States. *Journal of Climate*, **15**(22), 3237–3251.

McSharry, P., Bouwman, S., and Bloemhof, G., 2005: Probabilistic forecasts of the magnitude and timing of peak electricity demand. *IEEE Transactions on Power Systems*, **20**(2), 1166–1172.

Meindl, E., and Hamilton, G., 1992: Programs of the National Data Buoy Center. *Bulletin of the American Meteorological Society*, **73**(7), 985–993.

Mesinger, F., DiMego, G., Kalnay, E., Mitchell, K., Shafran, P., Ebisuzaki, W., Jović, D., Woollen, J., Rogers, E., Berbery, E., et al., 2006: North American regional reanalysis. *Bulletin of the American Meteorological Society*, **87**(3), 343–360.

Miller, N., and Schlegel, N., 2006: Climate change projected fire weather sensitivity: California Santa Ana wind occurrence. *Geophysical Research Letters*, **33**(15), L15711.

Miller, S., Keim, B., Talbot, R., and Mao, H., 2003: Sea breeze: Structure, forecasting, and impacts. *Reviews of geophysics*, **41**(3), 1011.

Mudelsee, M., 2003: Estimating Pearson's correlation coefficient with bootstrap confidence interval from serially dependent time series. *Mathematical Geology*, **35**(6), 651–665.

Najac, J., Boe, J., and Terray, L., 2009: A multi-model ensemble approach for assessment of climate change impact on surface winds in france. *Climate Dynamics*, **32**(5), 615–634.

Norris, J. R., 1998a: Low cloud type over the ocean from surface observations. Part I: Relationship to surface meteorology and the vertical distribution of temperature and moisture. *J. Climate*, **11**, 369–382.

Norris, J. R., 1998b: Low cloud type over the ocean from surface observations. Part II: Geographical and seasonal variations. *J. Climate*, **11**, 383–403.

Norris, J. R., and Iacobellis, S. F., 2005: North Pacific Cloud Feedbacks Inferred from Synoptic-Scale Dynamic and Thermodynamic Relationships. *Journal of Climate*, **18**, 4862–4878.

Norris, J. R., and Leovy, C. B., 1994: Interannual variability in stratiform cloudiness and sea-surface temperature. *J. Climate*, **7**, 1915–1925.

Norris, J. R., and Weaver, C. P., 2001: Improved techniques for evaluating GCM cloudiness applied to the NCAR ccm3. *J. Climate*, **14**, 2540–2550.

Ookouchi, Y., Segal, M., Kessler, R., and Pielke, R., 1984: Evaluation of soil moisture effects on the generation and modification of mesoscale circulations. *Monthly Weather Review*, **112**(11), 2281–2292.

Paluch, I. R., McFarquhar, G., Lenschow, D. H., and Zhu, Y., 1999: Marine boundary layers associated with ocean upwelling over the eastern equatorial Pacific ocean. *J. Geophysical Research-atmospheres*, **104**, 30913–30936.

Park, S., and Leovy, C. B., 2004: Marine low-cloud anomalies associated with ENSO. *J. Climate*, **17**, 3448–3469.

Petersen, E., Mortensen, N., Landberg, L., Højstrup, J., and Frank, H., 1999: Wind power meteorology. Part I: climate and turbulence. *Wind Energy*, **1**(1), 2–22.

Peterson, E., and Hennessey Jr, J., 1978: On the use of power laws for estimates of wind power potential. *Journal of Applied Meteorology*, **17**(3), 390–394.

Physick, W., 1980: Numerical experiments on the inland penetration of the sea breeze. *Quart. J. Roy. Meteor. Soc*, **106**(450), 735–746.

Politis, D., and Romano, J., 1994: The Stationary Bootstrap. *Journal of the American Statistical Association*, **89**(428).

Pryor, S., and Barthelmie, R., 2003: Long-term trends in near-surface flow over the Baltic. *International Journal of Climatology*, **23**(3), 271–289.

Pryor, S., Barthelmie, R., and Kjellstrom, E., 2005a: Potential climate change impact on wind energy resources in northern Europe: analyses using a regional climate model. *Climate Dynamics*, **25**(7), 815–835.

Pryor, S., Barthelmie, R., and Schoof, J., 2006: Inter-annual variability of wind indices across Europe. *Wind Energy*, **9**.

Pryor, S., Barthelmie, R., Young, D., Takle, E., Arritt, R., Flory, D., Gutowski Jr, W., Nunes, A., and Roads, J., 2009: Wind speed trends over the contiguous United States. *Journal of Geophysical Research-Atmospheres*, **114**(D14), D14105.

Pryor, S., Schoof, J., and Barthelmie, R., 2005b: Climate change impacts on wind speeds and wind energy density in northern Europe: empirical downscaling of multiple AOGCMs. *Climate Research*, **29**(3), 183.

Pyatt, H. E., Albrecht, B. A., Fairall, C., Hare, J. E., Bond, N., Minnis, P., and Ayers, J. K., 2005: Evolution of marine atmospheric boundary layer structure across the cold tongue-ITCZ complex. *J. Climate*, **18**, 737–753.

Ramachandran, G., Rao, K., and Krishna, K., 1980: An Observational Study of the Boundary-Layer Winds in the Exit Region of a Mountain Gap. *Journal of Applied Meteorology*, **19**(7), 881–888.

Ramanathan, V., Cess, R. D., Harrison, E. F., Minnis, P., Barkstrom, B. R., Ahmad, E., and Hartmann, D., 1989: Cloud-Radiative Forcing and Climate: Results from the Earth Radiation Budget Experiment. *Science*, **243**, 57–63.

Raphael, M., 2003: The santa ana winds of california. *Earth Interactions*, **7**(8).

Rasmusson, E. M., and Carpenter, T. H., 1982: Variations in tropical sea-surface temperature and surface wind fields associated with the southern oscillation El Niño. *Monthly Weather Rev.*, **110**, 354–384.

Roeckner, E., Bauml, G., Bonaventura, L., Brokopf, R., Esch, M., Giorgetta, M., Hagemann, S., Kirchner, I., Kornblueh, L., Manzini, E., et al., 2003: The atmospheric general circulation model ECHAM5: part 1: model description.

Ronca, R. E., and Battisti, D. S., 1997: Anomalous Sea Surface Temperatures and Local Air-Sea Energy Exchange on Intraannual Timescales in the Northeastern Subtropical Pacific*. *Journal of Climate*, **10**, 102–117.

Rossow, W. B., and Schiffer, R. A., 1999: Advances in Understanding Clouds from ISCCP. *Bulletin of the American Meteorological Society*, **80**, 2261–2288.

Rowson, D., and Colucci, S., 1992: Synoptic climatology of thermal low-pressure systems over south-western North America. *International Journal of Climatology*, **12**(6).

Rozendaal, M. A., Leovy, C. B., and Klein, S. A., 1995: An observational study of diurnal variations of marine stratiform cloud. *J. Climate*, **8**, 1795–1809.

Rozendaal, M. A., and Rossow, W. B., 2003: Characterizing some of the influences of the general circulation on subtropical marine boundary layer clouds. *J. Atmospheric Sciences*, **60**, 711–728.

Sailor, D., Hu, T., Li, X., and Rosen, J., 2000: A neural network approach to local downscaling of GCM output for assessing wind power implications of climate change. *Renewable energy*, **19**(3), 359–378.

Sailor, D., Smith, M., and Hart, M., 2008: Climate change implications for wind power resources in the Northwest United States. *Renewable Energy*, **33**(11), 2393–2406.

Segal, M., Avissar, R., McCumber, M., and Pielke, R., 1988: Evaluation of vegetation effects on the generation and modification of mesoscale circulations. *Journal of the Atmospheric Sciences*, **45**(16), 2268–2293.

Segal, M., Schreiber, W., Kallos, G., Rodi, A., Weaver, J., and Pielke, R., 1989: The impact of crop areas in northeast Colorado on midsummer mesoscale thermal circulations. *Mon. Wea. Rev*, **117**, 809–825.

Skamarock, W., Klemp, J., Dudhia, J., Gill, D., Barker, D., Duda, M., Huang, X., Wang, W., and Powers, J., 2008: A description of the Advanced Research WRF Version 3. Technical report, Technical Report NCAR/TN475+ STR, National Center for Atmospheric Research TECHNICAL NOTE, Boulder (Co).

Solman, S., and Nuñez, M., 1999: Local estimates of global climate change: A statistical downscaling approach. *International Journal of Climatology*, **19**(8), 835–861.

Solomon, S., Qin, D., Manning, M., Chen, Z., Marquis, M., Averyt, K., Tignor, M., and Miller, H., 2008: *Climate change 2007: the physical science basis.* Cambridge University Press, Cambridge, New York, Melbourne, Madrid, Cape Town, Singapore, São Paulo, Delhi.

Stephens, G. L., 2005: Cloud feedbacks in the climate system: A critical review. *J. Climate*, **18**(2), 237–273.

Stewart, J., Whiteman, C., Steenburgh, W., and Bian, X., 2002: A climatological study of thermally driven wind systems of the US Intermountain West. *Bulletin of the American Meteorological Society*, **83**(5), 699–708.

Straus, D., and Shukla, J., 2002: Does ENSO force the PNA? *Journal of Climate*, **15**(17), 2340–2358.

Stull, R. B., 1988: *An Introduction to Boundary Layer Meteorology.* Kluwer Academic Press, Dordrecht, The Netherlands.

Taylor, S., Cayan, D., Graham, N., and Georgakakos, K., 2008: Northerly surface winds over the eastern North Pacific Ocean in spring and summer. *Journal of Geophysical Research-Atmospheres*, **113**(D2), D02110.

Tennekes, H., 1973: A model for the dynamics of the inversion above a convective boundary layer. *Journal of the atmospheric sciences*, **30**(4), 558–567.

Thompson, D., and Wallace, J., 2000: Annular modes in the extratropical circulation. Part I: Month-to-month variability. *Journal of Climate*, **13**(5), 1000–1016.

Tiedtke, M., 1993: Representation of clouds in large-scale models. *Monthly Weather Rev.*, **121**, 3040–3061.

von Storch, H., and Weisse, R., 2008: Regional storm climate and related marine hazards in the northeast atlantic. In *Climate Extremes and Society*, editors H. Diaz, and R. Murnane. Cambridge Univ Pr, Cambridge, UK.

Wallace, J., and Gutzler, D., 1981: Teleconnections in the geopotential height field during the Northern Hemisphere winter. *Monthly Weather Review*, **109**(4), 784–812.

Wallace, J., Zhang, Y., and Lau, K., 1993: Structure and seasonality of interannual and interdecadal variability of the geopotential height and temperature fields in the Northern Hemisphere troposphere. *Journal of Climate*, **6**(11), 2063–2082.

Wallace, J. M., Mitchell, T. P., and Deser, C., 1989: The influence of sea-surface temperature on surface wind in the eastern equatorial Pacific - seasonal and interannual variability. *J. Climate*, **2**, 1492–1499.

Wang, J. H., Cole, H. L., Carlson, D. J., Miller, E. R., Beierle, K., Paukkunen, A., and Laine, T. K., 2002: Corrections of humidity measurement errors from the Vaisala RS80 radiosonde - Application to TOGA COARE data. *J. Atmospheric Oceanic Technology*, **19**, 981–1002.

Warner, T., 2004: *Desert meteorology.* Cambridge University Press.

Welch, P., 1967: The use of fast Fourier transform for the estimation of power spectra: a method based on time averaging over short, modified periodograms. *IEEE Transactions on Audio and Electroacoustics*, **15**(2), 70–73.

Westerling, A., Cayan, D., Brown, T., Hall, B., , and Riddle, L., 2004: Climate, Santa Ana winds and autumn wildfires in Southern California. *Eos*, **85**, 31.

Wigley, T., Jones, P., Briffa, K., and Smith, G., 1990: Obtaining sub-grid-scale information from coarse-resolution general circulation model output. *Journal of Geophysical Research*, **95**(D2), 1943–1953.

Wilby, R., and Wigley, T., 1997: Downscaling general circulation model output: a review of methods and limitations. *Progress in Physical Geography*, **21**(4), 530.

Winant, C., and Dorman, C., 1997: Seasonal patterns of surface wind stress and heat flux over the Southern California Bight. *Journal of Geophysical Research*, **102**(C3).

Winant, C., Dorman, C., Friehe, C., and Beardsley, R., 1988: The marine layer off northern California: An example of supercritical channel flow. *Journal of the Atmospheric Sciences*, **45**(23), 3588–3605.

Wittenberg, A. T., Rosati, A., Lau, N. C., and Ploshay, J. J., 2006: Gfdl's CM2 global coupled climate models. Part III: Tropical pacific climate and enso. *J. Climate*, **19**, 698–722.

Woodhouse, C., 1997: Winter climate and atmospheric circulation patterns in the Sonoran Desert region, USA. *International Journal of Climatology*, **17**(8).

Xu, H. M., Xie, S. P., and Wang, Y. Q., 2005: Subseasonal variability of the southeast Pacific stratus cloud deck. *J. Climate*, **18**, 131–142.

Yan, H., and Anthes, R., 1988: The effect of variations in surface moisture on mesoscale circulation. *Monthly Weather Review*, **116**(1), 192–208.

Yin, B. F., and Albrecht, B. A., 2000: Spatial variability of atmospheric boundary layer structure over the eastern equatorial Pacific. *J. Climate*, **13**, 1574–1592.

Yu, B., 2007: The Pacific-North American pattern associated diabatic heating and its relationship to ENSO. *Atmospheric Science Letters*, **8**(4).

Yu, J. Y., and Mechoso, C. R., 1999: Links between annual variations of Peruvian stratocumulus clouds and of SST in the eastern equatorial pacific. *J. Climate*, **12**, 3305–3318.

Zhong, S., Whiteman, C., and Bian, X., 2004: Diurnal evolution of three-dimensional wind and temperature structure in California's Central Valley. *Journal of Applied Meteorology*, **43**(11), 1679–1699.

Zorita, E., and Von Storch, H., 1999: The analog method as a simple statistical downscaling technique: Comparison with more complicated methods. *Journal of Climate*, **12**(8), 2474–2489.